Strongly Correlated Topological Phases

Tianhan Liu

To cite this version:

Tianhan Liu. Strongly Correlated Topological Phases. Strongly Correlated Electrons [cond-mat.str-el]. UPMC, Sorbonne Universites CNRS, 2015. English. NNT : . tel-01270697

HAL Id: tel-01270697
https://theses.hal.science/tel-01270697v1

Submitted on 8 Feb 2016

THÈSE DE DOCTORAT
DE L'UNIVERSITÉ PIERRE ET MARIE CURIE

Spécialité : Physique

École doctorale : Physique en île-de-France

réalisée au

Laboratoire de Physique Théorique et Hautes Energies, UPMC
Centre de Physique Théorique, Ecole Polytechnique

présentée par

Tianhan Liu

pour obtenir le grade de :

DOCTEUR DE L'UNIVERSITÉ PIERRE ET MARIE CURIE

Sujet de la thèse :

Strongly Correlated Topological Phases

soutenue le 28 Septembre 2015

devant le jury composé de :

Mme.	Claudine Lacroix	Rapporteure
Mr.	Frédéric Mila	Rapporteur
Mr.	Sylvain Capponi	Examinateur
Mr.	Philippe Lecheminant	Examinateur
Mme.	Catherine Pépin	Examinatrice
Mr.	Julien Vidal	Examinateur
Mr.	Benoît Douçot	Directeur de thèse
Mme.	Karyn Le Hur	Directrice de thèse
Mr.	Nicolas Regnault	Membre Invité

à Françoise et Alain

Subject : Strongly Correlated Topological Phases

Résumé : This thesis is dedicated largely to the study of theoretical models describing interacting fermions with a spin-orbit coupling. These models (i) can describe a class of 2D iridate materials on the honeycomb lattice or (ii) could be realized artificially in ultra-cold gases in optical lattices. We have studied, in the first part, the half-filled honeycomb lattice model with on-site Hubbard interaction and anisotropic spin-orbit coupling. We find several different phases: the topological insulator phase at weak coupling, and two frustrated magnetic phases, the Néel order and spiral order, in the limit of strong correlations. The transition between the weak and strong correlation regimes is a Mott transition, through which electrons are fractionalized into spins and charges. Charges are localized by the interactions. The spin sector exhibits strong fluctuations which are modeled by an instanton gas. Then, we have explored a system described by the Kitaev-Heisenberg spin Hamiltonian at half-filling, which exhibits a zig-zag magnetic order. While doping the system around the quarter filling, the band structure presents novel symmetry centers apart from the inversion symmetry point. The Kitaev-Heisenberg coupling favors the formation of triplet Cooper pairs around these new symmetry centers. The condensation of these pairs around these non-trivial wave vectors is manifested by the spatial modulation of the superconducting order parameter, by analogy to the Fulde–Ferrell–Larkin–Ovchinnikov (FFLO) superconductivity. The last part of the thesis is dedicated to an implementation of the Haldane and Kane-Mele topological phases in a system composed of two fermionic species on the honeycomb lattice. The driving mechanism is the RKKY interaction induced by the fast fermion species on the slower one.

Keywords : Strongly Correlated Fermions; Spin-Orbit Coupling; Topological Phases; Frustrated Magnetism; Kitaev-Heisenberg Spin Hamiltonian; FFLO Superconductivity.

Contents

Chapter 1

Introduction

Solids are composed of atoms disposed in an array with electrons hopping between them. Analysis of the band structure historically provides a preliminary classification of solids. Solids are basically categorized into metals, semi-conductors and insulators depending on the Fermi level and the gap between bands [1]. Recent developments in condensed matter physics delve into materials which are beyond this simple classification according to band theory. Transition element compound displays a significant correlation between electrons, entailing the Coulumb interaction and Hund coupling [2, 3, 4, 6]. The correlation between electrons can localize electron charges and order spins, entailing the Mott physics. Spin-orbit coupling, designating the coupling between the angular momentum of the orbitals and the magnetic moment of the electrons, comes also into play in these compounds. A major interest has been the implementation of topological insulators by means of the spin-orbit coupling[11]. Topological condensed matter systems are gapped in the bulk while hosting a gapless conducting mode on the edge. The appearance of edge states in such systems is independent of the band structure details, disorder and small deformation of the system. In spite of one possible explanation of the topological system through band inversion[13, 14], a more generic feature characterizing these systems is attributed to topology.

This thesis is dedicated largely to the study of theoretical models describing interacting fermions with a spin-orbit coupling. These models (i) can describe a class of 2D iridate materials on the honeycomb lattice or (ii) could be realized artificially in ultra-cold gases in optical lattices. The competition of the band structure, the spin-orbit coupling and electron correlation makes iridates and systems likewise an arena with a number of exotic phases in competition. Iridate compound has aroused particular interests because the Kitaev-Heisenberg coupling stemming from the spin-orbit coupling implies possible realisation of the Kitaev model on honeycomb lattice [15], a theoretical model with spins fractionalised into Majorana fermions triggering a liquid phase. The Kitaev model enables probably quantum computation in certain regime, motivating the search for materials with ferromagnetic Kitaev coupling. The anisotropy of the Kitaev spin coupling and the link dependent anisotropic spin-orbit coupling may bring about a number of new phases both in the weakly or strongly correlated regime.

The manuscript is organized in the following way: In chapter 1, we give firstly a brief introduction of topology in condensed matter and a succinct presentation of the Mott physics triggered by correlations; then we present a general review of iridates with a schematic phase diagram indicating various phases in different iridate compounds. In chapter 2, we present our work on the half-filled iridate model on the honeycomb lattice in the limit of weak spin-orbit coupling [36]. In chapter 3, we present the doped honeycomb iridate system in the limit of strong spin-orbit coupling, with the possible realization of an inhomogeneous spin-triplet superconductor phase [37]. In chapter 4, we account for our work on the possible realization of topological phases via the engineering of RKKY interaction on a honeycomb heterostructure with two copies of fermions [38].

1.1 Topology in Condensed Matter

Topology is the branch of mathematics that studies the properties of spatial objects from their inherent connnectivity while ignoring the detailed form. Physical phenomemon depending only on the topology of the system are particularly interesting because of its robustness and its exactitude: physical phenomena is free from detailed properties such as disorder, geometry or deformation of the system and observables are quantized with a high precision. One simple quantity that characterizes the topology of a surface is the Chern number which depicts the winding behavior of the surface's tangent bundles.

One of the earlies important discovery in the condensed matter theory related to topology was in quantum Hall systems, in which a 2D electron gas subject to a magnetic field sees a transversal conduction [7, 8]. The Hall conductance in low temperature is quantized with an extremely refined exactitude, independent of disorder and the geometry of the sample. This robust property of the conductance was later understood through its implication with the topology of the system: the electrons in cyclotron motion have a Chern number 1 for each Landau level and the quantization of the Hall conductance is related to the number of Landau levels below the Fermi level in the bulk. In 1998, Haldane proposed another model with zero net magnetic flux, in which chiral anomaly breaks the time-reversal symmetry [10]. Electrons in this model travel with a certain chirality depending on the sign rather than the magnitude of the Haldane mass, which we will explain in the following. The quantum anomalous Hall system illustrated by the Haldane model, though insulating in the bulk, has a chiral edge mode which is conducting. Band electrons in the lower band in the Haldane model has a Chern number 1, which coincide with 1 conducting mode on the edge. In 2005, Kane and Mele proposed a quantum spin Hall model consisting of two Haldane models with opposite Haldane masses, restoring the time-reversal symmetry [11]. The Kane-Mele model has a helical spin current that is conducting on the edge with spin up and spin down move in opposite directions on the edge. The Kane-Mele model has a total Chern number zero, but the $\mathbf{Z}_2$ topological invariant characterizing the twisting of the rank 2 bundle related to time-reversal symmetry illustrates the topology of the quantum spin Hall effect. The topology of the condensed matter systems has also its arena in superconductivity. Superconductor with p-wave orbital symmetry has been theoretically proposed which has a Chern number 1 for the lower Bogoliubov band, and there exists a zero energy mode on the edge for the quasi-particle (Bogoliubon) as a manifestation of the topology of the system [16].

In a general sense, there are systems in condensed matter physics that are insulating in the bulk and metallic on the edge thus enabling the edge transport. The edge transport is robust against impurity, disorder and deformation of the sample, and such a property is related to the topology of the bulk which is characterized by a topological invariant either the Chern number or the $\mathbf{Z}_2$ invariant. Intuitively, two insulators juxtaposed (the world outside the sample is also insulating) both gapped in the bulk with different topological invariant have necessarily a band closure on the edge giving rise to the edge transport, because insulators with different topology cannot be connected to each other without band closure. In Fig. 1.1, we show an example of conducting edge mode for a system characterized by the Chern number.

Generically, there are systems in condensed matter with gapped band that can be described

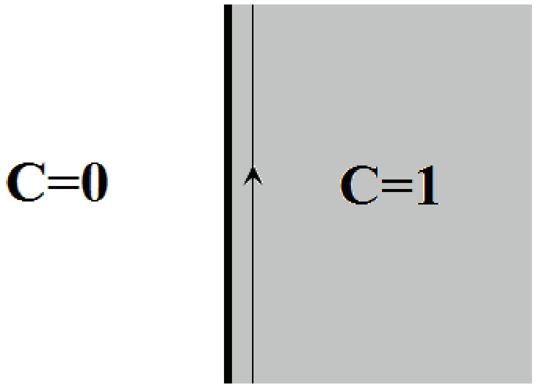

Figure 1.1: Two insulators with different topological invariants juxtaposed has necessarily band closure on the edge, and then metallic edge transport.

by a spin or an isospin that lives on a unit sphere as in equation 1.1.1. The topology of the system is determined by the number of times that the spin or isospin wraps around the unit sphere when electrons are situated in different part of the band or the first Brillouin zone. The wraping behavior of the mapping from the band to the unit sphere can be described by the Chern number, which determines the number of conducting edge mode in such a way that the conductance of a topological system is quantized with regard to the Chern number.

$$\mathcal{H} = \vec{d}(\mathbf{k}) \cdot \vec{\sigma} \quad \vec{d}(\mathbf{k}) : \text{FBZ or band} \to S^2 \tag{1.1.1}$$

in which $\vec{\sigma}$ is the Pauli matrix characterizing the spin or the isospin.

Mathematically speaking, the function $\vec{d}(\mathbf{k})$ which maps one space (the band) into a number of copies of space (unit sphere wrapped around for a certain number of times) is the inverse of the covering map, and Chern number $\mathcal{C}$ in this context characterizes the degree of the cover (or the cardinality of fiber.) We will try to show through several examples, that the conductance σ_{xy} of the system is quantized by the Chern number $\mathcal{C}$ with the resistance quantum $\frac{e^2}{h}$ [17].

$$\sigma_{xy} = \mathcal{C}\frac{e^2}{h} \tag{1.1.2}$$

1.1.1 Quantum Hall System

Topology in the field of condensed matter prospers from the study of quantum Hall effect. The Hall effect appears in 2D electrons subject to magnetic field and transversal electrical field [7]. Electron transport in the perpendicular direction to the electrical magnetic field emerges, which allows us to define a Hall conductance $\sigma_{xy} = \frac{I_\perp}{E} = \frac{BqV}{n_e qV} = \frac{B}{n_e}$, in which $\vec{E} = q\vec{B} \times \vec{V}$ the electric field compensates the Lorentz force of electrons in motion, and the perpendicular electric current $I_\perp = n_e qV$ in which n_e is the electron density, e the electrical charge for one electron and V the velocity of the electrons in motion. The Hall effect under classical regime tells us that the Hall resistance is proportional to the magnetic field. However, experiments in the quantum regime of electrons in the 2D GaAs at $T = 85mK$ show different behavior. Instead of the linear relation, the Hall conductance forms plateaus which are integer multiples of the conductance quantum $\frac{e^2}{h}$.

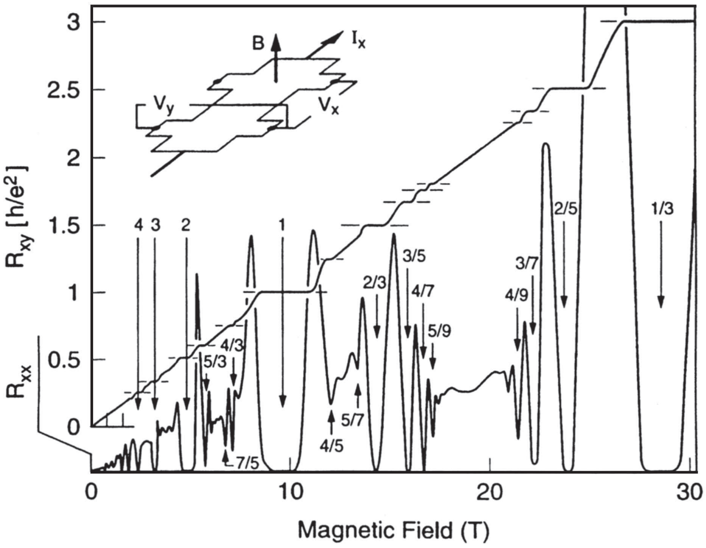

Figure 1.2: The quantum Hall resistance R_{xy} as a function of magnetic field from Tsui et al [8]: The quantum Hall effect consists of 2D electrons under magnetic field, and the Hall conductance as a function of the magnetic field forming the quantum Hall plateaus rather than linear as is the case with classical Hall effect [7, 8]. Electrons in the quantum Hall system undergo a cyclotron motion, with conducting edge mode.

The Hamiltonian of electrons under magnetic field is $\hat{H} = \frac{1}{2m}(\hat{p} - q\hat{A}/c)^2$, and this quantum harmonic oscillator has only one good quantum number p_x if we take the Landau gauge $A_x = By$, $A_y = 0$: $\hat{H} = \frac{\hat{p}_y^2}{2m} + \frac{1}{2m}(\hat{p}_x - \frac{qBy}{c})^2$. Electrons in this quantum harmonic oscillator undergo the cyclotron motion, and the spectrum of the harmonic oscillator form gapped Landau levels:

$$E_n = \hbar\omega_c(n + \frac{1}{2}) \tag{1.1.3}$$

in which $\omega_c = \frac{qB}{mc}$ is the cyclotron frequency, and n is the Landau level index. The Landau level is highly degenerate with translational invariance in the k_x direction and the harmonic oscillator is in the y direction $H_y = \frac{\hat{p}_y^2}{2m} + \frac{1}{2}m\omega_c^2(\hat{y} - y_0)^2$ in which $y_0 = \frac{qBp_x}{c} = l^2 p_x$ with the magnetic length $l = \sqrt{\frac{qB}{c}}$. If the quantum Hall sample has a dimension of $L_x \times L_y$ and we have the quantized momentum $p_x = \frac{2\pi m}{L_x}$, then we have the magnetic translation $\Delta y = l^2 \Delta p_x = \frac{2\pi l^2}{L_x}$. Then we obtain the degeneracy of one Landau level $\Omega_n = \frac{L_y}{\Delta L_y} = \frac{L_x L_y}{2\pi l^2}$ and the filling factor:

$$\nu = \frac{\text{number of electrons}}{\Omega_n} = 2\pi l^2 n_e = \frac{2\pi n_e q B}{c} \tag{1.1.4}$$

By adjusting the magnetic field, we can alter the filling factor of the quantum Hall system. The Hall conductance is proportional to the filling factor with a quantized conductance quantum as shown in experiment (See Fig. 1.2). Filling factor indicates us the number of filled Landau levels, and because of the existence of confining potential (see Fig.1.3), the Landau levels are metallic on the edge giving rise to conducting edge modes and number of edge modes is equal to the number of entirely filled Landau levels, thus leading to the quantized

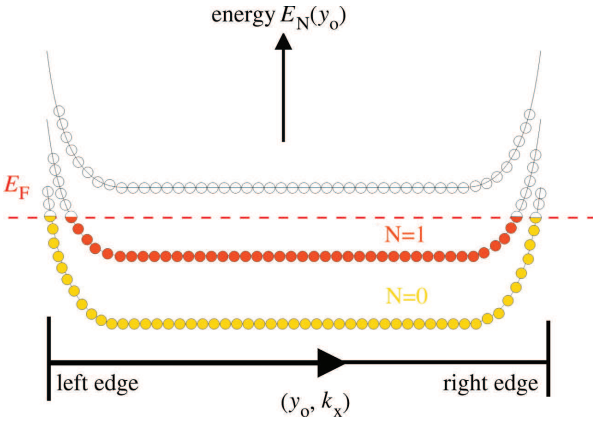

Figure 1.3: Landau levels for a quantum Hall system with periodic condition in the x direction and two edges in the y direction (Figure from Klitzing [9]): 2D electrons under magnetic field form Landau levels, with only one good quantum number k_x. The system is insulating in the bulk and Landau levels crosses the Fermi level on the edge because of the disappearance of the confining energy leading to a metallic edge mode, and the quantized Hall conductance for the edge conduction is proportional to the filling factor of the system: if two Landau levels are filled, the Hall conductance is two times the conductance quantum.

Hall plateaus. Each of these conduction channel contributes one conductance quantum.

$$\sigma_{xy} = \frac{1}{R_{xy}} = \nu\frac{e^2}{h} \tag{1.1.5}$$

The role of topology is obvious in the quantum Hall effect in that electrons in each Landau level are in cyclotron motion with winding number 1, giving a Chern number 1. Since Landau levels are flat band, the Fermi level normally lies in the gap, and the Chern number is just equal to the number of bands below the Fermi level. However, we shall proceed to present a few examples revealing the topological nature of such a phenomenon.

1.1.2 Haldane Model and Chern Number

In order to illustrate the fact that the generic feature in the Hall conductance is the topology rather than the magnetic field, we present here briefly the Haldane model for the quantum anomalous Hall effect with zero magnetic flux [10]. The Haldane model consists of electrons hopping on a graphene lattice which are subject to opposite fluxes on different sublattices (see Fig. 1.4). The total net magnetic flux is zero on the lattice, however the time-reversal symmetry is broken.

$$H_H = \sum_{\langle i,j\rangle} t(c_i^\dagger d_j + d_j^\dagger c_i) + \sum_{\langle\langle i,j\rangle\rangle} it'(c_i^\dagger c_j - d_i^\dagger d_j) - M_S \sum_i (c_i^\dagger c_i - d_i^\dagger d_i) \tag{1.1.6}$$

in which c_i and d_j are electron annihilator operator on the two sublattices A and B, and M_S is the Semenoff mass (See Fig. 1.4). We can diagonalize the Hamiltonian with the Fourier

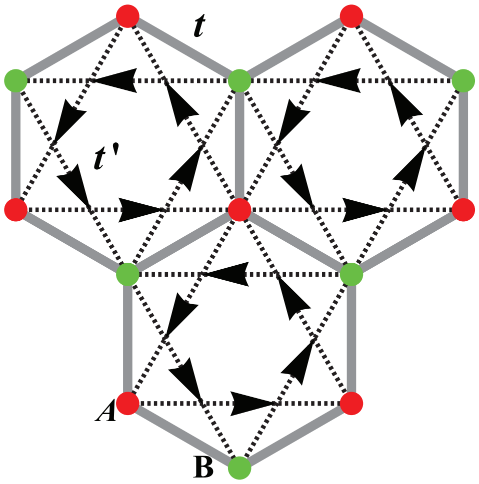

Figure 1.4: The Haldane model consists of electrons hopping on a honeycomb lattice subject to opposite fluxes on the two sublattices. The net magnetic flux is zero but the time reversal symmetry is broken.

transformation, and write the Hamiltonian in terms of the spinor $\Psi_k = (c_k, d_k)^T$

$$H_H = \sum_k \Psi_k^\dagger \mathcal{H}_H(\mathbf{k})\Psi_k \quad \mathcal{H}_H(\mathbf{k}) = \begin{pmatrix} d_{zH}(\mathbf{k}) & d_{xH}(\mathbf{k}) - id_{yH}(\mathbf{k}) \\ d_{xH}(\mathbf{k}) + id_{yH}(\mathbf{k}) & -d_{zH}(\mathbf{k}) \end{pmatrix} = \vec{d}_H(\mathbf{k}) \cdot \vec{\tau} \tag{1.1.7}$$

in which $g(\mathbf{k}) = \sum_{\alpha=x,y,z} e^{i\mathbf{k}\cdot\delta_\alpha}$. $\delta_x = (0,0)\mathbf{a}$, $\delta_y = (-\sqrt{3},0)\mathbf{a}$ and $\delta_z = (\frac{\sqrt{3}}{2}, -\frac{3}{2})\mathbf{a}$. $\mathbf{a}$ is the inter-atomic distance, $d_{xH}(\mathbf{k}) = t\Re eg(\mathbf{k})$, $d_{yH}(\mathbf{k}) = t\Im mg(\mathbf{k})$ and $d_{zH}(\mathbf{k}) = t'(\sin\sqrt{3}k_x\mathbf{a} - 2\sin\frac{\sqrt{3}}{2}k_x\mathbf{a}\cos\frac{3}{2}k_y\mathbf{a}) - M_S$. $\vec{\tau} = (\tau_x, \tau_y, \tau_z)$ are the Pauli matrices for the sublattices. The function $g(\mathbf{k})$ is written in such a way that after a lattice translation the function $g(\mathbf{k})$ is gauge invariant.

We have plotted the band structure of Haldane model at $t' = 0.1t$ in comparison with graphene when $t' = 0$ in Fig. 1.5. There are two bands for the Haldane model and the band projectors are:

$$\begin{aligned} E_H(\mathbf{k}) &= \pm E_{0H}(\mathbf{k}) = \pm\sqrt{|g(\mathbf{k})|^2 + (d_z(\mathbf{k}))^2} = \pm|\vec{d}_H(\mathbf{k})| \\ P_{\pm H}(\mathbf{k}) &= \frac{1}{2}(1 \mp \hat{\vec{d}}_H(\mathbf{k})\cdot\vec{\tau}) \quad \hat{\vec{d}}_H(\mathbf{k}) = \frac{\vec{d}_H(\mathbf{k})}{|\vec{d}_H(\mathbf{k})|} \end{aligned} \tag{1.1.8}$$

The graphene band structure $E_{graphene}(\mathbf{k}) = \pm|g(\mathbf{k})|$ has gap closure at particular points in the first Brillouin zone called Dirac points, and the dispersion relation is linear around these points. There are six of them, separated into two valleys which we denote as $\mathbf{K}_{i\pm}$ (i=1,2,3), around which we have the expansion $g(\mathbf{K}_{i\pm} + \mathbf{k}) \simeq \frac{3t\mathbf{a}}{2}(k_x \pm ik_y)$ and the energy dispersion is photon like:

$$E_{graphene}(\mathbf{K}_\pm + \mathbf{k}) = \pm\frac{3t\mathbf{a}}{2}|\mathbf{k}| \tag{1.1.9}$$

The topology of the system either in the graphene model or the Haldane model is manifested by the mapping $\hat{\vec{d}}_H(\mathbf{k}) : FBZ \to S^2$ from the first Brillouin zone to the unit sphere S^2. We can see that around the Dirac cones of the two valleys, $\hat{\vec{d}}_H(\mathbf{K}_{i\pm} + \mathbf{k})$ rotates respectively

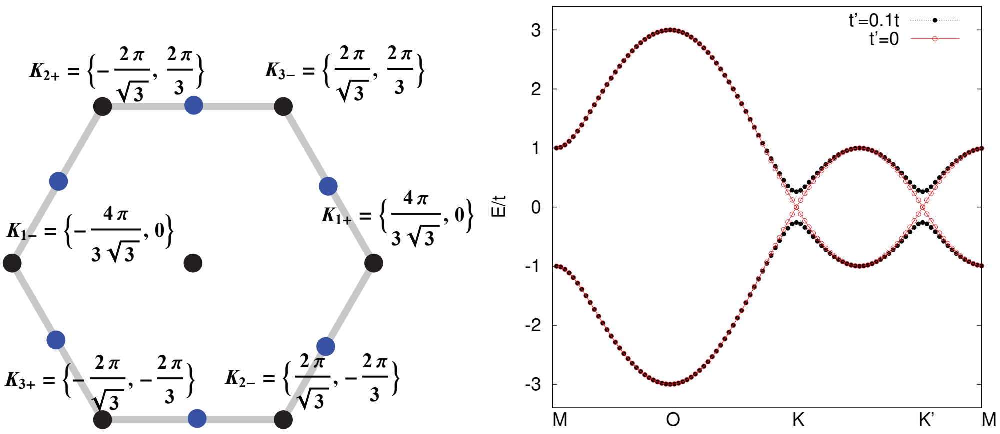

Figure 1.5: *Left panel*: the first Brillouin zone for the honeycomb lattice with Dirac cones at two different valleys $\mathbf{K}_{i\pm}$ in which ± designates the valley. *Right panel*: the flux in the lattice (proportional to the t' next-nearest-neighbour terms) opens a gap at the Dirac cones on the base of the graphene band structure.

in the clockwise and counterclockwise direction in the $x - y$ plane or the opposite chirality. The rotation orientation of a vector is also called chirality. For both graphene and Haldane model, the total chirality is zero for the vector $\hat{\vec{d}}_H(\mathbf{k})$; however, we can define the helicity or the Chern number of the system as follows, which is zero for the graphene model, and non zero for the Haldane model depending on the magnitude of the Semenoff mass.

$$\mathcal{C} = \frac{1}{2\pi}\int_{FBZ} d^2k\hat{d}_{zH}(\mathbf{k})\cdot(\partial_{k_x}\hat{d}_{yH}(\mathbf{k}) - \partial_{k_y}\hat{d}_{xH}(\mathbf{k})), \tag{1.1.10}$$

which is the generic Chern number of the mapping $\hat{\vec{d}}(\mathbf{k})$. Specifically, for the Haldane model we have

$$\mathcal{C}_H = \begin{cases} \mathrm{sign}[t'] & |M_S| < \frac{3\sqrt{3}}{2}t' \\ 0 & |M_S| > \frac{3\sqrt{3}}{2}t' \end{cases} \tag{1.1.11}$$

We remark that there exists a quantum phase transition namely when $|M_S| < \frac{3\sqrt{3}}{2}t'$, the Chern number equals ±1 depending on the sign of t' regardless of its magnitude, while the Chern number is zero when $|M_S| > \frac{3\sqrt{3}}{2}t'$. Graphically, the topological invariant (Chern number) characterizes whether the unit sphere depicted by $\hat{\vec{d}}$ wraps around the origin in the 3D space as shown in right panel of Fig. 1.6.

Numerically, we can generalize the above Chern number calculation to any problem with band electrons, because band projectors are inherently gauge invariant projectors which avoids the ambiguity of the gauge at the border of the first Brillouin zone. Specifically, if we have the band electron projector P_{i-} for the electron band with index i which is under the Fermi level, and the Chern number is:

$$\mathcal{C} = \frac{1}{2\pi i}\int_{FBZ} d^2k \sum_i \mathrm{Tr}[P_{-i}(\vec{k})(\partial_{k_x}P_{-i}(\vec{k}) - \partial_{k_y}P_{-i}(\vec{k}))] \tag{1.1.12}$$

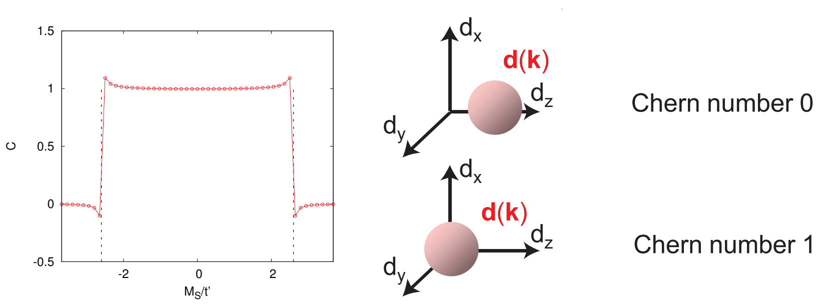

Figure 1.6: The Chern number of the Haldane model as a function of the Semenoff mass M_S calculated numerically by the discretization of 100×100 of the first Brillouin zone. There is a quantum phase transition at $|M_S| = \frac{3\sqrt{3}}{2}t'$ noted by the dashed line. The Chern number counts whether the vector $\hat{\vec{d}}_H$ wraps around the origin.

The numerical calculation of the Chern number is shown in the right panel of Fig. 1.6 as a function of the Semenoff mass M_S, which coincides with the prediction in equation 1.1.11.

As a consequence of the non-zero Chern number of the Haldane model, we have a zero energy edge mode when the model is placed on the cylinder geometry. The more detailed treatment of Hamiltonian on cylinder and the transfer matrix method for the edge state is presented in Sec. 2.1. The zero net magnetic flux in the Haldane model of quantum anomalous Hall effect demonstrates the Chern number as a more intrinsic property for the appearance of the metallic edge mode.

In a general sense, if we have some function $d_z(\mathbf{k}) = d_{zo}(\mathbf{k}) + d_{ze}(\mathbf{k})$ which is the coefficient in front of the matrix τ_z, we call the odd parity part $d_{zo}(\mathbf{k}) = -d_{zo}(-\mathbf{k})$ the Haldane mass and the even parity part $d_{ze}(\mathbf{k}) = d_{ze}(-\mathbf{k})$ Semenoff mass. These two notions will be useful in chapter 4. Since the two valleys of the Dirac points have opposite helicity, $d_z(\mathbf{k})$ has to have opposite sign in the two valley in order that the system is topological with non-zero Chern number.

1.1.3 Kane-Mele Model and Z_2 Topological Invariant

Besides Chern number, there exists also another topological invariant identifying the topology of a system. Spin-orbit coupling can result from the hybridization of the higher angular momentum orbit and it exerts, in fact, opposite magnetic fields upon electrons with opposite spin polarizations, thus making the system two copies of Haldane model coupled together. We introduce the Kane-Mele model consisting of electrons on graphene with spin-orbit coupling [11, 12, 20].

$$H_{KM} = -\sum_{\langle i,j\rangle,\sigma} t c^{\dagger}_{i\sigma} d_{j\sigma} - it' \sum_{\langle\langle i,j\rangle\rangle,\sigma,\sigma'} \sigma^{z}_{\sigma\sigma'} (c^{\dagger}_{i\sigma} c_{j\sigma'} - d^{\dagger}_{i\sigma} d_{j\sigma'}) + h.c. \tag{1.1.13}$$

Again, we can do the Fourier transformation and write down the spinor $\Psi^{\dagger}_k = (c^{\dagger}_{k\uparrow}, d^{\dagger}_{k\uparrow}, c^{\dagger}_{k\downarrow}, d^{\dagger}_{k\downarrow})$:

$$H_{KM} = \sum_k \Psi^{\dagger}_k \mathcal{H}_{KM}(\mathbf{k}) \Psi_k \quad \mathcal{H}_{KM}(\mathbf{k}) = \begin{pmatrix} t'g_z(\mathbf{k}) & tg^*(\mathbf{k}) & 0 & 0 \\ tg(\mathbf{k}) & -t'g_z(\mathbf{k}) & 0 & 0 \\ 0 & 0 & -t'g_z(\mathbf{k}) & tg^*(\mathbf{k}) \\ 0 & 0 & tg(\mathbf{k}) & t'g_z(\mathbf{k}) \end{pmatrix} \tag{1.1.14}$$

in which $g(\mathbf{k}) = \sum_j e^{i\mathbf{k}\cdot\delta_j}$ and $g_z(\mathbf{k}) = (\sin\sqrt{3}k_x - 2\sin\frac{\sqrt{3}}{2}k_x\cos\frac{3}{2}k_y)$. The energy levels are all doubly degenerate:

$$E = \pm\sqrt{(t|g(\mathbf{k})|)^2 + (t'g_z(\mathbf{k}))^2} \tag{1.1.15}$$

The Kane-Mele model respects the time-reversal symmetry, which is absent in the Haldane model. If we denote the time-reversal operator as T, then for spinfull system, the time reversal operator writes as:

$$\begin{aligned} &T = i\sigma_y\hat{C} \quad \& \quad T^2 = -1 \\ &T\hat{X}T^{-1} = \hat{X} \quad T\hat{P}T^{-1} = -\hat{P} \quad T\hat{\vec{L}}T^{-1} = -\hat{\vec{L}} \quad T\hat{\vec{\sigma}}T^{-1} = -\hat{\vec{\sigma}} \end{aligned} \tag{1.1.16}$$

in which the operator $\hat{C}$ is the complex conjugate operator, and $\hat{\vec{L}}$ the angular momentum operator. We can see that the Kane-Mele model consists of actually two copies of Haldane model with Haldane masses with opposite signs. In other words, the spin up model has a Chern number $+1$ and the spin down model has a Chern number of -1 (see Fig. 1.7). On one given edge, we have spin up transport in one direction and spin down transport in the opposite direction. We can therefore construct the effective edge model for only 1 pair of edge states :

$$\mathcal{H}_{edge}(\mathbf{k}) = \begin{pmatrix} v_F k & 0 \\ 0 & -v_F k \end{pmatrix} = v_F k \sigma_z \tag{1.1.17}$$

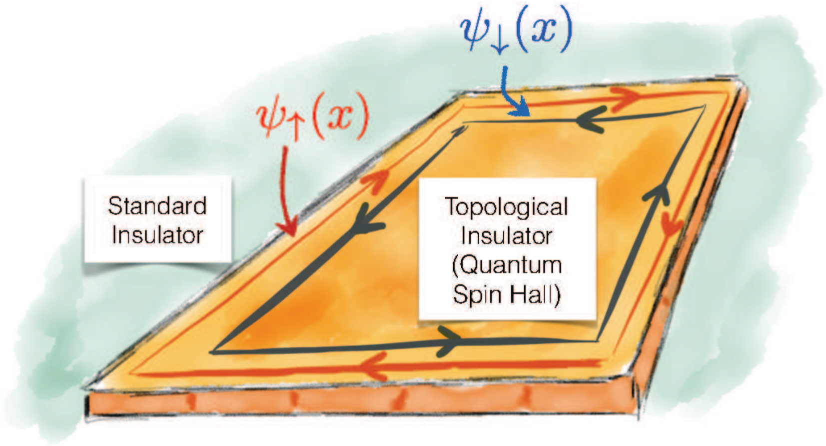

Figure 1.7: The quantum spin Hall effect consists of electrons with opposite spin polarizations travelling in opposite directions on the edge Figure from David Carpentier [139]. The theoretical model for such an effect is the Kane-Mele model which is actually 2 copies of Haldane model with Haldane masses with opposite signs. The Kane-Mele model is protected by the time-reversal invariant symmetry, which entails a $\mathbf{Z}_2$ symmetry.

We can see that any process that opens a gap involves a spin flip term proportional to σ_x, σ_y which breaks the time-reversal symmetry. Therefore, the edge remains metallic for 1 pair of edge states, which is protected by the time-reversal symmetry. However, if we study the effective Hamiltonian for 2 pairs of edge states, Chern number for spin up is $+2$ and Chern number for spin down is -2. We can write down the effective Hamiltonian:

$$\mathcal{H}_{edge}(\mathbf{k}) = \Psi_k^\dagger \begin{pmatrix} v_{F1}k & 0 & 0 & 0 \\ 0 & v_{F2}k & 0 & 0 \\ 0 & 0 & -v_{F1}k & 0 \\ 0 & 0 & 0 & -v_{F2}k \end{pmatrix} \Psi_k \quad \Psi_k^\dagger = (c_{1k\uparrow}^\dagger, c_{2k\uparrow}^\dagger, c_{1k\downarrow}^\dagger, c_{2k\downarrow}^\dagger) \tag{1.1.18}$$

In this case, we can however have one spin scattering processes preserving the time-reversal symmetry which opens the gap, making the edge an insulator, then the topological edge state is not protected by the time-reversal symmetry.

$$\mathcal{H}_{edge}(\mathbf{k}) = \Psi_k^\dagger \begin{pmatrix} v_{F1}k & 0 & 0 & m \\ 0 & v_{F2}k & -m & 0 \\ 0 & -m & -v_{F1}k & 0 \\ m & 0 & 0 & -v_{F2}k \end{pmatrix} \Psi_k \quad \Psi_k^\dagger = (c_{1k\uparrow}^\dagger, c_{2k\uparrow}^\dagger, c_{1k\downarrow}^\dagger, c_{2k\downarrow}^\dagger) \tag{1.1.19}$$

In general, a system with odd number of time-reversal pairs has a metallic edge state and system with even number of pairs can be smoothly deformed into a trivial insulator everywhere gapped. The concerned topology is the $\mathbf{Z}_2$ topology: we can choose a phase such that $\Psi_k = \Psi_{-k}^*$ and for a TI we find that there is no way to define a wave function for every $\mathbf{k}$ and the first Brillouin zone needs to be cut into different regions. The gauge transformations around the boundaries of these regions defines a winding number. The $\mathbf{Z}_2$ invariant arises from the calculation of the winding number of the gauge field around the first Brillouin zone: if it is odd, the system is topological; if even, trivial.

In summary, we have shown several examples ranging from band electron problems such as quantum (anomalous) Hall system and quantum spin Hall system to superconductivity with p-wave symmetry. The quantum anomalous Hall effect can be viewed as a mapping from the band or the first Brillouin zone to the $SU(2)$ sphere in the sublattice isospin space. The topology of the system refers to specifically the number of times that the mapping wraps around the $SU(2)$ sphere. The quantum spin Hall effect involves the Z_2 symmetry, a residual symmetry of the $SU(2)$ symmetry related to the time-reversal symmetry. If we view the world as an insulator separated from the topological system by the edges, then there is necessarily band closure on the edge, since two systems with different topology cannot be connected to each other without band closure.

1.2 Mott Physics

Solids are made of atoms aligned in arrays whose hybridized electron orbitals enables electron hopping from one atom to another, which is firstly described by band theories. Real world materials can be classified according to band theories into four major categories: metal, semi-metal, semi-conductor and insulators. We call the closest superior and inferior band to the Fermi level respectively the conduction and valence band. If the Fermi level lies in the band or the band is partially filled in other terms, we have the conducting metal in which electron propagate in the form of Bloch waves. When the overlap of the conduction band and the valence band is very small, we have a semi-metal with very limited density of states at the Fermi level participating in the conduction. When the Fermi level lies in between the valence and conduction band while the two bands are energetically not very far from each other, we have a semi-conductor with electron and hole like excitation at finite temperature. And when the Fermi level lies in between the two bands that are isolated from each other, we have an insulator in which electron conduction is very hard.

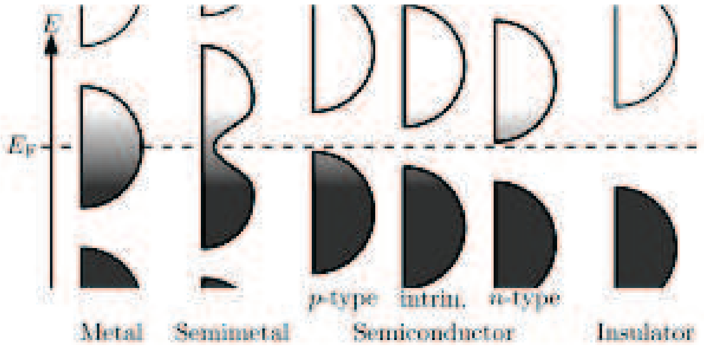

Figure 1.8: From Kittel [5]: Band structure of metal, semi-metal, semi-conductor and insulator.

In spite of its simplicity, the band theories do not manage to categorize the transitional metal compounds, in which there are several orbitals participating in the hybridization. Due to the Coulomb interaction between the electrons, there exists a non-negligible effect of correlation in these transitional metal compounds. People have introduced the Hubbard model in the first place to characterize the behavior of these materials[2]:

$$H = -\sum_{\langle i,j\rangle} t(c^{\dagger}_{i\sigma}c_{j\sigma} + c^{\dagger}_{j\sigma}c_{i\sigma}) + U\sum_{i} n_{i\uparrow}n_{i\downarrow} \tag{1.2.1}$$

in which electron hopping between nearest-neighbour sites is described by the first two terms and the Hubbard onsite interaction depicts the electron-electron interaction on each given site or in each atom. We discuss firstly the half-filled Hubbard model here.

When the Hubbard interaction is strong enough (the strongly correlated regime), we enter the Coulomb blockade regime in which the Hubbard interaction forbids two electrons on the same site, killing the electron hoppings since electrons exchanging their positions is energetically penalized by the Hubbard interaction. The electron charges are therefore localized in this regime making the material an insulator (Mott insulator) and injection of one electron or hole will cost an energy in the order of U. The new origin of this insulating behavior makes the Mott insulator different from the normal insulator in the frame of band theory. In the weakly correlated regime, the correlation renormalizes the conducting behavior predicted by the band theory and this regime is baptized Fermi liquid and the injection of one electron or hole cost nearly zero energy since the band is partially filled. Therefore, there exists a transition between the weakly correlated regime with small Hubbard interaction described largely by the band theory and the strongly correlated regime of Mott insulator vis-à-vis the injection of one electron. This metal-insulator transition is baptized the Mott transition [4].

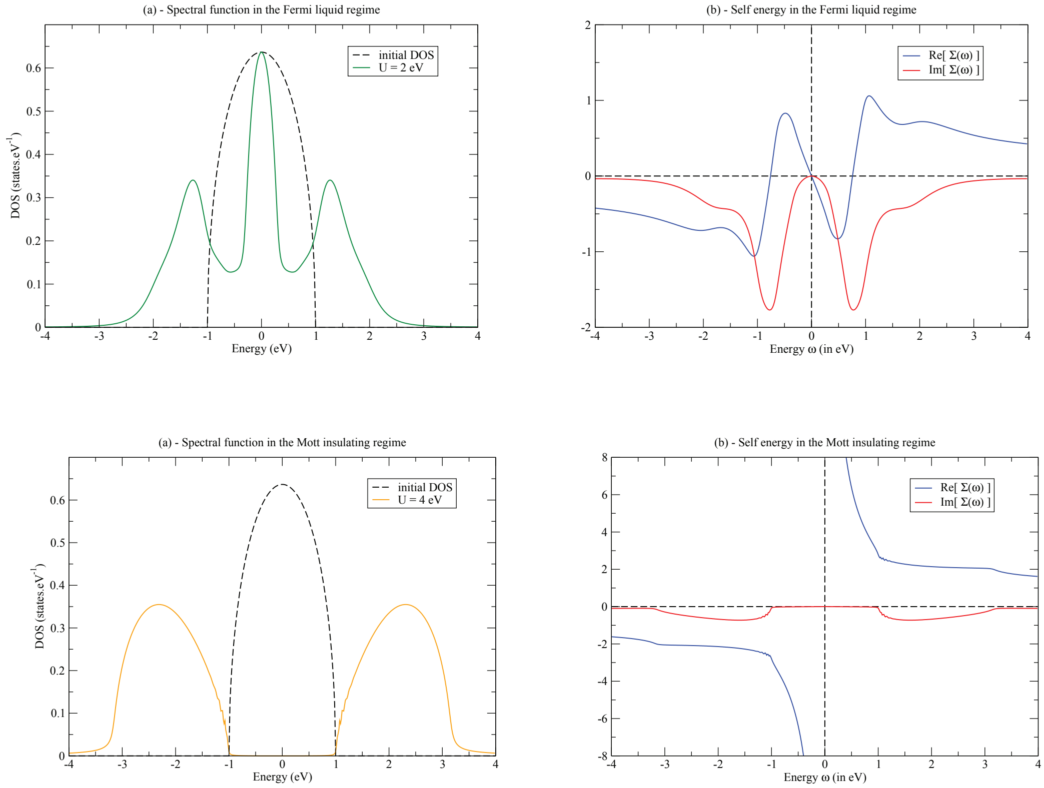
(a) - Spectral function in the Fermi liquid regime

(b) - Self energy in the Fermi liquid regime

(a) - Spectral function in the Mott insulating regime

(b) - Self energy in the Mott insulating regime

Figure 1.9: Figure from thesis of Cyril Martins [115]: The spectral function of the Fermi liquid in the upper panel, in which intermediate Hubbard interaction widen the spectral peak around zero energy and the spectral function of the Coulomb blockade regime in the lower panel when Hubbard interaction is significant enough.

We introduce the spectral function to describe the low energy excitation which corresponds to adding one electron or hole to the system, that quantitatively characterizes the different regimes described above[21, 22].

$$A(k,\omega) = \begin{cases} \sum_\alpha |\langle\Psi_0|\, c_k \,|\Psi_\alpha\rangle|^2 \delta(\omega + \mu + E_0^{(N)} - E_0^{(N+1)}) & (\omega > 0) \\ \sum_\alpha |\langle\Psi_0|\, c_k^\dagger \,|\Psi_\alpha\rangle|^2 \delta(\omega + \mu + E_0^{(N)} - E_0^{(N+1)}) & (\omega < 0) \end{cases} \tag{1.2.2}$$

in which the matrix elements $\langle\Psi_0|\, c_k \,|\Psi_\alpha\rangle$ measure the overlap between the wave function obtained by injection of one electron with momentum k into the ground state wave function with N particles and the excited state $|\Psi_\alpha\rangle$ with N+1 particles.

Experimentally, the ARPES can measure the spectral function directly. In the Fermi liquid regime, the density of states is concentrated around zero energy, while in the strongly correlated limit the density of states is concentrated around the energy scale of the Hubbard interaction due to the Coulomb blockade as shown in Fig. 1.9. The Mott transition is characterized by the splitting of peak at zero energy in the spectral function into two peaks centering around the Hubbard interaction.

In the Mott insulator regime, electrons are localized because of the energy penalisation of the Hubbard interaction. We have one electron per site incapable of propagating in the material, however, virtual processes of electrons exchanging positions are allowed. Knowing that the electron is composed of spin and electron charge, we have, as a result, the spin exchanging places while the charges remain localized. The lowest order of the virtual electron exchange is of second order, and by applying the second order perturbation theory based on the infinite Hubbard limit, we can establish the effective theory for the spins. The effective spin theory indicates us the magnetism in the Mott insulator. In the case of Hubbard model in equation 1.2.1, we can derive the super-exchange Heisenberg model hosting the Néel order:

$$H_{ex} = \sum_{\langle i,j \rangle} J\mathbf{S}_i \cdot \mathbf{S}_j \tag{1.2.3}$$

We have shown in Fig. 1.10 the bipartite Néel order on the square lattice which minimizes the classical energy of the anti-ferromagnetic Heisenberg model derived above. Spins for the Néel order in the two sublattices point in the opposite direction for the ground state.

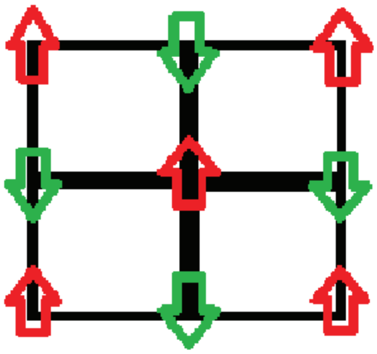

Figure 1.10: The bipartite Néel order on the square lattice which minimizes the classical energy of the anti-ferromagnetic Heisenberg model.

In Fig. 1.11, we have shown the periodic table and this thesis is mainly dedicated to the physics of iridates, the iridium-oxide compounds, which belongs to the transitional metal elements, in which correlation plays an important role. Besides the complication of correlation, the significant spin of the 4d and 5d elements leads to the essential intervention of the spin-orbit coupling in this family of materials. Typical energy scales for this family of material are very close to each other, $W \simeq \lambda \simeq U$ in which W is the band width proportional to the hopping amplitude t for the material, λ is the amplitude of the spin-orbit coupling while U is the on site Hubbard interaction mimicking the Coulomb interaction between electrons. The closeness of the three energy scale makes iridates an arena with several exotic phases in competition.

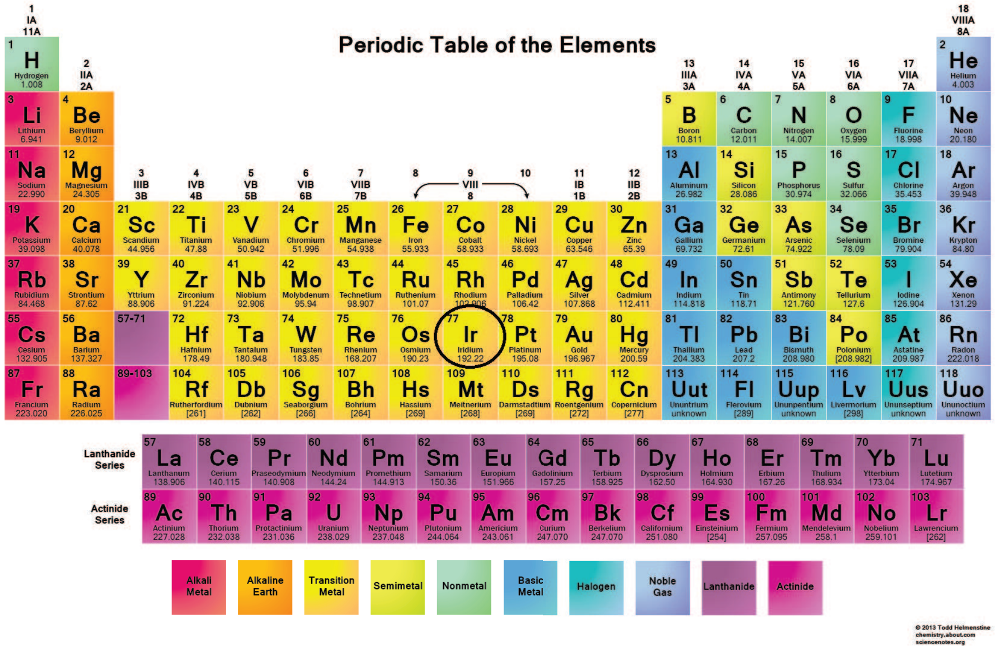

Figure 1.11: The periodic table of elements and the highlighted iridium in the class of transitional metal belonging to the 4d and 5d elements.

1.2.1 Doped Mott Insulators

The half-filled Mott insulator as explained previously hosts an anti-ferromagnetic order stemming from the super-exchange processes while the charges are localized. However, if we dope the system with holes or electrons, states with zero or two electrons on one site will be allowed in the system. If we look at only the Heisenberg J coupling term, states with one surplus electron or one surplus hole on one site contributes zero energy for the links connecting the given site, while the coupling energy for the links connecting two sites both with one electron gives energy $-J$ (anti-ferromagnetism). In order to minimize the energy of the spin coupling interaction $J\mathbf{S}_i \cdot \mathbf{S}_j$, doped electrons and holes tend to form pairs. The hopping terms which are forbidden in the half-filled Mott insulator because of the energy penalisation will re-enter into play in the doped system. The kinetic and coupling term cause respectively the motion and formation of electron or hole pairs, leading to superconductivity in certain conditions.

One effective model for the doped Mott insulator is the t-J model in which the t kinetic term allows for the motion of doped electrons and holes and the J spin-spin coupling favors the coupling of the electron or hole pairs[23]:

$$H_{tJ} = -\sum_{\langle i,j\rangle} t(c^\dagger_{i\sigma}c_{j\sigma} + c^\dagger_{j\sigma}c_{i\sigma}) + J\sum_{\langle i,j\rangle} \mathbf{S}_i \cdot \mathbf{S}_j \qquad (1.2.4)$$

In Fig. 1.12, we have shown one representative phase diagram of doped Mott insulator, which is indicative and not complete: we have not taken in account here all sophisticated physics in the intermediate regime including the quadruple state, the spin and charge density-wave, etc [26, 27, 189, 193, 194]. We merely try to highlight the fact that doping the Mott insulator may give rise to superconductivity in certain conditions considering the intuitive argument that we gave with the two-fold interplay of the kinetic term and the coupling term.

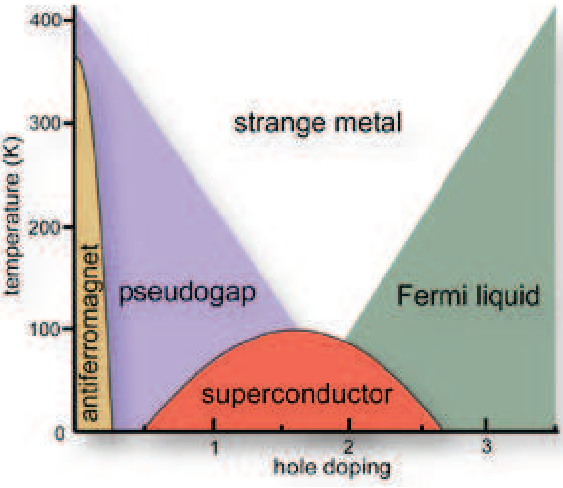

Figure 1.12: Figure from Philip Phillips [19]: The phase diagram of the doped Mott insulator.

1.3 Frustrated Magnetism

We try to show in this section several elements of the magnetic frustration and its complication in a few magnetic orders more complicated than the Néel order (anti-ferromagnetism). Frustration refers to spins in non-trivial positions with underlying conflicting couplings on the lattice, which may lead to complex structures or a plethora of ground states. Some of them exhibits a liquid behavior (alias spin liquid).

1.3.1 Geometrical Frustration

We show a brief formulation of various magnetic frustration scenarios in this section following the review of J.T. Chalker [29]. The first category of frustration comes from the geometry: the real lattice is composed by larger clusters in which antiferromagnetism cannot be satisfied on every links. We define a cluster as a subset of the lattice in which one spin interacts with every other spin in the same cluster. We give two examples here: the honeycomb or Kagomé lattices are composed of triangles while the pyrochlore lattice is composed of tetrahedrons, and the triangles and tetrahedrons satisfy the definition of cluster given above. The minimization of the classical energy retracts to the minimization of the classical energy in the cluster rather than a simple link. We start with the nearest-neighbour Heisenberg model on two different lattices, the triangular and pyrochlore lattices:

$$H = \sum_{\langle i,j \rangle} J \mathbf{S}_i \cdot \mathbf{S}_j \tag{1.3.1}$$

The classical energy minimization can be carried out in the following way: since the lattice consists of clusters, it suffices to study the magnetism in one cluster, specifically we can rewrite the cluster Heisenberg model :

$$H_c = \frac{1}{2} J[(\sum_{i \in \mathcal{C}} \mathbf{S}_i)^2 - N_c \mathbf{S}^2] \tag{1.3.2}$$

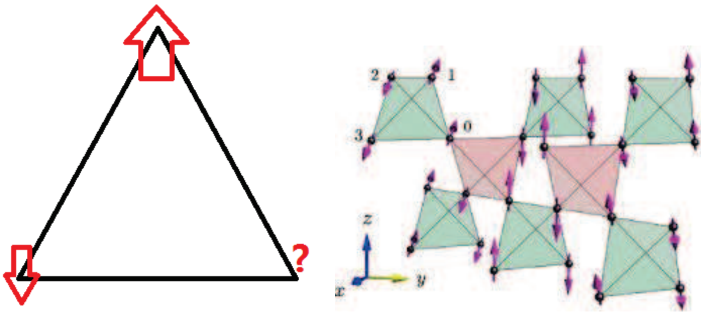

Figure 1.13: The geometrical frustration on the triangular and pyrochlore lattice. The figure of the pyrochlore lattice from E. Choi et al. [140].

in which $\mathcal{C}$ denotes the cluster and N_c the number of spins in the cluster. And naturally we have the condition of the ground state and the ground state energy of the cluster:

$$\sum_{i\in\mathcal{C}} \mathbf{S}_i = 0 \quad E_{c0} = -\frac{JN_c}{2}\mathbf{S}^2 \tag{1.3.3}$$

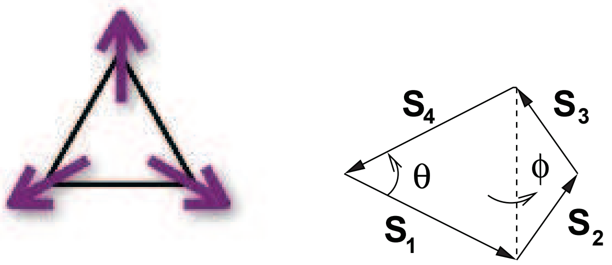

Figure 1.14: Figure from J.T. Chalker [29]: One realisation of the ground state of anti-ferromagnetism on respectively the triangular and the pyrochlore lattice.

The condition in 1.3.3 gives a plethora of states for the ground state. We have shown in Fig. 1.14 one realisation of the ground state on the triangular and pyrochlore lattice. The ground state of the Heisenberg model on the triangular lattice is the 120 degree Néel state with a rotational degree of freedom around the center of the triangle while the ground state of anti-ferromagnetism on the pyrochlore lattice has two degrees of freedom described by angles θ and ϕ. Geometrical frustration in clusters can bring about additional degeneracy (degrees of freedom) in the system; one cluster consisting of N ($N > 2$) spins will have $N - 2$ degrees of freedom.

1.3.2 Order by Disorder

Without losing any generality, we have seen in the previous section the emergence of degeneracy due to the geometry of the lattice, specifically the frustration in the cluster. The geometrical frustration gives us a plethora of ground states (the ground state manifold), indicating that the system is plausibly disordered. However, these classical degenerate ground states may be situated in very different regimes: they experience different classical and quantum fluctuations lifting the degeneracy among them. Thereafter, the ground state manifold may be reduced to a smaller manifold or even simply several points. The system, instead of disordered because of the degeneracy, is probably finally ordered due to the ground state selection in the classical or quantum level [30, 31], which we call order by disorder.

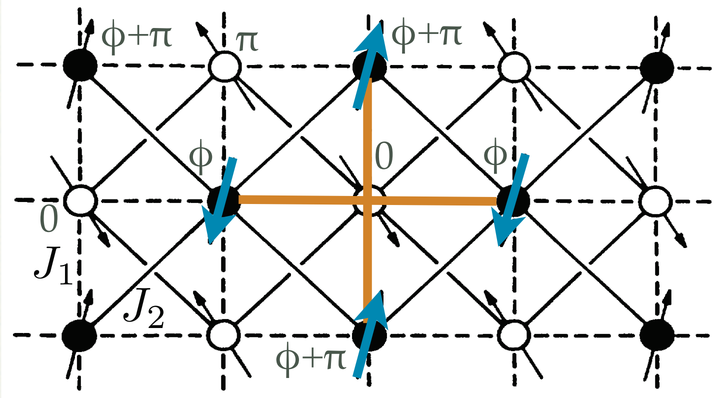

Figure 1.15: The $J_1 - J_2$ model on the square lattice with ϕ designating the angle between the two copies of the tilted sublattices.

We give here a simple example of the $J_1 - J_2$ XY model in the two dimensional square lattice, in which there exists a nearest-neighbour anti-ferromagnetic J_1 coupling and a next-nearest-neighbour anti-ferromagnetic J_2 coupling. The J_1 coupling favors the bipartite Néel state while the J_2 coupling favors a bipartite Néel state in the two tilted sublattices which are also square lattice as shown in Fig. 1.15. The system is frustrated because of the conflict between the two different scénarios. When $J_2 > J_1/2$, there is a continuous family of classical ground states, notably the surplus degrees of freedom of the angle ϕ designating the angle of the Néel order between the two copies of the tilted sublattices. However, if we take into account the classical fluctuation of the Néel order in the tilted square sublattice, then the classical fluctuation of the $J_1 - J_2$ ($J_2 > J_1/2$) model will select a subset of the ground state manifold. Specifically, if we denote the two tilted square sublattices as A and B, and we attribute a little variation on each sublattice such that the angle between the two antiparallel spins is $\pi + \beta$ instead of π, then in the limit of $\beta \to 0$ the classical energy variation will be proportional to:

$$\Delta E_{XY} = [2J_2 + J_1 \cos^2 \phi]\beta^2 \tag{1.3.4}$$

The classical variational energy is proportional to the entropy S, then the free energy is $F = E - TS$. In order to minimize the free energy, the entropy should be maximized and the maximum is reached at $\phi = 0, \pi$. Instead of the whole $U(1)$ symmetry of ϕ, the minimization of the free energy reduces the ground state manifold from $U(1)$ to two points.

We list below a number of possible ingredients that can break the degeneracy to trigger the order by disorder phenomenon:

1. Further neighbour interactions (dipolar, exchange)
2. spin-orbit coupling & crystal fields
3. spin-phonon coupling

4. multiple-spin terms.

The quantum fluctuations can be manifested through the spin wave analysis in the large S limit: around the possible order, we apply a Holstein-Primakoff transformation: we define the z axis as the direction of the order parameter $S_z = S - a^\dagger a$, $S_+ = \sqrt{2S}a$ and $S_- = \sqrt{2S}a^\dagger$ thereafter, we describe the quantum fluctuation as a quantum harmonic oscillator problem whose Casimir energy refers to the zero point fluctuation. We can therefore calculate the expectation value of the spin S_z out of this quantum expansion. Specifically, we calculate the value of the expectation value of the observable $\langle S_z \rangle$. In some frustrated magnetism model, this value $\langle S_z \rangle$ will vanish indicating a total disordered state with a large number of degeneracy [40].

1.3.3 Spin Liquid

Despite the order by disorder phenomenon, some frustrated magnetism model still retains a large number of degeneracy, with soft Goldstone modes connecting various possible degenerate states [32]. The disordered state with a liquid behavior is baptized a spin liquid. Emergence of spin liquid is also closely related to the Mott physics: upon Mott transition electron charges are localized while spins can still exchange their position. One point of view is the spin-charge separation: the physical electrons are cracked into chargeon and spinon and there exists an attractive force between the chargeon and spinon in the form of a gauge field. The spinon has also a band structure: if the spinon band structure is gapless we will have possibly a spin liquid. The gauge field as a clinging force between the chargeon and the spinon is also an important factor in the emergence of spin liquid: if monopoles are confined, the spinons are deconfined and we will probably have a spin liquid, while if the monopoles are deconfined, the spinons are confined, and we will possibly have a long range order. People have proposed a number of quantum spin liquid such as VBS, Z_2 spin liquid, quantum dimer model, etc, which we try not to elaborate here [192, 152, 153, 54].

1.3.4 Kane-Mele-Hubbard Model.

We present in this section a brief review of the Kane-Mele-Hubbard model, which describes the physics of a correlated topological insulator [62]. We have the Hubbard interaction describing the Coulomb interaction between electrons in equation 1.3.5. We try to explain in details the phase diagram of this model and how different phases in the different region of the phase diagram are connected together.

$$\begin{aligned} H =& H_{KM} + H_I \quad H_I = \sum_i U n_{i\uparrow} n_{i\downarrow} \\ H_{KM} =& -\sum_{\langle i,j\rangle,\sigma} t c^\dagger_{i\sigma} d_{j\sigma} - it' \sum_{\langle\langle i,j\rangle\rangle,\sigma,\sigma'} \sigma^z_{\sigma\sigma'} (c^\dagger_{i\sigma} c_{j\sigma'} - d^\dagger_{i\sigma} d_{j\sigma'}) + h.c. \end{aligned} \tag{1.3.5}$$

Deep in the strongly correlated region, the second order super-exchange processes mediates the magnetism. As a result, we have the $J_1 - J_2$ model for the infinite U limit for the Kane-Mele-Hubbard model:

$$H_{J1J2} = \sum_{\langle i,j\rangle} J_1 \vec{S}_i \cdot \vec{S}_j + \sum_{\langle\langle i,j\rangle\rangle} J_2 (S^z_i S^z_j - S^x_i S^x_j - S^y_i S^y_j) \tag{1.3.6}$$

The J_2 term stabilizes antiferromagnetism in the z component and ferromagnetism in the xy direction while the J_1 term favors antiferromagnetism on the bipartite lattice. Consequentially, the magnetism is Néel order on the bipartite lattice with spins on the same sublattice lying in the $X-Y$ plane. Hartree-Fock approximation has been applied in [62] in order to determine the critical value of the critical U that stabilizes the spin-density wave.

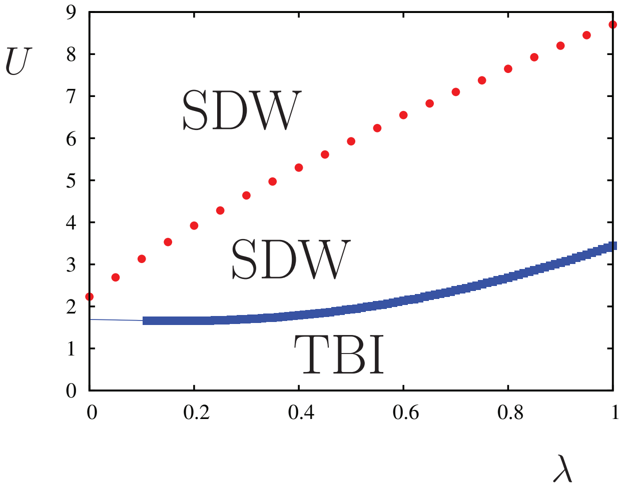

Figure 1.16: The phase diagram of the Kane-Mele-Hubbard model from Rachel and Le Hur [62] in which $\lambda = t'/t$. We have spin density wave in the strongly coupling limit , and topological band insulator for the weakly correlated limit. The real dashed line is the limit of the spin density wave phase (SDW) estimated using Hartree-Fock approximation. The Mott transition line (blue) is obtained within the slave rotor mean-field approximation.

On the other side of the weakly coupling limit when $U \to 0$, we have the phase of quantum spin Hall effect, in which we have the Kane-Mele model with helical edge state. Two spin current with opposite polarization along the z axis counter-propagate on the edge. The spin observable $S_i^z = c_{i\sigma}^\dagger c_{i\sigma'} \sigma_{\sigma\sigma'}^z$ commutes with the Hamiltonian. We can therefore explore the spin transport on the edge using the Kubo formula because of spin conservation.

The Mott physics is related to the separation of spin and charge, which are connected by an emergent gauge field. The charge particle acquires a gap upon Mott transition, while the spin particle are subject to the large gauge field fluctuation. In order to study the physics of the Mott insulator, we can write down the following action for the spin particle:

$$\mathcal{L}_f = \frac{1}{2} m_z (f_{k\uparrow}^\dagger f_{k\uparrow} - f_{k\downarrow}^\dagger f_{k\downarrow}) \tag{1.3.7}$$

Under insertion of one 2π flux, it is equivalent to the transport of one spin up and the transport of one spin down in the opposite direction by the Laughlin argument [144]. As a result, the relevent operator is $S_k^+ = f_{k\uparrow}^\dagger f_{k\downarrow}$, which designates the spin response under the flux insertion. This operator S_k^+ corresponds to the magnetic order in the plane $X-Y$, which is compatible with the magnetic coupling $S_i^z S_j^z - S_i^x S_j^x - S_i^y S_j^y$ in the infinite U limit.

To summarize, we have the quantum spin Hall effect at the weakly correlation region, spin density at the strongly correlated region. The two are connected together by the gauge field argument all due to the conservation of the spin observable in the system.

1.4 Introduction to Iridate System

Iridates have attracted the attention of condensed matter physicists because of the possibility of the realisation of Kitaev spin liquid which has its implications in quantum computation. As an introduction, we follow the presentation of the review paper by W. Witczak-Krempa et al [42]. Apart from the Hubbard interaction and band structure elucidated in the previous section, one particularity about iridate compound is the presence of the strong spin-orbit coupling, another complication that might induce new phases. Spin-orbit coupling is normally considered as a small perturbation to the system. However, such effect becomes significant in heavy metals since it increases proportionally to Z^4, in which Z is the atomic number. Descending from 3d to 4d and to 5d series, the d orbitals become more extended, reducing the Coulomb interaction or the Hubbard interaction in other terms. The increasing tendency of the spin-orbit coupling also reduces the kinetic energy t via splittings between degenerate and nearly degenerate bands. As a result, the energy scales of the three factors mentioned above in the iridate compounds are very close $W \simeq \lambda \simeq U$, in which W is the band width.

1.4.1 Balents' Diagram

We can write down the generic model Hamiltonian comprising all the three elements:

$$H = \sum_{i,j,\alpha,\beta} t_{i,j,\alpha,\beta} c^{\dagger}_{i\alpha} c_{j\beta} + h.c. + \lambda \sum_{i} \mathbf{L}_i \cdot \mathbf{S}_i + U \sum_{i,\alpha} n_{i\alpha}(n_{i\alpha} - 1) \tag{1.4.1}$$

where α is the orbital index and $n_{i\alpha} = c^{\dagger}_{i\alpha} c_{i\alpha}$ and λ is the amplitude of the spin-orbit coupling with $\mathbf{L}_i$ the orbital angular momentum and $\mathbf{S}_i$ the electron spin. A schematic phase diagram is given in Fig.1.17 in terms of the two ratios U/t and λ/t, and this phase diagram is figurative in the sense that it is independent of lattice and band structure details.

When $\lambda \to 0$, we have the conventional Hubbard model with two phases: the simple metal or band insulator depending on the band structure detail when the Hubbard interaction is small compared to the band width W; and the Mott insulator when the Hubbard interaction becomes bigger or comparable to the band width $U \geq W$. Another simple limit is the free fermion limit where $U \to 0$. The increase of the spin-orbit coupling induces the emergence of a semi-metal or topological insulator phase depending on whether the spin-orbit coupling opens a gap in the spectrum. When spin-orbit coupling and Hubbard interaction are equally significant, there are a plethora of exotic phases. We will proceed by listing a number of effective interactions that the spin-orbit coupling might induce. Then, we will enumerate various iridates exhibiting possibly different exotic phases.

1. The super-exchange processes of the spin-orbit coupling may induce a Kitaev-Heisenberg coupling. If we write the spin-orbit coupling as: $H^{ij\alpha}_{SO} = \lambda c^{\dagger}_{i\sigma} d_{j\sigma'} \sigma^{\alpha}_{\sigma\sigma'}$, then the super-exchange coupling is:

$$H_{KH} = -H^{ij\alpha}_{SO} H^{ji\alpha}_{SO}/U = J_2(S^{\alpha}_i S^{\alpha}_j - S^{\beta}_i S^{\beta}_j - S^{\gamma}_i S^{\gamma}_j) \quad (\beta, \gamma \neq \alpha, J_2 = 4\lambda^2/U) \tag{1.4.2}$$

2. The super-exchange processes of the spin-orbit coupling and the normal hopping term may induce a Dzyaloshinskii-Moriya interaction. If we write the spin-orbit coupling as $\tilde{H}^{ij\alpha}_{SO} = i\lambda c^{\dagger}_{i\sigma} d_{j\sigma'} \sigma^{\alpha}_{\sigma\sigma'}$ and the normal hopping as: $H^{ij}_0 = c^{\dagger}_{i\sigma} d_{j\sigma}$, then the D-M interaction originates from the second order processes consisting of electron hopping from site i to j with normal hopping and hopping back from site j to i with spin-orbit coupling:

$$H^{ij\alpha}_{DM} = -H^{ij}_0 \tilde{H}^{ji\alpha}_{SO}/U = J_3 \mathbf{e}_{\alpha} \cdot (\mathbf{S}_i \times \mathbf{S}_j) \quad J_3 = 4t\lambda/U \tag{1.4.3}$$

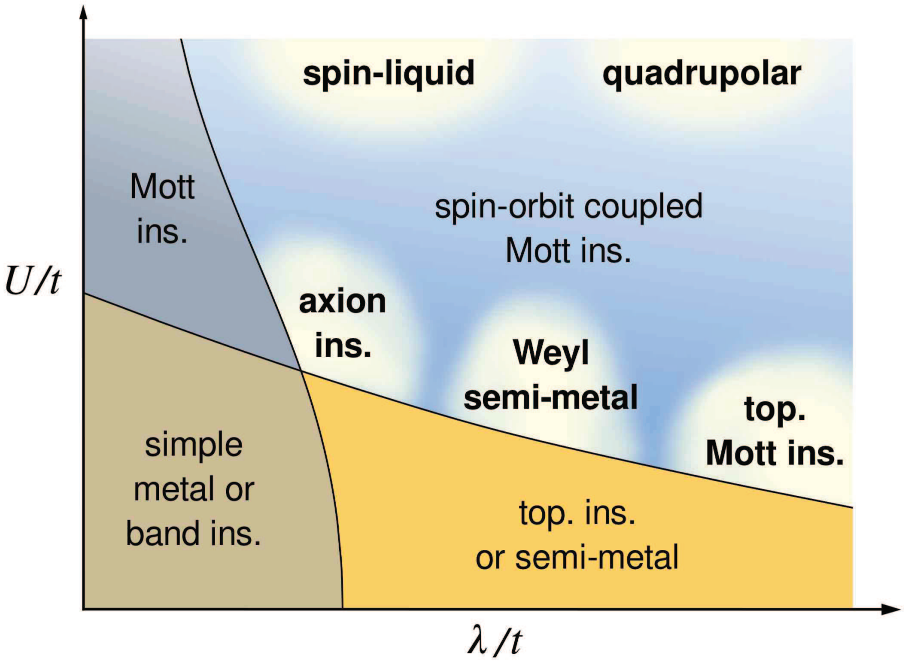

Figure 1.17: The Balents' phase diagram of the instructive model in equation 1.4.1 describing iridate materials. [42]

in which $\mathbf{e}_\alpha$ is a unity vector pointing along the α axis.

3. Zeeman interaction in 2D: $\tilde{H}_{SO} = H_{Rashba} + H_{Dresselhaus} = \alpha(\sigma_x k_y - \sigma_y k_x) + \gamma(\sigma_x k_x - \sigma_y k_y) \simeq \hat{\sigma} \cdot \mathbf{B}_{eff}$ the combination of a Rashba interaction and Dresselhaus interaction will generate an effective Zeeman interaction that will split the degeneracy in the spin subspace shifting the Fermi surface for the two spin species in the α polarization. The mixed super-exchange processes of this term with the normal hopping will not generate any exotic effective magnetic coupling.

We have included in table 1.1 different phases suggested by the figurative phase diagram by Leon Balents identified in different materials. One crucial property of some of these phases is topology induced by the essential ingredient of the spin-orbit coupling. The bulk is gapped by the spin-orbit coupling while the surface state is metallic and topologically protected by the time-reversal symmetry. Topological phases can only arise when correlation is not very strong so as to localize electrons to single atoms. In the bulk, correlations may enhance the gap in some cases, while on the surface, time-reversal symmetry may be spontaneously broken, with the emergence of magnetism. In this scenario, Chern insulators may occur [89]. In the presence of crystalline symmetries, notably inversion, the Z_2 symmetry may reappear [90]. Such is the case with the axion insulator which is characterized by a quantized magnetoelectric effect: the electric polarization $\mathbf{P}$ can be generated by applying a magnetic field $\mathbf{B}$, $\mathbf{P} = \frac{\theta}{(2\pi)^2}\mathbf{B}$ with $\theta = \pi$ such that the ratio P/B is universal and quantized [91].

Non-trivial topology can also emerge in gapless phases, such as Weyl semi-metals [94], with a Fermi surface consisting of points, where only two bands meet linearly, as a three-dimensional analog of Dirac fermions. Such phenomenon only appears at sufficiently large

U where either TRS or inversion symmetry is broken, since all bands would be two-fold degenerate otherwise. Around the band closure point, the band electron winds around the Dirac points with certain orientation in the $X - Y$ plane or chirality. The band touchings always come in pairs with opposite chirality. An example of a Weyl fermion is given by the following Bloch Hamiltonian:

$$\mathbf{H}(\mathbf{k}) = \pm v(\delta k_x \sigma_x + \delta k_y \sigma_y + \delta k_z \sigma_z) \quad \delta \mathbf{k} = \mathbf{k} - \mathbf{k}_w \tag{1.4.4}$$

where $\mathbf{k}_w$ are the two band touching points and σ_α are Pauli matrices acting on the touching point subspace. The two Weyl points behave like topological objects - monopoles or hedgehogs in momentum space- they have opposite chiralities acting like positive and negative monopole charges, contributing to the non-trivial bulk topology resulting in the non-trivial surface states on certain boundaries.

Phase	Symmetry	Correlation	Property	Proposed Materials
TI	TRS	W-I	Bulk gap, TME, protected surface state	many
Axion Insulator	P	I	Magnetic Insulator, TME, no protected surface state	$R_2Ir_2O_7$ $A_2Os_2O_7$
WSM	Not both TRS & P	W-I	Dirac-like bulk states, surface Fermi arcs, anomalous Hall	$R_2Ir_2O_7$ $HgCr_2Se_4$
LAB Semi-metal	cubic+TRS	W-I	non-Fermi liquid	$R_2Ir_2O_7$
Chern Insulator	broken TRS	I	Bulk gap, QHE	$Sr[Ir/Ti]O_3$ $R_2[B/B']_20_7$
FCI	Broken TRS	I-S	Bulk gap, FQHE	$Sr[Ir/Ti]O_3$
FTI, TMI	TRS	S	Several possible phases. Charge gap, fractional excitations	$Sr[Ir/Ti]O_3$
QSL	any	S	Several possible phases. Charge gap, fractional excitations	$(Na, Li)_2IrO_3$ Ba_2YMoO_6
Multiple order	various	S	Suppressed or zero magnetic moments. Exotic order parameters.	$A_2BB'O_6$

Table 1.1: Emergent quantum phases in correlated spin-orbit coupled materials. All phases have U(1) particle-conservation symmetry – i.e. superconductivity is not included. Abbreviations are as follows: TME = topological magnetoelectric effect, TRS = time reversal symmetry, P = inversion (parity), (F)QHE = (fractional) quantum Hall effect, LAB = Luttinger-Abrikosov-Beneslavskii, WSM=Weyl Semi-Metal. Correlations are W-I = weak-intermediate, I = intermediate (requiring magnetic order, say, but mean field-like), and S = strong. [A/B] in a material's designation signifies a heterostructure with alternating A and B elements. TI=topological insulator, FTI= fractional topological insulator, TMI=topological Mott insulator, QSL=quantum spin liquid and FCI=fractional Chern insulator.

Correlations can also trigger exotic phases such as fractional Chern insulators which display a fractional quantum Hall effect without an external magnetic field and topological Mott insulator which exhibits spin-charge separation and TI-like surface states composed of neutral fermions [93].

1.4.2 The Honeycomb Iridates

The hexagonal iridates Na_2IrO_3 and Li_2IrO_3 realize a layered structure consisting of a honeycomb lattice of Ir^{4+} ions, and they provide a concrete example of the full orbital degeneracy lift with a maximally quantum effective spin-1/2 Hamiltonian. Both compounds appear to be in the strong Mott regime. As shown by Jackeli and Khaliullin [43, 44], the edge sharing octahedral structure and the structure of the entangled $J_{eff} = 1/2$ orbitals leads to a cancellation of the usually dominant antiferromagnetic oxygen-mediated exchange interactions. A subdominant term is generated by Hund's coupling, which takes the form of a highly anisotropic Kitaev exchange coupling:

$$H_K = -K \sum_{\alpha=x,y,z} \sum_{\langle i,j\rangle \in \alpha} S_i^\alpha S_j^\alpha, \tag{1.4.5}$$

where $\mathbf{S}_i$ are the effective spin-1/2 operators and $\alpha = x, y, z$ labels both spin components and the three orientations of links on the honeycomb lattice. This particular Hamiltonian realizes the exactly solvable model of the quantum spin liquid phase proposed by Alexei Kitaev[15], which describes the fractionalization of the spins into Majorana fermions, stemming from the geometry and entanglement in the strong spin-orbit coupling limit. In Chapter 3 section 3.2, we have shown how this geometry and orbital entanglement brings extra symmetry, endowing the Kitaev model a self-duality point with extra symmetry. In antiferromagnets, spin-orbit coupling will remove accidental degeneracy and favor order via the Dzyaloshinskii-Moriya interaction, while the Kitaev model is a counterexample, in which spin-orbit coupling can suppress ordering. The experimental studies through neutron scattering and other studies show that the ground state of Na_2IrO_3 displays a collinear magnetic order, the zigzag state with a four-sublattice structure, arising from possible Heisenberg coupling [116, 117]. However, the Kitaev coupling might be much larger in Li_2IrO_3 and the system may be closer to the quantum spin liquid phase. There has also been proposition in ultra cold atoms for the the realization of the Kitaev model [46].

We have shown here the geometric configuration of the two honeycomb iridate compound Na_2IrO_3 and Li_2IrO_3 in Fig. 1.18 from the paper [111, 122].

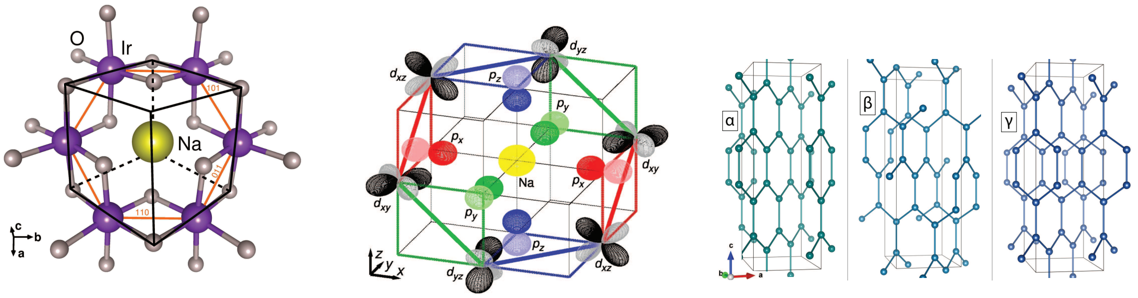

Figure 1.18: The geometric structure of the two honeycomb iridates Na_2IrO_3 (left and middle panel) and Li_2IrO_3 (right panel). (Figures from [111, 122])

The Na_2IrO_3 compound has one sodium atom in the center surrounded by 6 iridium atoms, linked by oxygen atoms. The hybridization of orbitals is complicated: it is a mixture of overlap of d orbitals of the iridium atoms and the overlap of the oxygen p orbital with the d orbital of the iridium atoms. A 90° overlap of the orbitals induces a Kitaev coupling of $S_i^\gamma S_j^\gamma$ and a 180° overlap of the orbitals induces a Heisenberg coupling of $\mathbf{S}_i \cdot \mathbf{S}_j$. The Kitaev Heisenberg coupling favors a spin liquid phase [15], which is paramagnetic with magnetic susceptibility obeying the Curie law $\chi \sim \frac{1}{T}$ while the Heisenberg coupling favors Néel antiferromagnetism with a certain Néel temperature below which the sample is ordered anti-ferromagnetically with finite susceptibility.

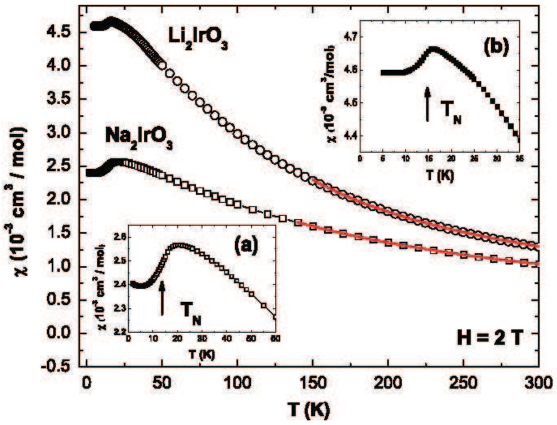

Figure 1.19: The magnetic susceptibility of the two honeycomb iridate compounds Na_2IrO_3 and $\alpha - Li_2IrO_3$ [114].

We have shown the magnetic susceptibility in Fig. 1.19 given in the paper [114]. We spot similar behavior of the two iridate compounds Na_2IrO_3 and Li_2IrO_3: (1) above the Néel temperature T_N, the magnetic susceptibility behaves according to the Curie law $\chi = \chi_0 + \frac{C}{T-\theta}$ in which θ is the Curie temperature; $\theta < 0$ indicates that the interaction is antiferromagnetic. (2) the two compounds share the same Néel temperature, at which the susceptibility sees an anomaly, and the susceptibility remains finite below T_N, which is related to the antiferromagnetic order at low temperature. One model describing the mixture of the two kinds of magnetic couplings is given:

$$H_{HK} = (1-\alpha)\sum_{\langle i,j\rangle} \mathbf{S}_i \cdot \mathbf{S}_j - 2\alpha \sum_{\gamma} S_i^\gamma S_j^\gamma \quad (0 \leq \alpha \leq 1) \tag{1.4.6}$$

in which the antiferromagnetic Heisenberg term is on the links between nearest neighbours while the spin component γ is in accordance with the link type denoted by γ. The Curie Weiss temperature is found to be $\simeq -120$K for Na_2IrO_3 and $\simeq -33$K for Li_2IrO_3. The increase of the Curie Weiss temperature indicates that Li_2IrO_3 is closer to paramagnetism indicating an increase of the ferromagnetic Kitaev coupling. This is in agreement with the ab-initio calculation [114] that the parameter α Li_2IrO_3 is found to be in the range of $0.6 \leq \alpha \leq 0.7$ which is quite close to the limit of Kitaev spin liquid phase $\alpha > 0.8$.

One still pending debate is whether the Kitaev coupling γ is between nearest-neighbours or the next-nearest-neighbours. On the one hand, the next-nearest-neighbour hopping comes into play when the d orbitals hybridize with the sodium atom in the center of the six surrounding iridium atoms and electrons can hop between the iridium atom generating an effective spin-orbit coupling. On the other hand, the spinorial anisotropy from the d-orbitals and the hybridization of the iridium atoms with the oxygen atoms constitutes a nearest-neighbour anisotropic coupling. In the paper [122], authors have argued that the nearest hopping term is found to be $\simeq$ 270meV and the next nearest neighbour hopping $\simeq$ 75meV. The Kitaev coupling is on the nearest-neighbour. This model is also confirmed by Chaloupka et al [43] who predicted a zigzag order which is confirmed by experiments. However, in the theoretical paper [101] and the experimental paper [127], people have identified a topological insulator phase with time-reversal symmetry, which is only possible when the spin-orbit coupling is between the next-nearest-neighbours.

In this thesis, we have taken into account both possibilities mentioned above: in chapter 2, we consider a model Hamiltonian with spin-orbit coupling between next-nearest-neighbors hosting a correlated topological insulator phase, while in chapter 3, we consider the spin-orbit coupling model on the nearest-neighbors hosting the zigzag magnetic order. We have identified new exotic phases in the phase diagrams of both the two different models.

1.5 Doped Honeycomb Iridates

One model including this mixture of Kitaev coupling and Heisenberg coupling is the honeycomb lattice model for iridate hosting the zig-zag order with both coupling on the nearest-neighbour links [43]. Following the idea of equation 1.4.6, Chaloupka et al have written down the Hamiltonian in the form:

$$H_{KH} = A\sum_{\langle i,j\rangle}(2\sin\varphi S_i^\gamma S_j^\gamma + \cos\varphi \mathbf{S}_i\cdot\mathbf{S}_j) = \sum_{\langle i,j\rangle}(J_K S_i^\gamma S_j^\gamma + 2J_H \mathbf{S}_i\cdot\mathbf{S}_j) \tag{1.5.1}$$

in which $A = \sqrt{J_K^2 + 4J_H^2}$ and $\gamma = x, y, z$ respectively on x, y and z links as shown in figure 1.20. With the change of the variable φ, we have different magnetic phases for the model: 1. the zigzag phase. 2. the Néel phase. 3. the ferromagnetic phase. 4. the liquid phase around $J_H \to 0$. It is worth noting that the Kitaev anyon liquid phase was located around $J_H \to 0$ while $J_K < 0$.

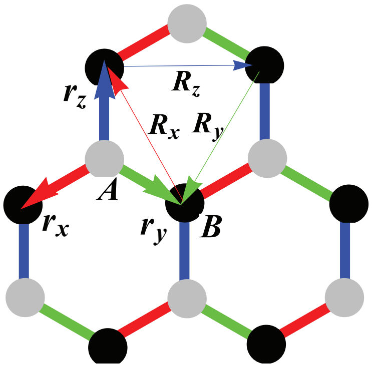

Figure 1.20: The Kitaev Heisenberg nearest-neighbour model on the honeycomb lattice with $S_i^\alpha S_j^\alpha - S_i^\beta S_j^\beta - S_i^\gamma S_j^\gamma$ on different correspondent links in which $\alpha = x,y,z$ respectively on the red, green and blue links and β, γ take other spin components than α.

We know that doping a spin liquid leads to superconductivity; for example, we can obtain the d-wave superconductivity by doping the VBS spin liquid[192]. With this theoretical

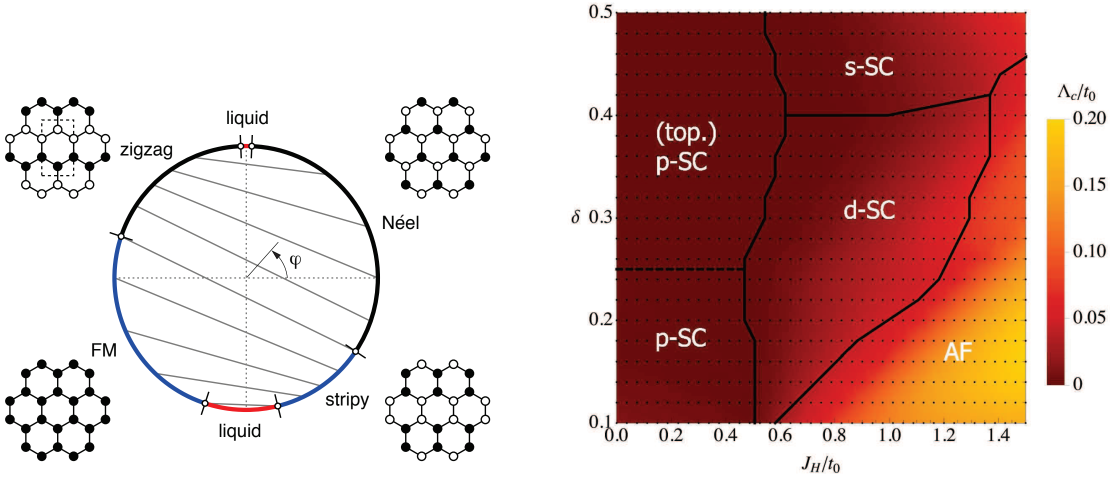

Figure 1.21: *Left panel*: The phase diagram of the Kitaev Heisenberg model with nearest-neighbour magnetic coupling on the honeycomb lattice as function of the angle φ in the magnetic coupling model $H_{KH} = A\sum_{\langle i,j\rangle}(2\sin\varphi S_i^\gamma S_j^\gamma + \cos\varphi \mathbf{S}_i\cdot\mathbf{S}_j)$ from the paper of Chaloupka et al [43]. *Right panel*: The phase diagram of the doped iridate system from Scherer et al [41] in which the Kitaev coupling $J_K = -t_0$ is fixed to be ferromagnetic.

motivation, Scherer et al have studied the doped Kitaev-Heisenberg model with ferromagnetic Kitaev coupling:

$$H_{Scherer} = -\sum_{\langle i,j\rangle} t_0(c^\dagger_{i\sigma} d_{j\sigma} + d^\dagger_{j\sigma} c_{i\sigma}) + \sum_{\langle i,j\rangle}(J_K S_i^\gamma S_j^\gamma + 2J_H \mathbf{S}_i\cdot\mathbf{S}_j) \tag{1.5.2}$$

in which they have fixed the Kitaev coupling $J_K = -t_0$ to be ferromagnetic in order to have the Kitaev spin liquid in the limit of $J_H \to 0$. $\gamma = x, y, z$ respectively on the x, y and z links. The kinetic term proportional to t_0 describes the motion of the holes. In accordance with the model, they have found the corresponding phase diagram (Fig. 1.21) for the superconductivity in which the emergent superconductivity is the $p-wave$ phase with which when the doping is beyond quarter filling, the superconductivity becomes topological. On the other limit where $J_H \gg J_K$, we have the $d-wave$ superconductivity in the $t_0 - J_H$ model on the honeycomb lattice.

However, the Kitaev coupling in the iridate compounds has proved to be anti-ferromagnetic in the experiments [125] and the half-filled Mott insulator hosts a zigzag magnetic order in the quartet of $J_K > 0, J_H < 0$. This disparity between the doped iridates from a theoretical point of view [41] and the experiment [125] motivates largely the study of doped iridate in Chapter 3, in which we study the exotic superconductivity from doping the zigzag order.

1.6 Summary

Iridates (Iridium compounds) incorporate at the same time significant spin-orbit coupling and Hubbard interaction. The iridate compound has attracted attention from condensed matter physicists because of its possible realization in the real world material of Kitaev anyon model [15]. The coexistence of different kinds of interaction along with the complication of geometrical factors of the lattice leads to different physics at different regimes: (1) Topological insulator physics at the weak correlated regime, (2) Frustrated magnetism at the strongly correlated regime (3) Exotic superconductivity in the doped Mott insulators.

Iridate compounds have been approached with different point of view: (1) Correlated topological insulators (2) frustrated magnetism. In analogy with traditional correlated systems, the difficulties in the study of iridate compounds lie in the incorporation of different regimes. The correlated topological insulator has been previously studied in the Kane-Mele-Hubbard model [62], in which spin current along the z polarization is a well defined quantity. The Polyakov gauge theory argument [146] allows for the connection of the topological insulator phase to the magnetic phase, in which the gauge fluctuation triggers spin transport to the bulk. However, spin observable is not a well defined observable in the context of iridates, in that the anisotropic spin-orbit coupling renders the description of spin transport more tricky than in the Kane-Mele model. The frustrated magnetism model has been studied by Chaloupka et al [43], in which they identified different magnetic phases as a function of the mixture of the Kitaev and Heisenberg magnetic coupling with enlarged unit cells. However, the detailed analyses of the order by disorder of the frustrated magnetism are still absent.

The compound Na_2IrO_3 and Li_2IrO_3 are the two compounds on the honeycomb lattice under investigation in this thesis. However, whether the spin-orbit coupling physics reside between nearest-neighbours or next-nearest-neighbours is still an open question : different experimental groups have observed respectively delocalisation effect of electrons [127], which indicates a topological insulator phase, and zigzag magnetic phase of $2D$ thin films of Na_2IrO_3, which indicates anti-ferromagnetic Kitaev coupling and ferromagnetic Heisenberg coupling [43, 113]. Doped Mott phase has been previously studied with the theoretical motivation with ferromagnetic Kitaev coupling [41] which is believed to be related to doped iridate, however the ferromagnetic Kitaev coupling is in disparity with the experimental fact showing anti-ferromagnetic Kitaev coupling.

In Chapter 2, we study a model with spin-orbit coupling between next-nearest neighbours [101] with interaction. We used different approaches in different regions of the phase diagram. In Chapter 3, we have presented our work of doped iridates, with anti-ferromagnetic Kitaev coupling hosting the zigzag magnetic order at half-filling. We deduce the hopping term with an itinerant magnetism point of view with which the second order super-exchange processes induce an anti-ferromagnetic Kitaev-Heisenberg coupling. We focus on the regime around quarter-filling, in which emergence of new symmetry centers of the Fermi surface leads to an FFLO superconductivity. The Chapter 4 contains the study of one different model, which is constituted with two fermion species. The RKKY interaction induced by the fast fermion opens a gap for the slow species and attaches a Haldane mass to the slow fermion thus inducing a topological phase.

The three different systems studied in these thesis incorporate all different aspects of Mott physics, in which correlation plays different roles. In Chapter 2, the correlation modifies the Fermi velocity of the edge mode in the topological insulator phase, and localizes charges upon the Mott transition. Deep in the Mott phase, charges are totally localized and spins are separated from the charges, inducing the super-exchange magnetism. In Chapter 3, the magnetic coupling induced by correlation couples holes together in the doped regime and brings about superconductivity. However, in Chapter 4, interaction plays a totally different role and introduces topology into the system by opening a gap and inducing a Haldane mass of the electron system on graphene lattice.

The spin-orbit coupling physics intervenes in the three model in different ways: in Chapter 2, the anisotropic spin-orbit coupling makes the spin current a non conserved observable, which manifests different physical properties than the Kane-Mele Hubbard model. In Chapter 3, the spin orbit coupling might induce other exotic superconductivity than the conventional spin-singlet electron pairing with zero Cooper pair momentum. In Chapter 4, the spin-orbit coupling is induced spontaneously by correlation. And this spin-orbit coupling then triggers a topological phase in the system.

Chapter 2

Iridates on Honeycomb Lattice at Half-filling

In this chapter we present our studies on one (sodium-iridate) model on the honeycomb lattice (graphene lattice) with spin orbit coupling and the Hubbard on-site interaction. This potentially describes 2D iridates with the motivation that experimental realisation of a thin layer of such compounds reveals a topological insulator phase [127]. The hybridization of orbitals between atoms gives a tight binding model with a mixture of normal electron hopping between the nearest-neighbour (NN) similar to graphene, and spin-orbit coupling within the next-nearest neighbours (NNN) which consists of a complex and anisotropic strength of $it'\sigma_x$, $it'\sigma_y$ and $it'\sigma_z$ in the counter-clockwise direction as in Fig. 2.1. We include also a Hubbard on-site interaction mimicking the Coulomb interaction of electrons within the orbitals of one atom. The interplay of the above mentioned three elements may give rise to different exotic phases in competition. Such a model is believed to be a good description of electrons behavior in the correlated Na_2IrO_3 sodium iridate compound [101] and possibly to other materials with spin-orbit coupling.

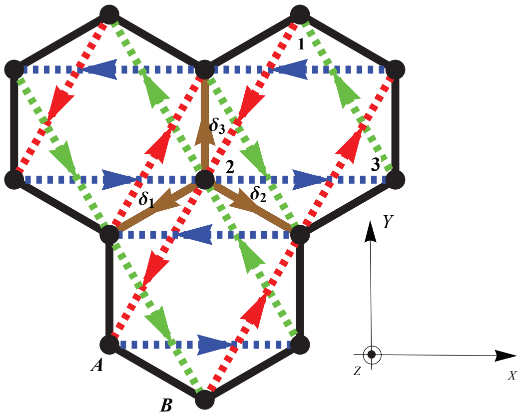

Figure 2.1: Illustration of the tight-binding model on the honeycomb lattice with complex next-nearest-neighbor spin-orbit couplings entailing hopping of $it'\sigma_x$ on the x red link, $it'\sigma_y$ on the y green link, and $it'\sigma_z$ on the blue z link, in which σ_w, $w = x,y,z$ is the Pauli matrix acting on the space of spins. The anisotropic spin-orbit coupling makes the spin no longer a conserved quantity in the system.

Specifically, the (sodium-iridate) model Hamiltonian is written as:

$$\begin{aligned} H_0 &= \sum_{<i,j>} t c^{\dagger}_{i\sigma} c_{j\sigma} + \sum_{\ll i,j \gg} i t' \sigma^{\alpha}_{\sigma\sigma'} c^{\dagger}_{i\sigma} c_{j\sigma'} \\ H &= H_0 + H_I \\ H_I &= \sum_i U n_{i\uparrow} n_{i\downarrow}, \end{aligned} \tag{2.0.1}$$

where $\langle i,j \rangle$ denotes a sum over the nearest neighbor and $\ll i,j \gg$ denotes a sum over the next-nearest-neighbors, and $\sigma^{\alpha}_{\sigma\sigma'}$ is a Pauli matrix with $\alpha = x$ on the x link painted in red, $\alpha = y$ on the y link painted in green and $\alpha = z$ on the z link painted in blue as in Fig. 2.1. To be precise, the hopping strengths of electrons on the next-nearest-neighbor links are denoted $it'\sigma_x$ on the red link $it'\sigma_y$ on the green link and $it'\sigma_z$ on the z link (t' is real). The free electron model is a topological insulator [101]. Here, the electrons travel in a counterclockwise orientation. The second nearest-neighbor hopping strengths pick a minus sign if electrons travel in the clockwise orientation. This model has been previously studied in the context of Quantum Spin Hall physics and magnetism [95, 101, 105], which respect the time-reversal symmetry.

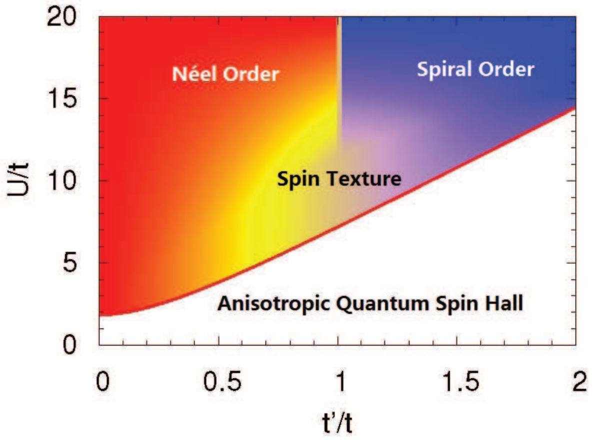

Figure 2.2: Our Phase diagram [36]. When $U < U_c$ (red line), the system is in the class of a $\mathbb{Z}_2$ two-dimensional topological band insulator. The edge modes are embodied by a peculiar spin texture as a result of the anisotropic spin-orbit coupling. We then refer to this phase as Anisotropic Quantum Spin Hall (AQSH) phase. Above the Mott critical point $U_c(t')$ as function of the spin-orbit coupling amplitude t', the spin texture now progressively develops into the bulk when increasing the spin-orbit coupling strength. At large interactions U, we identify two magnetic phases, the Néel and the Spiral phase.

Hereafter, combining theoretical and numerical procedures, our primary goal is to carefully address the phase diagram summarized in Fig. 2.2 of the quite generic tight-binding model in equation 2.0.1 at half-filling on the honeycomb lattice with an Hubbard on-site interaction and next-nearest-neighbor anisotropic spin-orbit coupling. The difficulty of this anisotropic spin-orbit coupling - Hubbard model lies in the non-conservation of the spin observable which renders the spin current a not well defined quantity. This difficulty intervenes both in the topological insulator physics and the intermediate interaction region where spin (spinon) are subject to large gauge fluctuation.

In section 2.1, we explain the physics of topological insulator situated in the lower area of the phase diagram 2.2. The difficulty of the treatment in this regime comes from the non conservation of spin observables, which makes the spin current a not well-defined quantity. We used respectively transfer matrix and exact diagonalization of Schrödinger equation in this regime to explicitly study the anisotropic spin transport on the edge. The anisotropy of the transporting spin texture on the edge depends on the amplitude of the spin-orbit coupling as shown in figure 2.6. The Hubbard interaction only modifies the fermi velocity of the transporting edge states and shifts the effective chemical potential in the bulk.

In section 2.2, we explore the infinite U limit of the phase diagram 2.2: (1) Néel order at $J_1 > J_2$ (2) Spiral order at $J_1 < J_2$. We carefully examine the phase diagram of the magnetic coupling model given in figure 2.8, in which we have identified different results from Reuther et al [105]. We study the classical ground state of the magnetism and study the frustration phenomena through analyses of order by disorder in both the classical and quantum level in addition to the magnetic phases already clarified in [105]. We also looked at the energy variation on the basis of the spiral phase in the regime $J_2 > J_1$ and identified the first order phase transition at $J_1 = J_2$. The frustration makes the goldstone mode (soft mode) disappear in both phases, which we will explain in detail.

We study the Mott transition using the slave rotor formalism in section 2.3 which is shown as the red line separating the colored Mott phase and the quantum spin Hall phase in the weakly correlated regime in figure 2.2. Correlation localizes charges and spins can still exchange position in the strongly correlated limit. Slave particle formalism aims to describe the related physics by splitting the physical electrons into chargeons and spinons. Chargeons acquire a gap upon Mott transition while spinons are subject to the emergent gauge field serving as a glue between the two particles. At the limit of zero spin-orbit coupling, we have the Mott transition of the traditional correlated system at $U_c = 1.68t$ found by Lee and Lee [132]. This value $U_c \simeq 4.3t$ found within QMC [39] is underestimated by slave rotor theory while it is overestimated by the slave spin approach ($U_c \simeq 8t$) [95]. There exists still a pending debate on whether the emergent gauge field should be $U(1)$ or Z_2. In the $U(1)$ phase, the weakly correlated phase is in the ordered 'superfluid' phase with one well defined phase in the whole system while the strongly correlated phase concerns a disordered phase for the slave rotors. The emergent $U(1)$ gauge field concerns a Maxwellian field in $2+1D$. The Z_2 representation describes the Mott transition using the image of Ising model and its ordered and disordered phase, however the emergent Z_2 gauge field exhibits different physical phenomena regarding the Mott transition [95], in which there exist topological vison excitations. Here, we choose the conventional $U(1)$ representation which gives different Mott transition critical value than the Z_2 representation [95]. The anisotropic spin orbit coupling does not change significantly the Mott transition value U_c compared to the Kane-Mele model, however the spinons' response to the fluctuating gauge field shows totally different behavior.

In Section 2.3.3, we address the problem of spinon response to the insertion of one monopole in the emergent gauge field above the Mott transition in the parameter region denoted as 'spin texture' in figure 2.2. Using the linear response formalism in the presence of one and two monopoles, we showed that a spin texture takes form around the flux. Using the Laughlin topological argument, we showed that the spin texture of the transporting edge states is pumped around the fluctuating flux in the bulk. The spin texture embodies the anisotropy analogously to the edge states: the dominant spin component on a given site coincides with the type of links intersecting the line connecting the site and the core of the vortex. And the anisotropy amplifies when spin-orbit coupling becomes more and more significant. This anisotropic spin texture can be associated with the spiral phase in the infinite U limit.

2.1 Topological Insulator Phase

In this section, we explore the physics in the weakly correlated regime, namely physics in the limit of $U \ll t, t'$. The normal hopping between nearest-neighbours (NN) with strength t gives a graphene band structure with Dirac cones at the corners of the first-Brillouin zone, while the spin-orbit coupling with strength t' opens a gap for the band electrons at the Dirac cones. The spin-orbit coupling introduces into the system opposite effective magnetic fields for spins with opposite polarizations pointing along different directions on different links. In the presence of time-reversal symmetry (TRS), Kramers Theorem states that system of spin 1/2 with time-reversal symmetry (TRS) is necessarily doubly degenerate, with one sector odd under TRS, and another even under TRS. The symmetry group related to TRS is $\mathbb{Z}_2$, and the gaplessness of the edge mode is ensured by the TRS in that any processes opening a gap for the edge mode breaks the TRS. The topological aspect of the Kane-Mele model can be easily illustrated by studying the spin transport on the edge knowing that the Pauli matrix σ_z commutes with the Hamiltonian, indicating well-defined spin current along the Z direction, in other words quantum spin Hall effect.

The anisotropic spin-orbit coupling model in the weakly correlated regime describes quantum spin Hall effect with the same $\mathbb{Z}_2$ topological index as the Kane-Mele model. Neglecting the Hubbard interaction in the first place, we diagonalize the tight binding model H_0 by Fourier transformation: 2.1.1:

$$H_0 = \sum_{<i,j>} t c^\dagger_{i\sigma} c_{j\sigma} + \sum_{\ll i,j \gg} i t' \sigma^\alpha_{\sigma\sigma'} c^\dagger_{i\sigma} c_{j\sigma'} = \sum_{\vec{k}} \Psi^\dagger_{\vec{k}} h(\vec{k}) \Psi_{\vec{k}} \tag{2.1.1}$$

in which the wave function in the momentum representation exhibits four components $\Psi^\dagger_{\vec{k}} = (a^\dagger_{\vec{k}\uparrow}, b^\dagger_{\vec{k}\uparrow}, a^\dagger_{\vec{k}\downarrow}, b^\dagger_{\vec{k}\downarrow})$ and the two sublattices of the honeycomb (A and B) give rise to the corresponding electron creation operators $a^\dagger$ and $b^\dagger$. We then identify

$$h(\vec{k}) = (\tau_x \Re e + \tau_y \Im m) g(\vec{k}) + (m_x \sigma_x + m_y \sigma_y + m_z \sigma_z)\tau_z, \tag{2.1.2}$$

where τ_x, τ_y and τ_z are Pauli matrices acting on the sublattice isospin A & B while σ_x, σ_y and σ_z are Pauli matrices acting on the spin space ↑ and ↓.

For convenience, we have introduced the notations $g(\vec{k}) = \sum_i t e^{i\vec{k}\cdot\vec{\delta}_i}$ and $m_x = 2t' \sin(\vec{k} \cdot \vec{R}_x)$, $\quad m_y = 2t' \sin(\vec{k} \cdot \vec{R}_y)$, $\quad m_z = 2t' \sin(\vec{k} \cdot \vec{R}_z)$.

Here, $\vec{\delta}_1 = (-\frac{\sqrt{3}}{2}, -\frac{1}{2})a$, $\vec{\delta}_2 = (\frac{\sqrt{3}}{2}, -\frac{1}{2})a$ and $\vec{\delta}_3 = (0,1)a$ refer to vectors connecting the nearest neighbours (see Fig. 2.1), while $\vec{R}_x = (-\frac{\sqrt{3}}{2}, -\frac{3}{2})a$, $\vec{R}_y = (-\frac{\sqrt{3}}{2}, \frac{3}{2})a$ and $\vec{R}_z = (\sqrt{3}, 0)a$ represent vectors connecting next nearest neighboring sites. Moreover, a is the closest interatomic distance and we set it equal to 1 for convenience.

The Hamiltonian represents a two band system with the energy levels:

$$E(\vec{k}) = \pm E_0(\vec{k}) = \pm\sqrt{m_x^2(\vec{k}) + m_y^2(\vec{k}) + m_z^2(\vec{k}) + |g(\vec{k})|^2}. \tag{2.1.3}$$

The system is an insulator with a gap $\Delta(k) = 2E_0(k)$, in which $E_0(k) > 0$ in the first Brillouin zone.

Each band is doubly degenerate and it is convenient to introduce the band projectors associated to the upper and lower band $P_\pm$ respectively:

$$P_\pm = \frac{1}{2}\left[1 \pm \left(\frac{\tau_x \Re e g}{E_0} + \frac{\tau_y \Im m g}{E_0} + \frac{\tau_z}{E_0}(m_x \sigma_x + m_y \sigma_y + m_z \sigma_z)\right)\right]. \tag{2.1.4}$$

We can illustrate the non-trivial topology by the $\mathbb{Z}_2$ invariant for system with inversion symmetry [12] namely the product of the time-reversal polarization for the four time-reversal and inversion symmetric points:

$$(-1)^{\nu} = \prod_{i=1}^{4} \gamma_i = -1; \tag{2.1.5}$$

here, we have defined $\gamma_i = -\mathrm{sgn}(\Re eg(\Gamma_i))$ and $\Gamma_i = (0{,}0); (0, \frac{2\pi}{3}); (\frac{\pm\pi}{\sqrt{3}}, \frac{2\pi}{3})$. The $\mathbb{Z}_2$ topological invariant depicts a twist of the rank 2 ground-state wave function in the first Brillouin zone. The anisotropic spin-orbit coupling model in the weak correlated limit shares the same $\mathbb{Z}_2$ topological invariant as the Kane-Mele model, implying similar physical consequences on the edge, however the sodium-iridate model differs from the Kane-Mele model in that spin is not conserved and spin current is not a well-defined quantity because of the anisotropic spin-orbit coupling. The spin physics depends on the edge configuration of the system and the ratio t'/t, thus implicating an anisotropic quantum spin Hall effect.

To illustrate this point, we have studied the edge transport in the case of zigzag boundaries as in Fig. 2.3 applying numerical diagonalization of the system on a cylinder in section 2.1.1 and the transfer matrix method summarized in section 2.1.2.

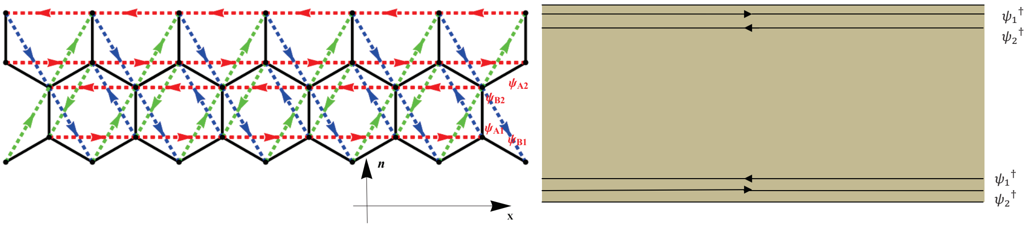

Figure 2.3: Left panel: The lower edge of the semi-infinite system with edges parallel to the x-type links. The system consists of layers of one-dimensional chains coupled together, and the edge mode decays exponentially when moving into the bulk. Right panel: the chiral edge transport corresponding to the boundary configuration. Two helical edge modes with opposite spin polarization counter-propagate on the boundary of the system.

2.1.1 Numerical Diagonalization

As a result of the non-conservation of the spin of the anisotropic spin-orbit coupling model, the spin polarization of the helical edge states is more sophisticated than in the Kane-Mele model. To thoroughly analyze this point, we consider a system with two zigzag boundaries as layers of one-dimensional chains coupled together as illustrated in Fig. 2.3. The existence of the two edges breaks the translational symmetry along one direction leaving only one good quantum number k_x. Intuitively, the edges also break the equivalence of the three links connected by $\pi/3$ rotation, triggering the helical emergent spin texture on the edge.

If we denote $\psi^n_{A/B}$ as the wave function of the n th layer in A or B sublattice, then the

Schrödinger equation of such a system takes the form:

$$\begin{aligned}&\begin{pmatrix} -it'(e^{-i\frac{\sqrt{3}}{2}k_x}\sigma_z - e^{i\frac{\sqrt{3}}{2}k_x}\sigma_y) & -t \\ 0 & it'(e^{-i\frac{\sqrt{3}}{2}k_x}\sigma_z - e^{i\frac{\sqrt{3}}{2}k_x}\sigma_y) \end{pmatrix} \begin{pmatrix} \psi_A^{n+1} \\ \psi_B^{n+1} \end{pmatrix} \\ &+ \begin{pmatrix} E + 2t'\sin\sqrt{3}k_x\sigma_x & -2t\cos\frac{\sqrt{3}}{2}k_x \\ -2t\cos\frac{\sqrt{3}}{2}k_x & E - 2t'\sin\sqrt{3}k_x\sigma_x \end{pmatrix} \begin{pmatrix} \psi_A^{n} \\ \psi_B^{n} \end{pmatrix} \\ &+ \begin{pmatrix} it'(e^{i\frac{\sqrt{3}}{2}k_x}\sigma_z - e^{-i\frac{\sqrt{3}}{2}k_x}\sigma_y) & 0 \\ -t & -it'(e^{i\frac{\sqrt{3}}{2}k_x}\sigma_z - e^{-i\frac{\sqrt{3}}{2}k_x}\sigma_y) \end{pmatrix} \begin{pmatrix} \psi_A^{n-1} \\ \psi_B^{n-1} \end{pmatrix} = 0. \end{aligned} \tag{2.1.6}$$

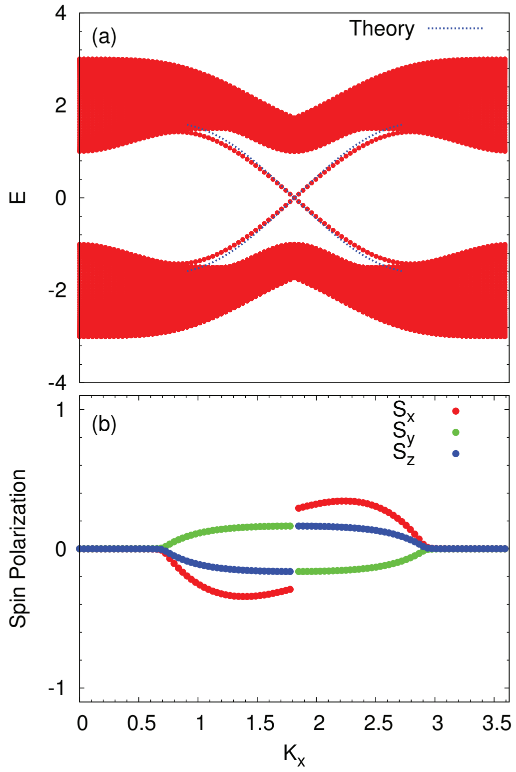

Figure 2.4: The edge states of the anisotropic spin-orbit coupling model with zigzag boundary and x links parallel to the boundary. (a): Spectrum of the system on a cylinder at $t'/t = 0.5$ obtained from numerical diagonalization of 70 layers of a one-dimensional system described by the Schrödinger equation 2.1.6. The non-trivial $\mathbb{Z}_2$ topological invariants ensures an helical edge states with opposite spin polarization. The energy dispersion obtained analytically using transfer matrix in section 2.1.2 fits well the numerics. The discrepency is most pronounced when the edge states enter the bulk band because of the finite scaling effect. (b): The different components of the spin polarization measured on the lower edge of the state with the lowest positive energy in the spectrum as a function of momentum, obtained from diagonalization of the system. We observe that states with opposite Fermi velocities on both sides of $k_x = \frac{\pi}{\sqrt{3}}$ have opposite spin polarizations, thus implying helical spin transport on the edge. The dominant spin component corresponds to the type of links parallel to the boundary.

We then perform a numerical diagonalization of such a system with 70 layers of one-dimensional chains (see Fig. 2.4) and a purely analytical transfer matrix approach is developed in 2.1.2. We address a system with boundaries parallel to the x-type links and the resulting spin polarization depends on how the system is cut and on the ratio t'/t. We observe that there are two edge modes crossing the gap connecting the upper and lower bands according to the results obtained from the numerical diagonalization presented in Fig. 2.4 (a). The discrepency between the exact dispersion relation obtained theoretically and numerically from exact diagonalization of the Schrödinger equation is most pronounced when the edge states enters the bulk bands. This is due to the finite scaling effect, and we have checked that the two dispersion relations tend to coincide in the thermal dynamic limit.

We have studied the spin polarization of one of the metalic edge state, which is the lowest positive energy state, by measuring its spin polarization on the boundary: spin have opposite components respectively at $k_x > \frac{\pi}{\sqrt{3}}$ and $k_x < \frac{\pi}{\sqrt{3}}$; since the Fermi velocity in these two intervals separated by $k_x = \frac{\pi}{\sqrt{3}}$ are opposite as well, this implies two counter-propagating states with opposite spin polarization. The energy dispersion of the edge state obtained analytically in section 2.1.2 fits well the edge states plotted in the spectrum in Fig. 2.4. As a result, we have two counter-propagating states with approximately linear dispersion in the spectrum on both upper and lower edges: the state with one polarization propagating to the left (right) on the lower (upper) edge and the state with the opposite polarization propagating to the right (left) on the lower (upper) edge as in Fig. 2.3. The time-reversal symmetry forbids the (elastic) backscattering, allowing for helical edge spin transport.

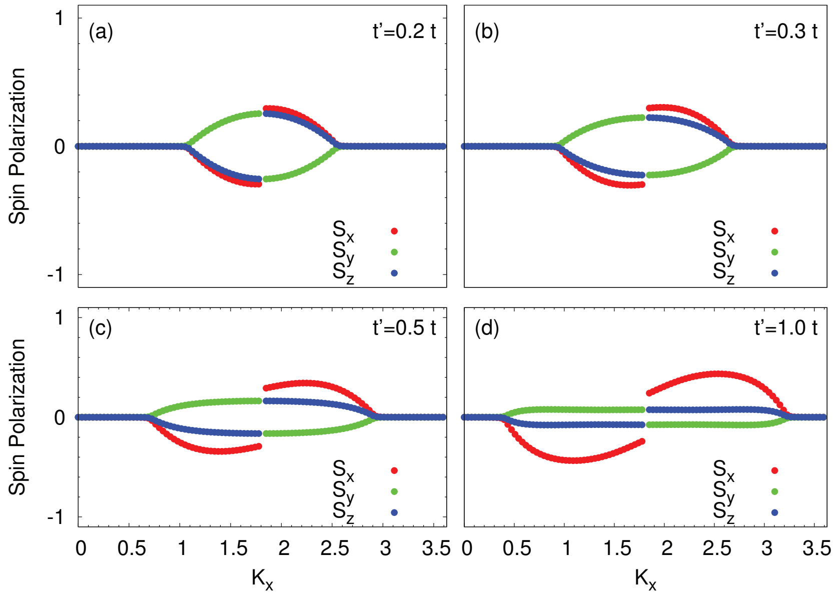

Figure 2.5: Spin polarization of the lowest positive energy state for the exactly diagonalized Hamiltonian on a cylinder with x links parallel to the boundary (see Fig. 2.3). k_x refers to the wavevector along the boundary. Spin polarization at the edge for (a) $t' = 0.2t$, (b) $t' = 0.3t$, (c) $t' = 0.5t$, (d) $t' = 1.0t$. The x component becomes dominant when t'/t increases. The spin polarization at the momentum k_x with the maximal dominant component is shown in Fig. 2.6 as a function of t'/t.

Consequentially, the effective Hamiltonian on the lower edge can be described as a 1D liquid, namely a helical Luttinger liquid with two types of wave functions $|\Psi_1\rangle$, $|\Psi_2\rangle$ with opposite spin polarizations (see Fig. 2.3) [128]. The spin polarization of the two helical states, which varies as a function of t'/t, is studied using exact diagonalization of the system on a cylinder. As shown in Fig. 2.5 lower panel, when $t' \ll t$ the helical states have equal components in all spin polarizations; when t'/t increases the helical states have a x component gradually dominating the spin polarization.

On the two edges of the system, we identify two counter-propagating helical spin states with opposite polarizations as a reminiscence of the Kane-Mele model [11]. As shown in Fig. 2.6, when t'/t is small, the spin polarization has equal components in the x, y and z directions, and when t'/t is large, one spin polarization component dominates and this dominant spin polarization coincides with the type of next-nearest-neighbour links parallel to the boundary (see Fig. 2.6), which implies that helical edge states point in x (y, z) direction if the two edges are parallel to the x (y and z) type link, respectively.

At a mean-field level, the interaction adds an effective chemical potential: $\sum_i U n_{i\uparrow} n_{i\downarrow} = \sum_{kl} \mu_{eff} \Psi^{\dagger}_{kl} \Psi_{kl}$ and Ψ_{kl} are the wave function of the band electron in which l is the band index, and $\mu_{eff} = \frac{U}{2}$ and the AQSH phase is robust as long as the chemical potential does not touch the conduction (valence) band: $\mu_{eff} < E_0(k)$ [62].

At a general level, one can show either using a mean-field type argument or by invoking the U(1) slave-rotor theory as explained in section 2.3.1, that such a Quantum Spin Hall phase is robust towards finite to moderate interactions. The notion of topological invariants can also been extended for an interacting system [134, 135, 136]. In section 2.3.1, we shall study in more details the disappearance of the helical edge modes resulting from the Mott transition in which Hubbard interaction localizes propagating edge electrons.

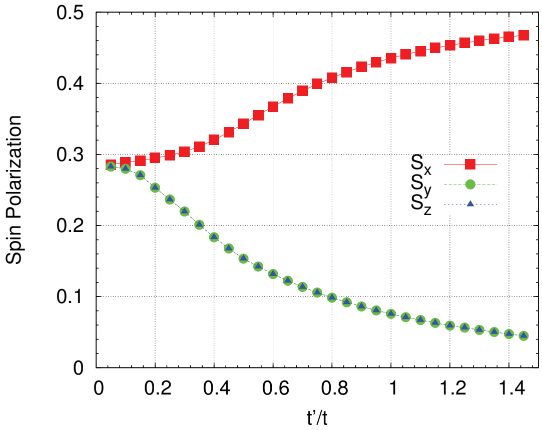

Figure 2.6: In the weak interaction regime, the anisotropic spin-orbit model lies in the phase of a topological band insulator on a cylinder, in which only the wave-vector k_x is a good quantum number. The two counter-propagating helical edge states protected by the $\mathbb{Z}_2$ topological invariant of the system have spin polarizations which explicitly depend on the ratio t'/t. Here, we show the spin polarization components of the edge state with a wave-vector k_x where S_x is maximum, as a function of t'/t (see, for example, Fig. 2.5). S_x prevails over S_y and S_z at large t'/t.

2.1.2 Edge State Solution via Transfer Matrix

In this section, we provide an analytical solution of the edge states, in the non-interacting limit at $U = 0$. We can view the system as semi-infinite with layers of one-dimensional two-sublattice chains coupled together as in Fig. 2.3 [159, 160]. We note the wave function on the n th layer as $\psi_{nJ\sigma}$ in which J designates the sublattice σ the spin, then we can write down the Schrödinger equation of the system:

$$\begin{aligned}&\left[-it'(e^{-i\frac{\sqrt{3}}{2}k_x}\sigma_z - e^{i\frac{\sqrt{3}}{2}k_x}\sigma_y)\tau_z - \frac{t}{2}(\tau_x + i\tau_y)\right]\psi_{n+1J\sigma} + E\psi_{nJ\sigma}\\ &+\left(2t'\sin\sqrt{3}k_x\sigma_x\tau_z - 2t\cos\frac{\sqrt{3}}{2}k_x\tau_x\right)\psi_{nJ\sigma} + [it'(e^{i\frac{\sqrt{3}}{2}k_x}\sigma_z - e^{-i\frac{\sqrt{3}}{2}k_x}\sigma_y)]\psi_{n-1J\sigma} = 0\end{aligned} \tag{2.1.7}$$

in which $\sigma_{x,y,z}$ denote the Pauli matrices for spin subspace and $\tau_{x,y,z}$ the Pauli matrices for the sublattice isospin subspace. Let us write down the wave function decaying when penetrating into the bulk: $\psi_{nJ\sigma} = \sum_i \lambda_i^n u_{iJ\sigma}$ such that the wave function vanishes at the edge $\psi_0 = \sum_i u_{iJ\sigma} = 0$. Then the Schrödinger equation reads:

$$Eu_{iJ\sigma} = [c_x^i\tau_x + c_y^i\tau_y + (m_x^i\sigma_x + m_y^i\sigma_y + m_z^i\sigma_z)\tau_z]u_{iJ\sigma} = M_i u_{iJ\sigma}, \tag{2.1.8}$$

in which

$$\begin{aligned}c_x^i &= \frac{t}{2}\left(\lambda_i + \frac{1}{\lambda_i}\right) - 2t\cos\frac{\sqrt{3}}{2}k_x\\ c_y^i &= \frac{it}{2}(\lambda_i - \frac{1}{\lambda_i})\\ m_x^i &= -2t'\sin\sqrt{3}k_x\sigma_x\\ m_y^i &= it'(\lambda_i e^{i\frac{\sqrt{3}}{2}k_x} - \frac{1}{\lambda_i}e^{-i\frac{\sqrt{3}}{2}k_x})\\ m_z^i &= -it'(\lambda_i e^{-i\frac{\sqrt{3}}{2}k_x} - \frac{1}{\lambda_i}e^{i\frac{\sqrt{3}}{2}k_x}).\end{aligned} \tag{2.1.9}$$

We can diagonalize the matrix in Eq. 2.1.8 by squaring it:

$$\begin{aligned}E^2 =& t^2 + 4t^2\cos^2\left(\frac{\sqrt{3}}{2}k_x\right) + 4t'^2 + 4t'^2\sin^2\sqrt{3}k_x + 4t'^2\cos\sqrt{3}k_x\\ &+ 2t^2\cos\frac{\sqrt{3}}{2}k_x(\lambda_i + \frac{1}{\lambda_i}) - 2t'^2\cos\left(\sqrt{3}k_x\right)(\lambda_i + \frac{1}{\lambda_i})^2.\end{aligned} \tag{2.1.10}$$

Eq. 2.1.10 is a second-order equation of $\lambda_i + \frac{1}{\lambda_i}$ and a fourth order equation of λ_i. There are 4 roots of λ_i among which two of them satisfy $|\lambda_i| < 1$, and if λ_i is a root of the equation so is $\frac{1}{\lambda_i}$. Therefore, we are allowed to write the wave function as a superposition of two eigenvectors:

$$\psi_n = u_1\lambda_1^n + u_2\lambda_2^n. \tag{2.1.11}$$

The vanishing of the wave function at the edge gives that $u_1 = -u_2 = u$, then the wave function shall be written as:

$$\psi_n = (\lambda_1^n - \lambda_2^n)u. \tag{2.1.12}$$

Equation 2.1.8 implies the fact that the two matrices $E - M_i$ ($i = 1{,}2$) in Eq. 2.1.8 are sharing a null-eigenvector, and this entails:

$$\mathrm{Det}(E - M_1) = \mathrm{Det}(E - M_2) = \mathrm{Det}(a_1(E - M_1) + a_2(E - M_2)) = 0, \tag{2.1.13}$$

in which a_1,a_2 are two arbitrary constants. This is equivalent to:

$$\begin{aligned} E^2 &= (c_x^1)^2 + (c_y^1)^2 + (m_x^1)^2 + (m_y^1)^2 + (m_z^1)^2 = (c_x^2)^2 + (c_y^2)^2 + (m_x^2)^2 + (m_y^2)^2 + (m_z^2)^2 \\ &= c_x^1 c_x^2 + c_y^1 c_y^2 + m_x^1 m_x^2 + m_y^1 m_y^2 + m_z^1 m_z^2. \end{aligned} \tag{2.1.14}$$

Then we have:

$$(c_x^1 - c_x^2)^2 + (c_y^1 - c_y^2)^2 + (m_x^1 - m_x^2)^2 + (m_y^1 - m_y^2)^2 + (m_z^1 - m_z^2)^2 = 0, \tag{2.1.15}$$

$$(\lambda_1 - \lambda_2)^2 \left[2t'^2 \cos\sqrt{3}k_x \left(1 + \left(\frac{1}{\lambda_1\lambda_2} \right)^2 \right) + \frac{t^2 + 4t'^2}{\lambda_1\lambda_2} \right] = 0. \tag{2.1.16}$$

$\lambda_1 = \lambda_2$ gives a trivial solution, then we can find $\lambda_1\lambda_2$ from the above equation. If we put $L = \frac{t^2+4t'^2}{2t'^2 \cos\sqrt{3}k_x}$, then:

$$M = \lambda_1\lambda_2 = \frac{-L \pm \sqrt{L^2 - 4}}{2}. \tag{2.1.17}$$

Since we must impose $|\lambda_i| < 1$ ($i = 1{,}2$), this implies that $|\lambda_1\lambda_2| < 1$. The first Brillouin zone for the one-dimensional chain is $[0, \frac{2\pi}{\sqrt{3}}]$, resulting in:

$$\begin{cases} \lambda_1\lambda_2 = -\frac{L-\sqrt{L^2-4}}{2} & k_x \in [0, \frac{\pi}{2\sqrt{3}}] \cup [\frac{3\pi}{2\sqrt{3}}, \frac{2\pi}{\sqrt{3}}] \\ \lambda_1\lambda_2 = -\frac{L+\sqrt{L^2-4}}{2} & k_x \in [\frac{\pi}{2\sqrt{3}}, \frac{3\pi}{2\sqrt{3}}]. \end{cases} \tag{2.1.18}$$

From Eq. (2.1.8) we find:

$$\lambda_1 + \frac{1}{\lambda_1} + \lambda_2 + \frac{1}{\lambda_2} = (1 + \frac{1}{\lambda_1\lambda_2})(\lambda_1 + \lambda_2) = \frac{t^2 \cos\frac{\sqrt{3}}{2}k_x}{t'^2 \cos\sqrt{3}k_x}. \tag{2.1.19}$$

From $\lambda_1 + \lambda_2 = \frac{t^2 \cos\frac{\sqrt{3}}{2}k_x}{t'^2 \cos\sqrt{3}k_x (1+\frac{1}{\lambda_1\lambda_2})} = N$ we can work out the two eigenvalues λ_1 and λ_2: $\lambda_{1,2} = \frac{-N\pm\sqrt{N^2-4M}}{2}$ which gives us the penetration length: $\xi_{1,2} = -\ln(\lambda_{1,2})$. From the relation:

$$\begin{aligned} (\lambda_1 + \frac{1}{\lambda_1})(\lambda_2 + \frac{1}{\lambda_2}) &= \frac{(\lambda_1 + \lambda_2)^2}{\lambda_1\lambda_2} - 2 + \lambda_1\lambda_2 + \frac{1}{\lambda_1\lambda_2} \\ &= \frac{E^2 - (t^2 + 4t^2 \cos^2\frac{\sqrt{3}}{2}k_x + 4t'^2 + 4t'^2 \sin^2\sqrt{3}k_x + 4t'^2 \cos\sqrt{3}k_x)}{2t'^2 \cos\sqrt{3}k_x} \end{aligned} \tag{2.1.20}$$

We find the dispersion relation for the edge states and this fits well with the spectrum obtained numerically in Fig. 2.7:

$$E_{\text{edge}} = \pm\sqrt{4t^2 \cos^2\frac{\sqrt{3}}{2}k_x + 4t'^2 \sin^2\sqrt{3}k_x - \frac{4t'^4 \cos^4\frac{\sqrt{3}}{2}k_x}{t^2 + 4t'^2 - 4t'^2 \cos\sqrt{3}k_x}}. \tag{2.1.21}$$

In order to find the wave function, we can use the projector:

$$P_\pm^i = \frac{1}{2}\left(1 \pm \left(\frac{c_x^i}{E_0}\tau_x + \frac{c_y^i}{E_0}\tau_y + (\frac{m_x^i}{E_0}\sigma_x + \frac{m_y^i}{E_0}\sigma_y + \frac{m_z^i}{E_0}\sigma_z)\tau_z\right)\right) \tag{2.1.22}$$

that diagonalizes Eq. (2.1.8). The eigenvector u is the intersection of the two projected spaces entailed by $P_-^{1,2}$.

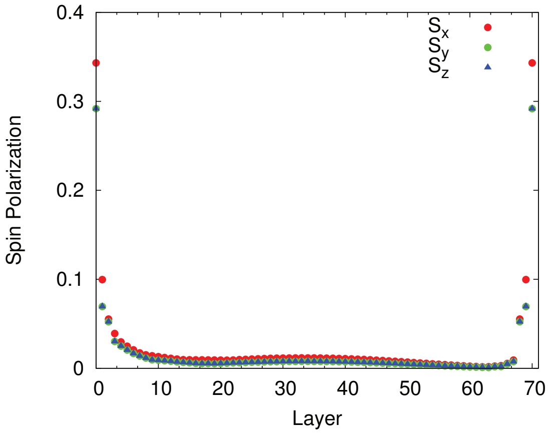

Figure 2.7: The numerical study of spin polarization magnitude as a function of layer in the system of 70 layers of one-dimensional chains described by Eq. 2.1.7 at $t' = 0.5t$.

2.2 The Frustrated Magnetism in Strong Coupling limit

In this section, we investigate the magnetism emerging in the limit of "infinite" interactions, the possible magnetic orders and the phase transition(s) between these phases. Since the electron-hole excitations in this limit would cost an energy proportional to U, electrons are subject to virtual tunneling processes in which they exchange their positions while leaving the filling unchanged. The induced super-exchange magnetism is a second-order process in H_0[92]:

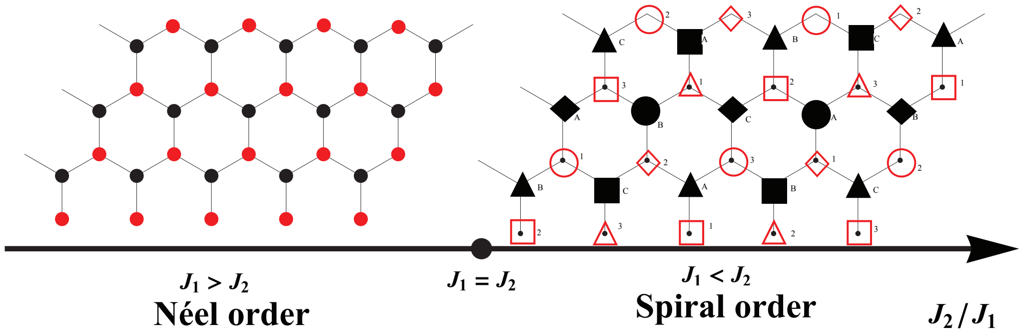

Figure 2.8: The magnetic phase diagram for the tight-binding model with anisotropic spin-orbit coupling on the honeycomb lattice in the limit of infinite U described by Eq. 2.2.1. The $J_1 - J_2$ model is highly frustrated because of the hexagonal geometry and the anisotropy of the J_2 coupling. We identify the bipartite Néel phase at $J_1 > J_2$, the Spiral phase with 24 sublattices at $J_1 < J_2$.

$$H_{J_1 J_2} = J_1 \sum_{<i,j>} \vec{S}_i \cdot \vec{S}_j + J_2 \sum_{\langle\langle i,j \rangle\rangle} (S_i^\alpha S_j^\alpha - S_i^\beta S_j^\beta - S_i^\gamma S_j^\gamma) \tag{2.2.1}$$

where $J_2 = 2t'^2/U$ and $J_1 = 2t^2/U$.

The term with J_2 indicates a next nearest-neighbor link in α spin polarization, with $\alpha = x$,y,z on respectively red, green and blue links in Fig. 2.1, β and γ are other spin polarizations than α. The frustration stems from several levels: the coexistence of first and second neighbor couplings, the anisotropy in the next-nearest-neighbour coupling as well as the lattice geometry. The minimization of the ground state energy will lead to different scenarios like enlarged unit cells, disappearance of Goldstone modes and the reduction of possible classical ground states manifold (degeneracy lift).

When evaluating the classical energy of the magnetic order, we identify two magnetic phases: the Néel order at $J_1 > J_2$ and the two copies of locked Spiral order on the two triangular sublattices at $J_1 < J_2$ with the critical point $J_1 = J_2$ as in Fig. 2.8. We also performed a spin wave analysis based on the classical magnetic order. Analytical and numerical investigations of the magnetism at all J_1/J_2 ratios are presented below, for completeness. We recover the existence of a quantum phase transition at $J_1 \approx J_2$.

2.2.1 Néel Phase for $J_1 > J_2$

In the $J_1 \gg J_2$ regime, the Heisenberg coupling dominates over Kitaev-Heisenberg coupling and the corresponding magnetic phase is the well-known bipartite Néel order on the bipartite honeycomb lattice: $\vec{S}_A = -\vec{S}_B$ and the classical energy of this state per site is $E_{\text{Néel}} = -\frac{3J_1}{2}\vec{S}^2 - J_2\vec{S}^2$. The $SU(2)$ spin rotation symmetry is spontaneously broken for the Néel state and in the absence of next-nearest-neighbor frustration, there exists a Goldstone mode underlying the whole original continuous spin symmetry $SU(2)$ on the unit sphere, restoring the spontanesouly $SU(2)$ symmetry. The energy of the Goldstone mode adds a quantum correction to the ground state. At the level of this Néel order, we carried out a semiclassical spin wave analysis in order to compute this correction to the energy of the Néel state, from which we will see that the anisotropy in the J_2 coupling lifts the degeneracy between the different possible orientations of the Néel order parameter. Specifically, the vacuum energy will become non-uniform on the $SU(2)$ sphere selecting certain spin polarization which minimize the vacuum energy.

In order to describe the quantum correction based on an arbitrary spin polarization, we begin by writing the Holstein-Primakoff representation of the spin in the z polarization, then we rotate the z quantization axis by the Euler rotation matrix in order to describe quantum fluctuations in all the spontaneously broken symmetry cases: we rotate the z axis first around the y axis by an angle θ then around z axis by an angle ϕ, resulting in

$$R(\phi,\theta) = R_z(\phi)R_y(\theta) = \begin{pmatrix} \cos\theta & -\sin\theta & 0 \\ \cos\phi\sin\theta & \cos\phi\cos\theta & -\sin\phi \\ \sin\phi\sin\theta & \sin\phi\cos\theta & \cos\phi \end{pmatrix} \tag{2.2.2}$$

$$\begin{pmatrix} S^z_{A0} \\ S^x_{A0} \\ S^y_{A0} \end{pmatrix} = \begin{pmatrix} S - a^\dagger a \\ \frac{\sqrt{2S}}{2}(a^\dagger + a) \\ \frac{\sqrt{2S}}{2i}(a - a^\dagger) \end{pmatrix}, \tag{2.2.3}$$

$$\begin{pmatrix} S^z_{B0} \\ S^x_{B0} \\ S^y_{B0} \end{pmatrix} = \begin{pmatrix} -S + b^\dagger b \\ \frac{\sqrt{2S}}{2}(b^\dagger + b) \\ \frac{\sqrt{2S}}{2i}(b^\dagger - b) \end{pmatrix}, \tag{2.2.4}$$

$$\begin{pmatrix} S^z_{A} \\ S^x_{A} \\ S^y_{A} \end{pmatrix} = R(\phi,\theta)\begin{pmatrix} S^z_{A0} \\ S^x_{A0} \\ S^y_{A0} \end{pmatrix}, \tag{2.2.5}$$

$$\begin{pmatrix} S_B^z \\ S_B^x \\ S_B^y \end{pmatrix} = R(\phi,\theta) \begin{pmatrix} S_{B0}^z \\ S_{B0}^x \\ S_{B0}^y \end{pmatrix}. \tag{2.2.6}$$

We insert the above semiclassical spin representation back into Eq. 2.2.1, then we will obtain the Bogoliubov-De Gennes type effective Hamiltonian describing the quantum fluctuation about the Néel state:

$$H = \sum_{\vec{q}} \Phi_{\vec{q}}^\dagger H_{\vec{q}} \Phi_{\vec{q}} - \frac{J_1}{2} N S^2 z - J_2 N S^2, \tag{2.2.7}$$

where $\Phi_{\vec{q}}^\dagger = (a_{\vec{q}}, b_{-\vec{q}}^\dagger, a_{-\vec{q}}^\dagger, b_{\vec{q}})$, $z = 3$ is the coordinate number, N the number of sites, and we define

$$H_q = \begin{pmatrix} \gamma_z & \gamma_{\vec{q}}^\star & \gamma_{xy}^\star & 0 \\ \gamma_{\vec{q}} & \gamma_z & 0 & \gamma_{xy}^\star \\ \gamma_{xy} & 0 & \gamma_z & \gamma_{\vec{q}}^\star \\ 0 & \gamma_{xy} & \gamma_{\vec{q}} & \gamma_z \end{pmatrix}, \tag{2.2.8}$$

$$\begin{aligned} \gamma_{\vec{q}} &= J_1 S \sum_i \exp(i\vec{q} \cdot \vec{\delta}_i) \\ \gamma_z &= 3J_1 S + 2J_2 S - 2J_2 S[\cos^2\phi \sin^2\theta \cos(\vec{q} \cdot \vec{R}_x) + \sin^2\phi \sin^2\theta \cos(\vec{q} \cdot \vec{R}_y) + \sin^2\theta \cos(\vec{q} \cdot \vec{R}_z)] \\ \gamma_{xy} &= J_2 S[\exp(i\vec{q} \cdot \vec{R}_z) \sin^2\theta + \exp(i\vec{q} \cdot \vec{R}_x)(\cos^2\phi \cos^2\theta \sin^2\phi - i \sin 2\phi \cos\theta) \\ &\quad + \exp(i\vec{q} \cdot \vec{R}_y)(\sin^2\phi \cos^2\theta - \cos^2\phi + i \sin 2\phi \cos\theta)]. \end{aligned}$$

We apply the Bogoliubov-De Gennes method to diagonalize the Hamiltonian: $\alpha_{\vec{q}} = u_1 a_{\vec{q}} + v_1 b_{-\vec{q}}^\dagger + u_2 a_{-\vec{q}}^\dagger + v_2 b_{\vec{q}}$, and $[\alpha_{\vec{q}}, H] = \omega_{\vec{q}} \alpha_{\vec{q}}$, then we will obtain the excitation energies for the spin wave and the corresponding wave function $\alpha_{i\vec{q}}; i = 1,2,3,4$. Thereafter, we have diagonalized the Hamiltonian with four energy levels:

$$\omega_{i\vec{q}} = \pm\sqrt{\gamma_z^2 - (|\gamma_{\vec{q}}| \pm |\gamma_{xy}|)^2} \quad i = 1,2,3,4 \tag{2.2.9}$$

$$H = \sum_{\vec{q}} \omega_{\vec{q}} (\alpha_{1\vec{q}}^\dagger \alpha_{1\vec{q}} + \alpha_{2\vec{q}} \alpha_{2\vec{q}}^\dagger + \alpha_{3\vec{q}}^\dagger \alpha_{3\vec{q}} + \alpha_{4\vec{q}} \alpha_{4\vec{q}}^\dagger). \tag{2.2.10}$$

By putting the Hamiltonian in 'normal order' (commuting $\alpha_{2\vec{q}} \alpha_{2\vec{q}}^\dagger$ and $\alpha_{4\vec{q}} \alpha_{4\vec{q}}^\dagger$), we obtain the energy of the vacuum:

$$E_0 = 2 \sum_{\vec{q}} \omega_{\vec{q}} = \sum_{\vec{q}} 2\sqrt{\gamma_z^2 - (|\gamma_{\vec{q}}| + |\gamma_{xy}|)^2}. \tag{2.2.11}$$

Noticing that the vacuum energy depends on the two Euler angles θ and ϕ, the vacuum quantum fluctuations shall choose an angle that minimizes E_0. Numerically, we find that the minimal vacuum energy is taken when the quantization axis coincides with the x y and z axis (see Fig. 2.9). The Goldstone mode is no longer soft in this case, because when we shift from one spontaneously broken symmetry vacuum to another, the variation of the vacuum energy makes this 'transversal' mode energetic, thus destroying the Goldstone mode. Conclusively, the spin wave analysis infers that the Néel phase in the limit of $J_1 > J_2$ loses its Goldstone mode due to the anisotropy, and that the zero-point vacuum fluctuations select only Néel orders pointing along the x, y and z directions.

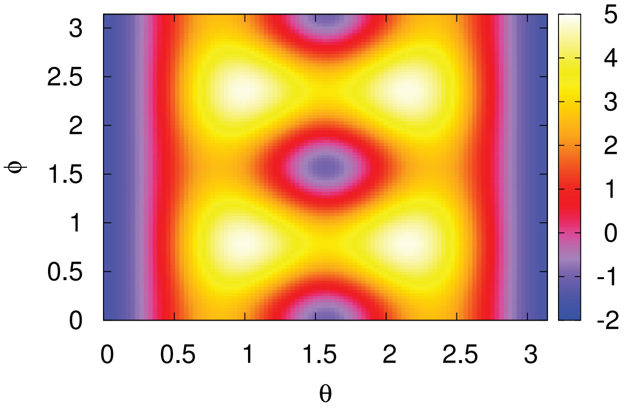

Figure 2.9: Color topography of the vacuum energy as a function of θ and ϕ in the Néel order phase when $J_1 > J_2$, in which θ and ϕ indicate the Euler angles describing the order parameter of the Néel order. The minimum of the vacuum energy is taken when the Néel order parameter coincides with the x y and z direction. The next-nearest-neighbor anisotropic coupling reduces the $SU(2)$ symmetry of the vacuum states for a conventional Néel order to a discrete symmetry of three possible order parameters of this frustrated Néel order.

2.2.2 Non-Colinear Spiral Phase for $J_1 < J_2$

Next, we focus on the Spiral phase of $J_1 < J_2$. If we only take into account the J_2 magnetic coupling, we can apply a global transformation to bring the spin model in Eq. 2.2.1 into an $SU(2)$ anti-ferromagnetic Heisenberg model on the triangular sublattices by introducing 4 patterns, namely: $H_{J_2} = J_2 \sum \widetilde{\vec{S}_i} \cdot \widetilde{\vec{S}_j}$ where $S_i^l = \epsilon_i^l \cdot \widetilde{S_i^l}$ and $l = x{,}y{,}z$ such that the global transformation obeys the following condition:

$$\begin{aligned} &\epsilon_i^z \epsilon_j^z = 1 \quad \epsilon_i^y \epsilon_j^y = -1 \quad \epsilon_i^x \epsilon_j^x = -1 \\ &\epsilon_j^z \epsilon_k^z = -1 \quad \epsilon_j^y \epsilon_k^y = -1 \quad \epsilon_j^x \epsilon_k^x = 1 \\ &\epsilon_k^z \epsilon_i^z = -1 \quad \epsilon_k^y \epsilon_i^y = 1 \quad \epsilon_k^x \epsilon_i^x = -1, \end{aligned} \tag{2.2.12}$$

where $\epsilon_l^w = \pm 1 \quad (l = i{,}j{,}k; \quad w = x{,}y{,}z)$. We can thus find out the four solutions of $\begin{pmatrix} \epsilon_{i,j,k}^x \\ \epsilon_{i,j,k}^y \\ \epsilon_{i,j,k}^z \end{pmatrix}$:

$$\begin{pmatrix} \epsilon_i^x \\ \epsilon_i^y \\ \epsilon_i^z \end{pmatrix} = \begin{pmatrix} 1 \\ 1 \\ 1 \end{pmatrix} \square, \begin{pmatrix} -1 \\ -1 \\ 1 \end{pmatrix} \triangle, \begin{pmatrix} -1 \\ 1 \\ -1 \end{pmatrix} \bigcirc, \begin{pmatrix} 1 \\ -1 \\ -1 \end{pmatrix} \diamondsuit. \tag{2.2.13}$$

The x, y, z links are all transformed into Heisenberg anti-ferromagnetic links after the global transformation but the introduced four patterns are paved to every sites. Then, the classical ground state on the triangular lattices is obviously the coplanar 120° Néel order for the transformed anti-ferromagnetic Heisenberg model, consisting of 3 sublattices (A, B, C or 1, 2, 3 in Fig. 10). The magnetic order will be a Spiral order with 12 sublattices on each triangular sublattice with 4 patterns □◇ ○ △ paved according to the following constraints:

1. X-link: □◯ or ◇△
2. Y-link: □◇ or △◯
3. Z-link: □△ or ◯◇.

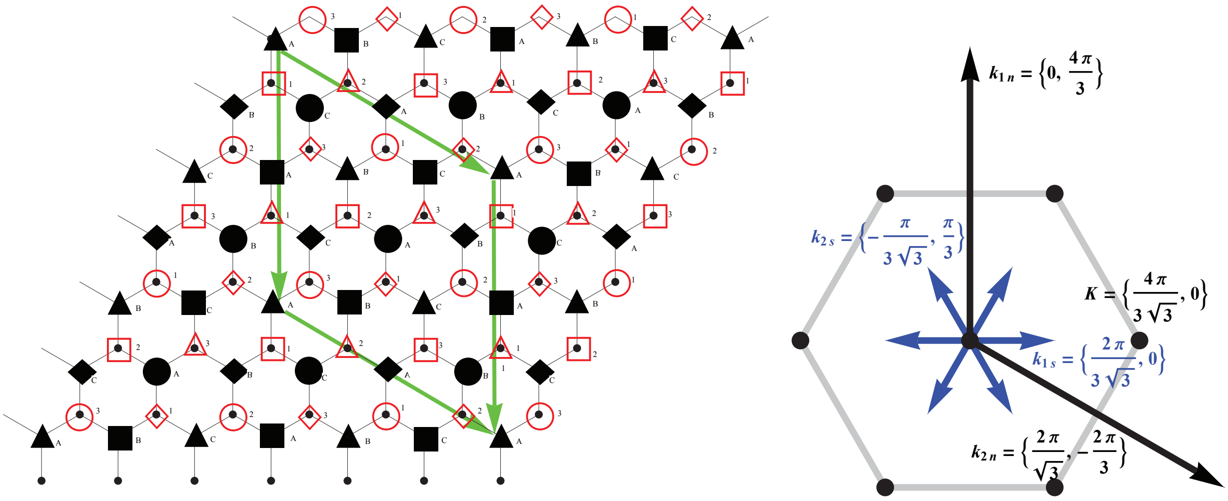

Figure 2.10: The global transformation brings the J_2 anisotropic magnetic model to an anti-ferromagnetic spin model on triangular lattices with four patterns: □◇ ◯ △ with black patterns on one sublattice and red patterns on the other. The nearest-neighbor J_1 Heisenberg coupling locks the angles between two copies of spiral orders and fixing the relative arrangement of the 4 patterns between the two sublattices as shown in the figure. The sites on which we studied the nearest-neighbor Heisenberg coupling namely the local fields $\vec{h}^1_\triangle$, $\vec{h}^2_\square$ and $\vec{h}^3_\bigcirc$ in Eqs. 2.2.15, 2.2.16 and 2.2.17 are painted in red color with their number indicating the sublattice for the transformed 120° Néel order. In Green, we depict the 12 sublattices (sites) on each triangular sublattice with 4 patterns, which finally constitutes 24 sublattices for the elementary cell of the magnetic order. We also represent the wave-vectors associated with the Spiral phase (in blue) and with the Néel phase (in black). The grey hexagon connects the Dirac points.

The magnetic order is spiral in that the 4 patterns □◇ ◯ △ and the 3 spins of the 120° Néel order are alternating when moving in one direction on the lattice. It is important to underline that in the Spiral phase, the spin order is non-colinear (see Fig. 2.11). We have given the wave vectors of the spiral magnetic order in the right panel of figure 2.10, which is not in agreement with the results obtained by Reuther et al by fermionic renormalization group [105]. The wave vector of the magnetic phase seems to vary continuously as a function of J_2/J_1 according to Reuther et al, which is not compatible with our analysis either.

In the absence of the J_1 coupling, the two copies of spiral order can rotate with respect to each other freely and the relative arrangement of the 4 patterns can be arbitrary between the two sublattices.At the classical level, the J_1 anti-ferromagnetic coupling shall impose the choice of the 4 pattern paving on the alternative sublattice once the 4 pattern paving is fixed in one triangular sublattice as in Fig. 2.10. Meanwhile, if we consider the J_1 coupling in terms of the 3 spins of the 120° Néel order after the global transformation, the two copies of the transformed 120° spins would be mutually locked reducing the degree of freedom of the angle between the two copies of the transformed 120° Néel order. The spiral order likewise the 120°

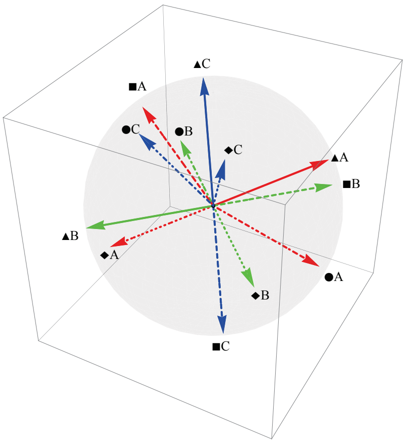

Figure 2.11: Here, we represent the orientations of the 12 black sites in the Green unit cell of the Spiral phase.

Néel state has another degree of freedom, namely the direction of the Néel order parameter. The energy of the J_1 coupling would depend on the latter. The minimization with regard to this degree of freedom would still reduce the possible choices of the Néel order parameter. We shall clarify the minimization of J_1 coupling energy with regard to these factors.

The 120° Néel state imposes that spins on the three vertices A, B and C of a triangle $\vec{\tilde{S}}_A + \vec{\tilde{S}}_B + \vec{\tilde{S}}_C = 0$. The J_1 Heisenberg coupling is equivalent to a local magnetic field produced by the three nearest neighbour spins of the alternative copy of the spiral order on the other copy of the 4 sublattice spiral order:

$$H_{J_1} = J_1 \sum_i (\vec{h}_{i\triangle} \cdot \vec{S}_{i\triangle} + \vec{h}_{i\square} \cdot \vec{S}_{i\square} + \vec{h}_{i\Diamond} \cdot \vec{S}_{i\Diamond} + \vec{h}_{i\bigcirc} \cdot \vec{S}_{i\bigcirc}), \tag{2.2.14}$$

where the sum is carried out in terms of 4 sublattices. Considering the 3-sublattices Néel order, we have to sum over 12 sites in order to get the classical energy of the J_1 coupling. However, when writing down the local magnetic field stemming from the J_1 coupling, we found that the 4 patterns could be simplified, and that we need only to sum over the 3 sublattices of the 120° order.

The effective local magnetic fields due to the nearest-neighbor Heisenberg coupling on the sites with numbers painted in red in Fig. 2.10 are:

$$\vec{h}^1_\triangle = D_\square \vec{\tilde{S}}_A + D_\bigcirc \vec{\tilde{S}}_B + D_\Diamond \vec{\tilde{S}}_C = 2D_\triangle \begin{pmatrix} \tilde{S}^x_B \\ \tilde{S}^y_C \\ \tilde{S}^z_A \end{pmatrix} \tag{2.2.15}$$

$$\vec{h}^2_\square = D_\triangle \vec{\tilde{S}}_B + D_\bigcirc \vec{\tilde{S}}_A + D_\Diamond \vec{\tilde{S}}_C = 2D_\square \begin{pmatrix} \tilde{S}^x_C \\ \tilde{S}^y_A \\ \tilde{S}^z_B \end{pmatrix} \tag{2.2.16}$$

$$\vec{h}^3_\bigcirc = D_\Diamond \vec{\tilde{S}}_C + D_\square \vec{\tilde{S}}_B + D_\triangle \vec{\tilde{S}}_A = 2D_\bigcirc \begin{pmatrix} \tilde{S}^x_A \\ \tilde{S}^y_B \\ \tilde{S}^z_C \end{pmatrix} \tag{2.2.17}$$

where $D_{\Box} = \begin{pmatrix} 1 & 0 & 0 \\ 0 & 1 & 0 \\ 0 & 0 & 1 \end{pmatrix}$, $D_{\triangle} = \begin{pmatrix} -1 & 0 & 0 \\ 0 & -1 & 0 \\ 0 & 0 & 1 \end{pmatrix}$, $D_{\bigcirc} = \begin{pmatrix} -1 & 0 & 0 \\ 0 & 1 & 0 \\ 0 & 0 & -1 \end{pmatrix}$, $D_{\Diamond} = \begin{pmatrix} 1 & 0 & 0 \\ 0 & -1 & 0 \\ 0 & 0 & -1 \end{pmatrix}$.

We found that the sum of the J_1 coupling on these three sites is independent of the 4 patterns:

$$\begin{aligned} &J_1(\vec{h}_{1\triangle} \cdot \vec{S}_{1\triangle} + \vec{h}_{2\Box} \cdot \vec{S}_{2\Box} + \vec{h}_{3\Diamond} \cdot \vec{S}_{3\Diamond}) \\ =&J_1(D_{\triangle}\tilde{\vec{h}}_1 D_{\triangle}\tilde{\vec{S}}_1 + D_{\Box}\tilde{\vec{h}}_2 D_{\Box}\tilde{\vec{S}}_2 + D_{\Diamond}\tilde{\vec{h}}_3 D_{\Diamond}\tilde{\vec{S}}_3) \\ =&J_1(\tilde{\vec{h}}_1 \cdot \tilde{\vec{S}}_1 + \tilde{\vec{h}}_2 \cdot \tilde{\vec{S}}_2 + \tilde{\vec{h}}_3 \cdot \tilde{\vec{S}}_3), \end{aligned} \tag{2.2.18}$$

in which $\tilde{\vec{h}}_1 = 2\begin{pmatrix} \tilde{S}_B^x \\ \tilde{S}_C^y \\ \tilde{S}_A^z \end{pmatrix}$, $\tilde{\vec{h}}_2 = 2\begin{pmatrix} \tilde{S}_C^x \\ \tilde{S}_A^y \\ \tilde{S}_B^z \end{pmatrix}$ and $\tilde{\vec{h}}_3 = 2\begin{pmatrix} \tilde{S}_A^x \\ \tilde{S}_B^y \\ \tilde{S}_C^z \end{pmatrix}$. As a result, the J_1 coupling turns into:

$$H_{J_1} = J_1 \sum_i \tilde{\vec{h}}_i \cdot \tilde{\vec{S}}_i, \tag{2.2.19}$$

in which the sum is carried over the 3 sublattices of the 120° Néel order and the transformed local magnetic field $\tilde{\vec{h}} = D_X \vec{h}_X$ $(X = \Box\Diamond\bigcirc\triangle)$ is independent of the choice of the 4 patterns.

We observe one property of these local fields that would allow us to simplify the analysis in terms of the choice of the Néel order parameter of the 120° transformed Néel order and the relative angle between the two copies of spiral order:

$$\tilde{\vec{h}}_1 + \tilde{\vec{h}}_2 + \tilde{\vec{h}}_3 = 0. \tag{2.2.20}$$

Then, the minimization of energy of the J_1 nearest neighbor coupling in equation 2.2.19 can be fulfilled by the use of Cauchy-Schwarz Inequality:

$$\begin{aligned} \tilde{\vec{h}}_1 \cdot \tilde{\vec{S}}_1 + \tilde{\vec{h}}_2 \cdot \tilde{\vec{S}}_2 + \tilde{\vec{h}}_3 \cdot \tilde{\vec{S}}_3 &\geq -(||\tilde{\vec{h}}_1|| \cdot ||\tilde{\vec{S}}_1|| + ||\tilde{\vec{h}}_2|| \cdot ||\tilde{\vec{S}}_2|| + ||\tilde{\vec{h}}_3|| \cdot ||\tilde{\vec{S}}_3||) \\ &\geq -\sqrt{3(||\tilde{\vec{h}}_1||^2 + ||\tilde{\vec{h}}_2||^2 + ||\tilde{\vec{h}}_3||^2)} = -6. \end{aligned} \tag{2.2.21}$$

The two equalities in Eq. 2.2.21 are taken simultaneously when the norms of the three local magnetic fields on the other copy of the triangular sublattice are equal as in Eq. 2.2.22:

$$\begin{aligned} &||\tilde{\vec{h}}_1|| = ||\tilde{\vec{h}}_2|| = ||\tilde{\vec{h}}_3|| \\ &\tilde{\vec{S}}_1 = -\frac{1}{2}\tilde{\vec{h}}_1 \quad \tilde{\vec{S}}_1 = -\frac{1}{2}\tilde{\vec{h}}_2 \quad \tilde{\vec{S}}_3 = -\frac{1}{2}\tilde{\vec{h}}_3. \end{aligned} \tag{2.2.22}$$

Since all the spins are prone to align in the opposite direction to the local magnetic field to lower the energy of the ground state, the equality of norms of the three magnetic field on the alternative triangular sublattice coincidentally implies as well: $\tilde{\vec{S}}_1 + \tilde{\vec{S}}_2 + \tilde{\vec{S}}_3 = 0$, in other words the 120° Néel state for $\tilde{\vec{S}}$ on the alternative sublattice.

Accordingly, the spiral order for $\vec{S}$ on the alternative sublattice is favored when the energy of the nearest-neighbor Heisenberg coupling is minimized, and the latter locks the angle between the two copies of spiral order of the ground state obtained from further analysis of Eq. 2.2.22. The fixing procedure of the relative arrangement between the two sublattices is presented in Fig. 2.10. We will further study Eq. 2.2.22 to find out how the choice of the

Néel order parameter for the 120° Néel order and the angle between the two copies of spiral order are constrained for the minimization of the classical energy.

Eqs. 2.2.22 impose extra restrictions on the three 120° Néel vectors, and these supplementary restrictions to spins will reduce the $SU(2)$ continuous symmetry for quantization axis choice to a smaller group:

$$\begin{cases} \widetilde{S}_B^{x2} + \widetilde{S}_C^{y2} + \widetilde{S}_A^{z2} = \widetilde{S}_A^{x2} + \widetilde{S}_B^{y2} + \widetilde{S}_C^{z2} = \widetilde{S}_C^{x2} + \widetilde{S}_A^{y2} + \widetilde{S}_B^{z2} = 1 \\ ||\vec{\widetilde{S}}_A|| = ||\vec{\widetilde{S}}_B|| = ||\vec{\widetilde{S}}_C|| = 1 \\ \vec{\widetilde{S}}_A + \vec{\widetilde{S}}_B + \vec{\widetilde{S}}_C = 0. \end{cases} \tag{2.2.23}$$

The last two equations in Eqs. 2.2.23 is implied by the construction of three arbitrary vectors in the space with 120° between each other by means of Olinde-Rodrigue formula:

$$\begin{cases} \vec{\widetilde{S}}_A = \cos(\alpha)\vec{u} + \sin(\alpha)\vec{v} \\ \vec{\widetilde{S}}_B = \cos(\alpha + \frac{2\pi}{3})\vec{u} + \sin(\alpha + \frac{2\pi}{3})\vec{v} \\ \vec{\widetilde{S}}_C = \cos(\alpha - \frac{2\pi}{3})\vec{u} + \sin(\alpha - \frac{2\pi}{3})\vec{v} \end{cases} \tag{2.2.24}$$

The two vectors $\vec{u}$ and $\vec{v}$ indicate the plane in which the Néel order parameter of the black sublattice lives: $\vec{u} = \begin{pmatrix} \cos\theta \\ \sin\theta \\ 0 \end{pmatrix}$ $\vec{v} = \begin{pmatrix} -\sin\phi\sin\theta \\ \sin\phi\cos\theta \\ \cos\phi \end{pmatrix}$, then $\vec{n}$ is the normal vector to the plane defined by ($\widetilde{S}_A$,$\widetilde{S}_B$,$\widetilde{S}_C$):

$$\vec{n} = \vec{u} \wedge \vec{v} = \begin{pmatrix} \sin\theta\cos\phi \\ -\cos\theta\cos\phi \\ \sin\phi \end{pmatrix}. \tag{2.2.25}$$

$\vec{n}$ plays the role of rotation axis of the three vectors composing the 120° Néel state.

Resolution of Eqs. 2.2.23 gives a group of solutions for θ and ϕ, therefore a family of rotation axes of the 120° Néel state on the unitary sphere. More precisely, we obtain the equations:

$$\begin{cases} (\cos\alpha\cos\theta - \sin\alpha\sin\phi\sin\theta)^2 + (\cos(\alpha + \frac{2\pi}{3})\sin\theta + \sin(\alpha + \frac{2\pi}{3})\sin\phi\cos\theta)^2 + (\sin(\alpha - \frac{2\pi}{3})\cos\phi)^2 = 1 \\ (\cos(\alpha - \frac{2\pi}{3})\cos\theta - \sin(\alpha - \frac{2\pi}{3})\sin\phi\sin\theta)^2 + (\cos\alpha\sin\theta + \sin\alpha\sin\phi\cos\theta)^2 + (\sin(\alpha + \frac{2\pi}{3})\cos\phi)^2 = 1. \end{cases} \tag{2.2.26}$$

The numerical solution gives that the rotational axis for the 120° Néel order (namely $\vec{n}$) takes the form(s):

$$\frac{1}{\sqrt{3}}\begin{pmatrix} -1 \\ -1 \\ -1 \end{pmatrix}, \frac{1}{\sqrt{3}}\begin{pmatrix} 1 \\ -1 \\ 1 \end{pmatrix}, \frac{1}{\sqrt{3}}\begin{pmatrix} 1 \\ 1 \\ -1 \end{pmatrix}, \frac{1}{\sqrt{3}}\begin{pmatrix} -1 \\ 1 \\ 1 \end{pmatrix}, \tag{2.2.27}$$

and the three 120° spins can rotate freely around these axes (α can take any value). Within our choice of notations, the solution $\vec{n}$ is equivalent to $-\vec{n}$ because they describe the same 'plane' of solutions for the spins. We should notice that there exists a spin permutation symmetry σ for the group formed by these axes and this symmetry is a reminiscence of symmetry group preserved by the original model:

$$\vec{n}' = \sigma\vec{n} = \begin{pmatrix} 0 & 0 & 1 \\ 1 & 0 & 0 \\ 0 & 1 & 0 \end{pmatrix}\vec{n}. \tag{2.2.28}$$

By analogy with the case $J_1 > J_2$ phase, the vacuum quantum fluctuations would depend on the rotational degrees of freedom α and the vacuum energy minimization would reduce the group of symmetry for ground state from a continuous rotational group to a discrete group similar to the $J_1 > J_2$ phase. The spin wave analysis, however, is not pursued here owing to its complexity because of the large number of degrees of freedom, but we can infer the absence of gapless Goldstone modes due to the quantum fluctuations in the presence of the anisotropic magnetic frustration.

2.2.3 Phase Transition at $J_1 = J_2$

The classical energy per site for the Néel state is $E_{\text{Néel}} = -\frac{3J_1}{2}S^2 - J_2S^2$, and the classical energy per site for spiral order is $E_{\text{Spiral}} = -\frac{3J_2}{2}S^2 - J_1S^2$. Apparently, a quantum phase transition would occur in varying the ratio of J_1/J_2 and a first-order phase transition at the critical point $J_1 = J_2$ where the $E_{\text{Néel}} = E_{\text{Spiral}}$.

The phase transition can be visualized by studying the deformation of the transformed 120° Néel order from the spiral phase. The deformation of the copies of the 120° Néel order can be manifested by the following expressions:

$$\begin{aligned}\vec{\tilde{\tilde{S}}}_A + \vec{\tilde{\tilde{S}}}_B + \vec{\tilde{\tilde{S}}}_C = \vec{\epsilon} \\ \vec{\tilde{\tilde{S}}}_1 + \vec{\tilde{\tilde{S}}}_2 + \vec{\tilde{\tilde{S}}}_3 = \vec{\eta},\end{aligned} \tag{2.2.29}$$

in which $\vec{\epsilon}$ and $\vec{\eta}$ are vectors describing deformations of the three spins on respectively the two triangular sublattices. The J_2 coupling is

$$\begin{aligned}H_{J_2} =& J_2 \sum (\vec{\tilde{\tilde{S}}}_1 \cdot \vec{\tilde{\tilde{S}}}_2 + \vec{\tilde{\tilde{S}}}_2 \cdot \vec{\tilde{\tilde{S}}}_3 + \vec{\tilde{\tilde{S}}}_3 \cdot \vec{\tilde{\tilde{S}}}_1) \\ =& \frac{1}{2} J_2 \sum [(\vec{\tilde{\tilde{S}}}_1 + \vec{\tilde{\tilde{S}}}_2 + \vec{\tilde{\tilde{S}}}_3)^2 - 3||\vec{\tilde{\tilde{S}}}||^2] \\ =& \frac{1}{2} J_2 \sum (\vec{\eta}^2 - 3||\vec{\tilde{\tilde{S}}}||^2),\end{aligned} \tag{2.2.30}$$

in which the sum is carried out over all the triangles of the sublattice. Then the energy variation of the J_2 coupling would be:

$$\Delta E_{J_2} = \frac{1}{2} J_2 \sum (\vec{\epsilon}^2 + \vec{\eta}^2). \tag{2.2.31}$$

For the J_1 coupling, we can proceed with the similar analysis as Eqs. 2.2.15,2.2.16 and 2.2.17:

$$\vec{h}^1_{\triangle} = \begin{pmatrix} \widetilde{S}^x_A - \widetilde{S}^x_B + \widetilde{S}^x_C \\ \widetilde{S}^y_A + \widetilde{S}^y_B - \widetilde{S}^y_C \\ \widetilde{S}^z_A - \widetilde{S}^z_B - \widetilde{S}^z_C \end{pmatrix} = D_{\triangle}(\vec{\tilde{\tilde{h}}}_1 - \vec{\epsilon}), \tag{2.2.32}$$

$$\vec{h}^2_{\square} = \begin{pmatrix} -\widetilde{S}^x_A - \widetilde{S}^x_B + \widetilde{S}^x_C \\ \widetilde{S}^y_A - \widetilde{S}^y_B - \widetilde{S}^y_C \\ -\widetilde{S}^z_A + \widetilde{S}^z_B - \widetilde{S}^z_C \end{pmatrix} = D_{\square}(\vec{\tilde{\tilde{h}}}_2 - \vec{\epsilon}), \tag{2.2.33}$$

$$\vec{h}^3_{\bigcirc} = \begin{pmatrix} -\widetilde{S}^x_A + \widetilde{S}^x_B + \widetilde{S}^x_C \\ -\widetilde{S}^y_A + \widetilde{S}^y_B - \widetilde{S}^y_C \\ \widetilde{S}^z_A + \widetilde{S}^z_B - \widetilde{S}^z_C \end{pmatrix} = D_{\bigcirc}(\vec{\tilde{\tilde{h}}}_3 - \vec{\epsilon}). \tag{2.2.34}$$

We also have:

$$\vec{\tilde{h}}_1 + \vec{\tilde{h}}_2 + \vec{\tilde{h}}_3 = 2\vec{\epsilon}. \tag{2.2.35}$$

We can pursue the same procedure as in Eq. 2.2.18 to get rid of the sum over 4 patterns and obtain the J_1 coupling:

$$\begin{aligned} H_{J_1} &= J_1 \sum((\vec{\tilde{h}}_1 - \vec{\epsilon}) \cdot \vec{\tilde{\tilde{S}}}_1 + (\vec{\tilde{h}}_2 - \vec{\epsilon}) \cdot \vec{\tilde{\tilde{S}}}_2 + (\vec{\tilde{h}}_3 - \vec{\epsilon}) \cdot \vec{\tilde{\tilde{S}}}_3) \\ &= J_1 \sum(\vec{\tilde{h}}_1 \cdot \vec{\tilde{\tilde{S}}}_1 + \vec{\tilde{h}}_2 \cdot \vec{\tilde{\tilde{S}}}_2 + \vec{\tilde{h}}_3 \cdot \vec{\tilde{\tilde{S}}}_3 - \vec{\epsilon} \cdot \vec{\eta}). \end{aligned} \tag{2.2.36}$$

The conditions in Eq. 2.2.22 are satisfied for both the Néel and Spiral orders, then the first three terms in Eq. 2.2.36 is a constant. Thereafter we could obtain an expression of the energy variation per site as a function of $\vec{\epsilon}$ and $\vec{\eta}$:

$$\Delta E_{\text{Spiral}} = \frac{1}{36}[J_2(\vec{\epsilon}^2 + \vec{\eta}^2) + 2J_1 \vec{\epsilon} \cdot \vec{\eta}]. \tag{2.2.37}$$

The energy variation of the deformed 120° Néel triangle is a positive semi-definite form of $\vec{\epsilon}$ and $\vec{\eta}$ when $J_1 < J_2$ on the one hand, the minimal energy variation $\Delta E_{\text{Spiral}} = 0$ is obtained when $\vec{\epsilon} = \vec{\eta} = 0$; when $J_1 > J_2$ on the other hand, Eq. 2.2.37 is no more a positive semi-definite form, the energy variation due to the deformation is capable of lowering the classical energy, and the minimal energy is reached when $\vec{\epsilon} = -\vec{\eta}$ and $||\vec{\epsilon}|| = ||\vec{\eta}|| = 3||\vec{S}||$. Note that here $\vec{\epsilon}$ is large and we don't have a small deformation. This implies that the spins on the two sublattices are oriented in opposite directions and spins on the same sublattice point in a unanimous direction, or the bipartite Néel order. We remark also $\Delta E_{\text{Spiral}} = E_{\text{Spiral}} - E_{\text{Néel}}$, which signifies that the deformation energy of the 120° triangle exactly lowers the energy of the spiral magnetic order to that of Néel order when $J_1 > J_2$.

Consequently, the magnetic order at all J_1/J_2 ratios is the bipartite Néel order when $J_1 > J_2$ and the two copies of locked Spiral order when $J_1 < J_2$. This approach rather suggests first order phase transition when $J_1 = J_2$. In both phases, Goldstone modes are absent because of the vacuum quantum fluctuation selection.

2.3 Intermediate Interaction Region - Mott Transition

When the Hubbard interaction becomes significant enough compared to the electron hopping energy for a system with half-filling, electron charges tend to be gradually localized by the interaction because the hopping processes bring about virtual states of a doubly occupied site, which is energetically very costly. However, the second order processes in which two electrons with different spins exchange their positions is allowed, and when the Hubbard interaction approaches infinity compared to electron hopping, charges are completely localized while the only reminiscent processes are the super-exchange processes of the spins, which gives rise to the magnetic order, as if the charge and spin of the electrons were totally separated [34]. The underlying physics describing this transition from free electrons to charge localization and spin-charge separation is the Mott transition. One way to describe this transition is the slave particle representation, in which electrons are represented as a charge particle (chargeon) and a spin particle (spinon) glued together by a gauge field[35]. In the weak coupling limit, the chargeon is in a gapless superfluid phase while at certain critical interaction strength U_c the chargeon acquires a gap, and the correlation length of the chargeon decays exponentially [22]. However, for a topological insulator in which the bulk is a gapped insulator and the edge is metallic, the bulk is gapped by the spin-orbit coupling in the weakly coupling limit and gapped by the interaction in the Mott phase, and the Mott transition is manifested rather on the edge by the disappearance of the helical edge modes[222]. The single-electron gap does not close at the Mott transition and the density of states now centers around the Hubbard energy in the spectral function [22], as an embodiment of the Coulomb blockade. A gauge field will however emerge in this spin-charge separation physics describing the confining force between the charge and the spin above the Mott transition. Gauge field in $2+1$D has monopoles as quantum tunneling processes or gauge fluctuations, and the particle corresponding to such processes are instantons that can be described as a the classical plasma. By this analogy, there exists a force between the monopoles. The nature of this confining force might determine whether above the Mott critical point the system is in a spin liquid phase [95] or already in a magnetically ordered phase. On the one hand, if the monopoles are confined, then gauge field is in a dielectric phase with equal positive and negative topological charges for the monopoles, spinons excitation are deconfined and the system is probably in the spin liquid phase; on the other hand, when the monopoles are in the deconfined plasma phase, monopoles proliferate and spinons are confined, leading to a long rang magnetic order.

In our model, the spin-orbit coupling gaps the band electrons and brings about the spin transport on the edge in the weak coupling limit, and in the intermediate interactive Mott phase, the spinons' behavior is governed by the spin-orbit coupling in that the spin texture on the edge would develop into the bulk in response to the gauge fluctuations. First, in the anisotropic spin-orbit coupling model with an Hubbard on-site interaction defined in Eq. 2.0.1, the AQSH phase will disappear when the on-site Hubbard interaction will exceed a certain critical value U_c, that needs to be determined. Then we shall only describe how the pseudo spin-orbital texture will develop from the edges into the bulk at the Mott transition.

The Mott transition is characterized by the acquisition of a gap for the chargeon and the localization of the charge particle. The critical value U_c of the Mott transition as a function of the anisotropic spin-orbit coupling-Hubbard model will be proved in this Section to be exactly the same as for the Kane-Mele-Hubbard model [62]: the chargeon effective Hamiltonian in the spin-charge fractionalized representation is the same as in the Kane-Mele-Hubbard model after doing the mean-field approximation. However, spinons that will be subject to the strong gauge field fluctuations behave distinctly for the anisotropic spin-orbit coupling model. By attaching a gauge field [146, 147, 148, 25] to the chargeon to describe the residual degrees of freedom in the phase of the localized chargeon, we will establish a gauge theory that will incorporate the apparition and proliferation of monopoles [146]. The monopoles will affect the spinons by insertion of fluxes, and the spinons respond to these fluxes by forming spin textures around the inserted flux. The gauge fluctuations in this anisotropic spin-orbit coupling model with on-site Hubbard interaction triggers anisotropic spin textures while the spin texture would be homogeneous in the XY plane in the Kane-Mele Hubbard model above the Mott critical point [62, 64, 150].

The U(1) slave-particle representation [130, 131] consists in cracking the physical electron down to the fermionic spinon particle for the spin and the bosonic chargeon particle for the charge. On each site of the system, there could be 4 electron states: $|\phi\rangle$, $|\uparrow\rangle$, $|\downarrow\rangle$ and $|\uparrow\downarrow\rangle$, and different representations in terms of slave particles use different descriptions of these 4 electron states. Two representations are currently applied to describe the Mott transition, namely the U(1) slave-rotor representation [130] and the $\mathbb{Z}_2$ slave-spin representation [141], [151]. In the U(1) formulation, the 'superfluid' phase of the rotors is characterized by an ordered rotor meaning the coherence of the wave function over the whole system. The 'Mott' phase, in which electrons are rather localized on lattice sites (rather than in k-space), is characterized by disordered rotors implying the loss of coherence of the wave function. The phase transition is described by the gap acquisition of the rotors and the disappearance of the quasiparticle poles in the electronic Green's function.

In contrast, in the $\mathbb{Z}_2$ slave-spin representation, the 'superfluid' phase is represented by ordered Ising spins of the quantum Ising model in a transverse field, and the Mott phase is embodied by disordered Ising spins. The main difference between the two representations lies in the gauge fluctuations: the $\mathbb{Z}_2$ effective gauge field predicts a phase with exotic vison excitations [152, 153, 95, 154], while the U(1) Maxwellian gauge theory only implies magnetic monopoles and is also widely used in the context of studies of Hubbard models [130, 131, 132, 155]. We choose here the U(1) rotor representation to study the Mott transition [130, 131], since there has not been till this day experimental evidence of vison predicted by the $\mathbb{Z}_2$ gauge field.

2.3.1 Slave Rotor Representation for the Mott Transition

The U(1) slave-rotor representation [130, 131] consists of labelling the 4 state Hilbert space by angular momentum: $|\uparrow\rangle_e = |\uparrow\rangle_s |0\rangle_\theta$, $|\downarrow\rangle_e = |\downarrow\rangle_s |0\rangle_\theta$, $|\uparrow\downarrow\rangle_e = |\uparrow\downarrow\rangle_s |1\rangle_\theta$ and $|\phi\rangle_e = |\phi\rangle_s |-1\rangle_\theta$. The creation of a physical electron is the creation of a spin in the spinon Hilbert space accompanied by raising the angular momentum in the rotor Hilbert space, while the measure of the number of electron is the measure of the angular momentum:

$$c_\sigma^\dagger = f_\sigma^\dagger e^{i\theta} \quad c_\sigma = f_\sigma e^{-i\theta}, \tag{2.3.1}$$

in which $f_\sigma^\dagger$ is a spinon creation operator with spin σ, and $e^{i\theta}$ is an angular momentum raising operator. The Hubbard interaction Hamiltonian turns into $H_I = \sum_i \frac{U}{2}(n_i - 1)^2 = \sum_i \frac{U}{2} L_i^2$, in which we used the fact that we consider the case of half filling.

Hence, we can write the Hamiltonian in the U(1) slave rotor representation as:

$$H_{\text{rotor}} = \sum_i \frac{U}{2} L_i^2 + \sum_{\langle i,j\rangle} \sum_\sigma t f_{i\sigma}^\dagger f_{j\sigma} e^{i\theta_i - i\theta_j} + \sum_{\langle\!\langle i,j\rangle\!\rangle} \sum_{\sigma,\sigma'} it' f_{i\sigma}^\dagger f_{j\sigma'} \sigma_{\sigma\sigma'}^\alpha e^{i\theta_i - i\theta_j} \tag{2.3.2}$$

When applying the rotor formalism, we enlarge the Hilbert space, therefore an extra constraint needs to be imposed:

$$L_i = \sum_\sigma \left[f_{i\sigma}^\dagger f_{i\sigma} - \frac{1}{2} \right]. \tag{2.3.3}$$

In the Hamiltonian formalism, we can replace $e^{i\theta_i - i\theta_j}$ and $f_{i\sigma}^\dagger f_{j\sigma}$ by their mean-field ansatz, and separate the spinon and chargeon. By working out the ground state mean value of these replaced observables, we obtain the self-consistent equations to solve, or specifically:

$$H_f = \sum_{<i,j>} tQ_f f_{i\sigma}^\dagger f_{j\sigma} + \sum_{\ll i,j \gg} it'\widetilde{Q}_f \sigma_{\sigma\sigma'}^\alpha f_{i\sigma}^\dagger f_{j\sigma'} \tag{2.3.4}$$

$$H_\theta = \sum_{<i,j>} tQ_x \cos(\theta_i - \theta_j) + \sum_{\ll i,j \gg} t'\widetilde{Q}_x \cos(\theta_i - \theta_j) + \frac{U}{2} L_i^2 \tag{2.3.5}$$

$$\begin{cases} \left\langle e^{i\theta_i - i\theta_j} \right\rangle_{\langle i,j \rangle} = Q_f & \left\langle e^{i\theta_i - i\theta_j} \right\rangle_{\ll i,j \gg} = \widetilde{Q}_f \\ \left\langle f_{i\sigma}^\dagger f_{j\sigma} \right\rangle_{\langle i,j \rangle} = Q_x & \left\langle i\sigma_{\sigma\sigma'}^\alpha f_{i\sigma}^\dagger f_{j\sigma'} \right\rangle_{\ll i,j \gg} = \widetilde{Q}_x. \end{cases} \tag{2.3.6}$$

We can obtain an effective rotor Hamiltonian by making use of the mean field ansatz and solving Eqs. 2.3.4, which is the anisotropic spin-orbit coupling model itself.

$$H_\theta = -\sum_{<i,j>} K \cos(\theta_i - \theta_j) - \sum_{\ll i,j \gg} G \cos(\theta_i - \theta_j) + \sum_i \frac{U}{2} L_i^2, \tag{2.3.7}$$

where

$$\begin{aligned} K &= \sum_{\vec{k}} \frac{|Q_f g(\vec{k})|^2}{\widetilde{E}_0(\vec{k})} \\ G &= \sum_{\vec{k}} \sum_\alpha \frac{(2\widetilde{Q}_f t' \sin(\vec{k}.\vec{R}_\alpha))^2}{\widetilde{E}_0(\vec{k})} \end{aligned} \tag{2.3.8}$$

and

$$\widetilde{E}_0(\vec{k}) = \sqrt{|Q_f g(\vec{k})|^2 + \sum_\alpha (2\widetilde{Q}_f t' \sin(\vec{k} \cdot \vec{R}_\alpha]))^2}. \tag{2.3.9}$$

We recall that $\alpha = x,y,z$. We observe that the effective rotor Hamiltonian is a non-frustrated XY model with first and second neighbours on the honeycomb lattice. By resorting to the one-site mean-field approximation as in Ref. [62], we can identify the critical interaction:

$$\begin{aligned} \langle \cos\theta \rangle &= -\frac{2K}{U} \\ U_c &= \frac{4}{N_\Lambda} \sum_{\vec{k}} |g(\vec{k})| \end{aligned} \tag{2.3.10}$$

in which N_Λ denotes the number of unit cells.

In order to do the mean field approximation in a more explicit way, we pursue here the Lagrangian formalism of which we can carry out the saddle-point approximation more easily in the path integral formulation. We keep the same notation for mean-field ansatz but they can take different values in the Lagrangian formalism from those in the Hamiltonian formalism.

The Hubbard interaction $\frac{U}{2} L_i^2$ in the rotor representation is a kinetic term, and the constraint in Eq. 2.3.3 is now imposed through the addition of the Lagrangian multiplier

$\sum_i h_i \sum_\sigma (f^\dagger_{i\sigma} f_{i\sigma} - L_i - \frac{1}{2})$ to the Lagrangian. By using $i\partial_\tau \theta_i = \frac{\partial H}{\partial L_i}$, we then obtain the whole action:

$$\begin{aligned} S &= \int_0^\beta d\tau \left[\sum_i (iL_i \partial_\tau \theta_i + f^\dagger_{i\sigma} \partial_\tau f_{i\sigma}) + \mathcal{H} \right] && (2.3.11) \\ &= \int_0^\beta d\tau \Bigg[\sum_{i,\sigma} f^\dagger_{i\sigma} (\partial_\tau + h_i) f_{i\sigma} + \frac{1}{2U} \sum_i (\partial_\tau \theta_i + ih_i)^2 + \sum_i \left(\frac{h_i^2}{2U} - h_i \right) \\ &+ t \sum_{<i,j>,\sigma} f^\dagger_{i\sigma} f_{j\sigma} e^{i\theta_i - i\theta_j} + h.c. + it' \sum_{\ll i,j \gg} \sum_{\sigma\sigma'} \sigma^\alpha_{\sigma\sigma'} f^\dagger_{i\sigma} f_{j\sigma'} e^{i\theta_i - i\theta_j} \Bigg], && (2.3.12) \end{aligned}$$

where

$$\mathcal{H} = H_{\mathrm{rotor}} + \sum_i \sum_\sigma h_i \left[f^\dagger_{i\sigma} f_{i\sigma} - L_i - \frac{1}{2} \right] \tag{2.3.13}$$

such that the constraint in Eq. 2.3.3 is imposed at a mean-field level.

To solve the rotor model in the above action, firstly we shall replace the rotor $e^{i\theta_i}$ by a $O(2)$ complex bosonic field X_i and treat the constraint $|X_i|^2 = 1$ by a mean field self-consistent equation (and formally treat the fermion $f^\dagger$ as a complex field $f^\star$). The Lagrangian for the rotors then takes the form:

$$\begin{aligned} \mathcal{L}_x &= \sum_{\vec{k}} -g(\vec{k}) Q_x X^{a\star}_{\vec{k}} X^b_{\vec{k}} - g(\vec{k})^\star Q_x X^a_{\vec{k}} X^{b\star}_{\vec{k}} + \tilde{Q}_x \sum_k t' g_2(\vec{k}) (X^{a\star}_{\vec{k}} X^a_{\vec{k}} + X^{b\star}_{\vec{k}} X^b_{\vec{k}}) + \sum_{\vec{k}} \rho X^\star_{\vec{k}} X_{\vec{k}} \\ &= \sum_{\vec{k}} -|g| Q_x X^{l\star}_{\vec{k}} X^l_{\vec{k}} + |g| Q_x X^{u\star}_{\vec{k}} X^u_{\vec{k}} + \sum_{\vec{k}} \tilde{Q}_x t' g_2(\vec{k}) (X^{l\star}_{\vec{k}} X^l_{\vec{k}} + X^{u\star}_{\vec{k}} X^u_{\vec{k}}) + \sum_{\vec{k}} \rho X^\star_{\vec{k}} X_{\vec{k}}, \end{aligned} \tag{2.3.14}$$

in which $g_2(\vec{k}) = \cos\left(\vec{k} \cdot \vec{R}_x\right) + \cos\left(\vec{k} \cdot \vec{R}_y\right) + \cos\left(\vec{k} \cdot \vec{R}_z\right)$. We can derive the Green function for the quantum rotor:

$$G_x = \frac{1}{\frac{\nu_n^2}{U} + \rho + \xi_{\vec{k}}}, \tag{2.3.15}$$

in which $\xi_{\vec{k}} = -Q_x |g(\vec{k})| + t' \tilde{Q}_x g_2(\vec{k})$, and ν_n is the Mastubara frequency.

Then we can use the self-consistent equation of the saddle-point for the rotor field $\langle |X_i|^2 \rangle = \sum_{\vec{k}} \frac{1}{G_x} = 1$ to determine the critical value of U:

$$1 = \frac{U}{N_\Lambda} \sum_{\vec{k}} \frac{1}{\sqrt{\Delta_g^2 + 4U(\xi_{\vec{k}} - \min_{\vec{k}}(\xi_{\vec{k}}))}}, \tag{2.3.16}$$

where $\Delta_g = 2\sqrt{U(\rho + \min_k(\xi_{\vec{k}}))}$ describes the gap acquired by the rotors which turns to be zero at the critical point due to the condensation of the rotors resulting in an extra constraint on the Lagrangian multiplier ρ.

The rotor gap formally becomes non-zero in the Mott insulating phase. Then we get the expression of the critical value U_c when $\Delta_g = 0$:

$$U_c = \left[\frac{1}{2N_\Lambda} \sum_{\vec{k}} \frac{1}{\sqrt{\xi_{\vec{k}} - \min_{\vec{k}}(\xi_{\vec{k}})}} \right]^{-2}. \tag{2.3.17}$$

We can numerically evaluate the Mott transition versus the spin-orbit coupling t' and it turns out that U_c increases monotonously when increasing t', substantiating the spin-induced induced Mott transition (see Fig. 2.2).

2.3.2 Gauge Fluctuation Upon Mott Transition

When we break the physical electron down to the fermionic spinon and the bosonic rotor, then emerges a $U(1)$ gauge symmetry:

$$f_i^\dagger \to f_i^\dagger e^{i\phi_i}, e^{i\theta_i} \to e^{i\theta_i - i\phi_i} \tag{2.3.18}$$

that binds the chargeon and spinon together. In the Mott phase, the rotors become disordered, and the local phase of the rotors fluctuates considerably. We describe this local gauge fluctuations by attaching a field strength $\mathcal{A}^c$ simultaneously to the spinon and chargeons. Then we can integrate out the rotors to get an effective action of the fluctuating gauge field [132, 62] and describe the effects of the fluctuating gauge field on the spinons. The response of the spinons to the fluctuating gauge field clarifies the emergence of a peculiar spin texture in the bulk.

We first apply the Hubbard-Stratonovich transformation to decouple the rotor field and the spinon field by using the complex Gaussian integral equality: $\int d\bar{z}dz \exp(-|z|^2 + uz + w\bar{z}) = \exp(uw)$ in which z and $\bar{z}$ are the auxiliary field and $\langle z \rangle = w$ and $\langle \bar{z} \rangle = u$ are the saddle point. For the anisotropic spin-orbit coupling model with an on-site Hubbard interaction, then this results in the effective Lagrangian:

$$\begin{aligned}\mathcal{L} =& \sum_i f_{i\sigma}^\dagger (\partial_\tau + h_i) f_{i\sigma} + \frac{1}{2U} (\partial_\tau \theta_i + i h_i)^2 \\ &+ \sum_{<i,j>} (-t|\eta_{ij}|^2 - t|\eta_{ji}|^2 + t f_{i\sigma}^\dagger f_{j\sigma} \eta_{ij} + t f_{j\sigma}^\dagger f_{i\sigma} \eta_{ji} + t e^{i(\theta_i - \theta_j)} \eta_{ij}^\star + t e^{i(\theta_j - \theta_i)} \eta_{ji}^\star) \\ &+ \sum_{\ll i,j \gg} (-t'|\zeta_{ij}|^2 - t'|\zeta_{ji}|^2 + it' f_{i\sigma}^\dagger f_{j\sigma'} \sigma_{\sigma\sigma'}^\alpha \zeta_{ij} + it' f_{j\sigma}^\dagger f_{i\sigma'} \sigma_{\sigma\sigma'}^\alpha \zeta_{ji} + t' e^{i(\theta_i - \theta_j)} \zeta_{ij}^\star + t' e^{i(\theta_j - \theta_i)} \zeta_{ji}^\star),\end{aligned} \tag{2.3.19}$$

where at the level of the saddle point solution $\eta_{ij} = \left\langle e^{i(\theta_i - \theta_j)} \right\rangle_{\langle i,j \rangle}$, $\eta_{ij}^\star = \left\langle f_{i\sigma}^\dagger f_{j\sigma} \right\rangle_{\langle i,j \rangle}$, $\zeta_{ij} = \left\langle e^{i(\theta_i - \theta_j)} \right\rangle_{\ll i,j \gg}$ and $\zeta_{ij}^\star = \left\langle i f_{i\sigma}^\dagger f_{j\sigma'} \sigma_{\sigma\sigma'}^\alpha \right\rangle_{\ll i,j \gg}$ respectively on the nearest-neighbor and next-nearest neighbor links, (similar relations of saddle points hold for η_{ji}, $\eta_{ji}^\star$, ζ_{ji} and $\zeta_{ji}^\star$) and it is worth noticing that $\eta_{ij} \neq \eta_{ji}$ and $\zeta_{ij} \neq \zeta_{ji}$. At half-filling h_i equals zero.

In the rotor ordered phase, $\eta_{ij} = \eta_{ji}^\star$ (same with ζ_{ij} on the next-nearest-neighbours) and the gauge fluctuation is suppressed, while in the rotor disordered phase η_{ij} and η_{ji} become independent, and this can be described by attaching a field strength $\mathcal{A}_{ij}^c$ to the behavior of the link variables η_{ij} and ζ_{ij} and the strong fluctuations of the gauge field elucidates the difference for the link variable in the two phases for the rotors:

$$\begin{cases} \zeta_{ij} \to \zeta_{ij} e^{i\mathcal{A}_{ij}^c} & \zeta_{ij}^\star \to \zeta_{ij}^\star e^{-i\mathcal{A}_{ij}^c} \\ \eta_{ij} \to \eta_{ij} e^{i\mathcal{A}_{ij}^c} & \eta_{ij}^\star \to \eta_{ij}^\star e^{-i\mathcal{A}_{ij}^c} \end{cases} \tag{2.3.20}$$

We explicitly introduce a temporal gauge field $\mathcal{A}_i^{\tau c}$ at site i in the action. We then obtain the spinon and rotor Lagrangians:

$$\mathcal{L}_f = \textstyle\sum_i \sum_\sigma f_{i\sigma}^\dagger (\partial_\tau - i\mathcal{A}_i^{\tau c}) f_{i\sigma} + t \sum_{<i,j>} f_{i\sigma}^\dagger f_{j\sigma} \eta_{ij} e^{i\mathcal{A}_{ij}^c} + it' \sum_{\ll i,j \gg} \zeta_{ij} f_{i\sigma}^\dagger f_{j\sigma'} \sigma_{\sigma\sigma'}^\alpha e^{i\mathcal{A}_{ij}^c}$$

$$\mathcal{L}_\theta = \textstyle\sum_i \frac{(\partial_\tau \theta_i - \mathcal{A}_i^{\tau c})^2}{2U} + t \sum_{<i,j>} e^{i(\theta_i - \theta_j - \mathcal{A}_{ij}^c)} \eta_{ij}^\star + t' \sum_{\ll i,j \gg} \zeta_{ij}^\star e^{i(\theta_i - \theta_j - \mathcal{A}_{ij}^c)}. \tag{2.3.21}$$

Integrating out the rotor $e^{i\theta}$, we get a Maxwellian gauge theory with coupling constants depending on the rotor gap with Δ_g indicating the magnitude of the gauge fluctuations:

$$\mathcal{L}_{\mathcal{A}^c} = \sum_{\triangle} \left(\frac{t'|\zeta_{ij}|}{\Delta_g} \right)^3 \cos(\nabla \times \mathcal{A}^c) + \sum_i \frac{1}{2U\Delta_g} [(\partial_\tau \mathcal{A}_i^{\tau c} - \partial_x \mathcal{A}_i^{\tau c})^2 + (\partial_\tau \mathcal{A}_i^{\tau c} - \partial_y \mathcal{A}_i^{\tau c})^2], \quad (2.3.22)$$

where the sum is carried out on all the triangle plaquettes; Δ_g is the rotor gap and $\nabla \times \mathcal{A}^c = \mathcal{A}_{ij}^c + \mathcal{A}_{jk}^c + \mathcal{A}_{ki}^c$ on one triangle (i,j,k are the three vertices of the triangle) and $\partial_x \mathcal{A}_i^{\tau c} = \mathcal{A}_i^{\tau c} - \mathcal{A}_j^{\tau c}$. In the rotor ordered phase, the rotor gap $\Delta_g = 0$, so it costs an infinite energy to insert any magnetic flux into the system, namely the gauge field barely fluctuates. In contrast, in the rotor disordered phase, the rotor gap Δ_g becomes finite making the insertion of the magnetic flux possible. Because the gauge field is compact, the insertion of a 2π flux $\nabla \times \mathcal{A}^c = 2\pi$ leaves the Maxwellian gauge action invariant, which means the flux can tunnel from 0 to 2π consisting a field of monopole. Monopoles in $2+1$ dimensions are deconfined [146]. This implies the proliferation of the monopoles in the space: the monopole correlation function in the space $\left\langle m^\star(\vec{r}) m(\vec{0}) \right\rangle$ is a constant, in which $m^\star(\vec{r})$ creates a 2π flux at $\vec{r}$. We now address the spinon response to this adiabatic insertion of monopoles above the Mott transition.

2.3.3 Spin Texture upon Insertion of Flux

The spinon Lagrangian under gauge fluctuation is the anisotropic spin-orbit coupling model in Eq. 2.0.1 upon insertion of flux of 2π brought by the rotor gauge field $\mathcal{A}_{ij}^c$. The spin-orbit coupling implies the spin Hall physics elucidated in Sec. 2.1. In the context of Gedanken experiment by Laughlin [144], the insertion of a $U(1)$ flux leads to an edge charge transport $Q = \sigma_{xy}\Phi$. In the context of spin Hall effect, the insertion of a U(1) flux implies a contour in the first Brillouin zone enclosing the time reversal points; this contour denotes an exchange of Kramer pairs, therefore a $\mathbb{Z}_2$ spin pump [149]. In other words, flux insertion triggers spin transport on the edge. The spinon of the anisotropic spin-orbit coupling system is a similar system, and flux insertion should lead to spin transport in the system. Some spin ‘charge’ would be transported near the monopole core as the ‘edge’ of the system. However, several difficulties are encountered in the anisotropic spin-orbit coupling model, in contrast to the Kane-Mele-Hubbard model [62] which exhibits an XY spin order above the Mott transition: 1. the non conservation of spin number and the not-defined spin current would make the Kubo formalism inapplicable here; 2. the insertion of the magnetic flux is local instead of onto the whole system as in the case of Laughlin U(1) pump and the $\mathbb{Z}_2$ spin pump.

In order to study the spin behavior around the fluctuating gauge field, here we apply the perturbation theory, and quantitatively describe how local spin observables on a given site are affected when a 2π magnetic flux of the gauge field $\mathcal{A}^c$ is adiabatically inserted into the spinon system. We describe the adiabatic insertion of a magnetic flux of the chargeon gauge field by making the gauge field dependent on time $\mathcal{A}_{ij}^c(\tau) = \mathcal{A}_{ij}^c e^{\eta\tau}$, $\eta > 0$ in the time interval of $\tau \in]-\infty,0]$ and the gauge field with a field strength $\mathcal{A}_{ij}^c$ is inserted adiabatically within this time interval. Considering the exceptional anisotropic properties of the system, we shall investigate the lattice gauge field on each link around the flux, presuming that gauge fields on different links X, Y or Z might have different influences on the spin polarization at a given site that we measure. We expect that a certain spin texture might appear around the inserted flux due to the spin-Hall nature of the system, which is the main subject here.

We get back to the Hamiltonian formalism and apply the perturbation method. The observable we measure is

$$S_M^\alpha = f^\dagger_{MJ\sigma} f_{MJ\sigma'} \sigma^\alpha_{\sigma\sigma'}, \tag{2.3.23}$$

in which α is the spin polarization, $\vec{R}_M$ is the site at which we measure the spin and $J = A{,}B$ is the sublattice isospin of the corresponding site. Resorting to the time evolution operator, we can express the spin polarization variation under the flux insertion perturbation $\delta\mathcal{H} = (\mathcal{H}_S - \mathcal{H}_S^0)$ in which $\mathcal{H}_S$ is the spinon Hamiltonian after the gauge insertion and $\mathcal{H}_S^0$ is the original spinon Hamiltonian:

$$\begin{aligned} \delta S_M^\alpha &= e^{\int_{-\infty}^0 i\delta\mathcal{H}d\tau} S_M^\alpha e^{-\int_{-\infty}^0 i\delta\mathcal{H}d\tau} - S_M^\alpha \\ &= \left[i\int_{-\infty}^0 \delta\mathcal{H}d\tau , S_M^\alpha \right]. \end{aligned} \tag{2.3.24}$$

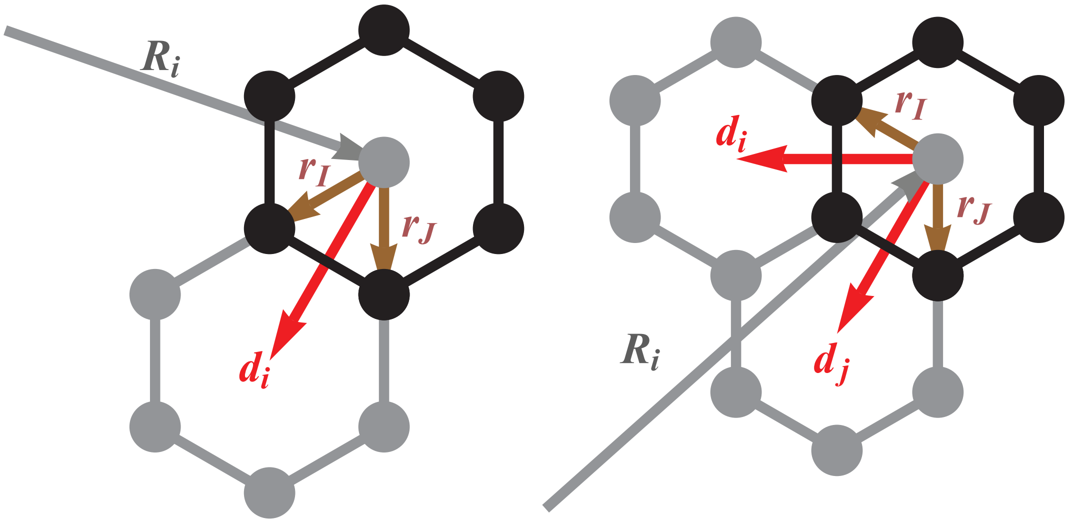

Figure 2.12: The configuration of $\vec{r}_I$, $\vec{r}_J$ and $\vec{R}_i$ related to Eq. 2.3.26, in which $\vec{r}_I$ $\vec{r}_J$ are vectors connecting the plaquette centers to its vertices and $|\vec{r}_I - \vec{r}_J|$ denotes the first neighbour link; $\vec{R}_i$ gives the coordinates of the studied plaquette. We have to pay special attention to coordinates in Eq. 2.3.26: $\vec{r}_i = \vec{r}_I + \vec{R}_i$ and $\vec{r}_j = \vec{r}_J + \vec{R}_i$. The sum over the coordinates of the studied plaquette at $\vec{R}_i$ in Eq. (2.3.26) shall induce the momentum conservation $\vec{k} - \vec{k}' = \vec{q}$ of the spinon excitations under the monopole insertion. The vectors $\vec{d}_I$ and $\vec{d}_J$ are vectors connecting the plaquettes for the configuration of gauge fields on the honeycomb lattice; see section 2.4.

The original and the perturbed spinon Hamiltonians are explicitly given by:

$$\begin{aligned} \mathcal{H}_S^0(\tau) &= \sum_{\langle i,j \rangle} tQ_f f^\dagger_{i\sigma}(\tau) f_{j\sigma}(\tau) + it' \sum_{\ll i,j \gg} \tilde{Q}_f f^\dagger_{i\sigma}(\tau) f_{j\sigma'}(\tau) \sigma^w_{\sigma\sigma'} \\ \mathcal{H}_S(\tau) &= \sum_{\langle i,j \rangle} tQ_f f^\dagger_{i\sigma}(\tau) f_{j\sigma}(\tau) e^{i\mathcal{A}^c_{ij}} + it' \sum_{\ll i,j \gg} \tilde{Q}_f f^\dagger_{i\sigma}(\tau) f_{j\sigma'}(\tau) \sigma^w_{\sigma\sigma'} e^{i\mathcal{A}^c_{ij}} \end{aligned} \tag{2.3.25}$$

such that $\delta\mathcal{H}(\tau) = \mathcal{H}_S - \mathcal{H}_S^0$ becomes equal to:

$$\begin{aligned}
&\approx \sum_{\vec{k},\vec{k}',\vec{q}} \sum_{\sigma\sigma'} f^\dagger_{I\sigma}(\vec{k},\tau) f_{I'\sigma'}(\vec{k}',\tau) \Bigg(\sum_{\substack{\langle \vec{r}_i,\vec{r}_j\rangle \\ \vec{\rho}=\vec{r}_i-\vec{r}_j}} itQ_f(\tau^x_{II'}\Re e + \tau^y_{II'}\Im m)\mathbf{1}_{\sigma\sigma'}\mathcal{A}^c_\rho(\vec{q}) \exp(-i\vec{k}\cdot\vec{r}_i + i\vec{k}'\cdot\vec{r}_j + i\vec{q}\cdot\vec{R}_i) \\
&- t'\tilde{Q}_f \sum_{\substack{\ll r_i,r_j \gg \\ \vec{\rho}_w=\vec{r}_i-\vec{r}_j}} \tau^z_{II'}\sigma^w_{\sigma\sigma'}\mathcal{A}^c_{\rho_w}(\vec{q}) \Big[\exp(-i\vec{k}\cdot\vec{r}_i + i\vec{k}'\cdot\vec{r}_j + i\vec{q}\cdot\vec{R}_i) + \exp(-i\vec{k}\cdot\vec{r}_j + i\vec{k}'\cdot\vec{r}_i + i\vec{q}\cdot\vec{R}_i)\Big]\Bigg) \qquad (2.3.26) \\
&\tau \in]-\infty,0],
\end{aligned}$$

in which $\vec{r}_i = \vec{R}_i + \vec{r}_I$ and $\vec{r}_j = \vec{R}_i + \vec{r}_J$ are coordinates on which spinon excitations due to the gauge field is considered. $\vec{r}_I$ and $\vec{r}_J$ are vectors connecting the center of the studied plaquette and the corresponding sites indicated in Fig. 2.12. In Eq. 2.3.26, we add up by hand the two terms of hopping on the next-nearest-neighbour links in order to avoid the ambiguity of $\pm i$ when electrons hop along or against the link orientation. Though the lattice is translational invariant, the gauge field is not, rendering the problem of Fourier transformation more sophisticated. We apply the Fourier transformation to derive the spinon response:

$$f_{iI\sigma}(\tau) = \frac{1}{\sqrt{N}} \sum_{\vec{k},\tau} e^{i\vec{k}\cdot\vec{r}_i} f_{I\sigma}(\vec{k},\tau), \qquad (2.3.27)$$

The spinon system has also two gapped bands as a reminiscence of AQSH phase. The energy of the bands of the spinon system and the band projectors are given explicitly by:

$$\epsilon_{\vec{k}} = \sqrt{|Q_f g(\vec{k})|^2 + (\tilde{Q}_f)^2(m_x^2(\vec{k}) + m_y^2(\vec{k}) + m_z^2(\vec{k}))} \qquad (2.3.28)$$

$$P_\pm(\vec{k})_{II'\sigma\sigma'} = \frac{1}{2}[1 \pm \frac{1}{\epsilon_{\vec{k}}}[Q_f g(\vec{k})(\tau^x_{II'}\Re e + \tau^y_{II'}\Im m)\mathbf{1}_{\sigma\sigma'} + \tilde{Q}_f\tau^z_{II'}(\sigma^x_{\sigma\sigma'}m_x + \sigma^y_{\sigma\sigma'}m_y + \sigma^z_{\sigma\sigma'}m_z)]]. \qquad (2.3.29)$$

The configuration of the lattice gauge field is explained in section 2.4 using the loop variable method and $\mathcal{A}^c(\vec{q})$ is the Fourier transformed form of the lattice gauge field. The idea of loop variable construction is to write the gauge field on a given link as the difference of the loop variables on the two juxtaposing plaquettes so that $\nabla\cdot\mathcal{A}^c = 0$ is automatically satisfied. If $\phi_{\vec{R}_i}$ and $\phi_{\vec{R}_i+\vec{d}_j}$ are two loop variables on the plaquettes centered at $\vec{R}_i$ and $\vec{R}_i + \vec{d}_j$, then the gauge field along the link vector $\vec{\rho}$ juxtaposed by these two neighbouring plaquettes is: $\mathcal{A}^c_\rho = \phi_{\vec{R}_i} - \phi_{\vec{R}_i+\vec{d}_j}$ and the link vector $\vec{\rho}$ is in the counterclockwise orientation with regard to the center plaquette at $\vec{R}_i$.

The commutator of the four fermions in Eq. 2.3.24 generates the band projectors indicating the excitations of particle-hole pairs, and the spinon response is proportional to the flux inserted. The sum over the center plaquette coordinates $\vec{R}_i$ in Eq. 2.3.26 imposes the momentum conservation of $\vec{k} - \vec{k}' = \vec{q}$ which means that the gauge fluctuations excite particle-hole pairs with the momentum exchange $\vec{q}$ equal to the momentum of the fluctuating gauge field. It is convenient to introduce the notations:

$$\delta\mathcal{H}(\tau) = \frac{1}{N}\sum_{\vec{k},\vec{k}'}\sum_{\sigma\sigma'} f^\dagger_{I\sigma}(\vec{k},\tau) f_{I'\sigma'}(\vec{k}',\tau)\delta\mathcal{H}^S_{II'\sigma\sigma'}(\tau). \qquad (2.3.30)$$

Then, in Eq. 2.3.31, the spin polarization variation is written as a trace over spin space

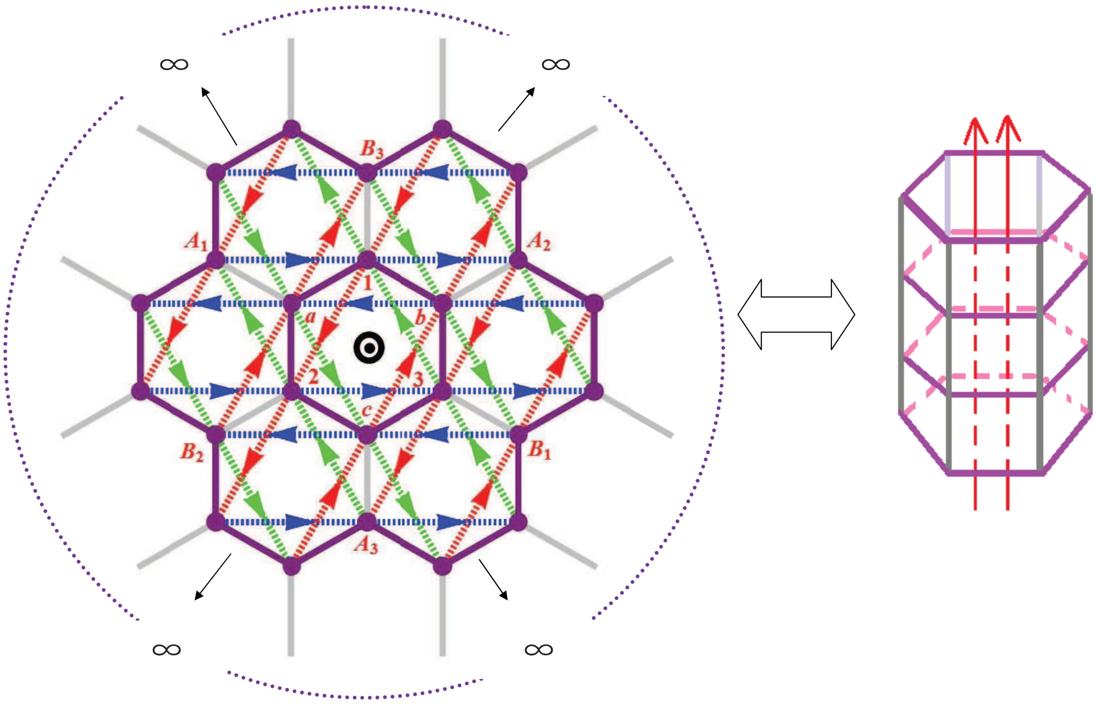

Figure 2.13: The anisotropic spin texture developing into the bulk above the Mott critical point U_c as a function of t'/t could be associated with the spin physics on the edge by invoking the $U(1)$ pump argument to a system on a cylinder by Laughlin [144]: the centered plaquette with flux inserted could be viewed as one edge and the infinity of the system as another. The different sites in Table 2.3.3 are labeled in the figure. The spin physics of insertion of flux could be mapped to the edge spin transport on a cylinder under the insertion of flux and the emergent spin texture could be viewed as 'spin charge'. When the gauge field fluctuations insert monopoles (flux in $2+1$ dimensions) into the system, the $U(1)$ spin pump would induce a spin texture around the 'edges', namely the core of the monopoles. The spin texture (See Fig. 2.14) as a spin response summed over all momenta shared similar configurations as the spin transport in Sec. 2.1: when $t'/t \ll 1$ the three components are comparable while $t'/t \gg 1$ one dominant component of spin polarization will appear. The dominant spin polarization depends on the type of links intersected by the line connecting the measured site and the monopole core. It resembles the dependence of the dominant spin polarization component on the types of links to which the boundary is parallel in the context of edge spin physics in the AQSH phase.

of the matrix product measured on the Hilbert space of the sublattices $|J\rangle$:

$$\delta S^{\alpha}_{M} = \frac{1}{N}\lim_{\eta\to 0}\sum_{\substack{\vec{k}_1,\vec{k}_1' \\ \vec{k}_2,\vec{k}_2'}}\int_{-\infty}^{0} d\tau \left[f^{\dagger}_{J\sigma}(\vec{k}_1,\tau) f_{J\sigma'}(\vec{k}_1',\tau)\sigma^{\alpha}_{\sigma\sigma'} e^{-i(\vec{k}_1-\vec{k}_1')\vec{R}_M}, f^{\dagger}_{I\tilde{\sigma}}(\vec{k}_2) f_{I'\tilde{\sigma}'}(\vec{k}_2') \frac{\delta\mathcal{H}^{S}_{II'\tilde{\sigma}\tilde{\sigma}'}(\tau)}{\epsilon_{\vec{k}_2}-\epsilon_{\vec{k}_2'}-i\eta} \right] \tag{2.3.31}$$

$$= \frac{1}{N}\lim_{\eta\to 0}\sum_{\vec{k},\vec{k}'} \mathrm{Tr}_{\sigma}(\langle J| [\frac{P_-(\vec{k}')\delta\mathcal{H}^{s}P_+(\vec{k})\sigma^{\alpha}}{\epsilon_{\vec{k}}+\epsilon_{\vec{k}'}-i\eta}\exp(-i(\vec{k}-\vec{k}').\vec{R}_M) + \frac{P_-(\vec{k})\delta\mathcal{H}^{s}P_+(\vec{k}')\sigma^{\alpha}}{\epsilon_{\vec{k}'}+\epsilon_{\vec{k}}-i\eta}\exp(i(\vec{k}-\vec{k}').\vec{R}_M)]\,|J\rangle).$$

The evaluation of the quantity in Eq. 2.3.31 is not so simple because of the integral over the whole first Brillouin zone and therefore we have done this numerically. The anisotropy is manifested by the spin texture dependence on the site $\vec{R}_M$ on which we measure the spin. A table of numerical results of δS^{α}_{M} is listed; see Table 2.1.

The spin texture is very localized around the inserted flux, and numerical studies shows that the spin texture becomes $S^{\alpha} \approx 1.0 \times 10^{-3}$ on the sites that are third neighbours to the center O in Fig. 2.13. Therefore, we focus on sites around the core of the inserted flux.

site	1	2	3	a	b	c
S_x	0.0302	0.0302	-0.142	0.142	-0.0302	-0.0302
S_y	0.0302	-0.142	0.0302	-0.0302	0.142	-0.0302
S_z	-0.142	0.0302	0.0302	-0.0302	-0.0302	0.142
site	A1	B1	A2	B2	A3	B3
S_x	0.0314	-0.0314	0.0378	-0.0378	0.0378	-0.0378
S_y	0.0378	-0.0378	0.0314	-0.0314	0.0378	-0.0378
S_z	0.0378	-0.0378	0.0378	-0.0378	0.0314	-0.0314

Table 2.1: Spin texture on the plaquette of inserted flux when $t = t' = 1$. The row represents the spin polarization in the x, y and z component and the column represents the sites labeled in Fig. 2.13.

From Table 2.1, we observe certain symmetries in the spin texture and these symmetries are in fact inherent to the original spinon system in Eqs. 2.3.4 and 2.3.21. Specifically, the symmetry of a combination of $2\pi/3$ rotation around the core of the inserted flux and spin polarization permutation. We denote the $2\pi/3$ rotation around the core of the inserted monopole as $R(\frac{2\pi}{3})$ under which different sites are connected:

$$\begin{cases} R(\frac{2\pi}{3})\vec{R}_1 = \vec{R}_2; R(\frac{2\pi}{3})\vec{R}_2 = \vec{R}_3; R(\frac{2\pi}{3})\vec{R}_3 = \vec{R}_1 \\ R(\frac{2\pi}{3})\vec{R}_a = \vec{R}_b; R(\frac{2\pi}{3})\vec{R}_b = \vec{R}_c; R(\frac{2\pi}{3})\vec{R}_c = \vec{R}_a \\ R(\frac{2\pi}{3})\vec{R}_{A1} = \vec{R}_{A3}; R(\frac{2\pi}{3})\vec{R}_{A3} = \vec{R}_{A2}; R(\frac{2\pi}{3})\vec{R}_{A2} = \vec{R}_{A1} \\ R(\frac{2\pi}{3})\vec{R}_{B1} = \vec{R}_{B3}; R(\frac{2\pi}{3})\vec{R}_{B3} = \vec{R}_{B2}; R(\frac{2\pi}{3})\vec{R}_{B2} = \vec{R}_{B1} \end{cases} \tag{2.3.32}$$

The spin polarization permutation σ is defined as follows:

$$\begin{cases} \sigma(S_z) = S_y \\ \sigma(S_y) = S_x \\ \sigma(S_x) = S_z. \end{cases} \tag{2.3.33}$$

If we write the symmetry operator as $U = R(\frac{2\pi}{3})\sigma$, which commutes with the spinon Hamiltonian in Eq. 2.3.4, then the spin texture response on different sites will be related by

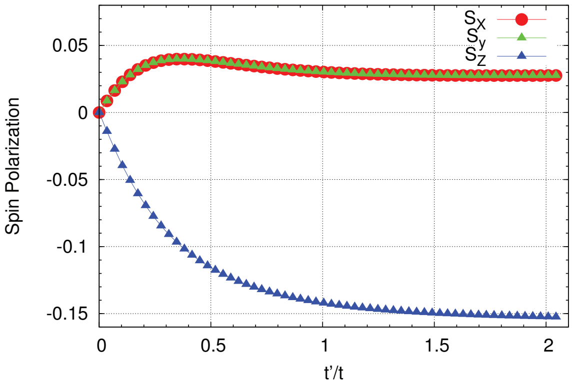

Figure 2.14: Spin texture in the intermediate U regime induced by the fluctuating gauge field within the U(1) slave-rotor theory. The spin polarization on site 1 in Fig. 2.1 as a function of t'/t. When $t'/t \ll 1$, the subordinate spin polarization is in the same order as the dominant spin polarization S_x,$S_y \approx -0.6S_z$ (see Fig. 2.15). When $t'/t > 1$ the subordinate spin polarization becomes (much) smaller in front of the dominant polarization: S_x,$S_y \approx -0.2S_z$. The spin texture above the Mott quantum critical point seems to evolve very gradually. Site 1 is facing the z type links in the system and it acquires a dominant z spin component. The spin texture on other different sites carries a symmetry which is a combination of a $2\pi/3$ rotation around the core of the fluctuating flux and a spin permutation, a symmetry inherent to this anisotropy model.

this symmetry operator. Thus, we confirm the numerical results that $S_1^z = S_2^y = S_3^x$, $S_1^y = S_2^x = S_3^z$ and $S_1^x = S_2^z = S_3^y$, etc. Another symmetry is that spin texture on corresponding sites on different sublattices have opposite signs: $S_1^\alpha = -S_c^\alpha, S_2^\alpha = -S_b^\alpha, S_3^\alpha = -S_a^\alpha, (\alpha = x,y,z)$ and identically for the sites A1 & B1, A2 & B2, A3 & B3, etc. This symmetry is also present in the original spinon Hamiltonian in that $i\sigma^\alpha$ is changed into $-i\sigma^\alpha$ for the next-nearest-neighbour hopping on different sublattices.

The anisotropy is manifested by one dominant component of the spin polarization on different types of sites: $S_1^z = S_2^y = S_3^x$ on site 1, 2 and 3. The lines linking these sites and the monopole core intersect respectively the z, y and x links, so the dominant spin polarization are $S_1^z = S_2^y = S_3^x$ on site 1, 2 and 3. Accordingly, the dominant spin polarization component on one site corresponds to the type of links intersected by the line linking the monopole core and the site under investigation. The subordinate components and dominant component on each site change differently when t'/t varies, thus generating two different types of spin texture above the Mott critical point as in figure 2.14. At small t'/t, the spin texture tends to zero (proportional to t') because the appearance of spin textures is due to the effective spin-orbit coupling in the spinon sector; the subordinate components are $S_x = S_y = -0.6S_z$ on site 1, for example. At large $t' > t$, the subordinate components are small compared to the dominant components $S_x = S_y \approx -0.2S_z$. The ratio between the subordinate components and the dominant components is analyzed in Fig. 2.15. This shows that the peculiar spin texture substantially develops by increasing the ratio t'/t.

As mentioned earlier, the analogy between the edge spin physics in the AQSH phase and the spin texture in the bulk in the intermediate interaction regime can be fleshed out using the argument of Laughlin [144], the $U(1)$ pump of a system on a cylinder with 2 edges, in which

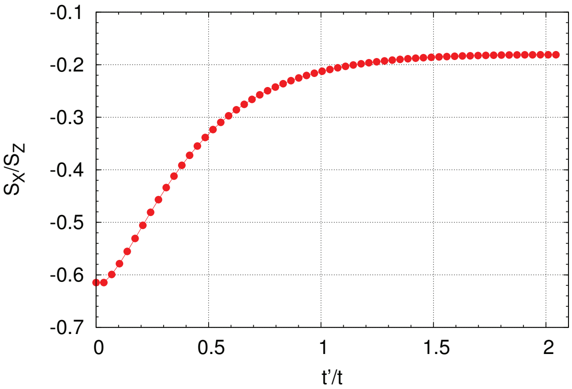

Figure 2.15: The ratio of S_x/S_z on site 1 in Fig. 2.13 as a function of t'/t. This indicates that there are two spin textures when varying t'/t: 1. The subordinate spin polarization have an opposite component as the dominant polarization $S_x = S_y = -0.6S_z$ when t' is small compared to t; and 2. $S_z \gg (S_x, S_y)$ when $t' > t$.

'charge' transport on the edges would be induced under insertion of flux of such topological system on cylinder. However, the 'charge' in this anisotropic spin-orbit coupling model is the 'spin charge'. Fig. 2.13 illustrates how the spin physics in the two different contexts, edges versus bulk, are related. The sites around the monopole core are analogous to one edge and the infinity to another, the spin texture on different sites are then 'spin charge' transported around under the insertion of a fluctuating flux. The anisotropy factor in the context of edge states of the AQSH effect is related to the type of links to which the boundary is parallel, and in the context of spin texture in the bulk, it is the type of links intersected by the line linking the monopole core and the corresponding site. These anisotropy factors determine the dominant spin polarization component when $t' > t$.

The spinon response is influenced by a plasma of monopoles rather than simply the insertion or destruction of one monopoles or two. Different from the Kane-Mele-Hubbard model in which the correlation of two monopoles separated far enough could trigger a homogeneous long-range magnetic order, the spin texture in this anisotropic spin-orbit model beyond the Mott critical point entails the coordination of several spin textures distributed around the monopole plasma; the real magnetic structure in this regime has to be considered as a statistical average of these spin textures, which remains to be explored in terms of difficulties such as frustration between spin texture induced by two juxtaposed monopoles and confinement of the $U(1)$ monopole plasma, etc.

The spin texture of two adjacent monopoles and one pair of adjacent monopole-antimonopole is provided in section 2.5. The results are heuristic and the spin-texture induced by two adjacent monopole-antimonopole seems to be in good agreement with the spiral order: when the monopole-antimonopole pair is positioned along the x (y or z) links the spin texture on the sites shared by the two plaquetttes with fluxes penetrated would be in the YZ (XZ or XY) plane. This result tends to agree with the super-exchange Hamiltonian in Eq. (2.2.1) when $J_2 \gg J_1$.

It is important to underline that the emergent magnetism induced by the Mott transition will break the time-reversal symmetry and the Kramers pairs which enables the edge spin transport to disappear.

2.4 Lattice Gauge Field by Construction of Loop Variables

Loop variables is a tool to trace out the lattice gauge field configuration by attaching a loop variable to each plaquette. We follow the notations of section 2.3.3, except that the gauge field is renamed $\mathcal{A}$ (instead of $\mathcal{A}^c$) for simplicity.

Then the gauge field on the links as the difference of left hand side and the right hand side loop variables when one is oriented along the gauge field direction on the link or $\nabla \times \phi = \mathcal{A}$ in the continuous limit. The advantage of this construction is the automatic satisfaction of $\nabla \cdot \mathcal{A} = \sum_j \mathcal{A}_{Oj} = 0$ on a given site O. Then the equation $\nabla \times \mathcal{A} = \Phi_m$ is translated into the Laplacian equation after doing the Fourier transformation:

$$\nabla \times \mathcal{A} = z\phi(\vec{R}_o) - \sum_j \phi(\vec{R}_o + \vec{r}_j) = \sum_{\vec{q}} \phi(\vec{q})(z - \sum_j \exp(i\vec{q}\cdot\vec{r}_j)) \exp(i\vec{q}\cdot\vec{R}_o) = \Phi_m \delta_{\vec{R}_o,\vec{O}}, \quad (2.4.1)$$

where z is the coordinate number, $\vec{r}_j$ are vectors connecting neighbours and $\vec{R}_o$ is the center of a plaquette. Now we look at the gauge field configuration for honeycomb lattice in Fig. 2.16. If we note $h(\vec{q}) = \sum_j \exp(i\vec{q} \cdot \vec{r}_j)$, then making use of the fact that center of the hexagonal plaquettes form a triangular lattice which is a Bravais lattice, we can implement the Fourier transformation naturally enough.

$$\begin{aligned}
\mathcal{A}_{1a} &= \phi_o - \phi_{a_2} = \int dq \exp(i\vec{q}\cdot\vec{R}_o)\Phi_m \frac{1-\exp(i\vec{q}\cdot\vec{r}_{a_2})}{6-h(\vec{q})} \\
\mathcal{A}_{a2} &= \phi_o - \phi_{a_1} = \int dq \exp(i\vec{q}\cdot\vec{R}_o)\Phi_m \frac{1-\exp(i\vec{q}\cdot\vec{r}_{a_1})}{6-h(\vec{q})} \\
\mathcal{A}_{2c} &= \phi_o - \phi_{c_2} = \int dq \exp(i\vec{q}\cdot\vec{R}_o)\Phi_m \frac{1-\exp(i\vec{q}\cdot\vec{r}_{c_2})}{6-h(\vec{q})} \\
\mathcal{A}_{c3} &= \phi_o - \phi_{c_1} = \int dq \exp(i\vec{q}\cdot\vec{R}_o)\Phi_m \frac{1-\exp(i\vec{q}\cdot\vec{r}_{c_1})}{6-h(\vec{q})} \\
\mathcal{A}_{3b} &= \phi_o - \phi_{b_2} = \int dq \exp(i\vec{q}\cdot\vec{R}_o)\Phi_m \frac{1-\exp(i\vec{q}\cdot\vec{r}_{b_2})}{6-h(\vec{q})} \\
\mathcal{A}_{b1} &= \phi_o - \phi_{b_1} = \int dq \exp(i\vec{q}\cdot\vec{R}_o)\Phi_m \frac{1-\exp(i\vec{q}\cdot\vec{r}_{b_1})}{6-h(\vec{q})}.
\end{aligned} \quad (2.4.2)$$

The field strength on vectors connecting next-nearest-neighbors are more complicated since the loop variables defined in the center of the triangular lattice are not on a Bravais lattice, and therefore in order to obtain the right configuration we need an extra constraint between the two sublattices to 'massage' the above construction into the right Fourier transformed expression. To take the example of the sublattice of a,b,c in Fig. 2.13, we apply the following constraints derived from $\nabla \times \mathcal{A} = 0$:

$$\begin{aligned}
3\phi_a &= \phi_0 + \phi_{a_1} + \phi_{a_2} \\
3\phi_b &= \phi_0 + \phi_{b_1} + \phi_{b_2} \\
3\phi_c &= \phi_0 + \phi_{c_1} + \phi_{c_2}.
\end{aligned} \quad (2.4.3)$$

Then we get eventually:

$$\begin{aligned}
\mathcal{A}_{12} &= \phi_0 - \phi_a = \int dq\Phi_m \frac{2-\exp(i\vec{q}\cdot\vec{r}_{a_1})-\exp(i\vec{q}\cdot\vec{r}_{a_2})}{6-h}\exp(i\vec{q}\cdot\vec{R}_o) \\
\mathcal{A}_{23} &= \phi_0 - \phi_c = \int dq\Phi_m \frac{2-\exp(i\vec{q}\cdot\vec{r}_{c_1})-\exp(i\vec{q}\cdot\vec{r}_{c_2})}{6-h}\exp(i\vec{q}\cdot\vec{R}_o) \\
\mathcal{A}_{31} &= \phi_0 - \phi_b = \int dq\Phi_m \frac{2-\exp(i\vec{q}\cdot\vec{r}_{b_1})-\exp(i\vec{q}\cdot\vec{r}_{b_2})}{6-h}\exp(i\vec{q}\cdot\vec{R}_o) \\
\mathcal{A}_{ac} &= \phi_0 - \phi_2 = \int dq\Phi_m \frac{2-\exp(i\vec{q}\cdot\vec{r}_{a_1})-\exp(i\vec{q}\cdot\vec{r}_{c_2})}{6-h}\exp(i\vec{q}\cdot\vec{R}_o) \\
\mathcal{A}_{cb} &= \phi_0 - \phi_3 = \int dq\Phi_m \frac{2-\exp(i\vec{q}\cdot\vec{r}_{c_1})-\exp(i\vec{q}\cdot\vec{r}_{b_2})}{6-h}\exp(i\vec{q}\cdot\vec{R}_o) \\
\mathcal{A}_{ba} &= \phi_0 - \phi_1 = \int dq\Phi_m \frac{2-\exp(i\vec{q}\cdot\vec{r}_{a_2})-\exp(i\vec{q}\cdot\vec{r}_{b_1})}{6-h}\exp(i\vec{q}\cdot\vec{R}_o).
\end{aligned} \tag{2.4.4}$$

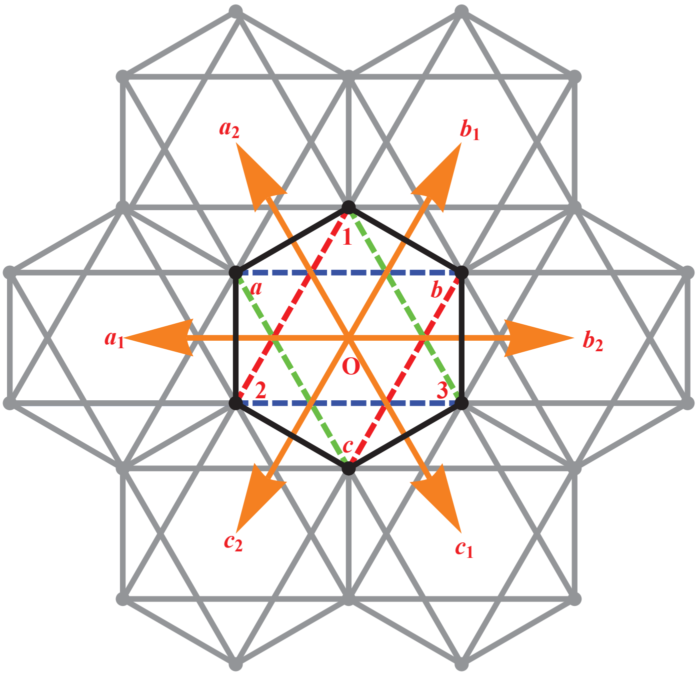

Figure 2.16: The lattice gauge field configuration on the honeycomb lattice. On each triangular and each honeycomb plaquette, a lattice loop variable is defined. The gauge field on the counterclockwise oriented links are defined as loop variables on the left hand side minus loop variables on the right hand side of the link when travelling parallel to the link orientation. For example, $\mathcal{A}_{a2} = \phi_0 - \phi_{a1}$. The loop variable construction satisfies automatically $\nabla\cdot\mathcal{A} = 0$, and $\nabla\times\mathcal{A} = \Phi_m\delta_{\vec{R}_o,\vec{O}}$ is expressed by a Laplace equation in Eq. 2.4.1, in which Φ_m is the magnetic flux penetrating the center of the plaquette.

2.5 Spin Texture under Two Adjacent Monopoles

We limit ourselves to the linear response regime in our study of the spin texture under insertion of two adjacent monopoles , considering that gauge fluctuation has less pronounced effect on sites that are third neighbour to the vortex core and that the $U(1)$ gauge theory has always confined phase with monopole-antimonopole pairs very close to each other. The spin texture in this case is most prominent on the link shared by two plaquettes onto which monopole and anti-monopole are inserted.

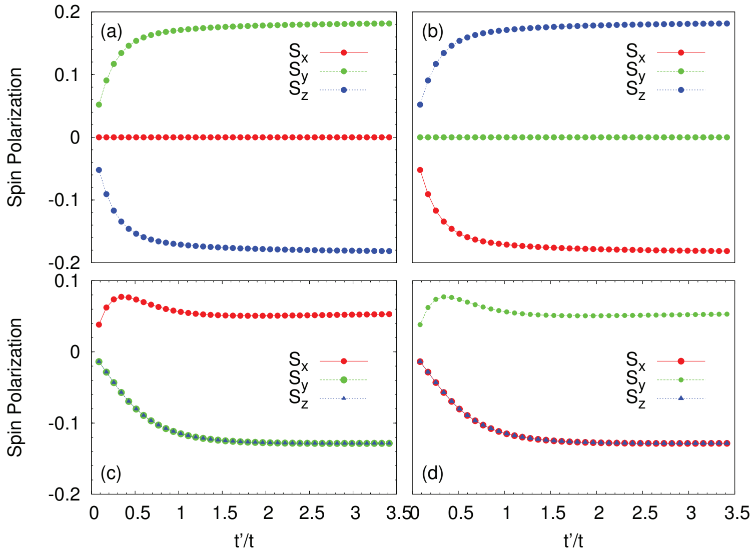

Figure 2.17: The spin texture under the monopole-antimonople pair (two monopoles) on two adjacent plaquettes: (a) the spin texture on site 1 when the monopole-antimonopole are respectively inserted on plaquette O and b1 Fig. 2.16. (b) the spin texture on site 3 when the monopole-antimonopole are respectively inserted on plaquette O and c1. (c) the spin texture on site 1 when two monopoles are inserted on plaquette O and b1. (d) the spin texture on site 3 when two monopoles are inserted on plaquette O and c1.

We can see from Fig. 2.17 (a) and (b) that when monopole-antimonopole pair is inserted, the dominant spin texture on the sites on the shared link of the two adjacent plaquettes has dominant polarization other than the type of link parallel to the segment connecting plaquettes centers with the monopole-antimonopole pair. In the case of (a) the site has dominant spin polarization in Y and Z direction with the bond connecting the monopole-antimonopole pair parallel to X links, while in the case of (b) the site has dominant spin polarization in X and Z direction, with the segment connecting the plaquettes with monopole-antimonopole pair parallel to Y links. The other two dominant spin polarization has opposite direction with $S_1^Y = -S_1^Z$ and $S_3^X = -S_3^Z$.

When two monopoles are inserted, the dominant spin texture is still these other than the type of link parallel to the segment connecting the plaquette centers with the monopoles pair. However, the other two dominant spin component has the same direction (See Fig. 2.17 (c) and (d)).

Sites other than those on the shared links of the two plaquettes with gauge fluctuation have also important spin texture contribution (See Fig. 2.18). The dominant spin polarization

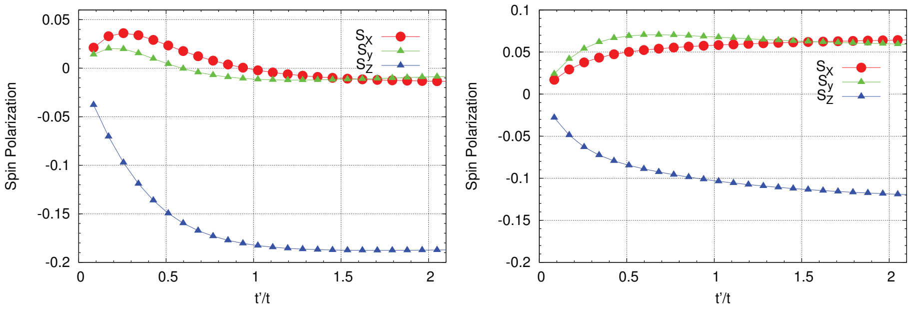

Figure 2.18: The spin texture on site 1 when the monopole-antimonopole pair (left panel) or the two monopoles are respectively inserted on plaquette O and b2 (right panel).

corresponds to the type of link parallel to the segment connecting plaquette centers with the pair. Monopole-antimonopole pair induces spin texture more pronounced than that induced by monopole-antimonopole pair.

2.6 Conclusion

In this chapter, we take the point of view that the spin-orbit coupling is the on the next-nearest-neighbour [101], which is supported by the experiment of thin films of Na_2IrO_3 [127], and studied the anisotropic spin-orbit coupling - Hubbard interaction model which contains a correlated topological insulator phase. Though the topological insulator phase is in the same class as the Z_2 Kane-Mele model, spin current is not well defined in the anisotropic spin-orbit coupling model, which requires finer treatment. As a result, we try to address the phase diagram in figure 2.2.

We have first clarified the edge transport properties of the topological insulator phase in the weak correlated limit in section 2.1 using both diagonalization of the Schrödinger equation and transfer matrix. The edge current has dominant spin component in accordance with the type of links that are parallel to the zigzag boundary. Then we carefully examined the magnetic phase diagram at the limit of infinite U in section 2.2, in which magnetic couplings result from second order super-exchange processes of the hopping terms. We have identified the Néel and spiral magnetic order and analyzed the frustration in the two phases. We have analyzed the order-by-disorder phenomenon in both classical magnetic phases. However, processes of higher order might lead to other intermediate magnetic phase than the Néel and zigzag magnetic order in the $J_1 - J_2$ model in equation 2.2.1, which we haven't explored here yet. We then concentrated on the Mott physics in the intermediate U regime in section 2.3, in which charges are localized and spin are fractionalized from the physical electron particles. We have used the slave-rotor formalism, in which charge particles (chargeons) acquire a mass upon Mott transition and the spin particles (spinons) are subject to large gauge fluctuation. In order to study the spin physics beyond the Mott transition, we studied the spin response under insertions of flux resulting from the gauge fluctuation. Upon Mott transition, we used the Laughlin topological pump argument to prove that the anisotropic spin texture on the edge develops into the bulk around fluxes and the transport edge states disappear. This anisotropic spin texture seems to be in connection with the spiral order in the infinite U limit, however, this complicated regime with proliferation of monopoles requires more precise treatment in the future beyond the linear response formalism used here.

Chapter 3

Doping Iridates on the Honeycomb Lattice - $t - J$ Model

3.1 Introduction

Half-filled Mott insulator can host magnetic order and spin liquid while doping such a Mott insulator will lead to pairings of electrons or holes, in other words high T_c superconductiviy[23, 142, 189, 190, 191, 192, 193, 195, 196, 215]. The related theoretical model is the $t - J$ model, in which the t kinetic term describes the motion of the holes and J term couples the holes and electrons. The kinetic term and magnetic coupling term shares the same origin, according to the super-exchange magnetism point of view: in the half-filled Mott insulator, one electron per site constitutes the ground state with charge localized and spin can exchange their places inducing the magnetic coupling. The ground state of the system of the induced magnetic coupling corresponds to the magnetic order. Recent theoretical and experimental advances show that in the strong spin-orbit coupling the magnetic coupling is short ranged, existing between the nearest-neighbour atoms in the honeycomb lattice [43, 44]. The nearest-neighbour magnetic coupling contains a mixture of Heisenberg and Kitaev coupling, which is essential for the occurence of the zigzag order. This is in accordance with the experiment [114] and the ab initio calculation [122]. The half-filled Mott insulator of the iridate can host different magnetic order depending on the mixture of the Kitaev and Heisenberg coupling as shown in Fig. 3.1. The magnetic model can be written as function of one parameter φ representing the mixture of the two kinds of magnetic coupling in the half-filled Mott insulator[43]:

$$
\begin{aligned}
H_{KH}(\varphi) =& A \sum_{\langle i,j \rangle} (2 \sin\varphi \, S_i^\gamma S_j^\gamma + \cos\varphi \, \mathbf{S}_i \cdot \mathbf{S}_j) \\
=& \sum_{\langle i,j \rangle} (J_K S_i^\gamma S_j^\gamma + J_H \mathbf{S}_i \cdot \mathbf{S}_j)
\end{aligned}
\tag{3.1.1}
$$

In Fig. 3.1, filled and empty circles represent spins in opposite directions. The Néel order exists in the first and part of the fourth quadrant (antiferromagnetic Heisenberg coupling), the zigzag order in part of the second quadrant (ferromagnetic Heisenberg and antiferromagnetic Kitaev coupling), ferromagnetism in part of the second and third quadrant (ferromagnetic Heisenberg coupling and ferromagnetic or small antiferromagnetic Kitaev coupling) and stripy order in the fourth quadrant (ferromagnetic Kitaev coupling and antiferromagnetic Heisenberg coupling). Experiments manifest evidences of the zigzag order in the iridates on honeycomb lattice [113, 114] in the Na_2IrO_3 compound, which corresponds to $J_K > 0$ and $J_H < 0$.

This is different from the theoretical motivation to dope the Kitaev anyon spin liquid with ferromagnetic Kitaev magnetic coupling $J_K < 0$ [41].

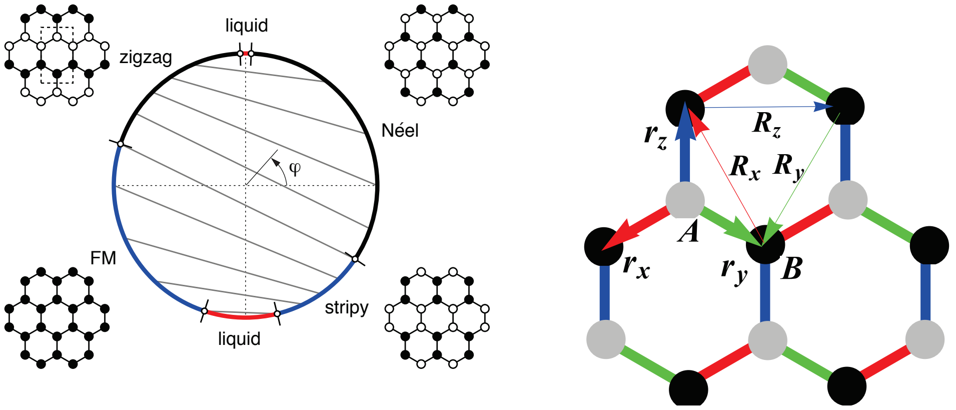

Figure 3.1: *Left panel*: The phase diagram of the Kitaev Heisenberg model with nearest-neighbour magnetic coupling on the honeycomb lattice as function of the angle φ in the magnetic coupling model $H_{KH} = A\sum_{\langle i,j\rangle}(2\sin\varphi S_i^\gamma S_j^\gamma + \cos\varphi \mathbf{S}_i\cdot\mathbf{S}_j)$ from the paper of Chaloupka et al [43]. *Right panel*: The Kitaev Heisenberg nearest-neighbour model on the honeycomb lattice with $S_i^\alpha S_j^\alpha - S_i^\beta S_j^\beta - S_i^\gamma S_j^\gamma$ and the spin-orbit coupling $c_{i\sigma}^\dagger d_{j\sigma'}\sigma_{\sigma\sigma'}^\alpha$ on different correspondent links in which $\alpha = x,y,z$ respectively on the red, green and blue links and β, γ take other spin components than α.

In accordance with the experimental fact that $J_K > 0$ and $J_H < 0$, we can write down the kinetic terms generating the Kitaev Heisenberg model following the super-exchange magnetism point of view in which magnetic coupling originates from second order super-exchange processes of the kinetic terms, and in order to establish the correspondance between the normal hopping inducing the Heisenberg coupling and the spin-orbit coupling inducing a certain mixture of Kitaev-Heisenberg coupling $H_{KH}(\frac{3\pi}{4})$, we write down the Kitaev-Heisenberg model in a different $J_1 - J_2$ language on the basis of equation 3.1.1:

$$\begin{aligned} H_{DKH} = &- t\sum_{\langle i,j\rangle} P_i[c_{i\sigma}^\dagger d_{j\sigma} + d_{j\sigma}^\dagger c_{i\sigma}]P_j - t'\sum_{\langle i,j\rangle} P_i[c_{i\sigma}^\dagger d_{j\sigma'}\sigma_{\sigma\sigma'}^\alpha + d_{i\sigma}^\dagger c_{j\sigma'}\sigma_{\sigma\sigma'}^\alpha]P_j \\ &+ J_1\sum_{\langle i,j\rangle}\vec{S}_i\cdot\vec{S}_j + J_2\sum_{\langle i,j\rangle}[S_i^\alpha S_j^\alpha - S_i^\beta S_j^\beta - S_i^\gamma S_j^\gamma] \end{aligned} \tag{3.1.2}$$

in which $J_K = 2J_2$ and $J_H = J_1 - J_2$ and $J_1, J_2 > 0$ so that the Kitaev coupling J_K is always positive. For simplicity, we will call the term $J_2\sum_{\langle i,j\rangle}[S_i^\alpha S_j^\alpha - S_i^\beta S_j^\beta - S_i^\gamma S_j^\gamma]$ the J_2 Kitaev-Heisenberg coupling.

When both the normal hopping t and the spin-orbit coupling t' are present, the realness of the spin-orbit coupling is important in order not to induce the Dzyaloshinskii-Moriya interaction $\sum_{\langle i,j\rangle} J_3\vec{e}_\alpha\cdot(\vec{S}_i\times\vec{S}_j)$ ($J_3 = 4t\cdot t'/U$) stemming from the cross term of the kinetic term t and t'. It is perhaps worth noticing that this real spin-orbit coupling breaks time-reversal symmetry in this case. However, when the normal hopping t and the Heisenberg coupling J_1 are absent, the spin-orbit coupling can take imaginary amplitude $t' \in \mathbb{C}$. The extreme case is $t' = it_1$ ($t_1 \in \mathbb{R}$), where the time-reversal symmetry is restored and the J_2 Kitaev-Heisenberg coupling remains unchanged.

The magnetic coupling constants are $J_1 = \frac{4t^2}{U}$, $J_2 = \frac{4t'^2}{U}$ and the spin component in the spin-orbit coupling $\sigma^{\alpha}_{\sigma\sigma'}$ and the J_2 Kitaev-Heisenberg coupling $J_2(S_i^{\alpha}S_j^{\alpha} - S_i^{\beta}S_j^{\beta} - S_i^{\gamma}S_j^{\gamma})$ α takes x, y, z component for red, green and blue links as shown in the right panel of Fig. 3.1. β, γ take other components than α. We note the Gutzwiller projectors as $P_i = (1 - \sum_\sigma c^{\dagger}_{i\sigma}c_{i\sigma})$ or $P_i = (1 - \sum_\sigma d^{\dagger}_{i\sigma}d_{i\sigma})$ according to the sublattice [185, 198, 199]. As shown in Fig. 3.1 right panel, we have the three vectors connecting the nearest-neighbours $\mathbf{r}_x = -(\frac{\sqrt{3}}{2}, \frac{1}{2})$, $\mathbf{r}_y = (\frac{\sqrt{3}}{2}, -\frac{1}{2})$ and $\mathbf{r}_z = (0, 1)$; and the three vectors connecting the next-nearest-neighbours $\mathbf{R}_x = (-\frac{\sqrt{3}}{2}, \frac{3}{2})$, $\mathbf{R}_y = (-\frac{\sqrt{3}}{2}, -\frac{3}{2})$ and $\mathbf{R}_z = (\sqrt{3}, 0)$. In the half-filled limit, the Gutzwiller projection will cancel the kinetic terms because of the forbiddance of the doubled filled state on one site. We could observe the presence of the Kitaev anyon spin liquid model when $t = t'$ for the half filling system.

As mentioned above, one interesting limit is the pure spin-orbit coupling limit $t, J_1 \to 0$, when the Heisenberg coupling is absent, where we have the J_2 Kitaev-Heisenberg model hosting the zigzag order. The complexity of the model involves the band structure of the spin-orbit coupling model, the intricated mixture of spin-singlet and spin-triplet electron pairing when doped away from half-filling and the frustration from the highly anisotropic J_2 coupling.

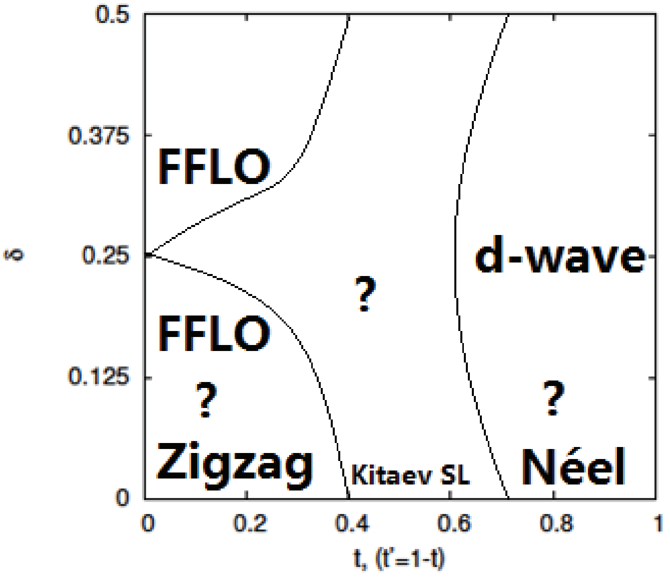

Figure 3.2: The phase diagram of the doped iridate model from the super-exchange magnetism point of view as written in equation 3.1.2. δ represents the doping of the system from half-filling.

We have given the figurative 'state of the art' phase diagram of the doped Kitaev-Heisenberg model in Fig. 3.2 as function of the doping δ and the amplitude of the normal hopping t (the spin-orbit coupling $t' = 1 - t$). At half-filling, we have respectively the Néel order and the zigzag order at the Heisenberg limit $J_2 \to 0$ and the J_2 Kitaev-Heisenberg limit $J_1 \to 0$, while the spin liquid is present when $J_1 = J_2$. In section 3.2, we will reformulate the hidden $SU(2)$ symmetry in order to relate the limit $J_1 = 0$ and $J_2 = 0$ [43]. Doped sufficiently away from the magnetic orders and the spin liquid at half-filling, we have superconductivity of different types: When the Heisenberg coupling is dominant over the J_2 Kitaev-Heisenberg coupling $J_1 \gg J_2$, we have the d-wave superconductivity in which the superconductor pairing has non-zero angular momentum: the pairing picks up a phase of $e^{\pm i\frac{2\pi}{3}}$ after a $\pi/3$ rotation [197, 220, 221, 222]. At the J_2 Kitaev-Heisenberg limit $J_2 \gg J_1$, we have one critical point at quarter-filling, at which the system of holes has conic band structure and very little density of electrons participates the superconductivity pairing. In section 3.4, we will show that the spin-orbit coupling endows the holes around quarter-filling a particular band structure with fermi surface which has new symmetry centers at non trivial momenta. In section 3.5, we will show how these new symmetry centers lead to superconducting pairing with electron pairs symmetric with regard to these symmetry centers with non-trivial momenta or the FFLO superconductivity. We have also conducted the intuitive exact diagonalization on one plaquette in section 3.3 to show that the J_2 Kitaev-Heisenberg coupling actually favors different triplet pairings on correspondent links, which is also confirmed by the intuitive procedure applying the hidden $SU(2)$ symmetry as developped in section 3.2.2. Finally, we have provided numerical proofs through exact diagonalization of the FFLO superconductivity in section 3.6.

The interesting limit is the J_2 Kitaev-Heisenberg limit when $t = J_1 = 0$, in which the FFLO superconductivity is also existent even with the time-reversal symmetry, since if $t' = it_1$ the physics does not change. This demonstrates that the essential ingrediant for FFLO superconductivity is symmetry centers of the Fermi surface at non-trivial momenta instead of Zeeman field which breaks time-reversal symmetry. In this chapter, we only limit ourselves close to this limit in the phase diagram 3.2.

We have put question marks on the unclear transitional region in which there is competition between the magnetic order and superconductivity. The superconductivity has several bands very close to each other making the calculation of the Chern number difficult. The topological aspect of the superconductivity is still under investigation.

3.2 Duality between Heisenberg and Kitaev-Heisenberg model

3.2.1 Duality at Half-filling

We write here the so-called hidden $SU(2)$ symmetry in another language [43, 45]. Here, we will study the magnetic order of the Kitaev-Heisenberg model using a spin transformation, for the half-filled Mott insulator. The spin transformation connects the pure J_1 Heisenberg model to the pure J_2 Kitaev-Heisenberg model, thereafter the transformation connects the two ground state wave functions. Specifically, we have:

$$H_{KH} = J_1 \sum_{\langle i,j\rangle} \vec{S}_i \cdot \vec{S}_j + J_2 \sum_{\langle i,j\rangle} [S_i^\alpha S_j^\alpha - S_i^\beta S_j^\beta - S_i^\gamma S_j^\gamma] \tag{3.2.1}$$

The super-exchange coupling consists of a mixture of Heisenberg antiferromagnetic coupling and J_2 antiferromagnetic Kitaev-Heisenberg coupling. We have found a global transformation graphically represented in figure 3.3 which connects the two super-exchange coupling together. The idea of the global transformation is to introduce the particle-hole pseudospinor $\begin{pmatrix} c_\uparrow \\ c_\downarrow^\dagger \end{pmatrix}$ and $\begin{pmatrix} c_\downarrow \\ c_\uparrow^\dagger \end{pmatrix}$, together with the spinor up and down, we end up having the tensor.

$$\Psi_i = \begin{pmatrix} c_{i\uparrow} & c_{i\downarrow} \\ (-1)^r c_{i\downarrow}^\dagger & -(-1)^r c_{i\uparrow}^\dagger \end{pmatrix} \quad r = 0 \quad \textbf{if i} \in \textbf{sublattice A}; \quad r = 1 \quad \textbf{if i} \in \textbf{sublattice B} \tag{3.2.2}$$

A matrix product with an $SU(2)$ matrix on the right hand side gives a spin rotation while the matrix product on the left hand side would give a $SU(2)$ pseudospin rotation. The spin rotation on the $SU(2)$ sphere is represented as $\Psi_i^{\alpha\beta} \to \Psi_i^{\alpha\gamma} g_\gamma^\beta$ while the $SU(2)$ isospin rotation in the particle hole space is represented as $\Psi_i^{\alpha\beta} \to g_\alpha^\gamma \Psi_i^{\gamma\beta}$ and $g_{\alpha\beta} = \exp(i \sum_\gamma \sigma_{\alpha\beta}^\gamma \theta_\gamma)$ is the transformation expressed in terms of the Pauli matrix $\sigma_{\alpha\beta}^\gamma$ in which γ is the index for the Pauli matrix while $\alpha\beta$ are the matrix indices. The spin observable in this language would be expressed as: $S^\alpha = \mathrm{Tr}(\sigma_\alpha^T \Psi_i^\dagger \Psi_i)$ and the hopping term would be expressed as $\mathrm{Tr}(\Psi_i^\dagger \Psi_j)$ and the spin orbit coupling as $\mathrm{Tr}(\sigma_\alpha^T \Psi_i^\dagger \Psi_j)$.

In this $SU(2)$ language, we introduce here a local spin $SU(2)$ rotation on the site i, which we denote as T_{si}, and the local spin observable will be transformed as:

$$\widetilde{\Psi_i} = \Psi_i T_{si} \quad S_i^\alpha = \mathrm{Tr}(\sigma_\alpha^T \Psi_i^\dagger \Psi_i) \to \widetilde{S_i^\alpha} = \mathrm{Tr}(T_{si} \sigma_\alpha^T T_{si}^\dagger \widetilde{\Psi_i}^\dagger \widetilde{\Psi_i}) \tag{3.2.3}$$

In other words in the projected $SU(2)$ Fermionic Hilbert space, the spin transforms in the following way: $\widetilde{\sigma_i^\alpha} = T_{si} \sigma_i^\alpha T_{si}^\dagger$. In the spin subspace, we introduce a unitary transformation G_i in correspondance with the transfromation T_{si} which applies on the spin operator in the following way: $G_i = \exp(i \sum_\gamma S_i^\gamma \theta_\gamma)$ then the spin transforms as $\tilde{\mathbf{S}}_i = G_i^\dagger \mathbf{S}_i G_i$. We have shown the graphic representation of the global transformation in Fig. 3.3 with the notation: $G_\bullet = \mathbf{1}$, $G_\blacksquare = S^x$, $G_\blacktriangle = S^y$, $G_\blacklozenge = S^z$ and spin observable under their action will experience respectively the identity transformation, the $\pi/2$ rotation around the x, y and z axis.

On each type of link, there are two different global transformations sending the Heisenberg coupling to the Kitaev-Heisenberg coupling:

$$\widetilde{\mathbf{S}_i} \cdot \widetilde{\mathbf{S}_j} = G_i^T \mathbf{S}_i G_i \cdot G_j^T \mathbf{S}_j G_j = \begin{cases} S_i^x S_j^x - S_i^y S_j^\beta - S_i^z S_j^z & \text{X links with } \bullet\ \blacksquare\text{or}\blacktriangle\blacklozenge \\ S_i^y S_j^y - S_i^z S_j^z - S_i^x S_j^x & \text{Y links with } \bullet\ \blacktriangle\text{or}\blacksquare\blacklozenge \\ S_i^z S_j^z - S_i^x S_j^x - S_i^y S_j^y & \text{Z links with } \bullet\ \blacklozenge\text{or}\blacksquare\blacktriangle. \end{cases} \tag{3.2.4}$$

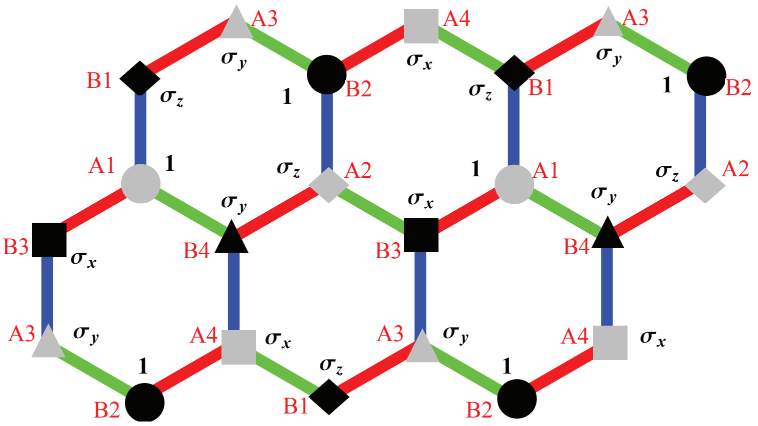

Figure 3.3: The global transformation bringing the anti-ferromagnetic Heisenberg model to the anti-ferromagnetic Kitaev-Heisenberg model and vice versa.

Under this global transformation $G = \prod_i G_i$ the super-exchange Hamiltonian has the coefficients J_1 and J_2 exchanged,

$$\begin{aligned}\tilde{H}_J =& G^\dagger H_J G \\ =& G^\dagger\{J_1 \sum_{\langle i,j\rangle} \mathbf{S}_i \cdot \mathbf{S}_j + J_2 \sum_{\langle i,j\rangle} [S_i^\alpha S_j^\alpha - S_i^\beta S_j^\beta - S_i^\gamma S_j^\gamma]\} G \\ =& J_2 \sum_{\langle i,j\rangle} \tilde{\mathbf{S}}_i \cdot \tilde{\mathbf{S}}_j + J_1 \sum_{\langle i,j\rangle} [\tilde{S}_i^\alpha \tilde{S}_j^\alpha - \tilde{S}_i^\beta \tilde{S}_j^\beta - \tilde{S}_i^\gamma \tilde{S}_j^\gamma]\end{aligned} \tag{3.2.5}$$

From this global transformation, we know that there exists a mapping from the Heisenberg model to the J_2 Kitaev-Heisenberg model and vice-versa. The anti-ferromagnetic Kitaev model when $J_1 = J_2$ is the self duality point, at which the spin flip of the global transformation sends the Hamiltonian back to itself, namely:

$$H_{Kitaev} = \sum_{\langle i,j\rangle} S_i^\gamma S_j^\gamma \quad [H_{Kitaev}, G] = 0 \tag{3.2.6}$$

The transformation G relates the two model as shown in equation 3.2.4. If $|\Psi_s\rangle$ is the (spin) ground state wave function for the Heisenberg model, then $G_S |\Psi_s\rangle$ is naturally the ground state wave function for the Kitaev Heisenberg model. Using this global transformation, we can identify the zigzag order by applying the transformation to the Néel order. For example, we have shown in Fig. 3.4, one state of Néel order in the y direction, with spin oriented in the opposite direction along the y axis on the two different sublattices. Under the global transformation G, we obtain on the right the zigzag order with antiferromagnetism along the y links and ferromagnetism along the x and z links.

$$|\Psi_{Zigzag}\rangle = G\,|\Psi_{N\acute{e}el}\rangle \tag{3.2.7}$$

The numerical exact diagonalization of the J_2 Kitaev-Heisenberg model corroborates the global transformation and the correspondence between the Heisenberg model and J_2 Kitaev-Heisenberg model at half-filling. We have carried out exact diagonalization of the Heisenberg

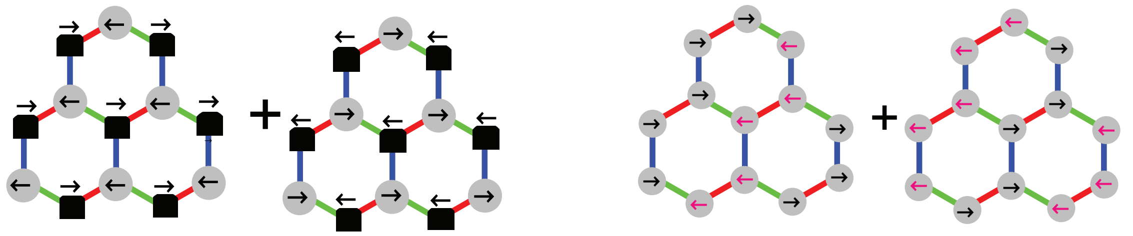

Figure 3.4: The global transformation maps the Néel state along the y polarization, which is one of the symmetry broken ground state for Heisenberg model, to the zigzag order with anti-ferromagnetism on the y links, which is one of the ground state for the Kitaev Heisenberg model.

and J_2 Kitaev-Heisenberg model on a 2 by 2 plaquette on the torus geometry. In figure 3.5, we have the spectrum of the zigzag order hosted by the J_2 Kitaev-Heisenberg model on the left with the singlet ground state at $\mathbf{k} = 0$ and triplet 1st excited state in momentum sectors $(1, 0)$, $(0, 1)$ $(1, 1)$; while we have the spectrum of the Néel order hosted by the Heisenberg model on the right with the singlet ground state and the triplet 1st excited state all in the momentum sector of $\mathbf{k} = 0$. The energy levels of the two system are numerically exactly the same and the gaps of the two systems behave both as $S(S + 1)$ $S = 0, 1, 2....$

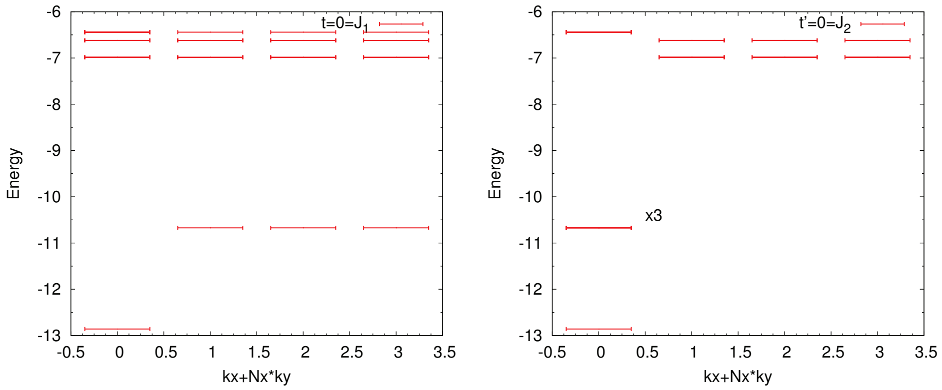

Figure 3.5: Spectrum of spins for 2×2 plaquettes on torus at half filling when $t = 0 = J_1$ on the left (the Kitaev-Heisenberg limit) and $t' = 0 = J_2$ on the right (Heisenberg limit). $J_1 = \frac{4t^2}{U}, J_2 = \frac{4t'^2}{U}, U = 6$. The momentum space is composed of momentum sectors $(0, 0)$, $(1, 0)$, $(0, 1)$ and $(1, 1)$, which correspond to momentum $(0, 0)$, $(\pi, 0)$, $(0, \pi)$ and (π, π).

The different momentum sector for the 1st excited state for the Heisenberg and J_2 Kitaev-Heisenberg model (Fig. 3.5) is related to the 4 sublattice patterns introduced by the global transformation shown in Fig. 3.3.

3.2.2 Duality beyond Half-filling

The Heisenberg and J_2 Kitaev-Heisenberg duality relates the two different systems at half-filling by a global spin rotation in the space enlarging the primitive lattice to a four plaquette unit cells, and numerical corroborations have been provided. If we adapt this strong coupling limit result to the $t-J$ model, we will have an educated guess of the superconductivity order parameter.

We know that the doped Heisenberg model has spin singlet superconductor pairings at the mean-field level: $\hat{\Delta}_0 = c_{i\uparrow}d_{j\downarrow} - c_{i\downarrow}d_{j\uparrow}$ and uniform particle density pattern $\hat{\chi}_0 = c^\dagger_{i\sigma}d_{j\sigma}$ [215]. In order to understand the superconductivity of the J_2 Kitaev-Heisenberg model, we use this global transformation which sends this singlet pairing to three different spin triplet pairings on the correspondent links. On the x, y and z links, the triplet pairings are respectively:

$$\begin{aligned}
&\hat{\Delta}^0_{ij} = c_{i\uparrow}d_{j\downarrow} - c_{i\downarrow}d_{j\uparrow} \\
&T_s\hat{\Delta}^0_{ij}T_s^{-1} = \begin{cases} \hat{\Delta}^x_{ij} = c_{i\uparrow}d_{j\uparrow} - c_{i\downarrow}d_{j\downarrow}; & \mathbf{r}_i - \mathbf{r}_j = \mathbf{r}_x \\ \hat{\Delta}^y_{ij} = -i(c_{i\uparrow}d_{j\uparrow} + c_{i\downarrow}d_{j\downarrow}); & \mathbf{r}_i - \mathbf{r}_j = \mathbf{r}_y \\ \hat{\Delta}^z_{ij} = -(c_{i\uparrow}d_{j\downarrow} + c_{i\downarrow}d_{j\uparrow}); & \mathbf{r}_i - \mathbf{r}_j = \mathbf{r}_z \end{cases}
\end{aligned} \tag{3.2.8}$$

$$\begin{aligned}
&\hat{\chi}^0_{ij} = c^\dagger_{i\sigma}d_{j\sigma} \\
&T_s\hat{\chi}^0_{ij}T_s^{-1} = \begin{cases} \hat{\chi}^x_{ij} = c^\dagger_{i\sigma}d_{j\sigma'}\sigma^x_{\sigma\sigma'} + h.c. & \mathbf{r}_i - \mathbf{r}_j = \mathbf{r}_x \\ \hat{\chi}^y_{ij} = c^\dagger_{i\sigma}d_{j\sigma'}\sigma^y_{\sigma\sigma'} + h.c. & \mathbf{r}_i - \mathbf{r}_j = \mathbf{r}_y \\ \hat{\chi}^z_{ij} = c^\dagger_{i\sigma}d_{j\sigma'}\sigma^z_{\sigma\sigma'} + h.c. & \mathbf{r}_i - \mathbf{r}_j = \mathbf{r}_z \end{cases}
\end{aligned} \tag{3.2.9}$$

Thereafter, we can do the Hubbard-Stratonovich transformation to the $J_1 - J_2$ terms, from which we will obtain two channels: the superconductor pairing term and spin (charge) density wave term:

$$\begin{aligned}
&J_1\sum_{\langle i,j\rangle}\mathbf{S}_i\cdot\mathbf{S}_j + J_2\sum_{\langle i,j\rangle}[S^\alpha_i S^\alpha_j - S^\beta_i S^\beta_j - S^\gamma_i S^\gamma_j] \\
=&\frac{3J_1N}{4}(|\Delta_0|^2 + |\chi_0|^2) + \frac{3J_2N}{4}(|\Delta_\alpha|^2 + |\chi_\alpha|^2) - \sum_{\langle i,j\rangle}[J_1\Delta_0\hat{\Delta}_0 + J_1\chi_0\hat{\chi}_0 \\
&+ J_2\Delta_\alpha\hat{\Delta}_\alpha + J_2\chi_\alpha\hat{\chi}_\alpha] + h.c.,
\end{aligned} \tag{3.2.10}$$

in which $\Delta_\alpha = \left\langle\hat{\Delta}_\alpha\right\rangle$, $\chi_\alpha = \langle\hat{\chi_\alpha}\rangle$ are expectation values of the corresponding operators. We will try to verify numerically this mean-field decomposition that we have written down in the next section.

Though the global transformation provides us with an educative guess of the superconductivity pairing for $J_2 > J_1$ and $t' > t$, such a global transformation loses its validity when doped away from half-filling in the establishment of the correspondance between the $t - J_1$ model with pure Heisenberg coupling and the $t' - J_2$ model with the pure J_2 Kitaev-Heisenberg coupling. When we consider the spin-orbit coupling in the $SU(2)$ language, the hopping terms describing the motion of Cooper pairs will bring new problems of fluxes into the system:

$$H_t = -t\sum_{\langle i,j\rangle}[c^\dagger_{i\sigma}d_{j\sigma} + d^\dagger_{j\sigma}c_{i\sigma}] - t'\sum_{\langle i,j\rangle}[c^\dagger_{i\sigma}d_{j\sigma'}\sigma^\alpha_{\sigma\sigma'} + d^\dagger_{i\sigma}c_{j\sigma'}\sigma^\alpha_{\sigma\sigma'}] \tag{3.2.11}$$

Specifically, the spin-orbit coupling $c^\dagger_{i\sigma}d_{j\sigma'}\sigma^\alpha_{\sigma\sigma'} = \mathrm{Tr}(\sigma^T_\alpha\Psi^\dagger_{ci}\Psi_{dj})$ can either be sent to $\pm i\,\mathrm{Tr}(\widetilde{\Psi^\dagger_{ci}}\widetilde{\Psi_{dj}})$ or $\mathrm{Tr}(\widetilde{\Psi^\dagger_{ci}}\widetilde{\Psi_{dj}})$ since $\sigma_\alpha\sigma_\beta\sigma_\gamma = i\epsilon_{\alpha\beta\gamma}$ and $\mathbf{1}\sigma_\alpha\sigma_\alpha = \mathbf{1}$. The global transformation will send the spin-orbit coupling and normal hopping into each other with a periodic π phase. However, the global transformation can offer us a guess of the superconductor pairing of the

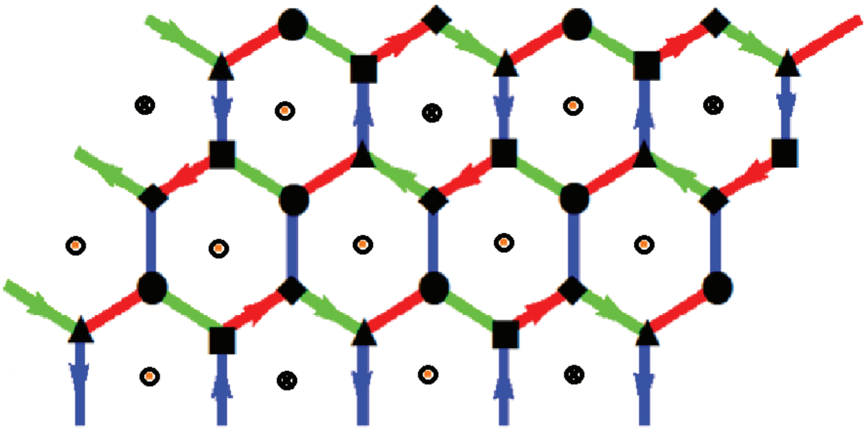

Figure 3.6: Applying the global spin transformation to the spin-orbit coupling model, we obtain a model with uniform π fluxes. Arrows represent a π flux attached to the hopping in the correspondent direction. The primitive cell is enlarged to 4 plaquettes with uniform π fluxes to the plaquettes.

pure J_2 Kitaev-Heisenberg model knowing that we have singlet pairing for the pure Heisenberg $t - J_1$ model.

In Fig. 3.6, we have shown the emergent periodic fluxes after applying the global transformation to the spin-orbit coupling terms of the model $t'\sigma^{\alpha}_{\sigma\sigma'} c^{\dagger}_{i\sigma} d_{j\sigma'} + h.c.$. The arrows represent a π flux of the hopping terms along the corresponding direction $i\tilde{c}^{\dagger}_{i\sigma}\tilde{d}_{j\sigma} + h.c.$ while the transformed hopping terms on other links without arrows is just the normal kinetic term $c^{\dagger}_{i\sigma} d_{j\sigma} + h.c.$. The transformed kinetic Hamiltonian will be written as:

$$\begin{aligned} \widetilde{H_t} &= G^{\dagger} H_t G \qquad (3.2.12) \\ &= -t \sum_{\langle i,j\rangle} [\tilde{c}^{\dagger}_{i\sigma}\tilde{d}_{j\sigma'}\sigma^{\alpha}_{\sigma\sigma'} + h.c.] - t' \sum_{<i,j>\in \text{plain line}} [\tilde{c}^{\dagger}_{i\sigma}\tilde{d}_{j\sigma} + h.c.] - t' \sum_{<i,j>\in \text{arrow line}} [i\tilde{c}^{\dagger}_{i\sigma}\tilde{d}_{j\sigma} + h.c.] \end{aligned}$$

From Fig. 3.6, we see that the transformation brings periodic fluxes π into the system (4 sublattice). The total net magnetic flux is zero, but the time-reversal symmetry is broken. The primitive cell is enlarged twice in the two directions, with 4 plaquettes consisting the primitive cell. In the primitive cell there is one plaquette with π flux going into the paper and three other plaquettes with π flux coming out of the paper. $\pi \equiv -\pi \mod (2\pi)$, the transformed Hamiltonian consists of a model with uniform π fluxes.

An intuitive understanding is that the spin-orbit coupling breaks the time-reversal symmetry alternating bringing magnetic fluxes into the system. A thorough understanding of the flux configuration and its frustration in the superconductivity is presented in the following section via various theoretical and numerical approaches complementing the intuition obtained from the global transformation.

3.3 Exact Diagonalization on one Plaquette - Triplet Pairings

We present in this section the numerical diagonalization of a Hamiltonian on one plaquette of the doped Kitaev-Heisenberg model. First, we look at half-filling (6 electrons) where the kinetic terms cancel because of the Gutzwiller projection, which entails a spin 1/2 system.

3.3.1 Half-filling

In order to study the magnetism in this highly entangled system, we have to use the density matrix to extract information: We diagonalize the system and compute the reduced density matrix for the X, Y and Z links respectively. For example, if the ground state is $|\Psi_6\rangle$, (the subscript signifies that there are 6 electrons on the plaquette) the reduced density matrix for the X link $1-2$ would be: $\rho_{12} = \mathrm{Tr}_{3456} |\Psi_6\rangle \langle\Psi_6|$

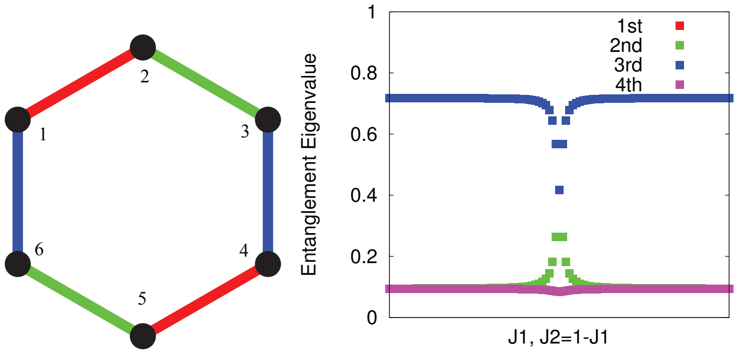

Figure 3.7: *Left panel*: Exact diagonalization of system on one plaquette with sites 1, 2, 3, 4, 5 and 6. *Right panel*:The 4 eigenvalues of the reduced density matrix of the ground state wave function for one link (identical on different links) as a function J_1, and $J_2 = 1 - J_1$ is fixed accordingly.

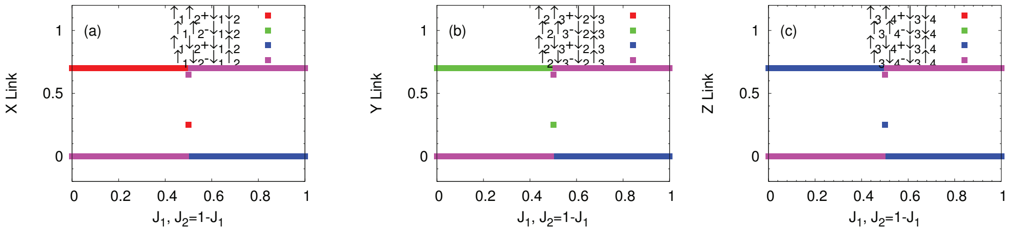

Figure 3.8: The weight of spin states of $|\uparrow_i\uparrow_j\rangle - |\downarrow_i\downarrow_j\rangle$, $|\uparrow_i\uparrow_j\rangle + |\downarrow_i\downarrow_j\rangle$, $|\uparrow_i\downarrow_j\rangle - |\downarrow_i\uparrow_j\rangle$ and $|\uparrow_i\downarrow_j\rangle + |\downarrow_i\uparrow_j\rangle$ respectively on (a) X links , (b) Y links and (c) Z links for the ground state wave function as a function of J_1, and $J_2 = 1 - J_1$ is fixed accordingly.

The reduced density matrix size is 4×4, since for the spin $\frac{1}{2}$ system on link 1-2 a base for the Hilbert space is $|\uparrow_1\uparrow_2\rangle$, $|\uparrow_1\downarrow_2\rangle$, $|\downarrow_1\uparrow_2\rangle$ and $|\downarrow_1\downarrow_2\rangle$, in which the subscripts denote the sites. As shown in Fig. 3.7 & 3.8 for the half filling system, we found that the eigenvector with the biggest statistical weight in the reduced density matrix for one link corresponds to

(1) the spin-triplet in accordance with the type of link on which it sits when $J_1 < J_2$ or (2) the singlet pairing when $J_1 > J_2$. By spin triplets, we mean: (1) triplet X: $|\uparrow_i\uparrow_j\rangle - |\downarrow_i\downarrow_j\rangle$ for the x link connecting sites i and j, (2) triplet Y $|\uparrow_i\uparrow_j\rangle + |\downarrow_i\downarrow_j\rangle$ for the Y links connecting the sites i and j and (3) triplet Z $|\uparrow_i\downarrow_j\rangle + |\uparrow_i\downarrow_j\rangle$ for the Z links connecting the sites i and j. One interesting property of the three spin triplet state is that the total spin of the states is zero $\langle\Psi_6|\sum_i \hat{\vec{S_i}}\,|\Psi_6\rangle = 0$, and the operators to characterize them are the bilinear operators $\langle\Psi_6|\sum_{\langle i,j\rangle}\hat{S_i^\alpha}\hat{S_j^\alpha}\,|\Psi_6\rangle \neq 0$. They are often referred to as polar states. We also observe the perfect symmetry between the left side of $t < t'$ ($J_1 < J_2$) and the right side of $t > t'$ ($J_1 > J_2$), which is due to the duality explained in the previous section. The coefficients in front of the Heisenberg and J_2 Kitaev-Heisenberg coupling will exchange their places.

3.3.2 Doped System

In order to study the pairing order parameter for such a system, it is useful to study the distribution of the holes when the system is doped with 2 holes, which corresponds to $\delta = 1/6$.

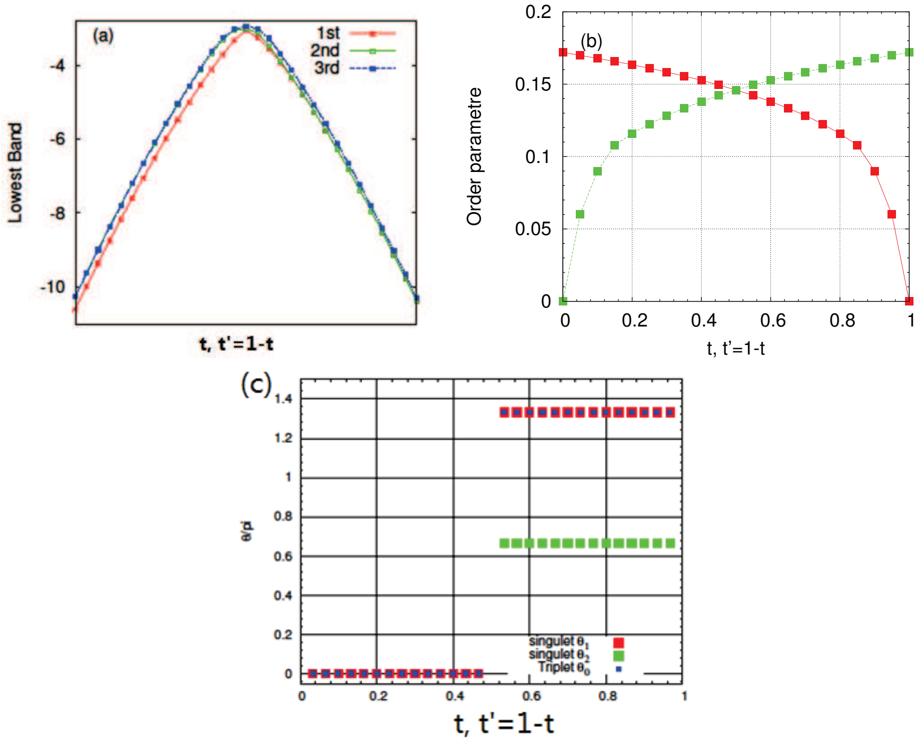

Figure 3.9: Exact diagonalization results for two-holes doped from half-filling on one plaquette: (a) The lowest energy levels and (b) the modulus of the spin triplet $|\Delta_{ij}^\alpha|$ ($\alpha = x,y,z$) and singlet on one link as a function of J_1 and J_2 when 2 holes are doped from half filling. (c): the relative phase (angular momentum) between order parametres on two adjacent links sharing one site. For the phase $J_2 > J_1$, the ground state is unique, and the relative phase is zero, while for the phase $J_1 > J_2$ the two lowest energy states are quasi-degenerate and their angular momentum corresponds respectively to $d \pm id$ ($\frac{4\pi}{3}\&\frac{2\pi}{3}$).

With the parametrization of $t, t' = 1 - t, J_1 = 4t^2/U, J_2 = 4t'^2/U (U = 6)$, we diagonalize the system with two holes (4 electrons on 6 sites), and we extract the ground state wave function which we note as $|\Psi_4\rangle$. In Fig. 3.9 left panel (a), we have shown the spectrum of one plaquette with two holes doped (4 electrons) as a function of t. We see that the ground state is unique when $t > t', J_1 > J_2$ while there is a quasi-degeneracy when $t' > t, J_2 > J_1$. The system becomes completely degenerate when $J_1 \to 0$ which corresponds to the $d \pm id$ symmetry.

The half filling wave function $|\Psi_6\rangle$ and two holes doped wave function $|\Psi_4\rangle$ are connected by the spin singlet and spin triplet operators Δ^α_{ij} on the link connecting sites i and j; amplitudes $|\Delta^\alpha_{ij}|$ and phases of these singlet and triplet operators give us an idea of the pairing order parametre and the symmetry of the ground state wave function:

$$\Delta^\alpha_{ij} = \langle\Psi_4| \hat{\Delta}^\alpha_{ij} |\Psi_6\rangle = |\Delta^\alpha_{ij}| e^{i\theta} \tag{3.3.1}$$

in which the pairing operator Δ^α_{ij} are defined in equation 3.2.8. We have calculated the expectation of the pairing order using equation 3.3.1 as shown in Fig. 3.9 left panel (b) and right panel. We have found that the singlet pairing order parameter is dominating when $J_1 > J_2$ and the spin singlet pairing order parameter Δ^0_{ij} is constant on different links. When $J_2 > J_1$ the spin triplet order parameter Δ^α_{ij} is dominant on the link α with the condition $\mathbf{r}_i - \mathbf{r}_j = \mathbf{r}_\alpha$ and the amplitude of Δ^α_{ij} is constant on different correspondent links α ($\alpha = x$,y, z). The phase of the pairing order parameter is arbitrary as the eigenvector from the exact diagonalization, however, the relative phase between the pairing order parameter on two adjacent links is well defined. It signifies actually the angular momentum of the superconductivity, specifically:

$$e^{i\theta} = \begin{cases} \Delta^\beta_{ij}/\Delta^\alpha_{jk} & |\Delta^\alpha_{ij}|(\mathbf{r}_i - \mathbf{r}_j = \mathbf{r}_\alpha) = |\Delta^\beta_{jk}|(\mathbf{r}_j - \mathbf{r}_k = \mathbf{r}_\beta) \quad \text{Triplet} \\ \Delta^0_{ij}/\Delta^0_{jk} & \Delta^0 = |\Delta^0_{ij}| = |\Delta^0_{jk}| \quad \forall i, j, k \end{cases} \tag{3.3.2}$$

in which ij and jk are two adjacent links with a counterclockwise rotation symmetry around the common site j.

(1) When $t > t', J_1 > J_2$ the lowest two quasi-degenerate state have $d \pm id$ symmetry (degeneracy lifted by the t' spin-orbit coupling which breaks the time-reversal symmetry): the angular momentum of these two quasi-degenerate wave functions $|\Psi^1_4\rangle$ & $|\Psi^2_4\rangle$: $\Delta^0_{12} = e^{i\frac{4\pi}{3}}\Delta^0_{23}$, $\Delta^0_{23} = e^{i\frac{4\pi}{3}}\Delta^0_{34}$.... are $\theta = \frac{4\pi}{3}$ for the lowest energy level and $\Delta^0_{12} = e^{i\frac{2\pi}{3}}\Delta^0_{23}$, $\Delta^0_{23} = e^{i\frac{2\pi}{3}}\Delta^0_{34}$.... $\theta = \frac{2\pi}{3}$ for the 1st excited state. If we denote the wave function of the $d \pm id$ symmetry respectively as $|\Psi_+\rangle$ and $|\Psi_-\rangle$, they are then related by the time-reversal operator: $|\Psi_+\rangle = T|\Psi_-\rangle$. When the spin-orbit coupling is absent $t' = 0$, the Hamiltonian commutes with the time-reversal operator. However the spin-orbit coupling breaks the time reversal symmetry $T\sigma^\alpha_{\sigma\sigma'}c^\dagger_{i\sigma}d_{j\sigma'}T^{-1} = -\sigma^\alpha_{\sigma\sigma'}c^\dagger_{i\sigma}d_{j\sigma'}$, which lifts the degeneracy between the $|\Psi_+\rangle$ and $|\Psi_-\rangle$ making the superconductivity chiral.

(2) When $t < t', J_1 < J_2$ we are situated in the spin triplet phase, the ground state is unique and the wave function symmetry is p-wave: $\Delta^x_{12} = \Delta^y_{23} = \Delta^z_{34} = \Delta^x_{45} = \Delta^y_{56} = \Delta^z_{61}$. By noticing that the spin triplet order parametre is antisymmetric $\Delta^\alpha_{ij} = -\Delta^\alpha_{ji}$ (unlike the symmetric property for singlets $\Delta^0_{ij} = \Delta^0_{ji}$), this fixes a certain chirality for the order parametres on one plaquette.

To sum up, the exact diagonalization result on one plaquette confirms the intuition obtained from the global transformation presented in the previous section: when $t' > t, J_2 > J_1$ the spin triplet pairing are in one to one correspondance with the spin singlet pairing $\Delta^\alpha_{ij} = T_s\Delta^0_{ij}T_s^{-1}$ as explained in equation 3.2.8. Nevertheless, one question arises naturally from the calculation of the angular momentum of the pairing order parameter on one plaquette: the antisymmetric p-wave superconductivity imposes a certain chirality on one plaquette; we can imagine that two juxtaposed plaquettes have opposite chirality, however, the dual lattice of the honeycomb latice is a triangular lattice, which is frustrated if we wish to alternate between the two chiralities (+ and -). We have also mentionned in the previous section that if we apply the same global spin transformation to the kinetic terms and spin-orbit coupling, we have a model with periodic fluxes. We will inspect carefully the band structure of the spin-orbit system in the next section to understand the peculiarity of this model and the coordination of chirality in a $2D$ doped system.

3.4 Band Structure of the Spin-Orbit Coupling System

From the previous sections, we see that the spin-orbit coupling brings complicated flux configurations into the system. It is thus worth having a careful investigation of the free electron model of the system, which has been previously studied in the cold atom context [200]. We have now the spin-orbit coupling model consisting of a mixture of normal hopping and spin-orbit coupling.

$$H_s = \sum_{\langle i,j \rangle} (t\delta_{\sigma\sigma'} + t'\sigma^{\alpha}_{\sigma\sigma'}) c^{\dagger}_{i\sigma} d_{j\sigma'} + h.c. - \mu_c \sum_i (c^{\dagger}_{i\sigma} c_{i\sigma} + d^{\dagger}_{i\sigma} d_{i\sigma}) \tag{3.4.1}$$

We can diagonalize the problem by applying the Fourier transformation, and we write down the spinor $\Psi_{sk} = (c_{k\uparrow}, c_{k\downarrow}, d_{k\uparrow}, d_{k\downarrow})$.

$$H_s = \sum_k \Psi^{\dagger}_{sk} \mathcal{H}_s(\mathbf{k}) \Psi_{sk} \tag{3.4.2}$$

$$\mathcal{H}_{sk} = \begin{pmatrix} -\mu_c & 0 & tg(\mathbf{k})^* + t'g_z(\mathbf{k})^* & t'[g_x(\mathbf{k})^* - ig_y(\mathbf{k})^*] \\ 0 & -\mu_c & t'[g_x(\mathbf{k})^* + ig_y(\mathbf{k})^*] & tg(\mathbf{k})^* - t'g_z(\mathbf{k})^* \\ tg(\mathbf{k}) + t'g_z(\mathbf{k}) & t'[g_x(\mathbf{k}) - ig_y(\mathbf{k})] & -\mu_c & 0 \\ t'[g_x(\mathbf{k}) + ig_y(\mathbf{k})] & tg(\mathbf{k}) - t'g_z(\mathbf{k}) & 0 & -\mu_c \end{pmatrix}$$

in which $g(\mathbf{k}) = \sum_{\alpha=x,y,z} e^{i\mathbf{k}\cdot\mathbf{r}_\alpha}$ and $g_\alpha(\mathbf{k}) = e^{i\mathbf{k}\cdot\mathbf{r}_\alpha}$ $(\alpha = x, y, z)$. There are four bands for such a model:

$$E(\mathbf{k}) = \pm E_p(\mathbf{k}) = \pm\sqrt{3t'^2 + t^2|g(\mathbf{k})|^2 + p\sqrt{(c_x(\mathbf{k}))^2 + (c_y(\mathbf{k}))^2 + (c_z(\mathbf{k}))^2}} \tag{3.4.3}$$

in which $p = \pm 1$ and

$$c_\alpha(\mathbf{k}) = 2t'^2 \sin\mathbf{k}\cdot\mathbf{R}_\alpha + 2tt'[1 + \cos\mathbf{k}\cdot\mathbf{R}_\beta + \cos\mathbf{k}\cdot\mathbf{R}_\gamma] \quad (\alpha \neq \beta \neq \gamma) \tag{3.4.4}$$

We have plotted the band structure along the circuit $M \to O \to K \to K' \to M$ in Fig. 3.10 in the spin-orbit coupling limit. We see that there are four bands at the limit $t = 0$, touching at point M and O between the third and fourth band and the first and second band has the mirror symmetry with regard to zero energy level. When $t \neq 0$, the normal hopping lifts the degeneracy at the conic band structure at point M and O while leaving the conic degeneracy structure between the second and third band.

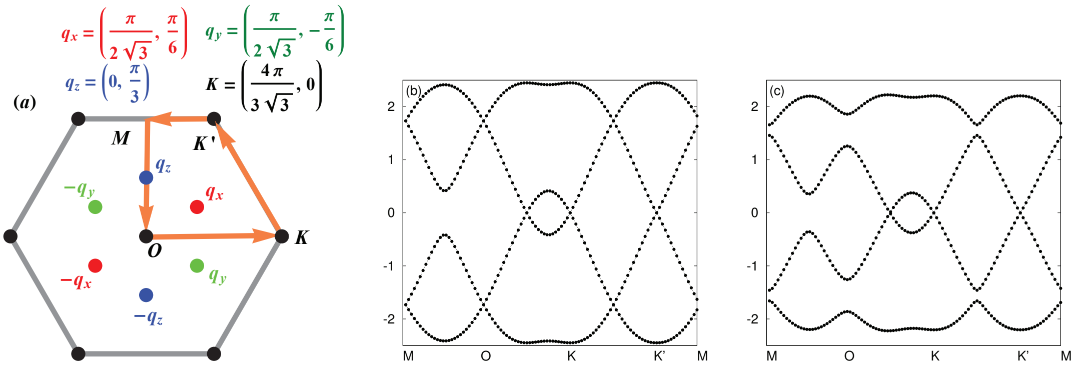

Figure 3.10: (a) the first Brillouin zone of the honeycomb lattice with three symmetry centers of the Fermi surface at non-trivial wave vectors $\pm\mathbf{q}_\alpha$ $(\alpha = x, y, z)$. The band structure $E_p(\mathbf{k})$ expressed in equation 3.4.3 of the spin-orbit coupling model at $t = 0, t' = 1$ (b) and $t = 0.1, t' = 0.9$ (c).

The geometric characteristics of the band is very particular at the pure spin-orbit coupling limit. As a matter of fact, when $t = 0$ we have new symmetry centers for the band structure at the following points:

$$\mathbf{q}_x = \pm(\frac{\pi}{2\sqrt{3}}, \frac{\pi}{6}), \quad \mathbf{q}_y = \pm(\frac{\pi}{2\sqrt{3}}, -\frac{\pi}{6}), \quad \mathbf{q}_z = \pm(0, \frac{\pi}{3}), \quad \mathbf{q}_0 = (0,0)$$
$$E_p(\mathbf{k}) = E_p(2\mathbf{q}_\alpha - \mathbf{k}) \quad (\alpha = x, y, z), \tag{3.4.5}$$

which means at a certain Fermi level, electrons with momentum $\mathbf{k}$ and $2\mathbf{q}_\alpha - \mathbf{k}$ are both on the Fermi surface. The new symmetry centers are related to spatial modulation of π phase. If we define the wave vectors $\mathbf{Q}_\alpha = 2\mathbf{q}_\alpha$, we have:

$$\mathbf{Q}_\alpha \cdot \mathbf{R}_\beta = \pi - \pi\delta_{\alpha\beta} \tag{3.4.6}$$

in which $\delta_{\alpha\beta}$ is the kronecker symbol and $\alpha, \beta = x, y, z$. This embedded flux in the spin subspace attributes actually a topological characteristic to the system. To illustrate this point, we can write the Hamiltonian in the form of:

$$\mathcal{H}_s(\mathbf{k}) = \begin{pmatrix} \mu_c & \Sigma_k^\dagger \\ \Sigma_k & \mu_c \end{pmatrix} \qquad \Sigma_k = tg(\mathbf{k}) + t'\sum_\alpha g_\alpha(\mathbf{k})\sigma_\alpha \tag{3.4.7}$$

and diagonalization of this Hamiltonian involves the calculation of the following matrix product:

$$\Sigma_k^\dagger \Sigma_k = 3t'^2 + t^2|g(\mathbf{k})|^2 + \hat{\vec{c}}(\mathbf{k}) \cdot \vec{\sigma}, \tag{3.4.8}$$

in which $\vec{c}(\mathbf{k}) = (c_x(\mathbf{k}), c_y(\mathbf{k}), c_z(\mathbf{k}))$ and $\hat{\vec{c}}(\mathbf{k})$ is the unit vector on the $SU(2)$ sphere, and $\vec{\sigma} = (\sigma_x, \sigma_y, \sigma_z)$ is a vector composed of Pauli matrices in the spin subspace. The topology is manifested by the wrapping of the vector $\hat{\vec{c}}(\mathbf{k})$ around the $SU(2)$ sphere when $\mathbf{k}$ sweeps around the first Brillouin zone. Mathematically speaking, the Chern class is the characterization of degree of the mapping $\vec{c}(\mathbf{k}) = (c_x(\mathbf{k}), c_y(\mathbf{k}), c_z(\mathbf{k})) : FBZ \to S^2$.

Without losing any generality, we can calculate the Chern number using the band projectors. The eigenvalues of the Hamiltonian can be written as:

$$\begin{pmatrix} v_p(\mathbf{k}) \\ e^{\chi_k} v_p(-\mathbf{k}) \end{pmatrix} \tag{3.4.9}$$

in which χ_k is a phase to be determined and the vector $v_p(\mathbf{k})$ is determined by:

$$P_{sp}(\mathbf{k}) = \frac{1}{2}[1 - p\hat{\vec{c}}(\mathbf{k}) \cdot \vec{\sigma}] \tag{3.4.10}$$

The projectors $P_{s\pm}$ projects to the bands $E_\pm$ ($p = \pm 1$) with respectively the eigenvectors $v_p(\mathbf{k})$. These projectors act in the spin subspace.

If we denote $P_I(\mathbf{k})$ as the band projector for the band I with energy level $E_I(\mathbf{k})$, then we have generically the Chern number for the band I as:

$$\mathcal{C}_I = \frac{1}{2\pi i}\int_{FBZ} d^2k \, \mathrm{Tr}[P_I(\mathbf{k})(\partial_{k_x} P_I(\mathbf{k}) - \partial_{k_y} P_I(\mathbf{k}))] = \frac{p}{2\pi}\int_{FBZ} d^2k \hat{\vec{c}}(\mathbf{k}) \cdot [\partial_{k_x}\hat{\vec{c}}(\mathbf{k}) - \partial_{k_y}\hat{\vec{c}}(\mathbf{k})] \tag{3.4.11}$$

in which in the second equality we have substituted $P_I(\mathbf{k})$ by $P_{sp\pm}(\mathbf{k})$. Thereafter, we can implement a numerical calculation of the Chern number.

In the spin-orbit coupling model, the tricky part of the Chern number numerical calculation comes from the fact that the second and the third band touches at several points making the Chern number senseless for the second and third band. In order to cope with this difficulty, we can define the Chern number for the second and third band. If $|\Psi_2\rangle$ and $|\Psi_3\rangle$ are the eigenvectors of the second and third band from the exact diagonalization, we do the Gram-Schmidt reorthogonalization to these two eigenvectors, then we have the band projectors to the second and third band:

$$\begin{aligned}
\widetilde{|\Psi_2\rangle} &= \frac{1}{N_2}|\Psi_2\rangle \\
\widetilde{|\Psi_3\rangle} &= \frac{1}{N_3}(|\Psi_3\rangle - \frac{\langle\Psi_2|\,\Psi_3\rangle}{\langle\Psi_2|\,\Psi_2\rangle}|\Psi_3\rangle) \\
P_{23} &= \widetilde{|\Psi_2\rangle}\widetilde{\langle\Psi_2|} + \widetilde{|\Psi_3\rangle}\widetilde{\langle\Psi_3|}
\end{aligned} \tag{3.4.12}$$

in which N_2 and N_3 are the renormalization of the vector $|\Psi_2\rangle$ and $|\Psi_3\rangle$ so that $\widetilde{|\Psi_2\rangle}$ and $\widetilde{|\Psi_3\rangle}$ form orthonormal bases. The Chern number for the spin orbit coupling model is defined when there is the normal kinetic term t that opens a gap. The vector $\hat{\vec{c}}(\mathbf{k})$ has singular behavior around $\mathbf{q}_\alpha$ and $\mathbf{q}_0$. It wraps around the unit sphere once when covering the first Brillouin zone. As a result, the Chern number for the bands are depending on the index p. The first and fourth band has Chern number equal to 1 ($p = +1$) while the Chern number of the second plus the third band is -2 ($p = -1$). The actual Chern number of the system is determined by the Fermi level, by summing the Chern number of all the bands below the Fermi level.

The Chern number is independent of the magnitude of t and t'. As a consequence of the Chern number, there is an edge mode connecting the lowest band and the medium band (the second plus the third band) and there is also another edge mode connecting the highest band and the medium band, and these two edge modes propagates in the opposite direction. We have also spoted the particle-hole symmetry in terms of the Chern number. As a result, the spin-orbit coupling model at the limit of $t \to 0$ is topological when the Fermi level lies beteween the 3rd and 4th band. We have identified new symmetry center of the free electron band in this section, and we will try to use these new symmetry properties to inspect the particularity of the superconductivity when we dope around quarter-filling $\delta = 0.25$.

3.5 FFLO Superconductivity

We have shown the particularity of the band structure of the spin-orbit coupling model in the previous section and identified new symmetry centers. When the system is doped away from half-filling, holes (or electrons) will form pairs inducing superconducting instability at not too large couplings. Superconductivity is a property that depends only on the Fermi surface rather than the bulk of the electron bands. In the BCS theory, electrons with momentum $\mathbf{k}$ and $-\mathbf{k}$ form Cooper pairs due to the electron-phonon coupling, which opens a superconductivity gap. In the context of high-T_c superconductor, most electron band structure has the inversion symmetry so that when the Fermi level is fixed, electrons with momentum $\mathbf{k}$ and $-\mathbf{k}$ form also pairs thanks to the correlation opening a superconductivity gap and the Cooper pair momentum is therefore zero. When there are other symmetry centers at wave vector $\mathbf{q}_\alpha$, electrons with momentum $\mathbf{k}$ and $2\mathbf{q}_\alpha - \mathbf{k}$ will also form Cooper pairs with Cooper pair momentum $\mathbf{Q}_\alpha = 2\mathbf{q}_\alpha$ to be in competition with the previous one.

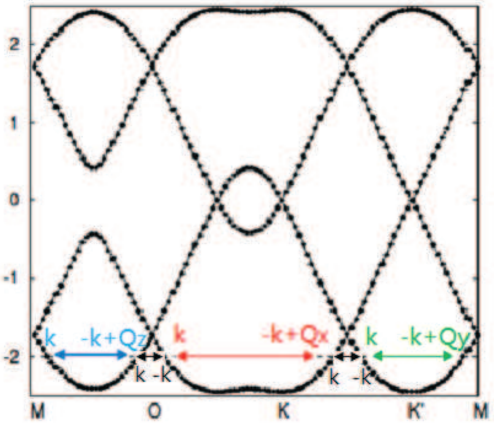

Figure 3.11: Elementary superconductivity excitations of the Fermi surface engage not only electron pairs with momentum $\mathbf{k}$ and $-\mathbf{k}$ but also electron pairs with momentum $\mathbf{k}$ and $\mathbf{Q}_\alpha - \mathbf{k}$. ($\alpha = x, y, z$.)

Apart from the inversion symmetry around the point O in the first Brillouin zone, we have supplementary symmetry centers for the band structure of the spin-orbit coupling model (See Fig. 3.11). Hence, we have also electron pairs with momentum $\mathbf{k}$ and $\mathbf{Q}_\alpha - \mathbf{k}$ both at the Fermi surface $\alpha = x, y, z$. There are actually 4 pairs of electrons in competition for the superconductivity instability, one for each $\mathbf{Q}_\alpha$ and one at zero momentum. We can measure the spin of the 4 electron pairs by using the projector introduced in equation 3.4.10 as $\langle \mathbf{S}_k \rangle = \mathrm{Tr}(P_{sp}(\mathbf{k})\hat{\mathbf{S}}P_{sp}(\mathbf{k}))$. Around the symmetry center $\mathbf{Q}_\alpha$, we have $\langle S^\alpha_\mathbf{k} \rangle = -\left\langle S^\alpha_{\mathbf{Q}_\alpha - \mathbf{k}} \right\rangle$ and $\left\langle S^\beta_\mathbf{k} \right\rangle = \left\langle S^\beta_{\mathbf{Q}_\alpha - \mathbf{k}} \right\rangle$ for $\alpha \neq \beta$ and $\alpha, \beta = x, y, z$ while around the inversion center O, we have $\langle \mathbf{S}_\mathbf{k} \rangle = -\langle \mathbf{S}_{-\mathbf{k}} \rangle$.

$$\begin{cases} \langle S^x_\mathbf{k} \rangle = -\left\langle S^x_{\mathbf{Q}_x - \mathbf{k}} \right\rangle & \langle S^y_\mathbf{k} \rangle = \left\langle S^y_{\mathbf{Q}_x - \mathbf{k}} \right\rangle & \langle S^z_\mathbf{k} \rangle = \left\langle S^z_{\mathbf{Q}_x - \mathbf{k}} \right\rangle \\ \langle S^y_\mathbf{k} \rangle = -\left\langle S^y_{\mathbf{Q}_y - \mathbf{k}} \right\rangle & \langle S^x_\mathbf{k} \rangle = \left\langle S^x_{\mathbf{Q}_y - \mathbf{k}} \right\rangle & \langle S^z_\mathbf{k} \rangle = \left\langle S^z_{\mathbf{Q}_y - \mathbf{k}} \right\rangle \\ \langle S^z_\mathbf{k} \rangle = -\left\langle S^z_{\mathbf{Q}_z - \mathbf{k}} \right\rangle & \langle S^x_\mathbf{k} \rangle = \left\langle S^x_{\mathbf{Q}_z - \mathbf{k}} \right\rangle & \langle S^y_\mathbf{k} \rangle = \left\langle S^y_{\mathbf{Q}_z - \mathbf{k}} \right\rangle \\ \langle \mathbf{S}_\mathbf{k} \rangle = -\langle \mathbf{S}_{-\mathbf{k}} \rangle & & \end{cases} \tag{3.5.1}$$

We can see obviously from equation 3.5.1 that electron pairs around symmetry center $\mathbf{Q}_\alpha$ minimize the coupling in the form of J_2 Kitaev-Heisenberg $J(S^\alpha_{\mathbf{k}} S^\alpha_{\mathbf{Q}_\alpha-\mathbf{k}} - S^\beta_{\mathbf{k}} S^\beta_{\mathbf{Q}_\alpha-\mathbf{k}} - S^\gamma_{\mathbf{k}} S^\gamma_{\mathbf{Q}_\alpha-\mathbf{k}}) = -J\mathbf{S}^2_k$ and the electron pairs around the inversion center O minimize the coupling in the form of Heisenberg $J\mathbf{S}_{\mathbf{k}} \cdot \mathbf{S}_{-\mathbf{k}} = -J\mathbf{S}^2_k$. In the language of wave function, we can interpret the above as (we denote $|\uparrow_{x,y,z}\rangle$ as spin up in the x, y and z polarization, etc):

$$\begin{aligned}
&\langle S^x_{\mathbf{k}}\rangle = -\left\langle S^x_{\mathbf{Q}_x-\mathbf{k}}\right\rangle : \\
&|\Psi_x\rangle = |\uparrow_x\rangle_k |\downarrow_x\rangle_{\mathbf{Q}_x-k} + |\downarrow_x\rangle_k |\uparrow_x\rangle_{\mathbf{Q}_x-k} \\
&\quad = \frac{1}{2}[(|\uparrow_z\rangle_k - |\downarrow_z\rangle_k)(|\uparrow_z\rangle_{\mathbf{Q}_x-k} + |\downarrow_z\rangle_{\mathbf{Q}_x-k}) + (|\uparrow_z\rangle_k + |\downarrow_z\rangle_k)(|\uparrow_z\rangle_{\mathbf{Q}_x-k} - |\downarrow_z\rangle_{\mathbf{Q}_x-k})] \\
&\quad = |\uparrow_z\rangle_{\mathbf{k}} |\uparrow_z\rangle_{\mathbf{Q}_x-\mathbf{k}} - |\downarrow_z\rangle_{\mathbf{k}} |\downarrow_z\rangle_{\mathbf{Q}_x-\mathbf{k}} \\
&\langle S^y_{\mathbf{k}}\rangle = -\left\langle S^y_{\mathbf{Q}_y-\mathbf{k}}\right\rangle : \\
&|\Psi_y\rangle = |\uparrow_y\rangle_k |\downarrow_y\rangle_{\mathbf{Q}_y-k} + |\downarrow_y\rangle_k |\uparrow_y\rangle_{\mathbf{Q}_y-k} \\
&\quad = \frac{1}{2}[(|\uparrow_z\rangle_k - i\,|\downarrow_z\rangle_k)(|\uparrow_z\rangle_{\mathbf{Q}_y-k} + i\,|\downarrow_z\rangle_{\mathbf{Q}_y-k}) + (|\uparrow_z\rangle_k + i\,|\downarrow_z\rangle_k)(|\uparrow_z\rangle_{\mathbf{Q}_y-k} - i\,|\downarrow_z\rangle_{\mathbf{Q}_y-k})] \\
&\quad = |\uparrow_z\rangle_{\mathbf{k}} |\uparrow_z\rangle_{\mathbf{Q}_y-\mathbf{k}} + |\downarrow_z\rangle_{\mathbf{k}} |\downarrow_z\rangle_{\mathbf{Q}_y-\mathbf{k}} \\
&\langle S^z_{\mathbf{k}}\rangle = -\left\langle S^z_{\mathbf{Q}_z-\mathbf{k}}\right\rangle : \\
&|\Psi_z\rangle = |\uparrow_z\rangle_k |\downarrow_z\rangle_{\mathbf{Q}_z-k} + |\downarrow_z\rangle_k |\uparrow_z\rangle_{\mathbf{Q}_z-k}
\end{aligned} \tag{3.5.2}$$

If we express the creation operator of electron pairs in accordance with the spin behavior in equation 3.5.1, we have:

$$\begin{cases}
\hat{\Delta}_{x\mathbf{Q}_x}(\mathbf{k}) = c_{\mathbf{k}\uparrow} d_{\mathbf{Q}_x-\mathbf{k}\uparrow} - c_{\mathbf{k}\downarrow} d_{\mathbf{Q}_x-\mathbf{k}\downarrow} \\
\hat{\Delta}_{y\mathbf{Q}_y}(\mathbf{k}) = i(c_{\mathbf{k}\uparrow} d_{\mathbf{Q}_y-\mathbf{k}\uparrow} + c_{\mathbf{k}\downarrow} d_{\mathbf{Q}_y-\mathbf{k}\downarrow}) \\
\hat{\Delta}_{z\mathbf{Q}_z}(\mathbf{k}) = -(c_{\mathbf{k}\uparrow} d_{\mathbf{Q}_z-\mathbf{k}\downarrow} + c_{\mathbf{k}\downarrow} d_{\mathbf{Q}_z-\mathbf{k}\uparrow}) \\
\hat{\Delta}_{0\mathbf{O}}(\mathbf{k}) = c_{\mathbf{k}\uparrow} d_{-\mathbf{k}\downarrow} - c_{\mathbf{k}\downarrow} d_{-\mathbf{k}\uparrow}
\end{cases} \tag{3.5.3}$$

At the mean-field level, we can decompose the J_2 Kitaev-Heisenberg coupling as:

$$\begin{aligned}
&J_2 \sum_{\langle i,j\rangle} [S^\alpha_i S^\alpha_j - S^\beta_i S^\beta_j - S^\gamma_i S^\gamma_j] \\
=&\frac{3J_2N}{4}|\Delta_\alpha|^2 - \sum_{\langle i,j\rangle} J_2[\Delta^\alpha_{ij}\hat{\Delta}^\alpha_{ij}\delta_{\mathbf{r}_i-\mathbf{r}_j,\mathbf{r}_\alpha} + \Delta^{\alpha\star}_{ij}\hat{\Delta}^{\alpha\dagger}_{ij}\delta_{\mathbf{r}_i-\mathbf{r}_j,\mathbf{r}_\alpha} - \Delta^0_{ij}\hat{\Delta}^0_{ij} - \Delta^{0*}_{ij}\hat{\Delta}^{0\dagger}_{ij}] + h.c.,
\end{aligned} \tag{3.5.4}$$

In equation 3.2.8, we have guessed the triplet pairing operators in the direct space, and we try to link them with the triplet pairings in the momentum space that we have obtained in equation 3.5.3. If we denote the mean value of the triplet pairing operators in the momentum space as $\Delta_{\alpha\mathbf{Q}_\alpha} = \left\langle \hat{\Delta}_{\alpha\mathbf{Q}_\alpha} \right\rangle$ then we can do the Fourier transformation to the terms for the pairing operators $\sum_{\langle i,j\rangle}\Delta^{\alpha}_{ij}\hat{\Delta}^{\alpha}_{ij}\delta_{\mathbf{r}_i-\mathbf{r}_j,\mathbf{r}_\alpha}$:

$$\begin{aligned}
&\sum_{\langle i,j\rangle}\Delta^{\alpha}_{ij}\hat{\Delta}^{\alpha}_{ij}\delta_{\mathbf{r}_i-\mathbf{r}_j,\mathbf{r}_\alpha}\\
=&\frac{1}{N}\sum_{\mathbf{k},\langle i,j\rangle}\Delta^{\alpha}_{ij}i\sigma^{y}_{\sigma\sigma^1}\sigma^{\alpha}_{\sigma^1\sigma'}c_{\mathbf{k}\sigma}d_{-\mathbf{k}+\mathbf{Q}\sigma'}e^{i\mathbf{k}\cdot(\mathbf{r}_i-\mathbf{r}_j)}e^{i\mathbf{Q}\cdot\mathbf{r}_j}\delta_{\mathbf{r}_i-\mathbf{r}_j,\mathbf{r}_\alpha}\\
=&\sum_{\mathbf{k}}\Delta_{\alpha\mathbf{Q}}ig_\alpha(\mathbf{k})\sigma^{y}_{\sigma\sigma^1}\sigma^{\alpha}_{\sigma^1\sigma'}c_{\mathbf{k}\sigma}d_{-\mathbf{k}+\mathbf{Q}\sigma'}\\
&\Delta_{\alpha\mathbf{Q}}=\frac{1}{N}\sum_{\langle i,j\rangle}e^{i\mathbf{Q}\cdot\mathbf{r}_j}\Delta^{\alpha}_{ij},
\end{aligned}\tag{3.5.5}$$

in which $\Delta_{\alpha\mathbf{Q}}$ denotes the spin-triplet pairing α with the spatial modulation $e^{i\mathbf{Q}\cdot\mathbf{r}_j}$ and $g_\alpha(\mathbf{k})=e^{i\mathbf{k}\cdot\mathbf{r}_\alpha}$. We can see that when $\mathbf{Q}=\mathbf{Q}_\alpha$, the spatial modulated order parameter $\Delta_{\alpha\mathbf{Q}}$ concurs with the triplet pairing order parameter in the momentum space:

$$\sum_{\langle i,j\rangle}\Delta^{\alpha}_{ij}\hat{\Delta}^{\alpha}_{ij}\delta_{\mathbf{r}_i-\mathbf{r}_j,\mathbf{r}_\alpha}=\sum_{\mathbf{k}}\Delta_{\alpha\mathbf{Q}_\alpha}\hat{\Delta}_{\alpha\mathbf{Q}_\alpha}(\mathbf{k})g_\alpha(\mathbf{k})\tag{3.5.6}$$

$$\Delta_{\alpha\mathbf{Q}_\alpha}=\frac{1}{N}\sum_{\langle i,j\rangle}e^{i\mathbf{Q}_\alpha\cdot\mathbf{r}_j}\Delta^{\alpha}_{ij}\tag{3.5.7}$$

and $\Delta_{\alpha\mathbf{Q}_\alpha}$, the order parameter of electron pairing around the symmetry center $\mathbf{Q}_\alpha$ equals the modulated order parameter Δ^{α}_{ij} with a momentum $\mathbf{Q}_\alpha$. It is worth noticing that around the inversion symmetry center O, the spin singlet operator $\Delta_{0\mathbf{O}}$ is uniform with zero electron pair momentum.

Consequentially, there are four types of electron pairs: (1) $\Delta_{\alpha\mathbf{Q}_\alpha}$ three spin triplet pairings with electron pair momentum $\mathbf{Q}_\alpha$ ($\alpha=x,y,z$) which has the spatial modulation of the order parameter with momentum $\mathbf{Q}_\alpha$ and (2) $\Delta_{0\mathbf{O}}$ the singlet electron pairing with zero pair momentum which has uniform order parameter. The four electron pairs form bosons constituting four types of condensates, and we will endeavor to understand the competition among the four condensates by calculating the superconductivity susceptibility and pursue the subsequent Landau expansion to study the interaction between the four condensates.

In order to simplify the discussion, we see that a little normal hopping t added to the spin-orbit coupling model opens a gap at the quarter-filling. When the chemical potential is fixed at quarter-filling within the gap, the electron pair density is zero making the superconductivity absent. Doped away from quarter-filling in the weak-coupling limit, the electron pair density becomes non-zero inducing the superconductivity. There are complexities around the half-filling with charge and spin density wave χ^{0}_{ij} and χ^{α}_{ij} as well as the mean-field treatment of the Gutzwiller projection. The study of the superconductivity around quarter-filling avoids all these technicalities since χ^{0}_{ij} and the Gutzwiller projectors disappears around this filling in the weak coupling limit.

We write down the Gor'kov-Green function whose diagonal blocks consist of the free electron Green function for respectively particles and holes and the non-diagonal blocks consist of the four kinds of different superconductivity pairing discussed above, specifically if we admit the Nambu spinor as $\Phi_{\mathbf{k}}=(\Psi_{s\mathbf{k}},\Psi^{\dagger}_{s\mathbf{Q}_\alpha-\mathbf{k}})$ and $\Psi_{s\mathbf{k}}=(c_{k\uparrow},c_{k\downarrow},d_{k\uparrow},d_{k\downarrow})$, the Gor'kov Green function $G_\alpha(\omega,\mathbf{k},\mathbf{Q})$ with electron pair momentum $\mathbf{Q}$ and the color index α ($\alpha=0,x,y,z$)

for respectively the spin singlet and spin triplet pairing writes as:

$$\begin{aligned}
G_\alpha^{-1}(\omega,\mathbf{k},\mathbf{Q}) &= \begin{pmatrix} G_0^{-1}(\omega,\mathbf{k}) & -H_{\alpha\mathbf{Q}}(\mathbf{k}) \\ -H_{\alpha\mathbf{Q}}(\mathbf{k})^H & -G_0^{-1}(\omega,-\mathbf{k}+\mathbf{Q}) \end{pmatrix} \\
G_0(\omega,\mathbf{k}) &= \frac{1}{i\omega-(\mathcal{H}_0(\mathbf{k})-\mu)} = \frac{P_I(\mathbf{k})}{i\omega-(\epsilon_I(\mathbf{k})-\mu)} \\
\mathcal{H}_0(\mathbf{k}) &= \begin{pmatrix} -\mu & -tg(\mathbf{k})^*-t'\sum_\alpha g_\alpha(\mathbf{k})^*\sigma_\alpha \\ -tg(\mathbf{k})-t'\sum_\alpha g_\alpha(\mathbf{k})\sigma_\alpha & -\mu \end{pmatrix} \\
H_{\alpha\mathbf{Q}}(\mathbf{k}) &= (J_2-J_1)\Delta_{\alpha\mathbf{Q}} \begin{pmatrix} 0 & -ig_\alpha(-\mathbf{k}+\mathbf{Q})\sigma_\alpha\sigma_y \\ ig_\alpha(\mathbf{k})\sigma_\alpha\sigma_y & 0 \end{pmatrix} \\
H_{0\mathbf{Q}}(\mathbf{k}) &= (J_1-J_2)\Delta_{0\mathbf{Q}} \begin{pmatrix} 0 & -i\sigma_y g(-\mathbf{k}+\mathbf{Q}) \\ i\sigma_y g(\mathbf{k}) & 0 \end{pmatrix}
\end{aligned} \tag{3.5.8}$$

in which $G_0(\omega,\mathbf{k})$ is the Green function for the band electron with momentum $\mathbf{k}$; $\epsilon_I(\mathbf{k})$ and $P_I(\mathbf{k})$ are respectively the band energy and band projector for the band with the index I. $\mathcal{H}_0(\mathbf{k})$ is the Hamiltonian for the free spin-orbit coupling model and $H_{\alpha\mathbf{Q}}(\mathbf{k})$ is the Hamiltonian for the triplet pairing α with momentum $\mathbf{Q}$. σ_α are the Pauli matrices for the spin subspace. We notice that when $\alpha=0$ and $\mathbf{Q}=0$ we have the normal BCS Green function. Then we can calculate the free energy for the superconductivity and expand the free energy by taking the superconductivity $H_{\alpha\mathbf{Q}}(\mathbf{k})$ as a perturbation:

$$F(\mathbf{Q},\mu,T) = -k_BT\ln Z(\mathbf{Q},\mu,T) = -k_BT\sum_{\omega,\mathbf{k}}\mathrm{Tr}\ln[G_\alpha^{-1}(\omega,\mathbf{k},\mathbf{Q})]+\frac{3N}{4}(J_1+J_2)(|\Delta_0|^2+|\Delta_\alpha|^2) \tag{3.5.9}$$

Using the fact that $\ln(1+x)=x-\frac{1}{2}x^2-...-\frac{1}{n}x^n-....$ the lowest order non zero term is the second order Landau expansion, which represents the 1-loop corrrection.

$$\begin{aligned}
&F^\alpha_{BCS}(\mathbf{Q},\mu,T) \\
&= -\sum_{\omega,\mathbf{k}} k_BT\,\mathrm{Tr}[G_0(\omega,\mathbf{k})H_{\alpha\mathbf{Q}}(\mathbf{k})G_0(-\omega,-\mathbf{k}+\mathbf{Q})H^H_{\alpha\mathbf{Q}}(\mathbf{k})] + \frac{3N}{4}(J_1+J_2)(|\Delta_0|^2+|\Delta_\alpha|^2) \\
&= \lim_{\eta\to 0}\sum_{\omega,\mathbf{k},I,J}\frac{1-n_f(\epsilon_I(\mathbf{k})-\mu)-n_f(\epsilon_J(-\mathbf{k}+\mathbf{Q})-\mu)}{\epsilon_I(\mathbf{k})+\epsilon_J(-\mathbf{k}+\mathbf{Q})-2\mu+i\eta}\mathrm{Tr}[P_I(\mathbf{k})H_{\alpha\mathbf{Q}}(\mathbf{k})P_J(-\mathbf{k}+\mathbf{Q})H^H_{\alpha\mathbf{Q}}(\mathbf{k})] \\
&+\frac{3N}{4}(J_1+J_2)(|\Delta_0|^2+|\Delta_\alpha|^2),
\end{aligned} \tag{3.5.10}$$

in which I, J and $\epsilon_I(\mathbf{k}), \epsilon_J(-\mathbf{k}+\mathbf{Q})$ are the indices and energies for the bands, and $P_I(\mathbf{k}), P_J(-\mathbf{k}+\mathbf{Q})$ the correspondent band projectors and $n_f(\epsilon_I(\mathbf{k})-\mu)$ is the Fermi-Dirac distribution.

3.5.1 The Spin-Orbit Coupling Limit $t = J_1 = 0$

We consider at the first place the J_2 Kitaev-Heisenberg limit in which $t=0$, $t'\neq 0$, and to the second order the free energy behaves as:

$$F^\alpha_{BCS}(\mathbf{Q},\mu,T)_{t=0} = -\chi_\alpha(\mathbf{Q},\mu,T)_{t=0}|\Delta_{\alpha\mathbf{Q}}|^2 \tag{3.5.11}$$

We show in figure 3.12 the spin triplet susceptibility $\chi_\alpha(\mathbf{Q},\mu,T)$ as a function of $\mathbf{q}=\frac{\mathbf{Q}}{2}$ in the first Brillouin zone at temperature $k_BT=0.01t'$ for $t=0, t'=1$, in which we can remark

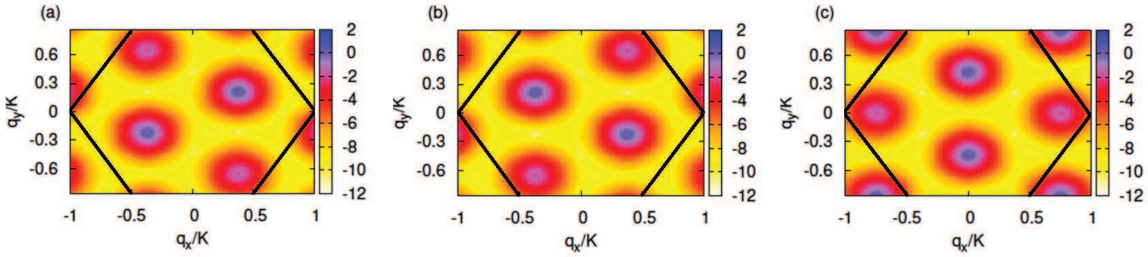

Figure 3.12: Triplet susceptibility $\chi_\alpha(\mathbf{Q},\mu,T)_{t=0}$ $\alpha=x,y,z$ as a function of $\mathbf{q}=\frac{\mathbf{Q}}{2}$ in the first Brillouin zone at quarter-filling. The susceptibility of spin triplet pairing (a) Δ_x, (b) Δ_y and (c) Δ_z at temperature $k_BT=0.01t'$ for $t=0,t'=1$.

the spin-triplet Cooper pairs condensates. The spin-triplet condensates $\Delta_{\alpha\mathbf{Q}}$ susceptibility $\chi_\alpha(\mathbf{Q},\mu,T)$ peaks at wave vector $\mathbf{q}_\alpha=\frac{\mathbf{Q}_\alpha}{2}$ which coincides with the symmetry centers of the spin-orbit coupling model shown in Fig. 3.10 left panel. We observe the $\pi/3$ symmetry among the three condensate profile in their superconductivity susceptibility which is related to the inherent symmetry of a combination of spin rotation and spatial rotation of the original model.

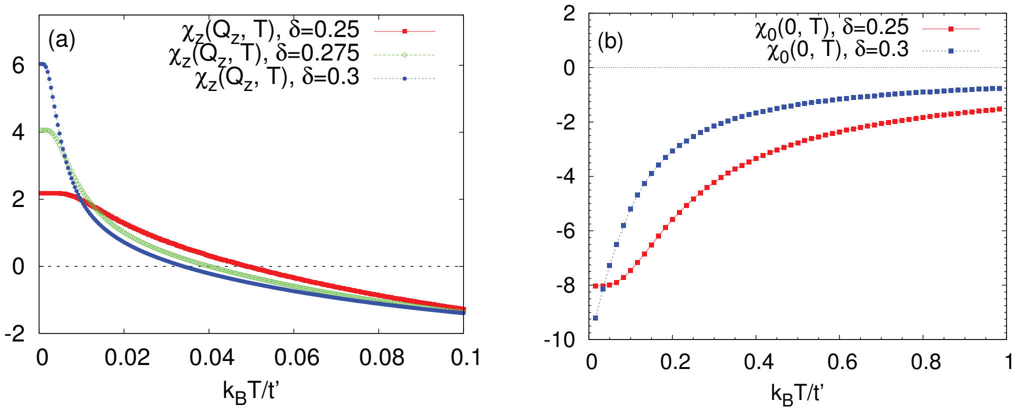

Figure 3.13: Pure spin-orbit coupling limit ($t=J_1=0$): (a) The susceptibility peak of Cooper pair $\chi_z(\mathbf{Q}_z,\mu,T)$ for spin triplet pairing Δ_z as a function of temperature at different dopings. (b): the susceptibility of singlet Cooper pair $\chi_0(0,\mu,T)$ Δ_0 as a function of temperature at different dopings.

At quarter-filling, the Fermi surface has particularly the conic structure with very limited density of electron pairs rendering the spin-triplet susceptibility finite at low temperature. Specifically, we can study the behavior of the susceptibility peak as a function of temperature at different doping by taking the representative susceptibility $\chi_z(\mathbf{Q}_z,\mu,T)$ for the spin-triplet $\Delta_{z\mathbf{Q}}$ as shown in the left panel of Fig. 3.13. We see that the susceptibility remains finite at quarter-filling $\delta=0.25$, while it tends to diverge at zero temperature when the doping diverts from quarter-filling where Fermi surface becomes arcs instead of mere points. We have also computed the singlet Cooper pair susceptibility as a function of temperature as shown in right panel of Fig. 3.13. The singlet susceptibility around the inversion symmetry center remains negative at all temperature, indicating that the spin singlet pairing is not favored.

We have checked that the singlet susceptibility remains negative in the spin-orbit limit $t = 0$ in the first Brillouin zone indicating that the spin-singlet pairing is not favored at this limit as shown in Fig. 3.13 right panel.

Still limited to the limit $t = 0$, we study the mutual interaction effects of the three condensates and we have calculated the box diagram by extending the Landau expansion to the fourth order, which designates the interaction of two Cooper pairs. We have the three kinds of bosons:

$$\begin{aligned} b^\dagger_{xq} &= \sum_{\mathbf{k}} c^\dagger_{\mathbf{k}\uparrow} d^\dagger_{-\mathbf{k}+\mathbf{q}\uparrow} - c^\dagger_{\mathbf{k}\downarrow} d^\dagger_{-\mathbf{k}+\mathbf{q}\downarrow} \\ b^\dagger_{yq} &= -i \sum_{\mathbf{k}} (c^\dagger_{\mathbf{k}\uparrow} d^\dagger_{-\mathbf{k}+\mathbf{q}\uparrow} + c^\dagger_{\mathbf{k}\downarrow} d^\dagger_{-\mathbf{k}+\mathbf{q}\downarrow}) \\ b^\dagger_{zq} &= -\sum_{\mathbf{k}} (c^\dagger_{\mathbf{k}\uparrow} d^\dagger_{-\mathbf{k}+\mathbf{q}\downarrow} + c^\dagger_{\mathbf{k}\downarrow} d^\dagger_{-\mathbf{k}+\mathbf{q}\uparrow}) \end{aligned} \tag{3.5.12}$$

The lowest order in the Feyman diagram with conserved particle number is the 4th order box diagram.

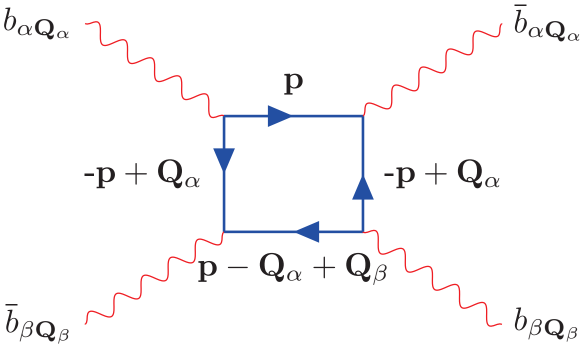

Figure 3.14: The Feyman diagram for two pairs of Cooper pairs which describes the interaction processes of the bosons from the three spin-triplet condensates in the pure spin-orbit limit of $t = J_1 = 0$.

In the box diagram describing the Cooper pair interaction, we can notice that there are two pairs of electrons entering the box and two leaving the box. Since the Cooper pair momentum is fixed to $\mathbf{Q}_\alpha$, the only possible terms from the 4th order expansion are $|\Delta_{x\mathbf{Q}_x}|^4$ and $|\Delta_{x\mathbf{Q}_x}\Delta_{y\mathbf{Q}_y}|^2$. Thereafter, we have the Landau expansion of the superconductivity to the 4th order:

$$\begin{aligned} F(\mu, T)_{t=0} = & - \chi_x(\mathbf{Q}_x, T)|\Delta_{x\mathbf{Q}_x}|^2 - \chi_y(\mathbf{Q}_y, T)|\Delta_{y\mathbf{Q}_y}|^2 - \chi_z(\mathbf{Q}_z, T)|\Delta_{z\mathbf{Q}_z}|^2 \\ & + C_1(|\Delta_{x\mathbf{Q}_x}|^4 + |\Delta_{y\mathbf{Q}_y}|^4 + |\Delta_{z\mathbf{Q}_z}|^4) + C_2(|\Delta_{x\mathbf{Q}_x}\Delta_{y\mathbf{Q}_y}|^2 + |\Delta_{x\mathbf{Q}_x}\Delta_{z\mathbf{Q}_z}|^2 + |\Delta_{y\mathbf{Q}_y}\Delta_{z\mathbf{Q}_z}|^2), \end{aligned} \tag{3.5.13}$$

in which C_1 and C_2 are positive numbers obtained from the calculation of the box diagram. Specifically the 4th order terms are:

$$\begin{aligned} \int d\omega d^2\mathbf{p} \frac{k_B T}{4} \, & \mathrm{Tr}[G_0(\omega, \mathbf{p}) H_{\alpha\mathbf{Q}_\alpha}(\mathbf{p}) G_0(-\omega, -\mathbf{k} + \mathbf{Q}_\alpha) H^H_{\beta\mathbf{Q}_\beta}(\mathbf{p}) \\ & G_0(\omega, \mathbf{p} - \mathbf{Q}_\alpha + \mathbf{Q}_\beta) H_{\beta\mathbf{Q}_\beta}(\mathbf{p}) G_0(-\omega, -\mathbf{p} + \mathbf{Q}_\alpha) H^H_{\alpha\mathbf{Q}_\alpha}(\mathbf{p})] \end{aligned} \tag{3.5.14}$$

When $\alpha = \beta$ we obtain the coefficient C_1 and when $\alpha \neq \beta$ we obtain the coefficient C_2. From the positiveness of the coefficient C_2, we deduce that mixing of the three bosons is not energetically favorable, and there is phase separation among the three type of bosons. Consequentially, wave function with one sole spin-triplet pairing $\Delta_{\alpha\mathbf{Q}_\alpha}$ lowers the free energy ($\alpha = x, y, z.$), namely the ground state wave function at zero temperature is three times degenerate in the real space represented in figure 3.15, in which the triplet pairings $\hat{\Delta}^{\alpha}_{ij}$ are represented by bold and dashed lines. (Red for X, green for Y and blue for Z) and dashed lines represents a π phase for the pairing. It is worth noticing that $\mathbf{q}\cdot\mathbf{R}_x + \mathbf{q}\cdot\mathbf{R}_y + \mathbf{q}\cdot\mathbf{R}_z \equiv 0 \bmod 2\pi$ for any vector $\mathbf{q}$. The Cooper pair momentum and the spatial modulation shown in figure 3.15 are related through the relation:

$$\mathbf{Q}_\alpha \cdot \mathbf{R}_\beta = \pi - \pi\delta_{\alpha\beta} \quad (\alpha, \beta = x, y, z), \tag{3.5.15}$$

in which $\delta_{\alpha\beta}$ is the Kronecker symbol.

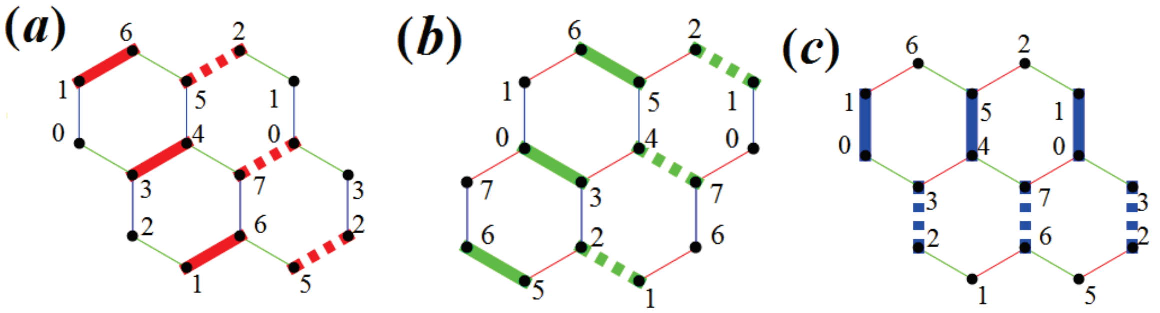

Figure 3.15: The graphical representation of the 3 times degenerate ground state for the wave function of the FFLO superconductivity. The bold line signifies a spin-triplet pairing on the link with the spin triplet type in correspondence with the type of the link ((a)X red, (b) Y green and (c) Z blue). The dashed line represents the same pairing but with a π phase attached. (opposite sign in the wave function)

In conclusion, the new symmetry centers of the band structure has brought into the superconductivity pairing a spatial modulation of π phase at the spin-orbit coupling limit $t = J_1 = 0$.

3.5.2 Near the Spin-Orbit Coupling Limit $t, J_1 \to 0$

Now, we inspect the effect of the normal hopping term proportional to t on the spin-orbit coupling which will make the centric symmetry around $\mathbf{q}_\alpha$ ($\alpha = x, y, z$) fade away gradually. The singlet condensate will also come into play because of the J_1 Heisenberg coupling favoring the singlet pairing. The normal hopping term will also open two gaps between the first and second as well as the third and fourth band, altering the conic structure around quarter-filling. The electron pair density at exact one quarter-filling is zero in this scenario, and one has to dope further more for the emergence of the superconductivity because of the gap opened by normal hopping. If we compare Fig. 3.16 with Fig. 3.12, we find that the triplet condensate in the pure spin-orbit limit is deeper than the triplet condensate with t,$J_1 \neq 0$ in the model.

The spin-singlet susceptibility is a negative in the first Brillouin zone, when the normal t hopping is turned on, a well around the inversion symmetry center O begins to form. This well constitutes a condensate around $t = 0.2$ ($t' = 0.8$) (See Fig. 3.17). With the increase of

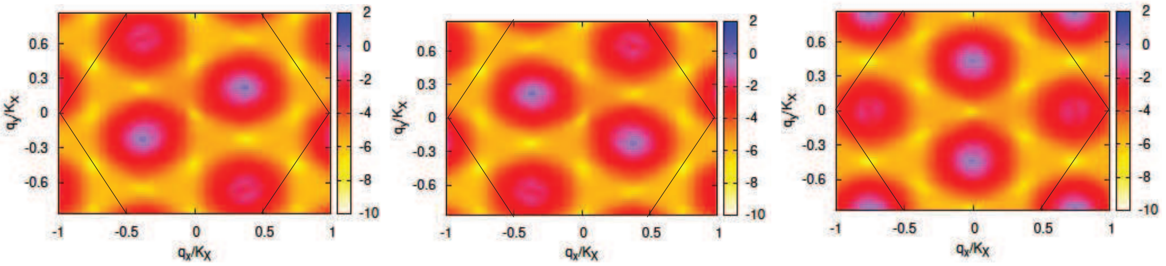

Figure 3.16: The suceptibility of the spin-triplet condensates when $t = 0.1$, $t' = 0.9$ and $T = 0.01(t + t')$ of the spin triplet superconductivity order parameter Δ_x on the left, Δ_y in the middle, Δ_z on the right.

the t term, the condensate turns deeper and deeper and the susceptibility becomes gradually positive, rendering the spin-singlet Cooper pairs stable. The condensate of the spin-singlet Cooper pair centers around $(0, 0)$ the inversion symmetry center indicating the singlet order parameter is uniform in space. Two spin-singlet condensate profiles are shown in Fig. 3.17 for $t = 0{,}1; t' = 0.9$ and $t = 0.2; t' = 0.8$.

The bosonic Cooper pair creation operator is written as:

$$b_0^\dagger = \sum_{\mathbf{k}} c^\dagger_{\mathbf{k}\uparrow} d^\dagger_{-\mathbf{k}\downarrow} - c^\dagger_{\mathbf{k}\downarrow} d^\dagger_{-\mathbf{k}\uparrow} \tag{3.5.16}$$

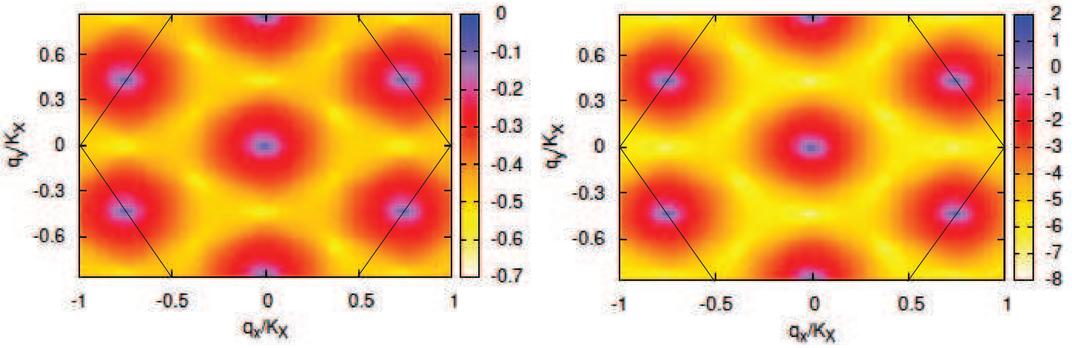

Figure 3.17: The suceptibility of the spin-singlet condensates when $t = 0.1$, $t' = 0.9$ (on the left) and $t = 0.2, t' = 0.8$ (on the right) and $T = 0.01(t + t')$.

With the presence of spin-singlet Cooper pairs, another effect that comes into play is the entanglement between the four different condensates: the three spin-triplet condensates and the spin singlet condensates. The spin-singlet condensate is gradually formed, and a new box-diagram becomes relevant. Since the sum of the Cooper pair momentum of the three condensates is zero, the new related processes involve the three triplet condensates and the singlet condensate which satisfies momentum conservation since $\mathbf{Q}_x + \mathbf{Q}_y + \mathbf{Q}_z = 0$. The processes involve the creation of one singlet Cooper pair $b_0^\dagger$ and one triplet Cooper pair $b^\dagger_{\alpha\mathbf{Q}_\alpha}$ and the destruction of Cooper pairs of two other triplet types $b_{\beta-\mathbf{Q}_\gamma}$ and $b_{\gamma-\mathbf{Q}_\gamma}$, entailing a crossing term of the form $\Delta_0 \Delta_{\alpha\mathbf{Q}_\alpha} \bar{\Delta}_{\beta-\mathbf{Q}_\beta} \bar{\Delta}_{\gamma-\mathbf{Q}_\gamma}$ $(\alpha \neq \beta \neq \gamma)$.

We will not pursue the Landau expansion here because of the complexity, but the consequence of this triplet-singlet mixture manifests in the fact that on a certain type of link there will be a coexistence of the modulated spin triplet pairing $\Delta_{\alpha\mathbf{Q}_\alpha}$ and the uniform spin-singlet pairing Δ_0.

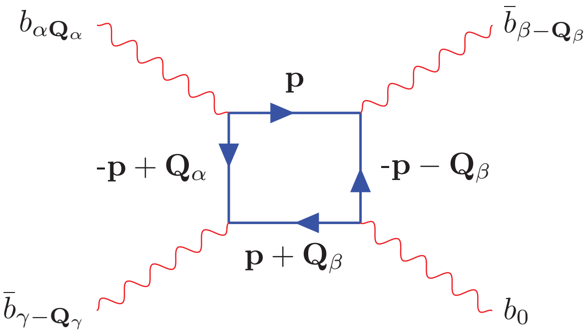

Figure 3.18: The Feyman diagram for two pairs of Cooper pairs which describes the interaction processes of the bosons from the three spin-triplet condensates and the singlet condensate when $t, J_1 \neq 0$. ($\alpha \neq \beta \neq \gamma$)

The t term will open up a gap to the Dirac band structure around quarter-filling making the dispersion relation parabolic rather than linear at the pure spin-orbit limit $t = J_1 = 0$. This will changes the density of states around quarter filling and affect the Cooper pair susceptibility for the spin triplet pairing as shown in figure 3.19. The susceptibility remains finite and decreases when t is turned on gradually.

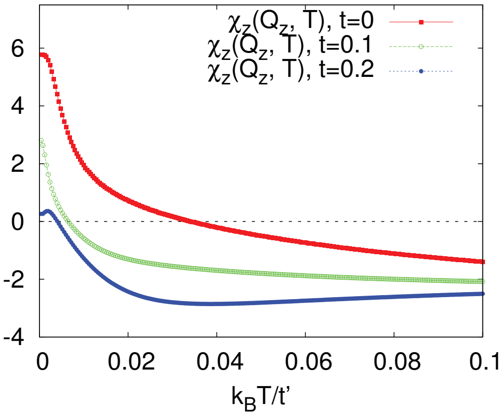

Figure 3.19: The susceptibility peak of Cooper pair $\chi_\alpha(\mathbf{Q}_\alpha, T)$ as a function of temperature at $\delta = 0.3$ with different value of t and $t' = 1 - t$.

3.6 Numerical Proofs of the FFLO Superconductivity

We have done exact diagonalizations for the Kitaev-Heisenberg model with different values of t, t' at different dopings and we fix the parametrization $J_1 = \frac{4t^2}{U}$, $J_2 = \frac{4t'^2}{U}$. (This numerical section is done in collaboration with Cécile Repellin and Nicolas Regnault.) We seek the trace of the FFLO superconductivity through the numerical spectra of the doped system on torus in the momentum space.

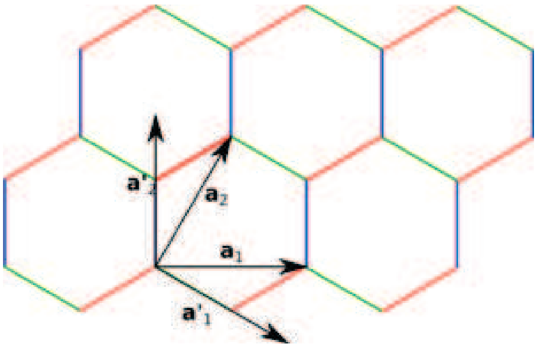

Figure 3.20: The geometric configuration of the exact diagonalization on torus with the primitive vectors noted as $\mathbf{a}_1$ and $\mathbf{a}_2$.

The geometry configuration of the system on torus is plotted in Fig. 3.20, with primitive wave vectors in the direct and reciprocal space denoted respectively as $\mathbf{a}_i$ (i=1, 2) and $\mathbf{a}'_i$ (i=1, 2). We numerically diagonalized the doped system and plot the energy levels in the different momentum sectors. On the discretized system of $N_x \times N_y$ plaquettes on torus, we will have thereafter N_x momentum sectors in the base of $\mathbf{a}'_1$ and N_y momentum sectors in the base of $\mathbf{a}'_2$, which leads to a total of $N_x \times N_y$ sectors. To represent the 2D numerical spectra in 1D, we adopt the Quantum Hall spectrum convention with the energy levels as a function of $k_x + N_x k_y$ in which N_x is the number of plaquettes in the x direction.

We can apply the Bloch theorem to analyze the footprints of the FFLO superconductivity. If we denote the three degenerate ground state with one Cooper pair as $|\Psi_x\rangle$, $|\Psi_y\rangle$ and $|\Psi_z\rangle$ for the spin-triplet x, y and z, we have:

$$\begin{cases} T_1 |\Psi_x\rangle = -|\Psi_x\rangle & T_2 |\Psi_x\rangle = -|\Psi_x\rangle & T_1T_2 |\Psi_x\rangle = |\Psi_x\rangle \\ T_1 |\Psi_y\rangle = -|\Psi_y\rangle & T_2 |\Psi_y\rangle = |\Psi_y\rangle & T_1T_2 |\Psi_y\rangle = -|\Psi_y\rangle \\ T_1 |\Psi_z\rangle = |\Psi_z\rangle & T_2 |\Psi_z\rangle = -|\Psi_z\rangle & T_1T_2 |\Psi_z\rangle = -|\Psi_z\rangle \end{cases} \tag{3.6.1}$$

We have: $T_i |\Psi\rangle = e^{i\mathbf{q}\cdot\mathbf{a}_i} |\Psi_i\rangle$ in which $\mathbf{q}$ is the momentum corresponding to the momentum sector of the ground state, we can therefore identify the three ground state Ansätze Ψ_x, Ψ_y and Ψ_z: $\mathbf{q}_x = (\pi, \pi)$, $\mathbf{q}_y = (\pi, 0)$ and $\mathbf{q}_z = (0, \pi)$. In the system with $N_x \times N_y$ plaquettes, N_x and N_y need to be even numbers so that the FFLO superconductivity is not frustrated and the three momentum sectors for the ground state wave function will be in $\mathbf{q}_x = (N_x/2, N_y/2)$, $\mathbf{q}_y = (N_x/2, 0)$ and $\mathbf{q}_z = (0, N_y/2)$. For example in Fig. 3.21, we have the ground state in the momentum sector $(1, 1)$, (1,0) and (0,1) for 2 and 6 particles while the spectrum with 4 particles is at quarter filling.

We can also calculate the pairing order parameter by diagonalizing the Hamiltonian numerically respectively for the half-filling system and the 2 holes doped case:

$$\Delta_\alpha = \langle\Psi_N| \hat{\Delta}_\alpha |\Psi_{N+2}\rangle \, \chi_\alpha = \langle\Psi_N| \hat{\chi}_\alpha |\Psi_N\rangle \quad \alpha = 0, x, y, z, \tag{3.6.2}$$

in which the subscript N and N+2 are the number of electrons for the wave function. Using this procedure, we have calculated the superconductor pairing order parameter on different links. For the numerical leading order (other order parameters are at least ten times smaller),

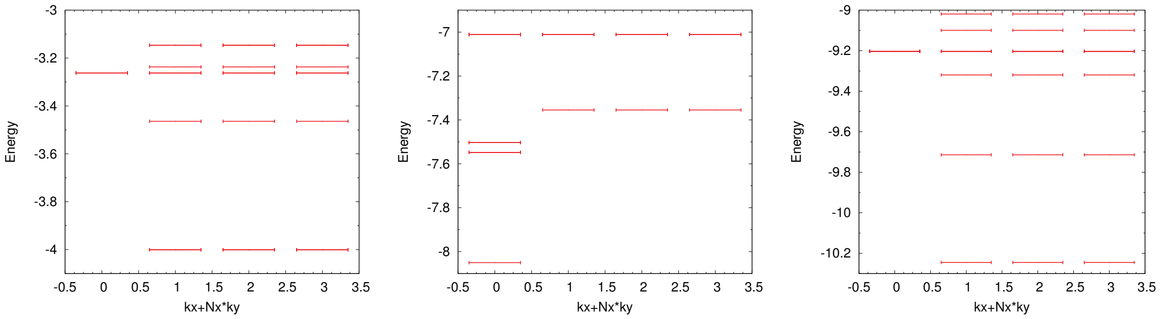

Figure 3.21: Spectrum of 2×2 plaquettes on torus when $t=0, t'=1$ with 2, 4 and 6 particles.

we have:

$$\begin{cases} |\Psi_6^1\rangle = (\hat{\Delta}_{16}^x - \hat{\Delta}_{52}^x + \hat{\Delta}_{34}^x - \hat{\Delta}_{70}^x)\,|\Psi_8\rangle \\ |\Psi_6^2\rangle = (\hat{\Delta}_{03}^y - \hat{\Delta}_{21}^y + \hat{\Delta}_{65}^y - \hat{\Delta}_{47}^y)\,|\Psi_8\rangle \\ |\Psi_6^3\rangle = (\hat{\Delta}_{01}^z - \hat{\Delta}_{23}^z + \hat{\Delta}_{45}^z - \hat{\Delta}_{67}^z)\,|\Psi_8\rangle \end{cases} \tag{3.6.3}$$

in which $|\Psi_6\rangle$ is the wave function for the 2 holes doped system and $|\Psi_8\rangle$ is the half-filling ($\delta=0$) system and the numerotation of the sites is represented in Fig. 3.15. It is worth noting that the spin triplet pairing operators are antisymmetric: $\hat{\Delta}_{ij}^\alpha = -\hat{\Delta}_{ji}^\alpha$. The expectation value of the superconductor pairing order parameter and the density order parameters are shown in figure 3.22, in which we parametrize as $t'=1-t, J_1=\frac{4t^2}{U}, J_2=\frac{4t'^2}{U}, U=6$. The numerical results confirm the emergence of triplet superconductivity with alternative patterns with π phase in the direct space when $t<t'$.

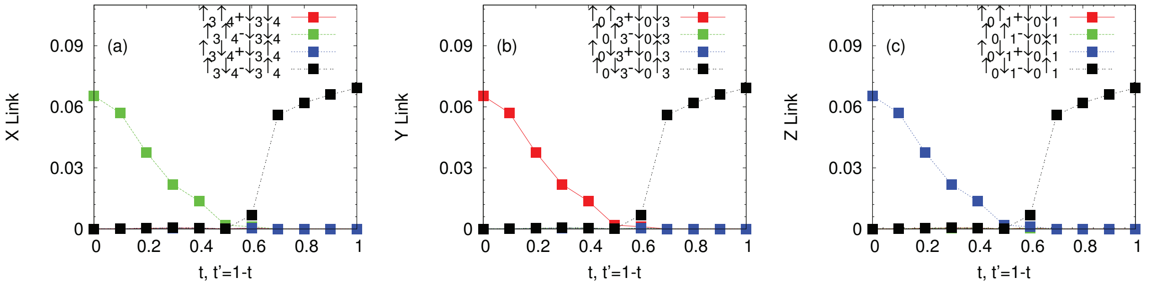

Figure 3.22: Order parameter calculated by equation 3.6.2 for the 4 plaquette system with periodic conditions: The sum of module square of the order parameter as a function of t. $t, t'=1-t, J_1=\frac{4t^2}{U}, J_2=\frac{4t'^2}{U}, U=6$. on different links. The triplet pairing when $t<1/2$ and singlet when $t>1/2$.

The number of Cooper pairs in the system is also influential on the ground state momentum sector when the system is bigger. For odd number of Cooper pairs, the total momentum for the FFLO wave function is: $Q_{2n+1}=(2n+1)\mathbf{q}_{x,y,z}\equiv \mathbf{q}_{x,y,z}$ mod2π while for even number of Cooper pairs the total momentum is $Q_{2n}=2n\mathbf{q}_{x,y,z}\equiv 0$ mod2π. We can spot this effect of the number of Cooper pairs in the spectrum of exact diagonalization on the 4×2 plaquettes on torus shown in Fig. 3.23.

We see from Fig. 3.23 that the ground state momentum sectors are $(2,0)$, (2,1) and $(0,1)$ in the spectra of 2, 6, 10 and 14 particles with the degeneracy lifted because of the asymmetry

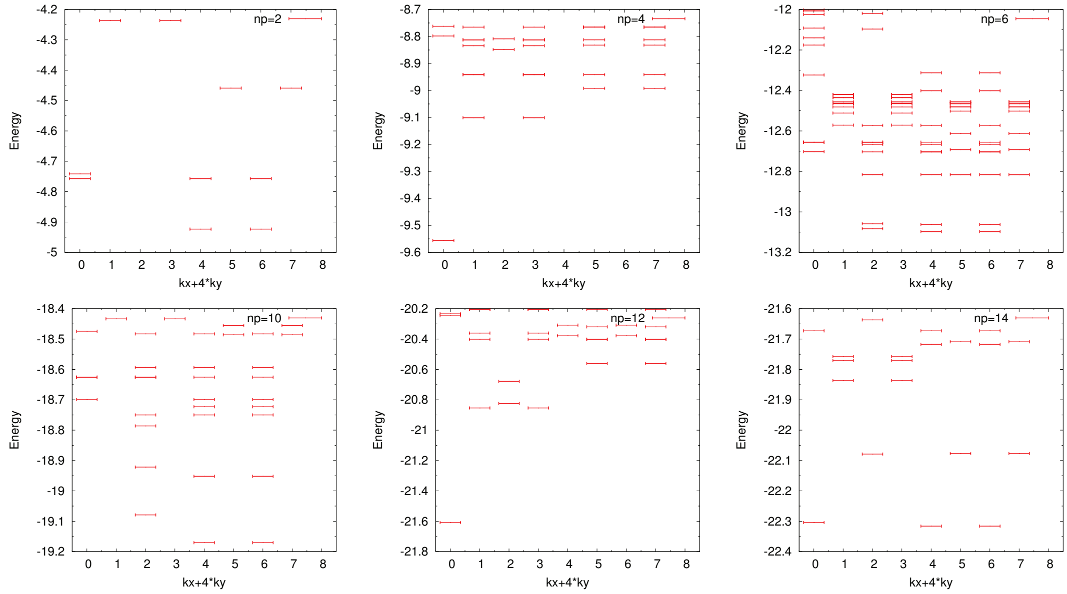

Figure 3.23: Exact diagonalization spectrum for 2, 4, 6, 10, 12 and 14 particles (np as number of particles) on the 4×2 plaquettes on torus at the pure spin-orbit coupling limit $t = 0, t' = 1$.

of the system. The side with 4 plaquettes is longer than the side with 2 plaquettes elevating the energy level of the momentum sector $(2, 0)$ compared to sectors $(0, 1)$ and $(2, 1)$. The spectra of 4 and 12 particles have ground state momentum sector in $(0, 0)$ with even number of Cooper pairs. The degeneracy-lift because of the elongated geometry is restored for the geometry with 4×4 plaquettes on torus as shown in Fig. 3.24 whose numerical degeneracy is exact for the states in the momentum sector $(2, 0)$, $(0, 2)$ and $(2, 2)$.

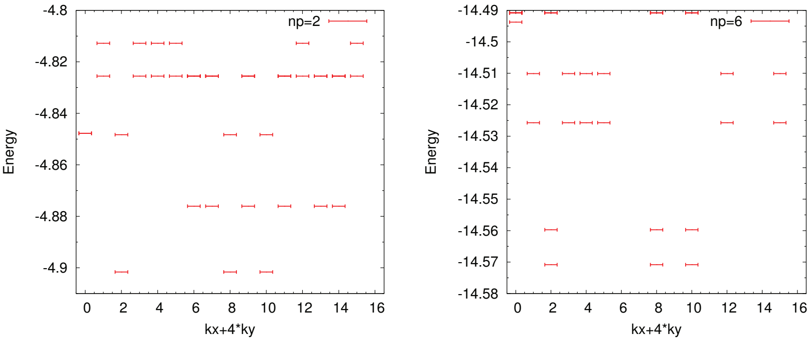

Figure 3.24: Exact diagonalization spectrum for 2 and 6 particles on the 4×4 plaquettes on torus with ground state momentum sector $(2, 0)$, $(0, 2)$ and $(2, 2)$.

One striking effect that we observe is the two very close energy levels in each of the three ground state momentum sectors for FFLO states in 6 particle spectrum for the 4×2 and 4×4 plaquette system on torus. This quasi-degeneracy exists for systems beyond quarter-doping while such phenomenon is absent for system below quarter doping. In order to clarify this point, we have studied the first gap as a function of the coupling constant J_2 as shown in Fig.

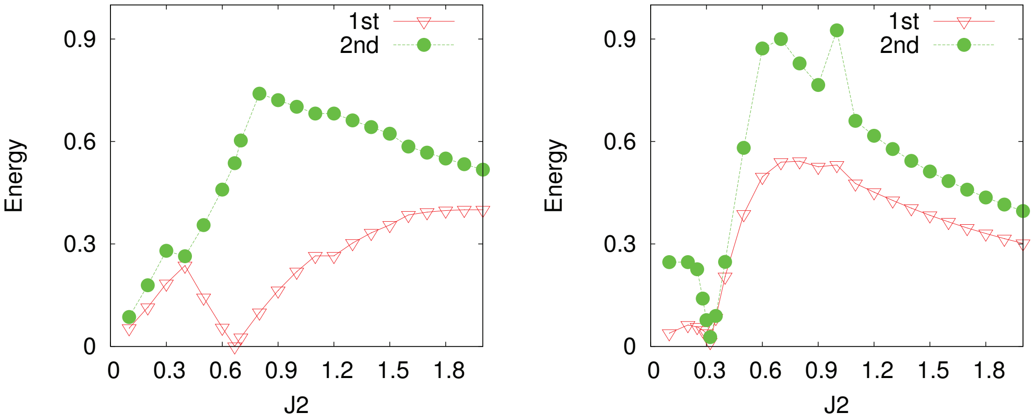

Figure 3.25: The first and second gap as a function of J_2 for doping 2 holes (left) and doping 2 electrons (right) from quarter-filling from diagonalisation of 2×2 plaquettes on torus geometry.

3.25 in the momentum sector of $(0, \pi)$ in the limit of pure spin-orbit coupling $t = J_1 = 0$. When J_2 is very big with regard to t' (we have fixed $t' = 1$), we are close to the infinite-correlated limit in which holes are bound together by the J_2 term. When J_2 is small, the kinetic terms dominate the system, and the motion of the doped holes are determined by the band electron validating the theoretical Cooper pair susceptibility analysis provided in the previous section. We see that around $J_2 = 0.67 (U = 6)$, there is a gap closure for the superconductivity, separating the two limits. Whether this band closure is related to the change of topology of the superconductivity is still an open question because of the existence of several bands separated by small gaps in the Bogoliubov De Gennes spectrum.

3.7 Conclusion

In this chapter, we have studied a model in which the spin-orbit coupling lies on the nearest-neighbours according to [43, 113] as shown in equation 3.1.2. The concerned model hosts a zigzag magnetic order with anti-ferromagnetic Kitaev coupling and ferromagnetic Heisenberg coupling, which is different from the previously studied model by Scherer et al [41], in which they have taken the Kitaev coupling to be ferromagnetic and they have found $p - wave$ superconductivity.

The strong spin-orbit coupling endows the electron a band structure with new symmetry centers apart from the one which corresponds to the inversion symmetry and this property holds even when the time-reversal symmetry is observed at the pure spin-orbit coupling limit $t = J_1 = 0$. Electrons around these new symmetry centers form spin-triplet superconductivity pairing, and the condensation of these superconductor Cooper pairs around the non-trivial Cooper pair momentum in correspondance with these new symmetry centers results in a spatial modulation of the superconductivity order parameter. We have analyzed the Cooper pair susceptibility of these spin triplets states around quarter-filling and have obtained the profile of the triplet Cooper pair condensates. Numerical evidences of the FFLO superconductivity have also been provided using exact diagonalization. The spectral low energy hierarchy in the momentum space coincides with the predicted FFLO wave function through the analysis by the Bloch theorem. Therefore, iridates provide a possible realization of the FFLO superconductivity other than the cold atom system[188] without breaking the time-reversal symmetry. The separation of the three spin-triplet condensates in the momentum space leads to the three times degenerate ground state.

The open question is the topology of such superconductivity, which is difficult to tackle because of several Bogoliubov De Gennes bands separated by small gaps. The spin-1 triplet superconductivity brings also possibilities of emergence of Majorana fermions in such systems.

Chapter 4

Engineering Topological Mott Phases

The quest of topological phases in the absence of a net uniform magnetic field, has attracted a great attention recently in the field of condensed matter physics, in connection with the spin-orbit coupling and artificial gauge fields [173, 174, 175, 176]. The realization of topological phases has become important due to their physical properties such as the edge transport and potential applications for spintronics [177]. The HgTe quantum well and three-dimensional Bismuth analogues have been a perfect area for the quantum spin Hall effect and topological band insulators [11, 13, 14, 178]. In addition, the quantum anomalous Hall effect and its version on the honeycomb lattice, the Haldane model [10], have been observed with photons [179, 180], cold atom systems [181] and magnetic topological insulators [182]. Engineering topological phases through interactions is also interesting on its own. An example of topological band insulators induced by interactions, resulting in topological Mott insulators, has also been proposed by Raghu et al. [202] on the honeycomb lattice. This scenario requires however that the next-nearest-neighbour interaction exceeds the nearest-neighbour repulsion [202, 203, 204, 205]. In this chapter, we propose a possible realisation of the topological Mott phase in a Fermion-Fermion mixture. A similar two-fluid model has been previously proposed on the honeycomb lattice [225], however our model insists on the honeycomb band structure of the fast fermion: this leads to an RKKY interaction connecting the Dirac points in the first Brillouin zone, which will open a gap around Dirac points of the slow fermion inducing potentially a topological phase. (See figure 4.1)

4.1 RKKY Interaction

Nuclear spins interact with each other via the conduction electrons in metals and the correlation energy between the two nuclear spins is referred to as Ruderman-Kittel-Kasuya-Yosida or RKKY interaction [214]. Since the conduction electron has the behavior of Bloch wave functions, the RKKY interaction has an oscillating profile. We try to make use of this interaction for the engineering of a topological Mott phase [202]. We consider here a system consisting of two Fermion species on the honeycomb lattice coupled together by an on-site interaction, with one fast species and one slow species. The fast species plays effectively the same role as the conduction electrons, while the slow species plays the role of the nuclear spins. The fast species will induce an effective interaction between the electrons of the slow species, with the nature of RKKY interaction. Specifically, we can write down the Hamiltonian of the system:

$$H = -t_c \sum_{\langle i,j \rangle} c_i^\dagger c_j + \mu_c \sum_i c_i^\dagger c_i - t_f \sum_{\langle i,j \rangle} f_i^\dagger f_j + g_{cf} \sum_i c_i^\dagger c_i f_i^\dagger f_i \tag{4.1.1}$$

in which the fermion c is the fast species and the fermion f the slow species characterized by the fact that $t_c \gg t_f$. The on-site interaction between the two copies of the fermions is proportional to g_{cf}^2. In order to work out the RKKY interaction for the fermion, we diagonalize firstly the fermion c. We write down the Green function for c particles with the projector $P_c(k)$:

$$\begin{gathered} G_c(\omega,\mathbf{k}) = \frac{P_c(\mathbf{k})}{\omega-(\epsilon_c(\mathbf{k})-\mu_c)+i\eta} \quad P_c(\mathbf{k}) = \frac{1}{2}(1+\tau_x\cos\theta_k+\tau_y\sin\theta_k) \\ \theta_k = \arctan g(\mathbf{k}) \quad g(\mathbf{k}) = \sum_j e^{i\mathbf{k}\cdot\delta_j} \quad \epsilon_c(\mathbf{k}) = -t_c|g(\mathbf{k})|, \end{gathered} \tag{4.1.2}$$

in which $\delta_1 = (\frac{\sqrt{3}}{2},\frac{1}{2})$, $\delta_2 = (-\frac{\sqrt{3}}{2},\frac{1}{2})$ and $\delta_3 = (0,-1)$ are the three vectors connecting the nearest-neighbours and τ_x, τ_y are the Pauli matrices in the sublattice subspace. We have the band structure of the graphene here. Thereafter, we write down the interaction between the two species and substitute $c_k^\dagger c_k$ by its mean value $\left\langle c_k^\dagger c_k \right\rangle = G_c(\omega,\mathbf{k})$. Specifically, if we denote I J as sub-lattice index and τ_α as Pauli matrices for the sub-lattices, then after the Fourier transformation, we will have:

$$g_{cf}\sum_i c_i^\dagger c_i f_i^\dagger f_i = g_{cf}\sum_{\mathbf{k}_1,\mathbf{k}_2,\mathbf{p}} c^\dagger_{\mathbf{k}_1 I} c_{\mathbf{k}_1+\mathbf{p}I} f^\dagger_{\mathbf{k_2}I} f_{\mathbf{k}_2-\mathbf{p}I} \tag{4.1.3}$$

To the second order, we can treat the interaction as :

$$\begin{aligned} & g_{cf}^2 \sum_{\mathbf{k},\mathbf{k}_1,\mathbf{k}_2,\mathbf{q}} c^\dagger_{\mathbf{k}I} c_{\mathbf{k}+\mathbf{q}I} c^\dagger_{\mathbf{k}+\mathbf{q}J} c_{\mathbf{k}J} f^\dagger_{\mathbf{k}_1 I} f_{\mathbf{k}_1-\mathbf{q}I} f^\dagger_{\mathbf{k}_2 J} f_{\mathbf{k}_2+\mathbf{q}J} \\ =& g_{cf}^2 \sum_{\omega_1,\omega_2}\sum_{\mathbf{k},\mathbf{k}_1,\mathbf{k}_2,\mathbf{q}} \frac{1}{\omega_1-(\epsilon_c(\mathbf{k})-\mu_c)+i\eta}\frac{1}{\omega_2-(\epsilon_c(\mathbf{k}+\mathbf{q})-\mu_c)-i\eta}\alpha_{IJ}(\mathbf{k},\mathbf{q}) f^\dagger_{\mathbf{k}_1 I} f_{\mathbf{k}_1-\mathbf{q}I} f^\dagger_{\mathbf{k}_2 J} f_{\mathbf{k}_2+\mathbf{q}J} \\ =& g_{cf}^2 \sum_{\omega}\sum_{\mathbf{k},\mathbf{k}_1,\mathbf{k}_2,\mathbf{q}} \frac{n_f(\epsilon_c(\mathbf{k}+\mathbf{q}))-n_f(\epsilon_c(\mathbf{k}))}{\omega+\epsilon_c(\mathbf{k}+\mathbf{q})-\epsilon_c(\mathbf{k})+i\eta}\alpha_{IJ}(\mathbf{k},\mathbf{q}) f^\dagger_{\mathbf{k}_1 I} f_{\mathbf{k}_1-\mathbf{q}I} f^\dagger_{\mathbf{k}_2 J} f_{\mathbf{k}_2+\mathbf{q}J} \\ & \alpha_{AA} = \alpha_{BB} = 1 \quad \alpha_{AB} = e^{i(\theta_{k+q}-\theta_k)} \quad \alpha_{BA} = e^{-i(\theta_{k+q}-\theta_k)} \end{aligned} \tag{4.1.4}$$

in which $\mathbf{q}$ is the momentum transfer, and second order perturbation is actually a one-loop expansion. We can write down the dynamical RKKY interaction:

$$\chi_{IJ}(\Omega,\mathbf{q},\mu_c) = \lim_{\eta\to 0}\sum_{\mathbf{k}} \frac{n_f(\epsilon_c(\mathbf{k}+\mathbf{q}))-n_f(\epsilon_c(\mathbf{k}))}{\Omega+\epsilon_c(\mathbf{k}+\mathbf{q})-\epsilon_c(\mathbf{k})+i\eta}\alpha_{IJ}(\mathbf{k},\mathbf{q}), \tag{4.1.5}$$

in which $n_f(\epsilon_c(\mathbf{k}))$ is the Fermi-Dirac distribution $n_f(\epsilon_c(\mathbf{k})) = \frac{1}{1+\exp(\beta(\epsilon_c(\mathbf{k})-\mu_c))}$. We denote the susceptibility on the same sublattice as $\chi_{II}(\Omega,\mathbf{q},\mu_c) = \chi_{AA}(\Omega,\mathbf{q},\mu_c) = \chi_{BB}(\Omega,\mathbf{q},\mu_c)$ and the sublattice on different lattice as $\chi_{AB}(\Omega,\mathbf{q},\mu_c) = \chi_{BA}(\Omega,\mathbf{q},\mu_c)^*$.

We have plotted in Fig. 4.1 the static RKKY susceptibility on the same sublattice $\chi_{II}(\Omega,\mathbf{q},\mu_c)$ at three different chemcial potential ($\mu_c = 0.6t_c, \mu_c = 0.8t_c, \mu_c = 0.9t_c, \mu_c = t_c$ in each row) as a function of $\mathbf{Q} = \frac{\mathbf{q}}{2}$ in the first Brillouin zone. We see that at quarter filling $\mu_c = t_c$, the RKKY interaction has its peaks around the nesting vectors for the Van Hove singularity. These vectors are:

$$\mathbf{Q}_1 = (0,\frac{4\pi}{3}) \quad \mathbf{Q}_2 = (\frac{2\pi}{\sqrt{3}},\frac{2\pi}{3}) \quad \mathbf{Q}_3 = (\frac{2\pi}{\sqrt{3}},-\frac{2\pi}{3}) \tag{4.1.6}$$

When doping is lower than quarter-filling ($\mu_c = -0.6t_c$ and $\mu_c = -0.8t_c$), we spot peaks smeared around the Dirac cones. Near the quarter-filling $\mu_c = -0.9t_c$ the smeared patterns around Dirac cones connects together forming smeared patterns around the nesting vectors. The RRKY interaction will connect electrons for the Fermion f around Dirac cones together, we will show that this RKKY interaction profile opens a gap around Dirac cones, then attaching a topological non-trivial property to the system.

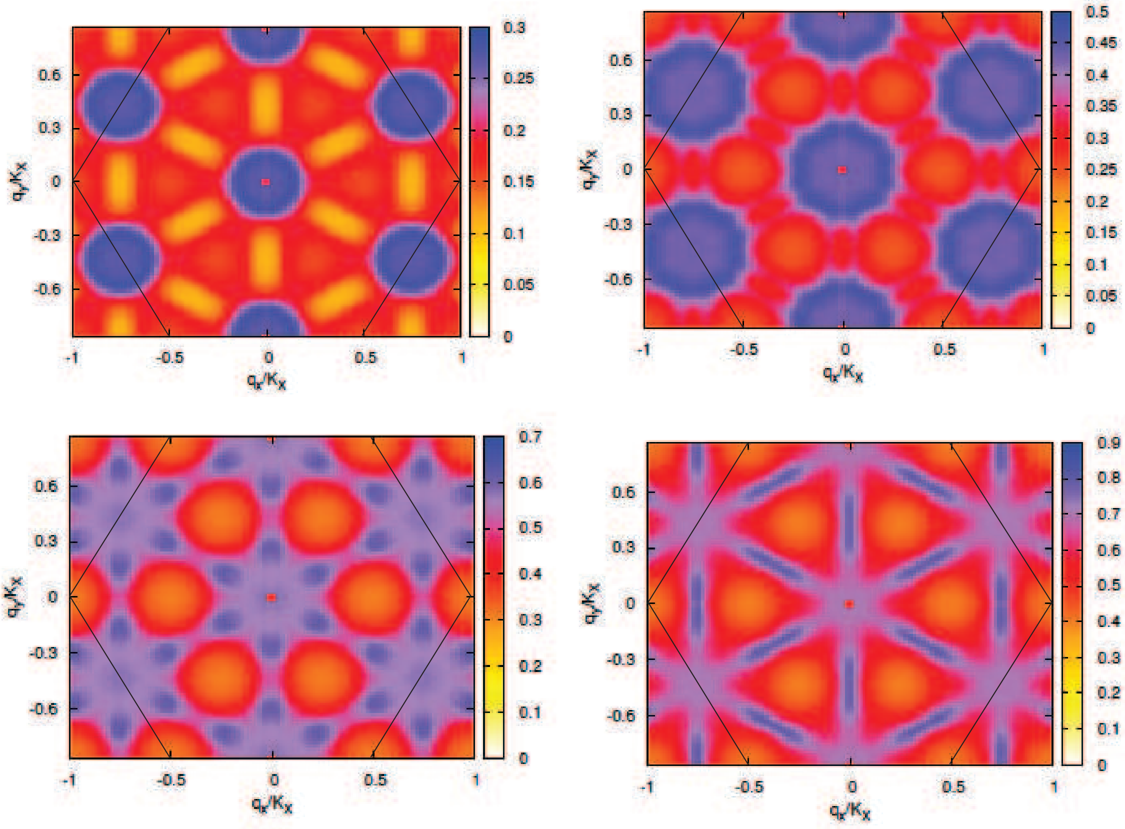

Figure 4.1: The RKKY susceptibility $\chi_{II}(\mathbf{q}, \mu_c, \eta)$ as a function of $\mathbf{Q} = \frac{\mathbf{q}}{2}$ with $\mu_c = -0.6t_c$ (left upper panel), $\mu_c = -0.8t_c$ (right upper panel), $\mu_c = -0.9t_c$ (left down panel) and $\mu_c = -t_c$ (right down panel).

4.2 Haldane Mass Induced by the RKKY Interaction.

In order to study the influence of RKKY interaction upon the fermion f, we apply the Lagrangian formalism to describe the behavior of the slow fermion species f. The bare Green function of the fermion f is the propagator of electrons in graphene system, and the RKKY interaction might add correction to the Green function.

$$\begin{aligned}\mathcal{L}_f =& \sum_{\mathbf{k}} \Psi^\dagger_{fk}[\omega_f - t_f(\tau_x \Re e + \tau_y \Im m) g(\mathbf{k}) - \mu_f]\Psi_{fk} \\ & - i\frac{g_{cf}^2}{2} \sum_{\omega_1,\omega_2,\Omega,\mathbf{k}_1,\mathbf{k}_2,\mathbf{q}} \chi_{IJ}(\Omega, \mathbf{q}, \mu_c) f^\dagger_{\omega_1 \mathbf{k}_1 I} f_{\omega_1 - \Omega \mathbf{k}_1 - \mathbf{q} I} f^\dagger_{\omega_2 \mathbf{k}_2 J} f_{\omega_2 + \Omega \mathbf{k}_2 + \mathbf{q} J}\end{aligned} \tag{4.2.1}$$

in which $\Psi_{fk} = (f^\dagger_{\mathbf{k}A}, f^\dagger_{\mathbf{k}B})$.

We first look at the effect of the self-interaction in the adjustment of the chemical potential namely terms proportional to the Fermion density $n_{kI} = f^\dagger_{kI} f_{kI}$: when $\mathbf{q} \to 0$ and $I = J$ we have the first contribution $g_{cf}^2 \chi(0, 0, \mu_c) \sum_{k \neq k'} n_k n_{k'}$, when $k = k' + q$ we have the second contribution $g_{cf}^2 \sum_{\mathbf{k},\mathbf{q}\neq 0} \chi(0, \mathbf{q}, \mu_c) n_k (1 - n_{k-q})$. We have the effective chemical potential:

$$\tilde{\mu}_f = \mu_f - g_{cf}^2 [\chi(0, 0, \mu_c) - \frac{1}{N} \sum_{\mathbf{q}\neq 0, \mu_c, \eta} \chi(0, \mathbf{q}, \mu_c)] \langle n_k \rangle + \frac{g_{cf}^2}{2N} \sum_{k,\mathbf{q}} \chi(0, \mathbf{q}, \mu_c) \tag{4.2.2}$$

in which $\langle n_k \rangle$ is the expectation value of the electron density. The modification to the potential is negligible when $g_{cf} < 20\sqrt{t_c t_f}$, then the chemical potential modification is $(|\tilde{\mu}_f - \mu_f| < 0.2 t_f)$. We can try to choose a filling for the electron f so that $\tilde{\mu}_f = 0$ so that the fermi surface excitations are around the Dirac cones (Fermi surface of the half-filled graphene).

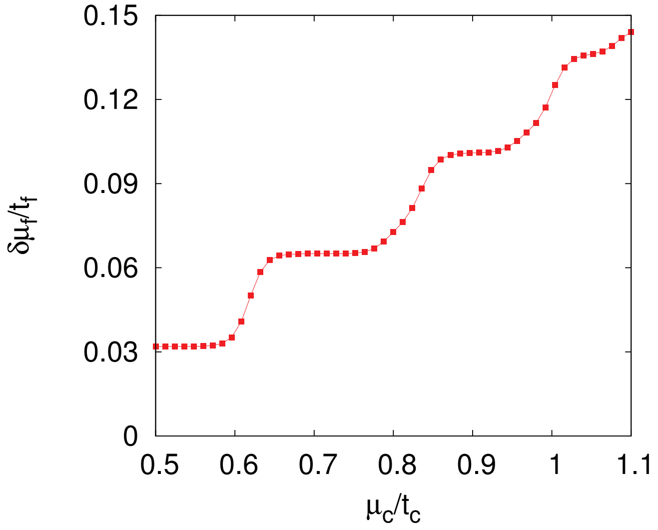

Figure 4.2: $\delta\mu_f/t_f = (\tilde{\mu}_f - \mu_f)/t_f$ as a function of μ_c/t_c when $g_{cf} = 20\sqrt{t_c t_f}$ which is much bigger than the critical value of g_{cf} for the instability threshold.

Now we do the Fock approximation to the interaction term, namely replacing the four-body interaction term by the Green functions. We can thereafter write down the Dyson equation which entails the self-consistent equation:

$$\begin{aligned} G_f(\omega, \mathbf{k})^{-1}_{IJ} &= G_0(\omega, \mathbf{k})^{-1}_{IJ} - i \sum_{\Omega, q} \frac{g_{cf}^2}{2} \chi(\Omega, \mathbf{q}, \mu_c)_{IJ} G_f(\omega + \Omega, \mathbf{k} + \mathbf{q})_{JI} \\ G_0(\omega, \mathbf{k})^{-1} &= \omega - t_f(\tau_x \Re e + \tau_y \Im m) g(\mathbf{k}) \end{aligned} \tag{4.2.3}$$

We can make an adiabatic approximation for the dynamical RKKY susceptibility by replacing it with the static susceptibility:

$$\chi(\Omega, \mathbf{q}, \mu_c)_{IJ} \simeq \chi(0, \mathbf{q}, \mu_c)_{IJ} \tag{4.2.4}$$

We can then simplify the self-consistent equation:

$$G_f(\omega, \mathbf{k})^{-1}_{IJ} = G_0(\omega, \mathbf{k})^{-1}_{IJ} + \sum_{\mathbf{q}} \frac{g_{cf}^2}{2} \chi_{IJ}(0, \mathbf{q}, \mu_c) [2P f_{JI}(\mathbf{k} + \mathbf{q}) - \delta_{JI}] \tag{4.2.5}$$

We can write down an Ansatz of the Green function $G_f(\omega, \mathbf{k})$ such that:

$$\begin{aligned} G_f(\omega,\mathbf{p})^{-1} &= \omega - a(\mathbf{p})\tau_x - b(\mathbf{p})\tau_y - c(\mathbf{p})\tau_z \quad a(\mathbf{p}), b(\mathbf{p}), c(\mathbf{p}) \in \mathbf{R} \\ G_f(\omega,\mathbf{p}) &= \frac{P_-(\mathbf{p})}{\omega + E(\mathbf{p}) + i\eta} \quad E(\mathbf{p}) = \sqrt{a^2(\mathbf{p}) + b^2(\mathbf{p}) + c^2(\mathbf{p})} \\ P_-(\mathbf{p}) &= \frac{1}{2}[1 - \frac{a(\mathbf{p})\tau_x + b(\mathbf{p})\tau_y + c(\mathbf{p})\tau_z}{E(\mathbf{p})}] \end{aligned} \tag{4.2.6}$$

Then we can write down the self-consistent equations for the real functions $a(\mathbf{p}), b(\mathbf{p}), c(\mathbf{p})$:

$$\begin{aligned} a(\mathbf{p}) =& t_f \Re e g(\mathbf{p}) + \frac{g_{cf}^2}{2} \sum_{\mathbf{q}} \frac{\chi_{AB}(0,\mathbf{q},\mu_c) a(\mathbf{p}+\mathbf{q})}{E(\mathbf{p}+\mathbf{q})} \\ b(\mathbf{p}) =& t_f \Im m g(\mathbf{p}) + \frac{g_{cf}^2}{2} \sum_{\mathbf{q}} \frac{\chi_{AB}(0,\mathbf{q},\mu_c) b(\mathbf{p}+\mathbf{q})}{E(\mathbf{p}+\mathbf{q})} \\ c(\mathbf{p}) =& \frac{g_{cf}^2}{2} \sum_{\mathbf{q}} \frac{\chi_{II}(0,\mathbf{q},\mu_c) c(\mathbf{p}+\mathbf{q})}{E(\mathbf{p}+\mathbf{q})} \end{aligned} \tag{4.2.7}$$

We substitute the $a(p)$ and $b(p)$ by $t_f \Re e g(p)$ and $t_f \Im m g(p)$ on the right hand side of the above equations to linearize the equations, then we will have first order perturbation theory:

$$\begin{aligned} a(\mathbf{p}) =& t_f \Re e g(\mathbf{p}) + \frac{g_{cf}^2}{2} \sum_{\mathbf{q}} \frac{\chi_{AB}(0,\mathbf{q},\mu_c) \Re e(t_f g(\mathbf{p}+\mathbf{q}))}{E(\mathbf{p}+\mathbf{q})} \\ b(\mathbf{p}) =& t_f \Im m g(\mathbf{p}) + \frac{g_{cf}^2}{2} \sum_{\mathbf{q}} \frac{\chi_{AB}(0,\mathbf{q},\mu_c) \Im m(t_f g(\mathbf{p}+\mathbf{q}))}{E(\mathbf{p}+\mathbf{q})} \\ c(\mathbf{p}) =& \frac{g_{cf}^2}{2} \sum_{\mathbf{q}} \frac{\chi_{II}(0,\mathbf{q},\mu_c)}{E(\mathbf{p}+\mathbf{q})} c(\mathbf{p}+\mathbf{q}) \end{aligned} \tag{4.2.8}$$

In the equations for the function $a(\mathbf{p})$ and $b(\mathbf{p})$, the RKKY interaction renormalizes the graphene band structure, and we have checked that the modification is of one order smaller than the function $a(\mathbf{p})$ and $b(\mathbf{p})$. However in the equation for the function $c(\mathbf{p})$, the RKKY interaction opens a gap in the system with the function $c(\mathbf{p})$.

We place ourselves at the onset of the instability onset that is to say $c(\mathbf{p}) \to 0$. We have the self-consistent equation for the function $c(\mathbf{p})$:

$$c(\mathbf{p}) = \frac{g_{cf}^2}{2} \sum_{\mathbf{q}} \frac{\chi_{II}(0,\mathbf{q},\mu_c)}{\sqrt{(a(\mathbf{p}+\mathbf{q}))^2 + (b(\mathbf{p}+\mathbf{q}))^2}} c(\mathbf{p}+\mathbf{q}) \tag{4.2.9}$$

We see that the equations for the function $c(\mathbf{p})$ form a linear equation set. $c(\mathbf{p}) = 0$ is obviously always a trivial solution of the equation 4.2.9 while there will be a non-trivial solution for the function $c(\mathbf{p})$ when g_{cf} is big enough. The non-trivial solution designate a spontaneous instability which opens a gap based on the graphene system. In order to resolve equation numerically, we can think of the function $c(\mathbf{p})$ with certain momentum as a real vector $c(\mathbf{p}) = Vc_{i_{\mathbf{p}}}$, in which $i_{\mathbf{p}}$ is the discretized index for the momentum $\mathbf{p}$. The $i_{\mathbf{p}}$ th component of the vector Vc is the value of the function $c(\mathbf{p})$ at momentum $\mathbf{p}$. Then the real function $c(\mathbf{p})$ constitutes a vector with the dimension of the number of discretization in the first Brillouin zone. We can therefore write down the matrix with the discretizied indices:

$$M_\chi[i_{\mathbf{p}}][j_{\mathbf{p}+\mathbf{q}}] = \frac{g_{cf}^2 \chi_{II}(0,\mathbf{q},\mu_c)}{2t_f|g(\mathbf{p}+\mathbf{q})|} \tag{4.2.10}$$

in which $i_{\mathbf{p}}$ and $j_{\mathbf{p+q}}$ are the discretized index for momentum $\mathbf{p}$ and $\mathbf{p+q}$. Then equation 4.2.9 with the vector $[Vc]$ writes as :

$$[Vc] = M_\chi[Vc] \tag{4.2.11}$$

Due to the property that $\chi_{II}(0,\mathbf{q},\mu_c) = \chi_{II}(0,-\mathbf{q},\mu_c)$, we find that the matrix $M_\chi[i][j]$ respect the symmetry $\mathbf{p} \leftrightarrow -\mathbf{p}$. Thereafter, we can write the matrix in the following block form in the odd subspace $c(\mathbf{p}) = -c(-\mathbf{p})$ and the even subspace $c(\mathbf{p}) = c(-\mathbf{p})$:

$$M_\chi[i_{\mathbf{p}}][j_{\mathbf{p+q}}] = \begin{pmatrix} M_{even} & 0 \\ 0 & M_{odd} \end{pmatrix} \tag{4.2.12}$$

And we implement the Pauli matrix ζ_x which send $c(\mathbf{p})$ to $c(-\mathbf{p})$. Then we have the two projectors to the even and odd sector: $P_{odd} = \frac{1}{2}(1-\zeta_x)$ and $P_{even} = \frac{1}{2}(1+\zeta_x)$ and:

$$M_{even} = P_{even}M_\chi[i_{\mathbf{p}}][j_{\mathbf{p+q}}]P_{even} \quad M_{odd} = P_{odd}M_\chi[i_{\mathbf{p}}][j_{\mathbf{p+q}}]P_{odd} \tag{4.2.13}$$

and we can check that $P_{even}M_\chi[i_{\mathbf{p}}][j_{\mathbf{p+q}}]P_{odd} = 0$. We can write down the function $c(\mathbf{p})$ as a sum of an even and an odd function, of which the former is the Semenoff mass while the latter is the Haldane mass:

$$\begin{aligned} &c(\mathbf{p}) = f_o(\mathbf{p}) + f_e(\mathbf{p}) \\ &f_o(-\mathbf{p}) = -f_o(\mathbf{p}) \quad f_e(\mathbf{p}) = f_e(-\mathbf{p}) \end{aligned} \tag{4.2.14}$$

Equation 4.2.11 then turns into two equations in the two subspaces:

$$V_o = M_{odd}V_o \quad V_e = M_{even}V_e \tag{4.2.15}$$

The stability competition between the emergence of τ_z term in the odd sector (Haldane mass) and the even sector (Semenoff mass) is mediated by the chemical potential of the fast species of fermion c. We find that the minimal critical value g_{cf} is reached when $\mu_c = 0.992t_c$ as shown in Fig. 4.3 left pane: $(g_{cf})_c = 4.64\sqrt{t_ct_f}$.

If we denote the renormalized eigenvector for the biggest eigenvalue of the matrix M_χ in the odd parity sector as VO_χ, then beyond the instability threshold $g_{cf} > (g_{cf})_c$ the Haldane mass should have the similar behavior as the non-trivial solution of Eq. 4.2.9:

$$c(\mathbf{p}) = \lambda VO_\chi(\mathbf{p}). \tag{4.2.16}$$

The amplitude of the Haldane mass λ is to be determined by minimizing the following energy as a function of λ deduced from the action 4.2.1:

$$E_0(\lambda) = -\sum_{\mathbf{p}}\sqrt{[a(\mathbf{p})]^2 + [b(\mathbf{p})]^2 + [\lambda VO_\chi(\mathbf{p})]^2} + g_{cf}^2\sum_{\mathbf{p},\mathbf{q}}\chi_{IJ}(0,\mathbf{q},\mu_c)\frac{\lambda^2 VO_\chi(\mathbf{p})VO_\chi(\mathbf{p+q})}{E(\mathbf{p})E(\mathbf{p+q})}, \tag{4.2.17}$$

in which $E_0(\lambda)$ is the energy of the half-filled fermion f under the RKKY interaction. In the left panel of Fig. 4.4, we show the amplitude of the Haldane mass λ as a function of $g_{cf}/\sqrt{t_ct_f}$ after minimization of $E_0(\lambda)$ with regard to λ.

Therefore, we have engineered a quantum anomalous Hall effect using the RKKY interaction. We have the critical value for the onset of the quantum anomalous Hall effect as a function of the chemical potential μ_c for fermion c shown in Fig. 4.3 left panel.

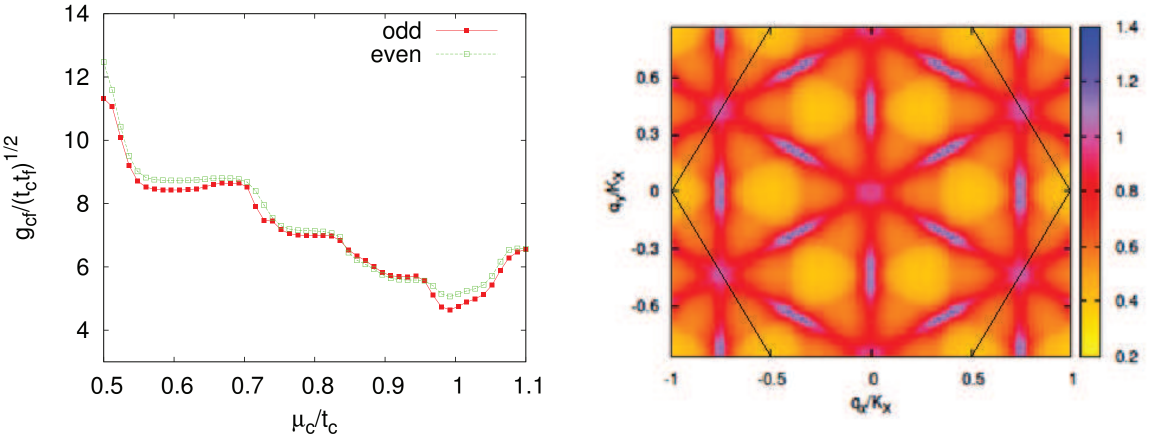

Figure 4.3: *Left panel*: The critical value g_{cf} as a function of μ_c so that equation 4.2.9 has a non trivial solution for the odd $c(\mathbf{p}) = -c(-\mathbf{p})$ (Haldane mass) and even parity subspace $c(\mathbf{p}) = c(-\mathbf{p})$ (Semenoff mass). *Right panel*: The static RKKY interaction susceptibility $\chi_{II}(0, \mathbf{q}, \mu_c = 0.992t_c)$ as a function of $\mathbf{Q} = \frac{\mathbf{q}}{2}$ in the first Brillouin zone. This susceptibility triggers the emergence of the topological phase.

4.3 Mott Transition Induced by the RKKY Interaction.

Next, we also consider the case of spins-1/2 f-fermions with $\mu_c = 0.992t_c$:

$$\begin{aligned} H_f =& \sum_{\mathbf{p}} [(a(\mathbf{p}) + ib(\mathbf{p}))f^\dagger_{a\mathbf{p}\sigma} f_{b\mathbf{p}\sigma} + (a(\mathbf{p}) - ib(\mathbf{p}))f^\dagger_{b\mathbf{p}\sigma} f_{a\mathbf{p}\sigma}] \\ &+ \sum_{\mathbf{p},I} c_I(\mathbf{p})(f^\dagger_{a\mathbf{p}\sigma} f_{a\mathbf{p}\sigma'} - f^\dagger_{b\mathbf{p}\sigma} f_{b\mathbf{p}\sigma'})\sigma^I_{\sigma\sigma'} + H_I \\ H_I =& U_f \sum_i f^\dagger_{i\uparrow} f_{i\uparrow} f^\dagger_{i\downarrow} f_{i\downarrow}. \end{aligned} \tag{4.3.1}$$

The function $a(\mathbf{p})$ and $b(\mathbf{p})$ are renormalised hopping amplitude which is insensible to spins, while besides the spontaneous charge density wave $c_0(\mathbf{p})$ (the Haldane mass discussed above) there could be spin density wave $c_I(\mathbf{p})$ resulting from the instability triggered by the RKKY interaction. We define here $\sigma^\mu = (1, \sigma^x, \sigma^y, \sigma^z)$ in terms of the Pauli matrices. Again, we adjust to zero the renormalised chemical potential of the f-fermions. Physically, if $c_0(\mathbf{q}) \neq 0$ then we are in a QAH phase, whereas when $c_I(\mathbf{q}) \neq 0$ with $I = (x,y,z)$ then we are in a QSH phase. Through a careful analysis of the quantum fluctuations [202], one establishes that the QSH phase is always favored compared to the QAH phase for spinful fermions, due to the presence of Goldstone modes appearing from the breaking of the continuous rotational symmetry in the QSH phase. Therefore, we only take into account the order parameter $c_I(\mathbf{p})$. This conclusion has been reinforced by a Functional Renormalization Group analysis [202]. We have solved similar self-consistent equation as 4.2.9, and found that for $U_f = 0$, the critical threshold $(g_{cf})_c = 4.64\sqrt{t_c t_f}$ as the spinless case.

We can do the spin-charge separation $f^\dagger_{a\mathbf{p}\sigma} = f^\dagger_{as\mathbf{p}\sigma} X^*_{a\mathbf{p}}$ and introduce the mean-field ansatz $Q_x = \langle X^\star_{\mathbf{k}a} X_{\mathbf{k}b} \rangle$, $Q'_x = \langle X^\star_{\mathbf{k}a} X_{\mathbf{k}a} \rangle = \langle X^\star_{\mathbf{k}b} X_{\mathbf{k}b} \rangle$, $Q_f = \langle f^\star_{\mathbf{k}a\sigma} f_{\mathbf{k}b\sigma} \rangle$ and the ansatz

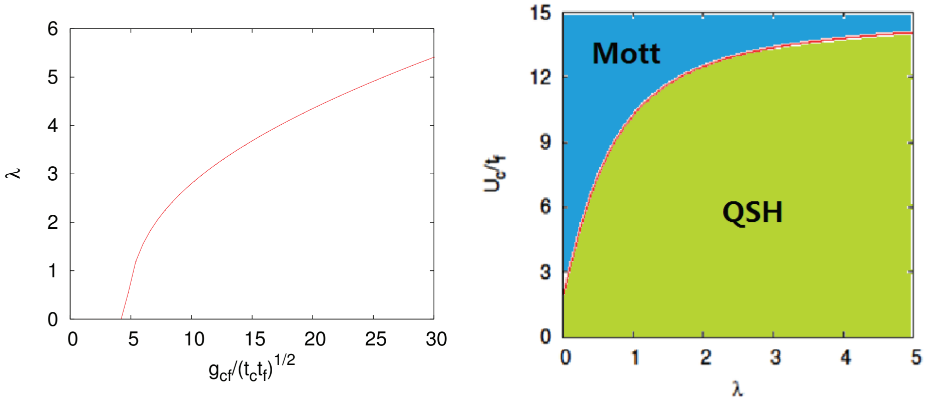

Figure 4.4: (Color online) *Left panel*: The amplitude of the spontaneous spin-orbit coupling λ as a function of g_{cf} calculated from the minimization of the energy in Eq. 4.2.17 when $\mu_c = 0.992t_c$. *Right panel*: The critical Mott transition threshold U_c as a function of λ for the case of spin-1/2 fermions.

for the emergent spin-orbit coupling $Q'_f = \left\langle \sigma^I_{\sigma\sigma'}(f^\star_{\mathbf{k}a\sigma} f_{\mathbf{k}a\sigma'} - f^\star_{\mathbf{k}b\sigma} f_{\mathbf{k}b\sigma'}) \right\rangle$ for the rotor and spinon order parameter on the same and different sublattices. Then we can work out the spectrum for the rotor $\xi(\mathbf{k})$ in the same way as [62], and rotor acquires a gap upon the Mott transition, therefore we can determine the critical interaction U as a function of g_{cf} for the Mott transition.

$$
\begin{aligned}
Q_x &= \frac{1}{3t_f N} \sum_{\mathbf{k}} \frac{|a(\mathbf{k})|^2 + |b(\mathbf{k})|^2}{\sqrt{|a(\mathbf{k})|^2 + |b(\mathbf{k})|^2 + [c(\mathbf{k})]^2}} \\
Q'_x &= -\frac{1}{6N} \sum_{\mathbf{k}} \frac{[c(\mathbf{k})]^2}{\sqrt{|a(\mathbf{k})|^2 + |b(\mathbf{k})|^2 + [c(\mathbf{k})]^2}},
\end{aligned}
\tag{4.3.2}
$$

from which we can calculate the mean-field ansatz Q_x and Q'_x.

$$
\begin{aligned}
\xi(\mathbf{k}) &= -Q_x \sqrt{(a(\mathbf{k}))^2 + (b(\mathbf{k}))^2} + Q'_x c(\mathbf{k}) \\
U(g_{cf}) &= [\frac{1}{2N} \sum_{\mathbf{k}} \frac{1}{\sqrt{\xi(\mathbf{k}) - \min(\xi(\mathbf{k}))}}]^{-2}
\end{aligned}
\tag{4.3.3}
$$

in which functions $a(\mathbf{p})$ and $b(\mathbf{p})$ are functions that can be determined as a function of g_{cf} as in equation 4.2.8. The function $c(\mathbf{p})$ is determined by equation 4.2.16 in the previous section. As a result, we have the phase diagram in the right panel of figure 4.4.

In the Mott phase, the super-exchange magnetism results in a $J_1 - J_2$ model [40], and J_2 comes from higher order of exchange processes. The RKKY interaction will only reinforce the amplitude t_f and the order parameter χ^I is destroyed in the Mott phase in two dimensions [62]

$$
H_M = J_1 \sum_{\langle i,j \rangle} \mathbf{S}_i \cdot \mathbf{S}_j + J_2 \sum_{\langle\langle i,j \rangle\rangle} \mathbf{S}_i \cdot \mathbf{S}_j, \tag{4.3.4}
$$

with $J_1 = 4t_f^2/U$ and $J_2 = 4t_f^4/U^3$. The resulting magnetic order is the bipartite Néel order.

4.4 Conclusion

In this chapter, we have introduced a Fermion-Fermion mixture in graphene-type lattices, with one fast component characterized by a large tunneling strength. We have shown that the interaction produced on the other species allows to implement in realistic conditions a Quantum Anomalous Hall phase or a Quantum Spin Hall phase. This gives the opportunity to observe topological Mott insulators in ultracold mixtures of ^{6}Li and ^{40}K.

Chapter 5

Conclusion

We have studied in this thesis condensed matter problems that are beyond band theories: on the one hand, topology in condensed matter physics with non-trivial topological invariants which is embodied in the non-trivial transport characteristics on edge; on the other hand, systems with strong correlation, in other words, the Mott physics in which correlation localizes electric charges and spins constitute a magnetic insulator. These two aspects are introduced to the system on the one hand by spin-orbit coupling physics, which brings to the system non-trivial topology; on the other hand by the Hubbard interaction, which triggers the Mott transition and the super-exchange magnetism in the infinite Hubbard interaction limit. Iridium oxides, or iridates, form a good arena with all these aspects intertwined with numerous exotic phases in competition. We have focused our attention on iridates on the honeycomb lattice, specifically the Na_2IrO_3 and $\alpha - Li_2IrO_3$ compound. Another interesting ingredient in iridate is the anisotropic Kitaev coupling. In the pure Kitaev coupling model there exists a spin liquid phase called Kitaev anyon model[15], which motivates theoretical physicists to study iridates.

There exists still a pending debate on whether the Kitaev coupling lies on the nearest-neighbour or next-nearest-neighbour links. Experiments have shown the evidence of a topological insulator phase [127] in the thin film of Na_2IrO_3 compound and a zigzag magnetic order phase [113] in the A_2IrO_3 $(A = Na, Li)$ system. Taking into account both possibilities for the real world materials, we studied the physics of the correlated topological insulator with next-nearest-neighbour spin-orbit coupling in Chapter 2 and we studied the doped iridate with spin-orbit coupling and Kitaev-Heisenberg magnetic coupling between nearest-neighbours which hosts a zigzag magnetic phase at half-filling in Chapter 3.

In chapter 2, we take the former point of view and consider a model with anisotropic spin-orbit coupling between next-nearest-neighbours hosting a topological insulator phase in the weak correlated regime. The non conservation of spin observables here constitutes the major difficulty and also the main difference from the Kane-Mele Hubbard model [62]. We have explored the anisotropic spin texture on the edges in the topological insulator phase which is associated to edge spin transport. The existence of the edge breaks the $2\pi/3$ rotation and the symmetry among the three spin components, and the dominant spin component of the edge states coincides with the type of links parallel to the edge. In this weakly correlated phase, the interaction only modifies the Fermi velocity of the transporting edge states. We apply the slave-rotor formalism to study the Mott transition, in which the rotor is in an ordered 'superfluid' phase below the Mott transition and the rotor is in a disordered phase above the Mott transition. We have also given arguments that the spin texture on the edge for the spin transport disappears and develops into the bulk upon Mott transition, using the Laughlin topological pump argument [144] where gauge fluctuation becomes considerable. This anisotropic spin texture may be associated with the spiral phase analyzed in the infinite interaction limit in which super-exchange processes consists of a mixture of Kitaev and Heisenberg magnetic couplings. A more proper description of the edge Luttinger liquid is desirable in the future, complementing the results obtained from transfer matrix and diagonalization of Schrödinger equation developped in this thesis. In order to treat properly the instanton gas emerged from the gauge field fluctuation, a more complete statistical analysis of monopoles is required instead of the naive study of spinon response to one simple monopole developped in this thesis.

In chapter 3, we have taken the latter point of view and studied a model with anisotropic spin-orbit coupling between the nearest neighbours hosting a zigzag magnetic order at half-filling. The previous theoretical study of doped iridate and the entailed superconductivity has fixed the Kitaev magnetic coupling to be ferromagnetic [41], in which case Scherer et al has identified p-wave topological superconductivity beyond quarter-filling. Here, we have fixed the Kitaev magnetic coupling to be antiferromagnetic and the Heisenberg coupling ferromagnetic. We have also taken an super-exchange magnetism point of view in which magnetic couplings stem from second order super-exchange processes of the normal hopping term and the spin-orbit coupling. The spin-orbit coupling gives a band structure with symmetry centers at non-trivial momenta. Superconductivity is most prominent around symmetry centers of the Fermi surface since every electron pairs with momentum $\mathbf{k}$ and $-\mathbf{k}+\mathbf{Q}$ contribute to the superconductivity, with $\mathbf{Q}$ the momentum designating the symmetry center. The condensation of Cooper pairs around these non-trivial momenta leads to an FFLO superconductor when the system is doped away from half-filling close around quarter-filling. The J_2 Kitaev-Heisenberg coupling introduces into the system triplet pairing of the electrons. The separation of the three triplet Cooper pair condensates in the momentum space results in the three times degenerate ground states in the system with respective spatial modulation of the pairing order parameters. At pure spin-orbit coupling limit $t = J_1 = 0$, the spin-orbit coupling can observe the time-reversal symmetry, which shows that the key ingredient to the FFLO superconductivity is the symmetry centers at non trivial momenta instead of the Zeeman field which breaks the time-reversal symmetry. This result proposes a possiblity to observe for the first time the FFLO superconductivity in real materials. However, the topological aspects of the superconductivity concerning explicitly the Chern number of the Bogoliubov De Gennes band are still unclear. And the spin-1 superconductivity may bring the problem of Majorana fermions into the system, which remains to be explored [226].

The chapter 4 presents a different system but also with the interplay of topology and correlation. We studied a two species fermion model in which the induced RKKY interaction from the fast species onto the slow species opens a gap around the Dirac points. By adjusting the chemical potential of the fast species, we can tune the system into a regime so that a Haldane mass is favored thus inducing a topological phase. The competition between the charge density wave and the topological phase is a big issue in the system [202] and the long range interaction in the RKKY interaction destablize the charge density wave favoring the topological phase.

Chapter A

Annexe

A.1 Loop Variables Construction: Curl and Divergence on a Lattice

As a generalization of section 2.4, we present here the loop variable construction respectively for curl free and divergence free field on a square lattice. We consider a suqare lattice and its dual, where the sites of the first lattice are identified by the coordinates (i,j) while those of the dual by the coordinates $(i+\frac{1}{2}, j+\frac{1}{2})$. Suppose that there are some variables defined along the links of the original lattice: denote by $\rho_{i+\frac{1}{2},j}$ the variable defined along the horizontal segment that links (i,j) to $(i,j+1)$ (see Fig. A.1). If the circulation along the perimeter $\mathcal{S}$ of the elementary cell of the lattice is zero, we have:

$$\rho_{i+\frac{1}{2},j} + \rho_{i+1,j+\frac{1}{2}} - \rho_{i+\frac{1}{2},j+1} - \rho_{i,j+\frac{1}{2}} = 0 \quad \leftrightarrow \quad \nabla \times \rho = 0 \tag{A.1.1}$$

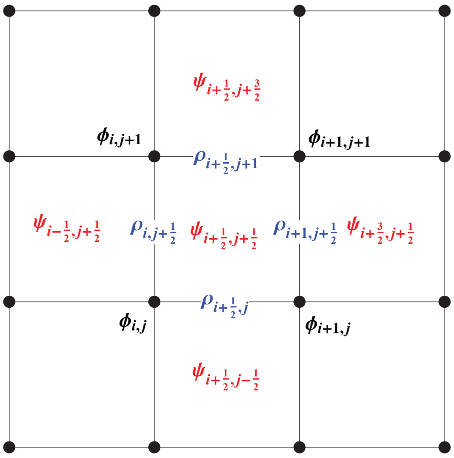

Figure A.1: The loop variables defined on the lattice sites $\phi_{i,j}$ on the links $\rho_{i+\frac{1}{2},j}$ and plaquettes $\Psi_{i+\frac{1}{2},j+\frac{1}{2}}$

This is the discrete version of the curl-free field equation. This can be identically satisfied in terms of a variable $\phi_{i,j}$ defined on the sites of the original lattice, by imposing:

$$\begin{aligned} \rho_{i+\frac{1}{2},j} &= \phi_{i+1,j} - \phi_{i,j} \\ \rho_{i,j+\frac{1}{2}} &= \phi_{i,j+1} - \phi_{i,j} \end{aligned} \tag{A.1.2}$$

Vice versa, the discrete version of the divergence-free condition is given by:

$$\rho_{i+\frac{1}{2},j} - \rho_{i-\frac{1}{2},j} + \rho_{i,j+\frac{1}{2}} - \rho_{i,j-\frac{1}{2}} = 0 \quad \leftrightarrow \quad \nabla \cdot \rho = 0 \tag{A.1.3}$$

This can be satisfied by expressing the variables ρ in terms of a discrete curl of a variable $\psi_{i+\frac{1}{2},j+\frac{1}{2}}$ defined on the dual lattice:

$$\begin{aligned} \rho_{i+\frac{1}{2},j} &= \psi_{i+\frac{1}{2},j+\frac{1}{2}} - \psi_{i+\frac{1}{2},j-\frac{1}{2}} \\ \rho_{i,j+\frac{1}{2}} &= -\psi_{i+\frac{1}{2},j+\frac{1}{2}} + \psi_{i-\frac{1}{2},j+\frac{1}{2}} \end{aligned} \tag{A.1.4}$$

Bibliography

[1] N.W. Ashcroft, N.D. Mermin, Solid State Physics, Harcourt, (1976).

[2] J. Hubbard, Proceedings of the Royal Society of London **276** 1365 (1963)

[3] N.F. Mott, R. Peierls, Proceedings of the Physical Society **49** 59 (1937).

[4] N.F. Mott, Rev. Mod. Phys., **40** 677.

[5] Kittel, Introduction to Solid State Physics 7th Edition, chapter 7.

[6] A.Georges, L.D.Medici, J. Mravlje, Annual Review of Condensed Matter Physics **4**, 137 (2013).

[7] K.V.Klitzing, G.Dorda, M.Pepper, Phys. Rev. Lett. **45**, 494 (1980).

[8] D. C. Tsui, H. L. Stormer, and A. C. Gossard, Phys. Rev. Lett. **48**, 1559 (1982).

[9] Phil. Trans. R. Soc. A (2005) **363**, 2203-2219.

[10] F. D. Haldane, Phys. Rev. Lett. **61**, 2015 (1988).

[11] C. L. Kane and E. J. Mele, Phys. Rev. Lett. **95**, 146802 (2005); *ibid.* **95**, 226801 (2005).

[12] L. Fu and C. L. Kane, Phys. Rev. B **76**, 045302 (2007).

[13] B. A. Bernevig, T. L. Hughes, and S.-C. Zhang, Science **314**, 1757 (2006).

[14] M. König, S. Wiedmann, C. Brüne, A. Roth, H. Buhmann, L. W. Molenkamp, X.-L. Qi, and S.-C. Zhang, Science **318**, 766 (2007). C. Brüne *et al.* Nature Physics **8**, 486 (2012); K. C. Nowack *et al.* Nature Materials **12**, 787-791 (2013); Y. Ma *et al.* Nature Communications **6**, 7252 (2015).

[15] A. Kitaev, Annals of Physics **321**, 2-111 (2006).

[16] D. Green and N. Read, Phys. Rev. B **61**, 10267 (2000).

[17] D.J. Thouless, M. Kohmoto, M. P. Nightingale and M. den Nijs, Phys. Rev. Lett. **49**, 405 (1982).

[18] R. B. Laughlin, Phys. Rev. Lett. **50**, 1395 (1983).

[19] Philip Phillips, Phil. Trans. R. Soc. A (2011) **369**, 1574-1598.

[20] A. L. Fetter, Rev. Mod. Phys. **81**, 647 (2009); D. Jaksch and P. Zoller, Annals of Physics **315**, 52-79 (2005); K. Osterloh *et al.*, Phys. Rev. Lett. **95**, 010403 (2005); Yu-Ju Lin *et al.*, Nature **462**, 628 (2009); N. Goldman *et al.*, Phys. Rev. Lett. **105**, 255302 (2010); M. Aidelsburger *et al.*, Phys. Rev. Lett. **107**, 255301 (2011); J. Heinze et al., Phys. Rev. Lett. **107**, 135303 (2011); J. Struck *et al.*, Phys. Rev. Lett. **108**, 225304 (2012); N. R. Cooper and J. Dalibard, Phys. Rev. Lett. **110**, 185301 (2013); H. Miyake *et al.* Phys. Rev. Lett. **111**, 185302 (2013); T. Liu, C. Repellin, B. A. Bernevig and N. Regnault, Phys. Rev. B *87*, 205136 (2013); M. Atala *et al.* Nature Physics **10**, 588-593 (2014); E. Orignac and T. Giamarchi, Phys. Rev. B. **64**, 144515 (2001); A. Petrescu, and K. Le Hur, Phys. Rev. Lett. **111**, 150601 (2013); A.Tokuno and A. Georges New. J. Phys. **16**, 073005 (2014); M. Piraud, Z. Cai, I. P. McCulloch and Schollwöck, Phys. Rev. A **89**, 063618 (2014); I. Vasic, A. Petrescu, K. Le Hur and W. Hofstetter, Phys. Rev. B **91**, 094502 (2015).

[21] A. Georges, G. Kotliar, W. Krauth, M.J.Rozenberg, Rev. Mod. Phys. **68** 13 (1996).

[22] S. Florens and A. Georges, Phys. Rev. B **70**, 035114 (2004).

[23] G. Kotliar, J.Liu, Phys. Rev. B **28**, 5142 (1988).

[24] F. D. M. Haldane, Phys. Lett. A **93**, 464 (1983).

[25] C. Pépin, Phys. Rev. B **77**, 245129 (2008).

[26] K.B.Efetov, H.Meier, C.Pépin, Nature Physics **9**, 442 (2013).

[27] S. Pathak, V.B.Shenoy, M.Randeria, N.Trivedi, Phys. Rev. Lett. **102**, 027002 (2009).

[28] X. G. Wen, Phys. Rev. B. **40**, 7387 (1989); X.-G. Wen, Int. J. Mod. Phys. **B4**, 239 (1990).

[29] J.T. Chalker, Geometrically frustrated antiferromagnets: statistical mechanis and dynamis, Springer Series in Solid-State Sciences, **164**, P.3, arxiv 0901.3492.

[30] L. Savary, K.A. Ross, B.D. Gaulin, J.P.C. Ruff, L. Balents, Phys. Rev. Lett. **109**, 167201/

[31] M.E. Zhitomirsky, M.V. Gvozdikova. P.C.W.Holdsworth, R.Moessner, Phys. Rev. Lett. **109**, 077201 (2012).

[32] G. Misguich, Quantum Spin Liquid, Lectures given at the Les Houches School on 'Exact Methods in Low-dimensional Statistical Physics and Quantum Computing' (2008) arxiv 0809.2257.

[33] B.A.Bernevig, T.L.Hughes, Topological Insulators and Topological Superconductors, Princeton Univresity Press (2012).

[34] E. Fradkin, Field Theory of Condensed Matter Physics, Cambridge University Press (2013).

[35] X.G.Wen, Quantum Field Theory of Many-Body Systems, Oxford Graduate Texts (2004).

[36] T. Liu, B. Douçot and K. Le Hur, Phys. Rev. B **88**, 245119 (2013).

[37] T. Liu, C. Repellin, N. Regnault, B. Douçot and K. Le Hur, work in progress.

[38] T. Liu, B. Douçot and K. Le Hur, arxiv: 1409.6237 (2014).

[39] Z.Y.Meng, T.C.Lang, S.Wessel, F.F.Assaad, and A.Muramatsu, Nature **464**, 847 (2010).

[40] P. Chandra and B. Douçot, Phys. Rev. B **38**, 9335 (1988); N. Read and S. Sachdev, Phys. Rev. Lett. **66**, 1773 (1991); B. K. Clark, D. A. Abanin and S. L. Sondhi, Phys. Rev. Lett. **107**, 087204 (2011); H. C. Jiang, H. Yao and L. Balents Phys. Rev. B **86**, 024424 (2012); Yuan-Ming Liu and Ying Ran, Phys. Rev. B **84**, 024420 (2011); W. Wu, M. Scherer, C. Honerkamp and K. Le Hur, Phys. Rev. B **87**, 094521 (2013); L. Wang, D. Poilblanc, Z.-C. Gu, X.-G. Wen and F. Verstraete, Phys.Rev.Lett. **111**, 037202 (2013).

[41] D.D.Scherer, M.M. Scherer, G.Khaliullin, C.Honerkamp, B.Rosenow.

[42] W. W. Krempa, G. Chen, Y.-B. Kim and L. Balents, Annual Review of Condensed Matter Physics, Vol. 5: 57-82 (2014).

[43] J. Chaloupka, G. Jackeli and G. Khaliullin Phys. Rev. Lett. **105**, 027204 (2010); Phys. Rev. Lett. **110**, 097204 (2013).

[44] G.Jackeli and G.Khaliullin Phys. Rev. Lett. **102**, 017205 (2009).

[45] J. Chaloupka and G.Khaliullin, Phys. Rev. B 92, 024413 (2015).

[46] L.-M. Duan, E. Demler and M.D. Lukin, Phys. Rev. Lett. **91**, 090402 (2003).

[47] G. Moore and N. Read, NuclPhys B **360**, 362 (1991).

[48] P. Leboeuf, J. Kurchan, M. Feingold and D. P. Arovas, Phys. Rev. **65**, 3076 (1990).

[49] C. Nayak, S. H. Simon, A. Stern, M. Freedman, and S. Das Sarma, Rev. Mod. Phys. **80**, 1083 (2008).

[50] B. Douçot and L. B. Ioffe, Rep. Prog. Phys. **75**, 072001 (2012).

[51] M. Z. Hasan and C. L. Kane, Rev. Mod. Phys. **82**, 3045 (2010); J. Moore, Nature **464**, 194 (2010); X.-L. Qi and S.-C. Zhang, Rev. Mod. Phys. **83**, 1057 (2011).

[52] A. Y. Kitaev Phys.-Usp. **44** 131 (2001); Y. Oreg, G. Refael, and F. von Oppen, Phys. Rev. Lett. **105**, 177002 (2010); R. M. Lutchyn, J. D. Sau, and S. Das Sarma, Phys. Rev. Lett. **105**, 077001 (2010); J. Alicea, Reports on Progress in Physics **75**, 076501 (2012); Jason Alicea, Yuval Oreg, Gil Refael, Felix von Oppen, Matthew P. A. Fisher Nature Physics **7**, 412-417 (2011); V. Mourik, K. Zuo, S. M. Frolov, S. R. Plissard, E. P. A. M. Bakkers, and L. P. Kouwenhoven, Science **336**, 1003 (2012); L. P. Rokhinson, X. Liu, and J. K. Furdyna, Nat Phys **8**, 795 (2012); J. R. Williams, A. J. Bestwick, P. Gallagher, S. S. Hong, Y. Cui, A. S. Bleich, J. G. Analytis, I. R. Fisher, and D. Goldhaber-Gordon, Phys. Rev. Lett. **109**, 056803 (2012); A. Das *et al.* Nature Phys. **8**(12) 887 (2012); S. Gangadharaiah, B. Braunecker, P. Simon and D. Loss Phys. Rev. Lett. **107**, 036801 (2011); E.M. Stoudenmire, J. Alicea, O. A. Starykh, M. P.A. Fisher Phys. Rev. B **84**, 014503 (2011); D. Sticlet, C. Bena and P. Simon Phys. Rev. Lett. **108**, 096802 (2012).

[53] C. Waldtmann *et al.* Eur. Phys. Jour. B **2**, 501 (1998); P. Lecheminant, B. Bernu, C. Lhuillier, L. Pierre, P. Sindzingre, Phys. Rev. B **56**, 2521-2529 (1997); L. Messio, B. Bernu and C. Lhuillier, Phys. Rev. Lett. **108**, 207204 (2012); B. Fak *et al.* Phys. Rev. Lett. **109**, 037208 (2012); S. Yan, D. A. Huse and S. R. White, Science **332**, 1173-1176 (2011); S. Depenbrock, I. P. McCulloch and U. Schollwoeck, Phys. Rev. Lett. **109**, 067201

(2012); H. C. Jiang, Z. Wang and L. Balents, Nature Phys. **8**, 902 (2012); Y. Iqbal, F. Becca, S. Sorella and D. Poilblanc, Phys. Rev. B **87**, 060405(R) (2013); S. S. Gong, D. N. Sheng, O. I. Motrunich and M. P. A Fisher, Phys. Rev. B **88**, 165138 (2013); L. Balents, M. P. A. Fisher and S. M. Girvin, Phys. Rev. B **65**, 224412 (2002).

[54] S.A. Kivelson, D.S.Rokhsar and J.P.Sethna, Phys. Rev. B **35**, 8865 (1987); D.S.Rokhsar and S.A. Kivelson, Phys. Rev. Lett. **61**, 2376 (1988); R.Moessner and S.L. Sondhi, Phys. Rev. Lett. **86**, 1881 (2001); G. Misguich, D. Serban and V. Pasquier, Phys. Rev. Lett. **89**, 137202 (2002).

[55] G. Misguich and C. Lhuillier, in *frustrated spin models*, edited by H. T. Diep (World Scientist, New Jersey, 2004).

[56] R. Mong *et al.* Phys. Rev. X **4**, 011036 (2014).

[57] J. E. Moore and L. Balents, Phys. Rev. B **75**, 121306(R) (2007).

[58] A. P. Schnyder, S. Ryu, A. Furusaki, and A. W. W. Ludwig, Phys. Rev. B **78**, 195125 (2008); E. Prodan, T. L. Hughes, and B. A. Bernevig, Phys. Rev. Lett. **105**, 115501 (2010).

[59] C. Wu, B. A. Bernevig, and S.-C. Zhang, Phys. Rev. Lett. **96**, 106401 (2006).

[60] C. Xu and J. E. Moore, Phys. Rev. B **73**, 045322 (2006); M. Levin and A. Stern, Phys. Rev. Lett. **103**, 196803 (2009); Z. Wang, X.-L. Qi, and S.-C. Zhang, *ibid.* **105**, 256803 (2010); V. Gurarie, Phys. Rev. B **83**, 085426 (2011); T. Neupert, L. Santos, C. Chamon and C. Mudry, Phys. Rev. B **86**, 165133 (2012).

[61] D. A. Pesin and L. Balents, Nature Phys. **6**, 376 (2010).

[62] S. Rachel and K. Le Hur, Phys. Rev. B **82**, 075106 (2010).

[63] M. W. Young, S.-S. Lee and C. Kallin, Phys. Rev. B **78**, 125316 (2008).

[64] M. Hohenadler, T. C. Lang, F. F. Assaad Phys. Rev. Lett. **106**, 100403 (2011); M. Hohenadler *et al.* Phys. Rev. B **85**, 115132 (2012); M. Hohenadler and F. F. Assaad J. Phys.: Condens. Matter **25**, 143201 (2013).

[65] W. Wu, S. Rachel, W.-M. Liu and K. Le Hur, Phys. Rev. B **85**, 205102 (2012); Y. Yamaji and M. Imada, Phys. Rev. B **83**, 205122 (2011); S. L. Yu, X. C. Xie and J. X. Li, Phys. Rev. Lett. **107**, 010401 (2011); D. Zheng, G.-M Zhang and C. Wu, Phys. Rev. B **84**, 205121 (2011).

[66] D. Hsieh *et al.* Nature **452**, 970-974 (2008).

[67] D. Hsieh *et al.* Science **323**, 919-922 (2009).

[68] H. Zhang *et al.* Nature Phys. **5**, 438 (2009).

[69] B. Fauqué *et al.* Phys. Rev. B **87**, 035133 (2013).

[70] M. Hajlaoui *et al.* Nano Lett. **12**, 3532 (2012).

[71] C. Brüne *et al.*, Phys. Rev. Lett. **106**, 126803 (2011).

[72] O. Crauste *et al.*, arXiv:1307.2008.

[73] Y. L. Chen *et al.* Science **325**, 178-181 (2009).

[74] T. L. Schmidt, S. Rachel, F. von Oppen and L. Glazman, Phys. Rev. Lett. **108**, 156402 (2012).

[75] P. Adroguer, C. Grenier, D. Carpentier, J. Cayssol, P. Degiovanni and E. Orignac, Phys. Rev. B **82**, 081303(R) (2010).

[76] I. Garate and K. Le Hur, Phys. Rev. B **85**, 195465 (2012).

[77] S. Raghu, Xiao-Liang Qi, C. Honerkamp and Shou-Cheng Zhang Phys.Rev.Lett. **100**, 156401 (2008); J. Wen, A. Ruegg, C.-C. J. Wang and G. A. Fiete, Phys. Rev. B **82**, 075125 (2010).

[78] M. C. Rechtsman *et al.*, Nature **496**, 196-200 (2013). Ling Lu et al. Nature Photonics, **8**, 821-829 (2014).

[79] T. Kitagawa *et al.* Nature Comm. **3**, 882 (2012); M. Bellec, U. Kuhl, G. Montambaux and F. Montessagne, Phys. Rev. Lett. **110**, 033902 (2012); F. D. M. Haldane and S. Raghu, Phys. Rev. Lett. **100**, 013904 (2008); S. Raghu and F. D. M. Haldane, Phys. Rev. A **78**, 033834 (2008); Z. Wang, Y. D. Chong, J. D. Joannopoulos and M. Soljacic, Phys. Rev. Lett. **100**, 013905 (2008); Z. Wang, Y. Chong, J. Joannopoulos and M. Soljacic, Nature **461**, 772 (2009); M. Hafezi, E. Demler, M. Lukin and J. Taylor, Nature Phys. **7**, 907 (2011); M. Hafezi, J. Fan, A. Migdall and J. Taylor, Nature Photonics **7**, 1001 (2013); J. Koch *et al.* Phys. Rev. A **82** 043811 (2010); A. B. Khanikaev *et al.*, Nature Mat. **12**, 233 (2013); I. Carusotto and C. Ciuti, Rev. Mod. Phys. **85**, 299 (2013).

[80] A. Petrescu, A. A. Houck and K. Le Hur, Phys. Rev. A **86**, 053804 (2012).

[81] T. Kitagawa, E. Berg, M. Rudner and E. Demler, Phys. Rev. B **82**, 235114 (2010); N. H. Lindner, G. Refael and V. Galitski, Nature Physics **7**, 490-495 (2011); P. Delplace, A. Gomez-Leon, G. Platero, Phys. Rev. B **88**, 245422 (2013); J. Cayssol, B. Dóra, F. Simon and R. Moessner, Phys. Status Solidi RRL **7**, 101 (2013).

[82] M. Taillefumier, V. K. Dugaev, B. Canals, C. Lacroix and P. Bruno, Phys. Rev. B **84**, 085427 (2011).

[83] W. P. Su, J. R. Schrieffer, and A. J. Heeger, Phys. Rev. Lett. **42** , 1698 (1979).

[84] J. K. Jain, Phys. Rev. Lett. **63**, 199 (1989).

[85] E. Tang, J.-W. Mei and X.-G. Wen, Phys. Rev. Lett. **106**, 236802 (2011); T. Neupert, L. Santos, C. Chamon and C. Mudry, Phys. Rev. Lett. 106, 236804 (2011); N. Regnault and B. A. Bernevig, Phys. Rev. X **1**, 021014 (2011); T. Liu, C. Repellin, B. A. Bernevig and N. Regnault, Phys. Rev. B **87**, 205136 (2013); Y.-F. Wang *et al.* Phys. Rev. Lett. 108, 126805 (2012); M. O. Goerbig, Eur. Phys. J B **85**(1), 15 (2012); N. Y. Yao *et al.* Phys. Rev. Lett. **110**, 185302 (2013).

[86] A. M. Turner and A. Vishwanath, arXiv:1301.0330, review article

[87] Y. Machida, S. Nakatsuji, S. Onoda, T. Tayama and T. Sakakibara, Nature **463**, 210-213 (2010).

[88] W. W. Krempa, T. P. Choy and Y. B. Kim, Phys. Rev. B **82** 165122 (2010).

[89] C. Wang, A. C. Potter, and T. Senthil, Phys. Rev. B. **88**, 115137 (2013); M. A. Metlitski, C. L. Kane, and M. P. A. Fisher, arXiv:1306.3286; L. Fidkowski, X. Chen, and A. Vishwanath, Phys. Rev. X **3**, 041016 (2013); P. Bonderson, C. Nayak, and X.-L. Qi, Journal of Statistical Mechanics: Theory and Experiment 2013, P09016 (2013).

[90] R. S. K. Mong, A. M. Essin, and J. E. Moore, Phys. Rev. B **81**, 245209 (2010). A. M. Turner, Y. Zhang, R. S. K. Mong, and A. Vishwanath, Phys. Rev. B **85**, 165120 (2012). T. L. Hughes, E. Prodan, and B. A. Bernevig, Phys. Rev. B **83**, 245132 (2011). C. Fang, M. J. Gilbert, and B. A. Bernevig, Phys. Rev. B **88**, 085406 (2013), Phys. Rev. B **88**, 085406 (2013). M. Kargarian and G. A. Fiete, Phys. Rev. Lett. **110**, 156403 (2013).

[91] A. M. Turner, Y. Zhang, R. S. K. Mong, and A. Vishwanath,Phys. Rev. B **85**, 165120 (2012). T. L. Hughes, E. Prodan, and B. A. Bernevig, Phys. Rev. B **83**, 245132 (2011).

[92] J.R.Schrieffer, P.A.Wolff, Phys. Rev. **149**, 491 (1966).

[93] D. N. Sheng, Z.-C. Gu, K. Sun, and L. Sheng, Nature Communications **2**, 389 (2011), 10.1038/ncomms1380. T. Neupert, L. Santos, C. Chamon, and C. Mudry, Phys. Rev. Lett. **106**, 236804 (2011). E. Tang, J.-W. Mei, and X.-G. Wen, Phys. Rev. Lett. **106**, 236802 (2011).

[94] G. A. Volovik, The Universe in a Helium Droplet (Oxford University Press, 2003). X. Wan, A. M. Turner, A. Vishwanath, and S. Y. Savrasov, Phys. Rev. B **83**, 205101 (2011).

[95] A. Rüegg and G. A. Fiete, Phys. Rev. Lett. **108**, 046401 (2012).

[96] Y. Okamoto, M. Nohara, H. Aruga-Katori, and H. Takagi, Phys. Rev. Lett. **99**, 137207 (2007);

[97] B. J. Kim et al., Phys. Rev. Lett. **101**, 076402 (2008).

[98] B. J. Kim, H. Ohsumi, T. Komesu, S. Sakai, T. Morita, H. Takagi, and T. Arima, Science **323**, 1329 (2009).

[99] C. Martins, M. Aichhorn, L. Vaugier and S. Biermann, Phys. Rev. Lett. **26**, 266404 (2011).

[100] A. Subedi, Phys. Rev. B **85**, 020408(R) (2012).

[101] A. Shitade, H. Katsura, J. Kunes, X.L. Qi, S.C. Zhang and N. Nagaosa, Phys. Rev. Lett **102**, 256403 (2009).

[102] H. C. Jiang, Z. C.Gu, X. L.Qi, and S. Trebst Phys. Rev. B **83**, 245104 (2011).

[103] C. Price and N. B. Perkins, Phys. Rev. Lett. **109**, 187201 (2012).

[104] I. Rousochatzakis, U. K. Rössler, J. van den Brink and M. Daghofer arXiv:1209.5895

[105] J. Reuther, R.Thomale and S. Rachel, Phys. Rev. B **86**, 155127 (2012).

[106] M. Kargarian, A. Langari and G. A. Fiete, Phys. Rev. B **86**, 205124 (2012).

[107] S. Bhattacharjee, S.-S. Lee, and Y. B. Kim, New Journal of Physics **14**, 073015 (2012).

[108] Y. Z.You, I. Kimchi and A.Vishwanath, Phys. Rev. B **86**, 085145 (2012).

[109] I. Kimchi and A.Vishwanath, Phys. Rev. B **89**, 014414 (2014).

[110] I. Kimchi and Y. Z.You, Phys. Rev. B **84**, 180407 (2011).

[111] I. Kimchi, R. Coldea, A. Vishwanath, Phys.Rev.B **91**, 245134 (2015).

[112] I. I. Mazin *et al.*, Phys. Rev. B **88**, 035115 (2013).

[113] Y. Singh and P. Gegenwart, Phys. Rev. B **82**, 064412 (2010).

[114] Y. Singh, S. Manni, J. Reuther, T. Berlijn, R. Thomale, W.Ku, S. Trebst, and P. Gegenwart, Phys. Rev. Lett. **108**, 127203 (2012)

[115] Cyril Martins. Interplay of Spin-Orbit Coupling and Electronic Coulomb Interactions in Strontium Iridate Sr2IrO4. Strongly Correlated Electrons. Ecole Polytechnique X, 2010. English. <pastel-00591068>

[116] X. Liu *et al.* Phys. Rev. B **83**, 220403(R) (2011).

[117] S. K. Choi *et al.* Phys. Rev. Lett. 108, 127204 (2012).

[118] R. Comin *et al.* Phys. Rev. Lett. **109**, 266406 (2012).

[119] H. Gretarsson *et et al.* Phys. Rev. Lett. **110**, 076402 (2013).

[120] K. Matsuhira *et al.* J. Phys. Soc. Jpn. **82** 023706 (2013).

[121] K. Foyevtsova *et al.* Phys. Rev. B **88**, 035107 (2013).

[122] I.I. Mazin, H.O.Jeschke, K. Foyevtsova, R. Valenti and D.I. Khomskii, Phys. Rev. Lett. **109**, 197201 (2012).

[123] Y. Singh *et al.* Phys. Rev. Lett. **108**, 127203 (2012); F.Ye et al. Phys. Rev. B **85**, 180403 (2012); Z. Nussinov and J. van den Brink, arXiv:1303.5922.

[124] X.Liu et al, Phys. Rev. B **83**(R), 220403 (2011).

[125] Y.Singh and Y.Gegenwart, Phys. Rev. B **82**, 064412 (2010).

[126] G. Cao, T. F. Qi, L. Li, J. Terzic, S. J. Yuan, M. Tovar, G. Murthy and R. K. Kaul, Phys. Rev. B **88**, 220414(R) (2013).

[127] M. Jenderka *et al*, Phys. Rev. B **88**, 045111 (2013).

[128] C. Wu, B.A.Bernevig, S.C.Zhang, Phys. Rev. Lett. **96**, 106401 (2006).

[129] J. B. Fouet, P. Sindzingre and C. Lhuillier, Eur. Phys J. B, **20**, 241-254 (2001); P. Lecheminant, B. Bernu, C. Lhuillier and L. Pierre, Phys. Rev. B **52**, 6647 (1995);

[130] S. Florens and A. Georges, Phys. Rev. B **70**, 035114 (2004).

[131] E. Zhao and A. Paramekanti, Phys. Rev. B **76**, 195101 (2007).

[132] S.-S. Lee and P. A. Lee, Phys. Rev. Lett **95**, 036403 (2005).

[133] G. Wang, M. O. Goerbig, C. Miniatura and B. Grémaud, EuroPhys. Lett. **95**, 47013 (2011).

[134] W. Witczak-Krempa and Y. B. Kim, Phys. Rev. B **85**, 045124 (2012).

[135] T. C. Lang, A. M. Essin, V. Gurarie and S. Wessel, Phys. Rev. B **87**, 205101 (2013).

[136] J. C. Budich, B. Trauzettel and G. Sangiovanni, Phys. Rev. B **87**, 235104 (2013).

[137] Z. Wang, X.-L. Qi and S.-C. Zhang, Phys. Rev. B **85**, 165126 (2012).

[138] Z. Wang and S.-C. Zhang, Phys. Rev. X **2**, 031008 (2012).

[139] David Carpentier: arXiv:1408.1867

[140] E. Choi, G. Chern and N.B.Perkins, EPL **101** 3/

[141] L. de' Medici, A. Georges and S. Biermann, Phys. Rev. B **72**, 205124 (2005).

[142] A. Paramekanti, M. Randeria, N. Trivedi, Phys. Rev. Lett. **87**, 217002 (2001).

[143] R. Nandkishore, M. A. Metlitski and T. Senthil, Phys. Rev. B **86**, 045128 (2012).

[144] R.B. Laughlin, Phys. Rev. B **23**, 5632 (1981).

[145] P. H. Y. Li *et al.* Phys. Rev. B **86** 144404 (2012).

[146] A. M. Polyakov, Gauge Fields and Strings, Contemporary Concepts in Physics, Taylor and Francis, 1987.

[147] L. B. Ioffe and A. Larkin, Phys. Rev. B **39**, 8988 (1988).

[148] I. Herbut, B. H. Seradjeh, S. Sachdev and G. Murthy, Phys. Rev. B **68**, 195110 (2003).

[149] L. Fu and C. L. Kane, Phys. Rev. B **74**, 195312 (2006).

[150] D.-H. Lee, Phys. Rev. Lett. **107**, 166806 (2011).

[151] A. Rüegg, S. D. Huber and M. Sigrist, Phys. Rev. B **81**, 155118 (2010).

[152] T. Senthil and M. P. A. Fisher, Phys. Rev. B **63**, 134521 (2001).

[153] T.Senthil and M. P. A. Fisher, Phys. Rev. B **64**, 214511 (2001).

[154] Matthias Punk, Debanjan Chowdhury, Subir Sachdev, Nature Physics **10**, 289-293 (2014).

[155] M. Hermele, Y. Ran, P. A. Lee, and X.G. Wen, Phys. Rev. B **77**, 224413 (2008).

[156] M. Hermele, Phys. Rev. B **76**, 035125 (2007).

[157] M. Hermele, T. Senthil, M. P. A. Fisher, P.A.Lee, N.Nagaosa and X.G.Wen, Phys. Rev. B **70**, 214437 (2004).

[158] F. S. Nogueira, H. Kleinert, **95**, Phys. Rev. Lett. 176406 (2005).

[159] R. S. K. Mong, V. Shivamoggi, Phys. Rev. B **83**, 125109 (2011).

[160] S. S.Pershoguba and V.Yakovenko, Phys. Rev. B **86**, 075403 (2012).

[161] J. Reuther, D. Abanin and R. Thomale, Phys. Rev. B **84**, 014417 (2011).

[162] Z. Y. Meng *et al.* Nature **464**, 847 (2010).

[163] S. Sorella, Y. Otsuka and S. Yunoki, Scientific Reports **2**, 992 (2012).

[164] S. R. Hassan and D. Sénéchal, Phys. Rev. Lett. **110**, 096402 (2013).

[165] F. Assaad and I. Herbut, Phys. Rev. X **3**, 031010 (2013).

[166] A. Liebsch and W. Wu, Phys. Rev. B **87**, 205127 (2013).

[167] C. Xu and S. Sachdev, Phys. Rev. Lett. **105** 057201 (2010).

[168] Marco Polini, Francisco Guinea, Maciej Lewenstein, Hari C. Manoharan and Vittorio Pellegrini, Nature Nanotech. **8**, 625 (2013).

[169] N. Goldman *et al.* New Journal of Physics **15** 013025 (2013).

[170] D. Cocks, P. P. Orth, S. Rachel, M. Buchhold, K. Le Hur and W. Hofstetter, Phys. Rev. Lett. **109**, 205303 (2012); N. R. Cooper and J. Dalibard, Phys. Rev. Lett. **110**, 185301 (2013); P. P. Orth, D. Cocks, S. Rachel, M. Buchhold, K. Le Hur and W. Hofstetter, J. Phys. B At. Mol. Opt. Phys. **46**, 134004 (2013).

[171] C. Castelnovo, R. Moessner and S. L. Sondhi, Nature **451**, 42 (2008); S. T. Bramwell *et al.* Nature 461, 956-959 (2009); D. J. P. Morris *et al.* Science **326**, 411 (2009); K. Kimura *et al.* Nature Communications **4** (2013); N. Shannon, O. Sikora, F. Pollmann, K. Penc, P. Fulde Phys. Rev. Lett. **108**, 067204 (2012).

[172] R. Hivet *et al.* Nature Phys. **8**, 724 (2012).

[173] M. Z. Hasan and C. L. Kane, Rev. Mod. Phys. **82**, 3045 (2010).

[174] X.-L. Qi and S.-C.Zhang, Rev. Mod. Phys. **83**, 1057-1110 (2011).

[175] J. Dalibard, F. Gerbier, G. Juzeliūnas and P. Ohberg, Rev. Mod. Phys. **83**, 1523 (2011);

[176] N. Goldman, G. Juzeliunas, P. Ohberg, and I. B. Spielman, Rep. Prog. Phys. **77**, 126401 (2014).

[177] D. A. Pesin and A. H. MacDonald, Nature Materials, **11**, 409-416 (2012).

[178] D. Hsieh *et al.* Nature **452**, 970-974 (2008).

[179] F. D. M. Haldane and S. Raghu, Phys. Rev. Lett. **100**, 013904 (2008).

[180] Z. Wang *et al.*, Nature **461**, 772 (2009).

[181] G. Jotzu *et al.*, Nature **515**, 237-240 (2014).

[182] C.-Z. Chang *et al.* Science **340**, 167 (2013).

[183] H. Hafezi, E. A. Demler, M. D. Lukin, and J. M. Taylor, Nature Physics **7**, 907 (2011); M. Hafezi, S. Mittal, J. Fan, A. Migdall, and J. M. Taylor, Nature Photonics **7**, 1001 (2013); M. C. Rechtsman, J. M. Zeuner, Y. Plotnik, Y. Lumer, D. Podolsky, F. Dreisow, S. Nolte, M. Segev, and A. Szameit, Nature (London) **496**, 196 (2013); I. Carusotto and C. Ciuti, Rev. Mod. Phys. **85**, 299 (2013); J. Koch, A. A. Houck, K. Le Hur, and S. M. Girvin, Phys. Rev. A **82**, 043811 (2010); A. A. Houck, H. E. Tureci, and J. Koch, Nature Physics **8**, 292 (2012); K. Fang, Z. Yu, and S. Fan, Nature Photonics **6**, 782787 (2012); V. G. Sala *et al.*, Phys. Rev. X **5**, 011034 (2015); A. B. Khanikaev *et al.*, Nature Materials **12**, 233 (2013).

[184] D. A. Pesin and L. Balents, Nature Phys. **6**, 376 (2010).

[185] K. Le Hur and T.M. Rice, Annals of Physics **324**, 1452-1515 (2009).

[186] A. Ruegg and G. A. Fiete Phys. Rev. Lett. **108**, 046401 (2012). M. Araujo, E. Castro and P. Sacramento, Phys. Rev. B **87**, 085109 (2013).

[187] D. Cocks *et al.* Phys. Rev. Lett. **109**, 205303 (2012); P. P. Orth *et al.* J. Phys. B: At. Mol. Opt. Phys. **46** 134004 (2013); M. S. Scheurer, S. Rachel and P. P. Orth Sci. Rep. **5**, 8386 (2015).

[188] Yean-an Liao, et al. Nature **467**, 567-569 (2010).

[189] C. Gros, D. Poilblanc, M. Rice, F.C. Zhang, Physica C. **153-155**, 543 (1988).

[190] M. Inui, S. Doniach, P.J. Hirschfeld, A.E. Ruckenstein **37**, 2320 (1988).

[191] F.C. Zhang, T.M. Rice, Phys. Rev. B **37**, 3759 (1988).

[192] P.W.Anderson, Science **235**, 4793 (1987).

[193] D.Sénéchal, P.-L. Lavertu, M.-A.Marois, A.-M.S. Tremblay **94**, 156404 (2005).

[194] H.Eisaki, H.Takagi, R.J.Cava, B.Batlogg, J.J.Krajewski, W.F.Peck, K.Mizehashi, J.O.Lee and S.Uchida, Phys. Rev. B **50**, 647 (1994).

[195] P.W. Anderson, P.A. Lee, M. Randeria, T.M. Rice, N. Trivedi, and F.C. Zhang, J. Phys. Condens. Matter **16**, R755 (2004)

[196] D.J.Scalapino, S.R.White, S.C.Zhang, Phys. Rev. B **47**, 7995 (1993).

[197] D.J.Scalapino, Physics Reports **250**, 329-365 (1995).

[198] T.M. Rice, K. Ueda, Phys. Rev. Lett **55**, 995 (1985)

[199] T.M. Rice, K. Ueda, Phys. Rev. Lett **55**, 2093 (1985)

[200] P. Corboz, M. Lajkó, A.M.Läuchli, K. Penc, F. Mila, Phys. Rev. X **2**, 041013 (2012); S.R.Hassan, S.K. Goyal, R.Shankar, D. Sénéchal, Phys. Rev. B **88**, 045301 (2013).

[201] M.A.Ruderman, C.Kittel, Phys.Rev. **96**, 99 (1954); T.Kasuya, Prg.Theor.Phys. **16**, 45 (1956); K.Yoshida, Phys.Rev.**106**, 893 (1957).

[202] S. Raghu, X.-L. Qi, C. Honerkamp and S.-C. Zhang Phys. Rev. Lett. **100**, 156401 (2008).

[203] A. G. Grushin *et al.* Phys. Rev. B **87**, 085136 (2013).

[204] T. Duric, N. Chancellor and I. F. Herbut, Phys. Rev. B **89**, 165123 (2014).

[205] C. Weeks and M. Franz, Phys. Rev. B **81**, 085105 (2010).

[206] F. D. M. Haldane, Phys. Rev. Lett. **50**, 1153 (1983) and Phys. Lett. A **93**, 464 (1983); I. Affleck and F. D. M. Haldane, Phys. Rev. B **36**, 5291 (1987); I. Affleck, J. Phys.: Condens. Matter. **1**, 3047 (1989).

[207] I. Affleck, T. Kennedy, E. H. Lieb and H. Tasaki, Phys. Rev. Lett. **59**, 799 (1987).

[208] M. Dzero, K. Sun, V. Galitski and P. Coleman, Phys. Rev. Lett. **104**, 106408 (2010).

[209] N. Xu *et al.*, Nature Communications **5**:4566 (2014).

[210] L. Tarruell *et al.* Nature **483**, 302-305 (2012); G. Grynberg, B. Louinis, P. Verkek, J.-Y. Courtois, and C. Salomon, Phys. Rev. Lett. **70**, 2249 (1993).

[211] M. W. Zwierlein *et al.* Nature **435**, 1047 (2005).

[212] M. Taglieber *et al.* Phys. Rev. Lett. **100**, 010401 (2008).

[213] Z.-F. Xu et al. Arxiv 1407.3720; Z.-X. Liu, Z.-C. Gu, X.-G. Wen, Arxiv 1404.2818; P. P. Orth, D. L. Bergman, K. Le Hur, Phys. Rev. A **100**, 80, 023624 (2009); H. P. Büchler and G. Blatter, Phys. Rev. Lett. **100**, 91, 130404 (2003).

[214] M. A. Ruderman and C. Kittel, Phys. Rev. **96**, 99 (1954); T. Kasuya, Prog. Theor. Phys. **16**, 45 (1956); K. Yosida, Phys. Rev. **106**, 893 (1957).

[215] M. Sigrist and K.Ueda, Rev. Mod. Phys. **63**, 239, (1991).

[216] B. Uchoa and A.-H. Castro-Neto, Phys. Rev. Lett. **98**, 146801 (2007).

[217] J. Gonzales, F. Guinea and M. A. H. Vozmediano, Phys. Rev. B **63**, 134421 (2001).

[218] D. Bergman and K. Le Hur, Phys. Rev. B **79**, 184520 (2009).

[219] A. -M. Black-Schaffer and S. Doniach, Phys. Rev. B **75**, 134512 (2007).

[220] R. Nandkishore, L. Levitov and A. Chubukov, Nature Physics **8**, 158-163 (2012).

[221] A.-M. Black-Schaffer, W. Wu and K. Le Hur, Phys. Rev. B **90**, 054521 (2014).

[222] W. Wu, M. M. Scherer, C. Honerkamp and K. Le Hur, Phys. Rev. B **87**, 094521 (2013).

[223] S. Sorella, Y. Otsuka and S. Yunoki, Scientific Reports **2**, 992 (2012).

[224] J.Motruk *et al.* Phys. Rev. B **92**, 085147 (2015); S.Capponi *et al.* Phys. Rev. B **92**, 085146 (2015).

[225] T. Pereg-Barnea, G. Refael, Phys. Rev. B **85**, 075127 (2012).

[226] X. Liu, Jay D. Sau, S.D.Sarma, Phys. Rev. B 92, 014513 (2015)